COMPUTATIONAL FLUID DYNAMICS ANALYSIS IN PRE-SURGERY PLANNING FOR CONGENITAL HEART DEFECT REPAIRS

A DISSERTATION SUBMITTED TO

THE GRADUTE SCHOOL OF

ENGINEERING AND NATURAL SCIENCES

OF ISTANBUL MEDIPOL UNIVERSITY

IN PARTIAL FULFILLMENT OF THE REQUIREMENTS FOR

THE DEGREE OF DOCTOR OF PHILOSOPHY

IN

BIOMEDICAL ENGINEERING AND BIOINFORMATICS

By

Kevser Banu Köse

October, 2019

COMPUTATIONAL FLUID DYNAMICS ANALYSIS IN PRE-SURGERY PLANNING FOR CONGENITAL HEART DEFECT REPAIRS

By Kevser Banu Köse
October, 2019

We certify that we have read this dissertation and that in our opinion it is fully adequate, in scope and in quality, as a dissertation for the degree of Doctor of Philosophy.

Prof. Dr. Kerem Pekkan

Prof. Dr. Ece Salihoğlu

Prof. Dr. Ufuk Şakul

Assist. Prof. Dr. Murad Kucur

Assoc. Prof. Dr. Yasemin Yüksel Durmaz

Approved by the Graduate School of Engineering and Natural Sciences:

Assoc. Prof. Dr. Yasemin Yüksel Durmaz

Director of the Graduate School of Engineering and Natural Sciences

I hereby declare that all information in this document has been obtained and presented in accordance with academic rules and ethical conduct. I also declare that, as required by these rules and conduct, I have fully cited and referenced all material and results that are not original to this work.

Name, Last Name: Kevser Banu Köse

Signature:

ABSTRACT

COMPUTATIONAL FLUID DYNAMICS ANALYSIS IN PRE-SURGERY PLANNING FOR CONGENITAL HEART DEFECT REPAIRS

Kevser Banu Köse
Ph.D. in Biomedical Engineering and Bioinformatics

Advisor: Prof. Dr. Kerem Pekkan
October, 2019

The treatment of complex congenital heart diseases (CHD) requires a careful patient-specific approach and surgical correction plan. In this thesis, a large radiological database was created to provide supportive information for the treatment planning of patients undergoing aortic hypoplasia, pulmonary stenosis, ventricular septal defect (VSD) and Fontan procedure. State-of-the-art repair alternatives using customized baffle and patch designs were virtually generated in the computer through image-based three-dimensional (3D) modeling, and their structural and hemodynamic analysis are evaluated. In aortic repair section, different virtual repair methods were performed for each selected hypopilastic aortic arch models. Blood flow analyzes were compared in preoperative, postoperative and virtual repair models. The methods were examined by computational fluid dynamics analysis in terms of velocity, wall shear stress and pressure distributions. In the pulmonary artery stenosis section, the deformation of the patch material was evaluated by computational structural analysis. In Fontan cases, the aim was to determine the geometry giving the optimum flow distribution from hepatic veins to the lungs. In VSD cases, virtual models obtained after segmentation provided information that could not be obtained from the image data to facilitate the decision whether the obtimum treatment by catheter intervention or surgery. It has been observed that the findings obtained by 3D modeling, virtual repair and numerical analysis can make significant contributions to the process of determining the repair method. Overall this dissertation aims to provide solution-oriented information to planning procedures in CHD treatment and to present more objective, case-specific and reproducible planning options with computerized modeling and numerical simulation techniques in the light of concrete data.

Keywords

Congenital Heart Disease, Computational Modeling, Surgical Planning, Hemodynamics, Blood Flow, Cardiovascular Biomechanics, Bioengineering

ÖZET

DOĞUMSAL KALP HASTALIKLARININ TAMİRİ İÇİN AKIŞKANLAR DİNAMİĞİ HESAPLAMALARI İLE AMELİYAT ÖNCESİ PLANLAMA

Kevser Banu Köse
Biyomedikal Mühendisliği ve Biyonenformatik, Doktora

Danışman: Prof. Dr. Kerem Pekkan
Ekim, 2019

Kompleks doğumsal kalp hastalıklarının (CHD) tedavisi hastaya özel dikkatli bir yaklaşım ve onarım planı gerektirir. Bu tez çalışmasında, geniş bir radyolojik veri tabanı oluşturulmuş; aort hipoplazisi, pulmoner darlık, ventrikül septal defekt (VSD) ve Fontan prosedürü uygulanan hastaların tedavi planlamasına mühendislik yaklaşımlarıyla destekleyen yardımcı bilgi sağlamak amaçlı bir yöntem geliştirilmiştir. Görüntü tabanlı üç boyutlu (3B) modelleme, yapıya özel şant ve yama tasarımı, hızlı prototipleme, bilgisayarlı yapısal ve hemodinamik analiz yardımı ile çeşitli sanal tamir yöntemleri ile oluşturulan modeller sonlu eleman analizleri sonrasında karşılaştırılmıştır. Seçilen aort hipopilazisi vakalarının her biri için birbirinden farklı sanal tamirler uygulanarak; kan akışı analizleri ameliyat öncesi, sonrası ve sanal tamir modellerinde karşılaştırılmıştır. Hastaya özel damar geometrisine uygun tamir yöntemi hız, kayma gerilimi ve basınç dağılımları açısından hesaplamalı akışkanlar dinamiği analizi ile irdelenmiştir. Pulmoner arter darlığı bölümünde hastaya özel yamanın deformasyonu da hesaplamalı yapısal analiz ile değerlendirilerek elde edilen modellerde akış simülasyonları yapılmıştır. Fontan vakalarında hasta için ortalama on farklı sanal şant konfigürasyonu oluşturlarak hesaplamalı akış görelleştirmeleri ile optimum akış dağılımını veren geometrinin belirlenmesi amaçlanmıştır. VSD vakalarında segmentasyon sonrası elde edilen sanal modeller ile görüntü verisinden sağlanamayan enformasyon sağlanabilmiş ve tedavinin kateter girişimi ile ya da cerrahi olarak çözümlenmesi kararını kolaylaştıracak bulgular elde edilmiştir. Üç boyutlu modelleme, sanal tamir ve sonlu eleman analizi ile elde edilen bulguların CHD tedavisini belirleme sürecine anlamlı katkılar sağlayabildiği birbirinden farklı hastalıklarda ve farklı damarlarda örnekler ile gözlemlenmiştir. Bu tez, CHD tedavisinde planlama prosedürlerine çözüm odaklı bilgi sağlamayı, bilgisayarlı modelleme ve nümerik simülasyon teknikleriyle daha objektif, vakaya özel ve tekrarlanabilir planlama seçeneklerini somut veriler eşliğinde sunmayı amaçlamaktadır.

Anahtar Kelimeler

Konjenital Kalp Hastalığı, Nümerik Modelleme, Cerrahi Planlama, Hemodinamik, Kan Akisi, Kalp Damar Biyomekanigi, Biyomühendislik

ACKNOWLEDGMENT

I want to express my appreciation to my advisor Prof. Dr. Kerem Pekkan, and all members of Biofluid Mechanics Laboratory at Koç University as well as to the faculty members of Biomedical Engineering Faculty of Medipol University, and Dr. Deniz Erbulut at University of Toledo. On the clinical arm, I had a chance to work with amazing mentors: Particularly, Prof. Dr. Ece Salihoğlu at Florence Nightingale Hospital, Dr. Okan Yıldız at Istanbul M. Akif Ersoy Chest Vascular Surgery Hospital, Assoc. Prof. Ahmet Şaşmazel at Siyami Ersek Vascular Surgery Training and Research Hospital, Prof. Dr. Ender Ödemiş at Acıbadem University Atakent Hospital, Şeyma Öztürk at Medipol University Mega Hospital Intensive Care Unit, and Dr. Volkan Tuncay at Philips Research Eindhoven.

This work was supported in part by The Scientific and Technological Research Council of Turkey (TUBITAK) under project (grant) number 115E691 (ARDEB) with the name of *"Computer Assisted Cardiovascular Pre-Surgery Planning and Patch Conduit Design for Congenital Heart Disease Patients"*.

Kevser Banu Köse
2019, Istanbul

CONTENTS

LIST OF FIGURES

LIST OF TABLES

CHAPTER 1

1. INTRODUCTION

In congenital heart disease cases, a complete understanding of the complex cardiac anatomy by the clinicians is extremely critical [1][2][3][4]. Interpretation of congenital anatomies, deciding on optimal surgical planning strategy and treatment is influenced by the patient's age and varies from childhood to adult, require years of clinical experience and expertise. In adult congenital cases, follow-up of 3D variations of anatomy is essential due to vascular growth and remodeling. Although high-resolution image data is recently available due to the developments in radiological imaging methods; these imaging techniques are not widely applied in congenital heart diseases and result in inefficient morphological information [5][6][7]. Therefore it is hypothesized that through the support of advanced engineering methods, the substantial clinical impact can be achieved through new validated anatomical information that will aid our understanding of morphology and allow pre-surgical planning processes.

Decision making and predicting intraoperative problems are significant in complicated CHD cases. Advanced engineering methods can contribute to achieving meaningful results by displaying a decision support system. Advanced engineering methods can contribute to achieving meaningful results by displaying a decision support system. Thus, pre-planning studies can be carried out with the contribution of quantitative data and visualization results [6][8][9][10].

In order to determine and follow the results, which can be considered as evaluation criteria in the circulatory system, measurements are made with different methods. The systems used should be in an easily applicable, reproducible, non-risky, and poses

acceptable cost-benefit balance [11]**.** However, these methods when used alone, may be limited in providing sufficient information.

While limited data can be obtained by monitoring, a numerical hemodynamic analysis can provide valuable information about the circulatory system problems by calculating parameters that are otherwise could not be measured clinically.

Numerical simulations of virtual scenarios and the patient-specific analysis of blood flow are realized, which provided useful assistance to the decision-making process of the treatment and the follow-up procedures [12][13]**.**

1.1 Literature Review

The heart supplies adequate blood flow and therefore delivers oxygen to the body. The inability of the circulatory system is the main character of all heart diseases. Any physiological or morphological problem that disrupts the heart function process can turn into a significant problem that can affect the whole body and systems. Cardiovascular disease (CVD) is a general term describing the conditions affecting the vascular system. The heart is a sophisticated functional organ that plays a central role in blood circulation [14]. CVD is the highest cause of mortality [15], and it contributes to approximately 30% of deaths globally [14],[16].

The main types of CVD include coronary artery disease, arrhythmias, congenital heart disease, heart valve disease, congestive heart disease, rheumatic heart disease, stroke, and high blood pressure, narrowed arteries. Heart and vascular malfunctions in children are most commonly attributable to concomitant CHD, with different risk factors depending on the specific type of malformations that are usually diverse and heterogeneous. It is the most common congenital disabilities among newborns [17][18]. Due to the variability in the cardiovascular morphology between individual patients, treatment management, and predicting future outcomes of repair, can be very challenging [19]. Congenital heart disease, with its critical and sometimes fragile physiology, combined with its complexity and rarity, challenges the training of a pediatric cardiovascular surgeon [20]. It is, therefore, considered to have a comprehensive perspicacity of dimensional and spatial contacts of the anatomical structures of the system, especially during preoperative planning or intra-operative

orientation [18]. Therefore, the effects of structural differences on the blood flow, the parameters that are specific to the individual, the optimum repair method to be preferred, and the many parameters related to them should be considered carefully. The most crucial factor in the treatment, of fetal and pediatric diseases is the decision-making process and the growth in tissues should be considered carefully.

The heart, which is a dynamic organ, must be able to ensure the proper functioning and continuity of the system, which can deform the internal and external mechanical effects and the blood flow. Blood flow phenomena have been studied for centuries, where one of the aims was to understand the conditions that contribute to circulatory system repairs.

Whether blood flow swirling in the heart or streaming through the arterial tree, various mathematical models have been assisted in quantifying the hemodynamic context in the cardiovascular system [21]. Cardiovascular system dynamics have been modeled with interdisciplinary methods using various analogies. The lumped parameter modeling has been employed as a reduced-order approximation of blood flow. Significant progress in mathematical modeling of the cardiovascular system has been achieved since the 90s [22][23]. More recently, image-based studies have become popular in evaluating blood flow, the mechanical effects that shape vessels and the mechanical consequences of flow [24][25][26]. Physical systems based on the models created by utilizing the actual imaging data of the patients and simulating the flow through these models have progressed significantly [3][27][28]. Many research groups have studied these methods to examine the pathogenesis of circulatory system diseases, endothelium wall deformations, vascular system dynamics, and surgical repair outcomes [29][30][31]. There are numerous investigations on modeling circulatory system and numerical analysis of aneurysmal and occlusive carotid and coronary arteries [32][33][34][35], aorta [36][37][24] pulmonary [38][27] and the cerebral arteries [39][40]. 3D circulatory system modeling has provided much information about pathology, the mechanical background of the blood flow behavior, and the soft tissue response to the flow dynamics [41][42][43].

Cardiovascular numerical analysis can be grouped into three branches; fluid flow, fluid-structure interaction, and structural analysis.

As such these individualized treatment methods have been used to predict rupture risk of aneurysms [44][45], comparing patch materials [30], defining the optimum surgical method [46][4] or testing a novel biomaterial [47] [48][49][50].

A precise evaluation of congenital heart defects anatomy is essential for optimal surgical planning [51][52][53]. This invaluable information is beneficial for surgical decision-making because even minor anatomical details can indicate the optimal surgical approach in each patient with a complex congenital heart defect [54] [55] [56]. Hence, the use of 3D virtual heart models allows the clinician to avoid unexpected findings during the actual interventions, especially in rare congenital heart defects [51][57][58][59][60][61]. Mathematical modeling and computer-aided design (CAD) tools were used extensively [62][6][9]. Through these methods, different surgical scenarios could be performed virtually and compared with each other [63][64][65][66]. Numerical calculations and flow regimes in these various models were evaluated [67][68][69]. For CHD, clinically relevant parameters were added to the surgical planning process [46]. Significant indications were obtained by performing computer-aided calculations to arrange the factors affecting the flow or the flow-related effects and to make the most accurate operation plan for the treatment of CHD [70][8][29][71]. With these validated methods, it was possible to evaluate repair methods, to test new surgical approaches, or to develop customized biomaterial designs [72][73][74]. Furthermore, the patient-specific models of the cardiovascular system are also used in the development of novel medical devices [75] [47][50].

In order to appraise the creation and functionality of innovative medical devices, the need to present a clinical need, a detailed 3D anatomy data of the location to be implanted and the structural region connected, should be evaluated and compared in different experimental subjects and the condition under physiological conditions should be evaluated. These are the mechanical factors applied to the device, and the load exerted by the device on the tissue, as well as the off-design conditions that occur [76][77][39][30].

However, the ability to generate 3D physical models from virtual reconstructions of complex anatomic structures is critical when the medical image data was not enough for understanding the structural details, or the on-screen models were not sufficient for complicated cases with rare critical abnormalities. In addition to positively

impacting the diagnostic and remedial approach, 3D printed models influence treatment by providing an opportunity to perform detailed and precise preoperative planning [78][7][79][80][57]. The use of 3D models enhances understanding of the complex anatomy, so these models are valuable for pre-operative planning and intra-operative orientation [80][81][82][83][18].

Therefore in this thesis, an image-based 3D patient-specific cardiovascular modeling and printing system is developed for surgical planning through the virtual surgery concept for the comparison of repair methods in CHD.

1.2 Cardiovascular System

The cardiovascular system is composed of the heart, veins, arteries, capillaries, and lymphatic components. The task of the cardiovascular system is assuring the oxygen and nutrients, removing waste, and adjusting the temperature [84].

The heart is a muscular organ composed of two pumps in parallel. The right side collects de-oxygenated blood from the systemic vessels and provides perfusion to the lungs. The left side collects oxygenated blood from the pulmonary veins and feeds the rest of the body. The heart has four chambers: upper left (LA) and right (RA) atria that collect the blood from the veins and lower left (LV) and right (RV) ventricles that contract to send the blood into the systemic and pulmonary veins (Fig.1.1) [85]. The oxygenated blood from the lungs is filled with LA from the pulmonary veins. Switch to LV with the mitral valve. With the LV contraction, the previous valve is closed, the aortic valve is opened, and the entire body is pumped with an aortic vein.

The deoxidized blood is brought to the right atrial cavity by the vena cava. From here, the tricuspid closes from RV to RV. When RV is contracted, the previous valve closes, and the lower pulmonary valve opens.

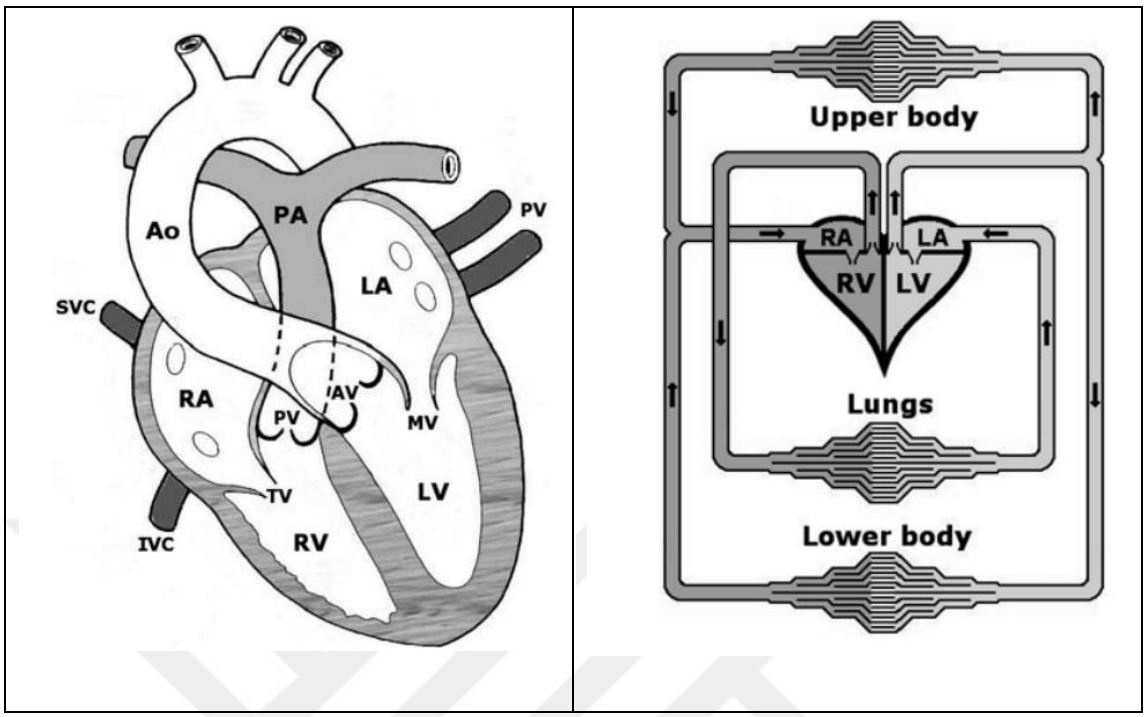

Figure 1.1 A sketch of a cross-section of the heart (left) and cardiovascular system (right). Left atrium (LA), Left ventricle (LV), Right atrium (RA), Right ventricle (RV). Aorta (Ao), Pulmonary artery (PA), superior vena cava (SVC), inferior vena cava (IVC), pulmonary veins (PV). Tricuspid valve (TV), aortic valve (AV), pulmonary valve (PV), mitral valve (MV) [85]. In single ventricle defects, LV is not adequately developed with/without some valve defects and a septum between LV and RV.

1.3 Intracardiac Malformations

Malformations within the heart cavity are significant in CHD. Ventricular abnormalities, septal defects, double outlet right ventricle (DORV), hypoplastic left heart syndrome (HLHS) transposition of the great arteries (TGA) are included in this group [86][55].

The majority of intracardiac malformations are septal defects, as it is common to have ventricular septal defects (VSD) together in other disorders. During embryonic development, the septum between the ventricles closes before birth [87][88].

Delayed closure before birth may cause higher pressure on the right side or lead to reduced oxygen saturation. Usually, the left side of the heart only pumps blood to the systemic circulation, and the right side of the heart pumps blood to the lungs. In a child with VSD, blood can mix through the hole from the left ventricle to the right ventricle and into the pulmonary arteries [89]. A large VSD allows more blood, heart,

and lungs to go to the lungs to work more, and the lungs may become clogged. Over time, this can cause permanent damage to the lung and blood vessels.

Septal defects are not only in the ventricle and maybe between the left and right atriums, similarly. Atrial septal defect (ASD) is a common congenital disability in the septum between the upper two chambers of the heart. However, a proportion of newborns with ASDs may have complicated pulmonary hypertension with a subsequent significant impact on management, morbidity, and mortality [90].

Another spectrum of intracardiac malformations includes DORV, in which both the arteries arise primarily from the right ventricle. Both the pulmonary artery and the aorta carrying blood from the heart to the body come from the same ventricle. Aorta and pulmonary artery are not attached to the left ventricle in DORV. Oxygenated blood from the lungs flows the left side of the heart, the VSD opening, and the RV. This allows oxygen-rich blood mixing with oxygen-poor blood. This arrangement results in lower oxygen saturation, and the heart needs to work harder to meet the perfusion demands of the tissues. There are different types of DORV according to the morphology of the ventricle, defect, and arteries.

Another common congenital abnormality is TGA, in which the two big arteries leaving the heart are reversed or not correctly connected [91]. The aorta is connected to the right ventricle instead of the left ventricle. The pulmonary artery is also connected to the left ventricle. Therefore, the blood pumped into the body is deficient in oxygen, and the blood returned to the lung [92][86].

According to morphological differences, different types of TGA are also defined with a large variety of atriovenous, ventriculoarterial, and arteriovenous discordance [93].

As illustrated through these CHD templates, a precise understanding of the intracardiac anatomy is critical for determining the ideal surgical approach for patients with CHD [94][55]. It is principal to properly understand dimensional and spatial contacts of anatomical structures during the pre-surgical planning procedure [18][20]. The use of these imaging models may clarify complex intracardiac anatomy, and they can be insufficient to imagine the relationship between VSD and large vessels [95][79][96][6]. It is more difficult to precisely visualize and reconstruct the cardiac anatomy with a dynamically moving structure. Besides, unlike bone structures, the heart has cavities; standardized visualizations derived from contrast-

enhanced CTA are mainly volumes of contrast-filled cardiac spaces with the limitation of 2D monitors [97][98][99].

In addition to routine clinical imaging, more information should be evaluated, and morphology and physical effects should be fully understood in surgical planning. The 3D virtual models, created in the pre-operative decision-making process, cover this deficiency when the imaging data is not sufficient. This is performed by image processing, segmentation, and computer-aided design tools of calculating a bulk by volume of the heart and subtracting the "blood pool contrast agent" section, as mentioned in CHAPTER 3.

Percutaneous interventions related to many structural heart diseases are widespread. Many diseases that have previously been treated with open-heart surgery can now be successfully performed in the heart catheterization laboratory.

If the diagnostic data can be collected before the intervention or surgery, it will be uncomplicated to make the right decision [100][101][102]. Furthermore, the published data on 3D modeling and printing in CHD are limited to single reports. This situation stimulated this thesis study to present our multi-center experience with 3D virtual models in cardiac surgery and interventional cardiology.

In limited-resource environments, complex cases with potential for biventricular corrections usually fall into single ventricular palliations due to uncertainty and resource constraints on the technical feasibility of repair complications.

There is a deliberative effort to perform the total correction even in technically challenging lesions with increasing expertise, but the efficient use of resources is essential [103][104]. DORV and TGA are conotruncal defects characterized by abnormal ventriculoarterial (VA) relationships [53]. After all, there is a broad range of variable pathologies for them [53][59]. In these patients, the relationship between ventricles, large arteries, and VSD, and the condition of atrioventricular valves determine the shape of the proper surgical approach with a reduced time [62].

1.4 Coarctations

Aortic coarctation is generally defined as a narrowing of the segment of the descending aorta in the isthmus (or the connection of the distal duct to the left

subclavian artery). The coarctated and adjacent segment of the aorta is associated with excessive collagen and reduced smooth muscles [105][106]. Consequently, impaired blood flow and nitroglycerin are reduced and result in vasodilation [107]. It is said that a hypoplastic aortic arch is present, similar to a coarctation when the aortic arch is occluded at a particular location. Unlike coarctation, the larger section of the aorta is blocked, and therefore the condition is more severe and requires complicated surgery to correct. The hypoplastic aortic arch can be seen in 81% of patients with aortic coarctation. VSD, tetralogy of Fallot, TGA, and other congenital anomalies such as DORV may occur [108].

In the presence of coarctation and hypoplasia of the aorta, the left ventricle must work more because it must produce a higher-than-normal pressure to force blood from the narrow lumen of the aorta to the lower part of the body [109][37]. If the contraction is very severe, the ventricle may not be strong enough to perform this extra work; this may result in congestive heart failure or insufficient blood flow to the organs. Treatment of cases of aortic stenosis or interruption also requires a very detailed planning approach. Geometric changes and hemodynamic limits caused by the correction method should also be considered. Abnormal aortic arch shape, folds, or lack of central blood flow as expected after repair may cause arterial hypertension [110].

The clinicians should be able to make a careful and detailed decision-making process in order to avoid the wrong correctşon methods when the aortic stenosis is asymptomatic. Future results should also be taken into consideration, as the selected method and the failure to altogether remove the problematic tissue may cause new problems in the growth process. The lumen associated with an increase in stiffness or an increase in central blood pressure is high due to geometric changes in the aorta with age, and these changes can be accelerated over time. However, there are studies with increased collagen deposition in the aorta close to the previous narrowing site in repaired aortic patients [111][112]. There is also evidence that the type of surgical intervention may affect the prevalence of hypertension in the long term. Results of end-to-end anastomosis repairs show a lower percentage of systolic blood pressure. However, for each case of the aorta, it may be possible to say which method would be more accurate when the shape of the coarctation or hypoplasia segment, the vessel

lumen, the repair method and the variations within the method were evaluated individually for the patient [110][113][114].

1.5 Fontan Procedure

The Fontan procedure is a procedure used in complex congenital heart diseases with a single functional ventricle, where bi-ventricular repair is impossible or not recommended [53], [55]. A single ventricular anomaly is used to identify a group of heart defects that can be quite dramatically different from each other [46][115][17]. These defects (such as tricuspid atresia, hypoplastic left heart syndrome, double-entry left ventricle, Heterotaxy defects, some variations of the right ventricle double outlet, etc.) share the common feature that only one of the two ventricles has sufficient functional size [92].

The Fontan procedure refers to the surgical procedure that results in systemic venous blood flowing through a ventricle into the lungs without passing through the usual way [116][117]. That is the last of the corrections realized in a three-step process (Figure 1.2).

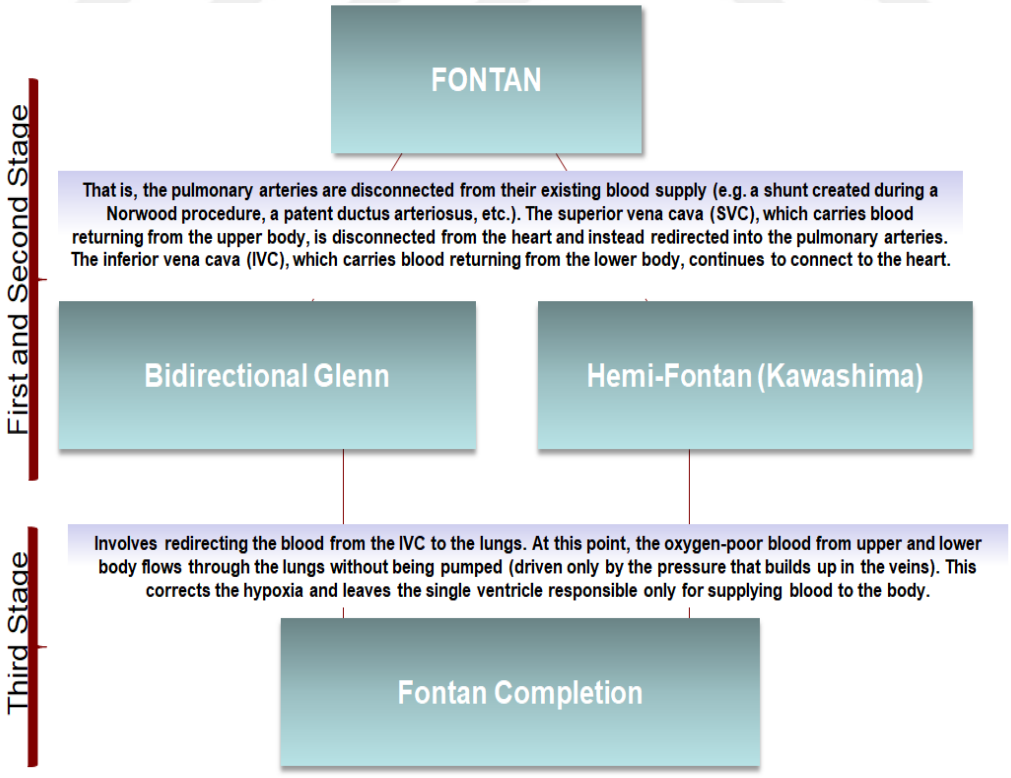

Figure 1.2 The Fontan repair procedure in CHD.

The trio of these surgeries includes a palliative solution for single ventricular patients. The first step of the surgical sequence is the Norwood Procedure [116]. The functional ventricle provides support for blood flow through a shunt. The second surgery is the Glenn Procedure or Kawashima [66][118]. Glenn connects the main artery and the pulmonary artery, which directs the weak oxygen to the upper half of the body. In Kawashima, however, in patients who discontinue IVC, most of the blood from the lower body combines blood from the upper body before returning to the heart through the upper vena cava (SVC). In both cases, the blood flow to the lungs is controlled. However, after Kawashima, the only de-oxygenated blood that returns to the heart is the abdominal organs (via hepatic veins). Kawashima is more preferred in heterotaxy patients [63].

Heterotaxy is an abnormal arrangement of specific organs and vessels associated with dysmorphism, which can be diagnosed by prenatal diagnosis with important diagnostic markers such as complex cardiac malformations, inferior vena cava anomalies, or slow heart rate [119][120].

As a result, there is less hypoxia than Glenn, and the heart pumps less blood than Glenn. However, hypoxia may worsen over time (due to the development of microscopic arteriovenous malformations that allow blood to pass through oxygenation in the lungs), and completion of the correction by Fontan procedure is expected for delivery of hepatic growth factors to the lungs and venous connection [3][121].

The third stage is the Fontan procedure. In this procedure, the surgeon directs the blood flow from the lower body to the lungs, which connects the inferior vena cava or azygous to the pulmonary artery if there is an inferior vena cava without continuity. Thus, a new connection channel is created [66]. The blood flow through the lower body is thus joined to the connection made in the second stage with this stage. Hepatic growth factors in the liver should be distributed equally to the right and left lungs in patients with Hetorataxia and atrial isomerism [120][79]. Although these growth factors have been scientifically proven to be critical, it is necessary to implant the conduit connection, the final stage of the Fontan procedure, in the position and configuration to provide accurate hemodynamic results in order to allow the hepatic growth factors necessary to achieve acceptable growth in a lung [122][121][3].

1.6 Congenital Heart Disease with Focus on Hemodynamics and Blood Flow

CHD has been designated as the presence of ‘a gross structural abnormality of the heart or intra-thoracic great vessels that are actually or potentially of functional significance’ [18].

CHD involving the cardiovascular system continues to be the crucial actor in newborn mortality related to congenital malformations.

Certain types of CHD, such as VSD, are not evident until a severe decline in pulmonary vascular resistance occurs. These anomalies have emerged during fetal development and are therefore noticeable during delivery or with fetal evaluation.

Some cases can only be realized when some symptoms appear in the postnatal growth process. Coarctation cases can also be diagnosed within weeks of growth, sometimes after a few months.

Additionally, there are several lesion groups thought to represent CHD. These can be genetic (a), arrhythmic (b), metabolic (c), and structural problems (d). Marfan Syndrome, Williams Syndrome, hypertrophic cardiomyopathy, and pulmonary hypertension are cardiovascular outcomes in the early period (a). Ventricular abnormalities producing ventricular pre-excitation pathways and long QT syndrome creates arrhythmic problems in the system (b). Cardiomyopathies with a genetic or metabolic etiology are responsible for some CHD types (c). Valvular anomalies and septal defects associated with and without arterial duct are some of the representative CHD samples (d). Persistent patency of the arterial duct in premature neonates is mostly related to newborn cardiovascular system dysfunctions (e) [123][124][86].

Long term survival rates of newborns having congenital heart diseases increase in parallel with investigations in medical and engineering domains. However, in most cases, this improved survival does not imply treatment of congenital heart disease but instead leads to improved palliation. These mature patients experience a sequela of heart disease and often undergo medical, pharmacological, and recurrent surgical intervention [1][86].

It is vital to make an accurate and useful treatment plan for these dysfunctions and to produce the patient-specific quality of health. On account of this, early diagnosis of CHD, meticulously obtained data to assist in treatment planning, choosing the

likeliest method for the patient's anatomy, improving the health status in proportion to the infant's growth, and predicting the situation for the future periods are vital.
In the congenital anomalies, the specific morphology and hemodynamic status of the cardiovascular structure should be evaluated thoroughly [125][71].

Because of the structural variations in connection with the growth process of the infant, the outcome of these changes on the flow, the mechanical effects of the system in the artery walls, and on the chamber walls can appear.

Many parameters, such as the effect on the system components, should be decided in the presence of preliminary studies [94][41][126].

The cardiovascular system is highly dynamic throughout life due to changes in growth and other physiological factors [84][127][128][129]. There is a bi-directional relationship between cardiovascular growth and endothelin shaping, with loads acting on hemodynamic forces or system components, such as the blood pressure and flow regime [22][127][54]. Mechanical stimuli due to blood flow (pressure and shear stress) have been shown to affect the endothelial structure. For example, wall tension can be predicted as the product of vessel radius and blood pressure. Initially, chronic changes in wall tension driven by increases in pressure are believed to be stimulants for vessel thickening, which can then restore wall shear stress (WSS) to the preferred operating range [33]. The deformation may also have consequences such as aortic deformation as in hypertension [122]. Quantification of blood flow is the most critical factor in cardiovascular hemodynamics [130]. Hemodynamic is the science that explains the motion of the blood in connection with the circulatory system and the factors affecting it through physical laws [11]**.** The understanding and quantification of the blood flow dynamics of the vascular system is the main subject of the treatment of CHD. To evaluate the principles and factors affecting the system-specific blood flow physics, to investigate the most appropriate treatment methods, the primary purpose of the CHD research [15].

1.7 Bioengineering Contributions in Congenital Heart Disease Treatment

The cardiovascular system is dynamic throughout life. Because of the movement of blood, growth, and other physiological factors are directly affected. There is a

significant relevance between cardiovascular development and remodeling with hemodynamic forces, such as blood pressure and flow [25][131]. Developments in engineering methods have led to the quantification of circulatory system mechanics in subject-specific anatomical and physiological models, and accordingly, the development of new approaches [28][77].

Mathematical models created with initial case-specific conditions, to test a hypothesis about the role of biomechanical components in cardiovascular diseases are directing cell culture and animal experiments.

These studies contributed significantly to the modeling of the arterial and venous circulation in the system, the behavior of the vascular system, and the results of the load on the components on the systemic ventricle or associated structures. Patient-specific morphology and flow have been progressively used to provide valuable clinical information with engineering methods [85][84][132]. Engineering studies, which are carried out to understand and quantify CHD, provide successful results with the contribution of many engineering disciplines. Many interdisciplinary studies such as the depiction of a physical system with mathematical language, the definition of mechanical principles, contributions of circuit analogies chemistry, and materials science are progressively increasing [133][134][15], [135]. It is essential to develop various tools to improve our knowledge of phases that contribute to the initiation and improvement of cardiovascular physiological phenomena and various congenital cardiovascular system problems. Hemodynamic loads are vital to the development of cardiovascular structural development and any changes in the shape or functionality of the cardiovascular system after delivery. Therefore, analyzing hemodynamic flow patterns and parameters of patient-specific heart models with various clinical and engineering tools can provide useful information about indicators leading to CHD, helping to develop innovative methods [15].

1.8 Research Question of the Thesis

The topics discussed in this dissertation aim to answer the following questions:

(1) Whether the virtual models generated from DICOM image data will contribute to the clinical decision support process of CHD?

(2) What is the applicability and benefit of the physical models obtained through 3D printers in the clinic?

(3) Are new image-based computational modeling approaches mainly focusing on solid mechanics and finite element modeling (FEM) possible?

The work plan of this thesis is created based on the image data of real patients, and the following topics are investigated:

- The utility of 3D modeling and prototyping studies for patients with VSD, TGA, and DORV.
- Computational hemodynamic and structural comparison of different virtual surgical techniques and configurations were accomplished for diseases of aortic hypoplasia and coarctation, pulmonary stenosis as well as heterotaxy cases to be completed by Fontan procedure.

Thus, this study is aimed to develop the contribution of image-based modeling and numerical analysis studies to complex CHD cases through clinical data.

1.9 Organization of The Thesis

In this thesis, an interdisciplinary methodology covering the clinical treatment of complex CHD cases are developed. Blood flow and related engineering parameters of different virtual repair methods for pre-surgery planning were compared. The organization of this thesis is depicted in Figure 1.3.

In the Surgical Planning section, which has the main load of the thesis study, CHD branches are nominated evaluated under the heading of surgical planning VSD, coarctation, and Fontan procedure (Figure 1.4).

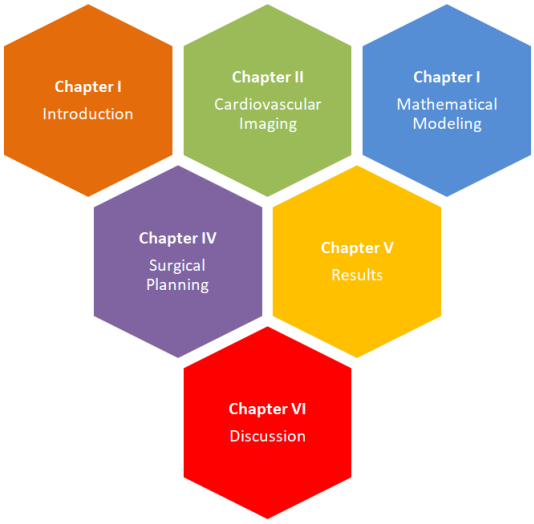

Figure 1.3 The organization of the thesis in chapters.

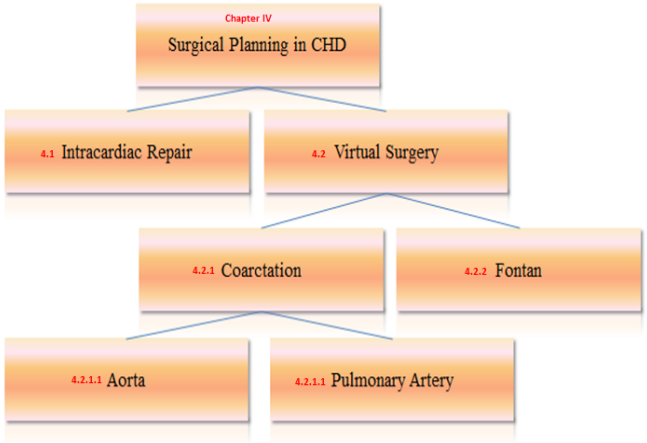

Figure 1.4 Surgical planning organization chart summarizes the diseases and anatomies studied in this thesis.

The Fontan study highlights the influence on the surgical effect of several shunt designs with various diameters and optimizes the surgery option from the following hemodynamic parameters: hepatic flow split and velocity distributions. Reconstructing intracardiac anatomy for VSD repair, blood flow behavior for coarctation, and Fontan sections and providing supportive information to the treatment decision process were discussed in terms of engineering.

CHAPTER 2

2. CARDIOVASCULAR IMAGING

Medical imaging techniques seek to elicit internal tissues hidden by the skin, fat, and bones as well as to identify and cure the disease. Medical imaging also arranges a database of healthy anatomy and physiology to make it feasible to identify abnormalities of the body.

In the diagnosis stage of CHD, image data provide essential information. Image quality is significant for the interpretation of morphology. The imaging technique, the resolution, the scanning time, and the multiplicity of sections, are the parameters that can affect the outcomes. Cardiac imaging is a sub-branch of diagnostic radiology. The complete diagnosis of CHD is provided after the inspection and interpretation of medical images accompanied by other symptoms. Structural and functional medical imaging techniques can also be used (Figure.2.1).

X-rays, ultrasound (US), magnetic resonance (MR) imaging, nuclear imaging devices such as SPECT and PET are primary image modalities involved.

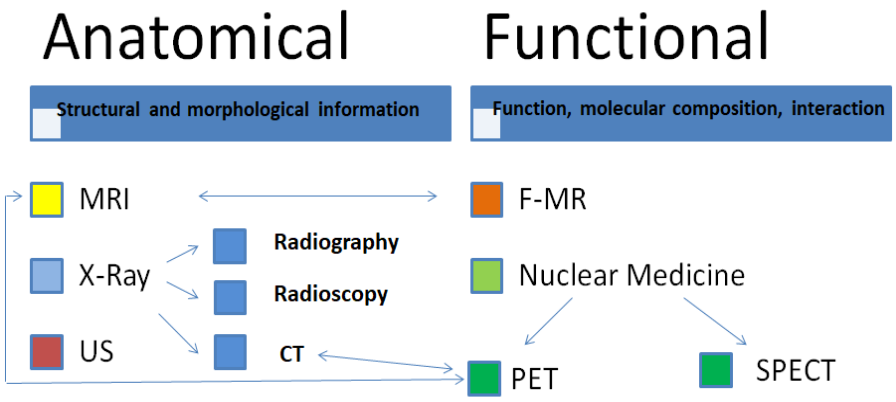

Figure 2.1 Fundamental diagnostic medical imaging modalities used in cardiac congenital heart diseases.

2.1.Imaging Modalities

Image is the definition of a scene consisting of three-dimensional objects in real life as a simple two-variable function. In other words, the medical image can be designated as a map of the 3D view on 2D. The images series can be transferred to a computer for detailed image processing.

Image processing is the creation of a new image sets by improving their properties and image quality in digital image format. In medical imaging methods other than conventional radiography, data (signal, intensity, etc.) are converted to picture elements (pixels) and volume elements (voxels). After the raw image is obtained, further image processing (repair, line capture, boundary determination, compression, decision algorithms) can be performed.

There are various methods for obtaining the image in medical imaging. These may be in the form of separate or hybrid applications. The main imaging techniques are listed as follows:

2.1.1. X-Ray Technique

Imaging techniques include Radiography, radioscopy, digital substruction angiography, fluoroscopy, and computed tomography (CT). X-ray is typically obtained by the Bremmstahlung, and Characteristic Radiations as a result of the impact of the electrons hit on a metal with a thermionic emission in the X-ray tube. Creating the projections of the tissues by the light intensity values remaining according to the degree of absorption of the tissues by X-ray, an image is formed with mapping a grey color tone to each different intensity value. Because it contains ionizing radiation, it is necessary to scan for minimal radiation exposure dose for living organisms with rapid cellular divisions.

With this technique, all of the imaging devices have their specific instrumentation. However, the main logic is the X-ray generation through accelerated electron paths and the difference of density of the mediums according to the difference of the absorption rates of X-Ray.

In this method, high-density media such as bone tissue is more comfortable to visualize. When blood flow is desired to be displayed, radiopaque contrast agents should be given invasively.

2.1.2. US Technique

Standard echocardiography (Echo), 3D transthoracic echocardiography (TTE), Intravascular ultrasound (IVUS), Doppler devices use the US.

Due to the piezoelectric effect, mechanical vibration is generated by oscillating voltage, the transmission of the generated sound waves to the tissues is based on the logic of converting the reflected waves back to the electrical signal with the same transducer. Since the acoustic impedance of the mediums is different, the rotating waves differ in appearance to the tissue they come from and are distinguished accordingly. It is preferable in fetal imaging for intracellular opalescent as loss of fluid is not much. It is not as successful as soft tissues in imaging high-density textures and air gaps like bones. A gel is used between the probe and the body so that air bubbles are not obstructed.

2.1.3. MR Technique

Magnetic resonance imaging (MRI) is a medical imaging method to create images of anatomy, physiological processes, and functional processes of the body. MRI devices use strong magnetic fields, radio waves, and gradients to label cross-sections to create internal images of organs within the body.

The energy that MR uses is radio waves. This energy called radiofrequency (RF), is within the range of electromagnetic radiation. The data source is the hydrogen nucleus (protons) in cell fluid and lipids. Typically our body is insensitive to RF energy. First of all, the protons, which are our data source, need to be stimulated by RF energy. For this, the patient is placed in a powerful magnetic field. With this magnetic effect, the protons are appropriately aligned to the magnetic field and ready to be stimulated. If an RF pulse at the Larmor frequency is applied to the nucleus of an atom, the protons will alter their alignment from the direction of the main magnetic field to the direction opposite the main magnetic field. As the proton tries to realign with the main magnetic field, it will emit energy at the Larmor frequency. By varying the magnetic field across the body with a magnetic field gradient, the corresponding variation of the Larmor frequency can be used to encode the position. For protons (hydrogen nuclei), the Larmor frequency is 42.58 MHz/Tesla. The hydrogen atom has a strong magnetic

field since its nucleus consists of a single proton. Abundant in the human body, this core is ideal as a signal source.

RF energy is sent to the section to be sectioned. Protons receive this energy and, depending on the amount of energy, they deviate from their position due to the high magnetic field lines. When RF energy is cut off, protons return to their original position. They emit the energy they receive in the form of a signal. Protons act as antennas that receive and emit signals through strong magnetic fields. MR images are generated from these signals.

The meaning of grey tones in MR images varies according to the examination protocol. However, white-light tones indicate increased signal areas, and dark-black tones indicate areas with little or no signal.

Among the radiological methods, MRI is the most accurate method showing soft tissue. Angiographic images can be obtained without direct contrast because of its direct visualization.

2.1.4. Nuclear Imaging Technique

It is based on the detection of the distribution of radionuclide materials in tissues and organs using detectors and creating images in the form of images.

While conventional imaging techniques such as Computed Tomography (CT) and Magnetic Resonance Imaging (MRI) provide anatomical and morphological changes related to the pathological condition; molecular imaging techniques using radioisotopes such as Positron Emission Tomography (PET) and Single Photon Emission Computed Tomography (SPECT) allow the visualization of functional and phenotypic changes related to the pathological condition.

In the SPECT technique, gamma photons emitted in one direction from radio from pharmaceutical substances are based on the principle of creating a cross-sectional image by detecting by SPECT detectors and processing them in a computer unit and the high accuracy of the numerical measurement of volume, size, and activity made use of SPECT devices prominent.

In the SPECT technique, a single-direction gamma photon is detected, while in the PET technique, photons that are generated in the same place at the same time and spread in the opposite direction are detected. The patient is injected with radioisotopes

that emit positron. The positron is a positively charged electron, and when it collides with (-) charged electrons along its path, the conversion of mass into energy occurs. As the colliding masses disappear, the 511 KeV energy annihilation photon oscillates at 180 ° from each other in opposite directions. In this event, annihilation; (disappearance) is formed in the photons called annihilation photons. These annihilation photons, scintillating into the detector, are turned into scintillation. Scintillations are converted to electrical signals in photo-multiplier tubes. Electrical signals are processed in other electronic circuits and converted into images.

2.2. Digital Imaging and Communications in Medicine

The product obtained from the medical imaging modalities is an image dataset and is subject to the medical scanning standards for image creation, labeling, and saving for medical information systems.

The transition to digital files is affecting all industries, and healthcare is a significant beneficiary of medical informatics, information system cloud database, standards, and protocols. 'A case in point is DICOM, which stands for Digital Imaging and Communications in Medicine' [136][137]. This standard incites better collaboration between clinicians, imaging scientists in the fields related to digital radiology approaches.

2.3. Anatomical Database Organisation

Within the scope of the study plan, ethics committee permission was obtained from the TUBITAK project (ARDEB 1003 project number: 115E691 "Computer Assisted Cardiovascular Pre-Surgery Planning and Patch Conduit Design for Congenital Heart Disease Patients) data from the radiology units of partner institutions with patient consent form at regular intervals.

Extensive labeling was done so that this data could contribute not only to this study but also to subsequent similar studies and classifications and statistical data. In this way, a unique sub-database of congenital heart diseases can be created in the PACS (picture archiving and communication system), and a platform that provides a source of encrypted and protected interdisciplinary studies by a wide range of query queries has been created. The medical images of the patients were anonymized and recorded by assigning specific codes instead of names (Figure 2.2).

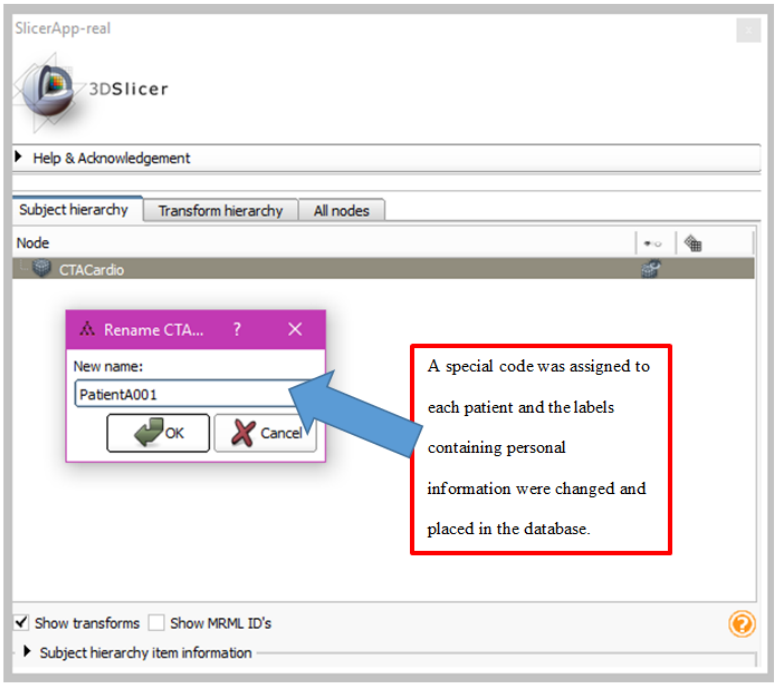

Figure 2.2 Defining code instead of a patient name in the label of DICOM datasets.

Since free DICOM cleaner platforms have been anonymized in exchange for uploading DICOM images to other servers, 3D Slicer software has been used instead of this type of platform to allow more secure and local tag changes (Figure 2.3). 3D Slicer is preferred for re-labeling the datasets [138].

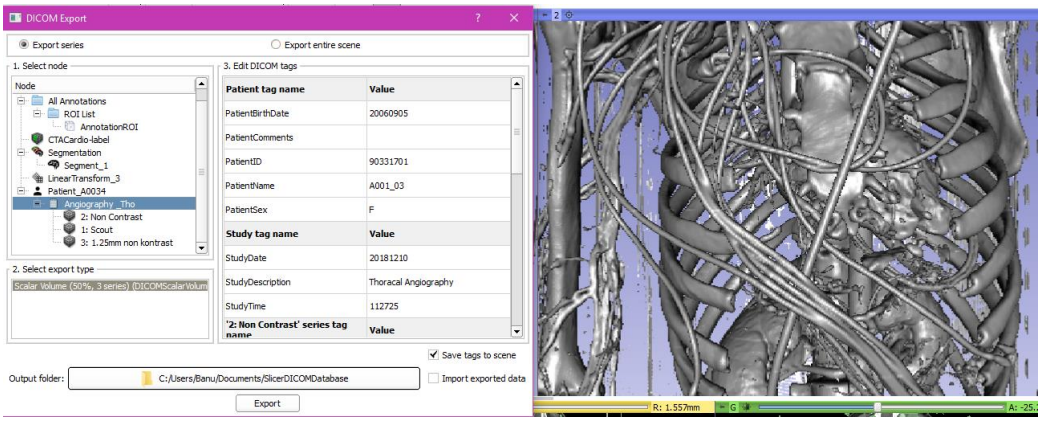

Figure 2.3 For all image data to be included in the database, it was edited to the work plan and was made on the labels and saved again.

MySql (An Oracle-backed open-source relational database management system based on Structured Query Language) is preferred for the database (Figure 2.4). As these image data are compared and evaluated in the project proposal, the labeling of the data is made as detailed as possible, since it is planned to be transformed into an

extensive database with web access and password protection in order to address a large number of researchers.

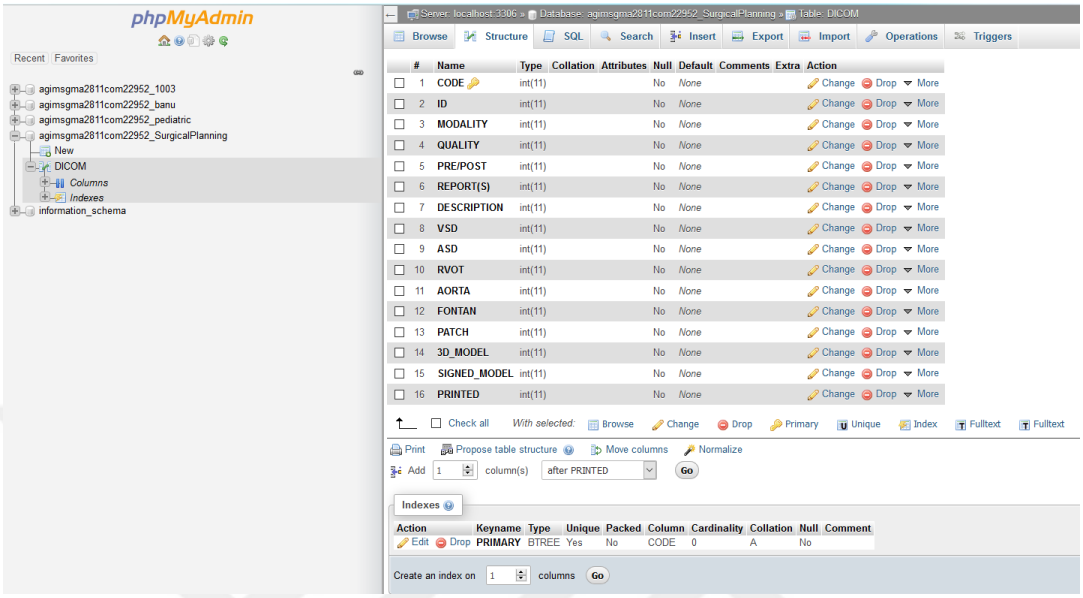

Figure 2.4 The additional labels to DICOM inputs in the project database.

Coronary artery anomalies, septal defects, and valve problems, if any, were also labeled in these patients, although the arteries to be evaluated. As the database expands, it is aimed to contribute to the studies on statistical disease relations (such as the relationship between structural defects and large artery outflow tunnels).

A hundred and five image datasets were listed in the database since the project subject included the treatment of congenital heart diseases (Table 2.1). The image data to be included in the study were added to the study database with appropriate labeling and classifications, provided that it complies with the following scanning protocols.

ACI-B-14	MR	Good	TOF		15Y
ACI-B-15	CT	Good	Aortic Aneurisym	DONE	13Y
ACI-B-16	CT	Good	Aortic Arch Coarctation	DONE	13Y
Medi-25	CT	Good	TAPVD, ASD	DONE	15 D
Medi-26	CT	Good	ASD, VSD, RPA Stenosis	DONE	
Medi-27	CT	Good	Aorta (Pre+Post), VSD, ASD, PDA, PAH	DONE	14 D
Med,-28	CT	Good	Post Op (Patch), Mitral Valve, LVOT	DONE	9 Y
Medi-29	CT	Good	VSD, Pulmonary Atresia, PDA, D-Malposed GA, Foramen Ovale	DONE	5 M
Medi-30	CT	Good	ASD, VSD, Pulmonary Atresia, Triküspit Atresia, TAPVD	DONE	11 M
Medi-31	CT	Good	VSD,TGA, Pulmonary Stenosis, ASD	DONE	10 M
Medi-32	CT	Good	TOF, ASD,RPA Hipoplasia	DONE	10 M
Medi-33	CT	Good	L-Malposed GA,PDA, Pulmonary Atresia	DONE	3 D
Medi-34	CT	Good	ASD,Pulmonary Hipoplasia	IN QUEUE	11 D
Medi-35	CT	Good	PDA, Foramen Ovale, PAH	DONE	1 M
Medi-36	CT	Good	VSD, ASD, DORV, PDA, Bilateral SVC, Right Arcus	DONE	8 M
Medi-37	CT	Good	VSD, PAH, ASD	DONE	2 M
Medi-38	CT	Good	Transvers Arcus, VSD, ASD, PAH, PDA	DONE	9 D
Medi-39	CT	Good	VSD, Pulmonary Atresia, Foramen Ovale	IN QUEUE	
Medi-40	CT	Good	VSD, Valve, Foramen Ovale, Post Op (Pulmonary Band)	DONE	1 D
Medi-41	CT	Good	Transvers Arcus, ASD, PDA, PAH	DONE	8 D
Medi-42	CT	Good	PAH, VSD, PDA, LV, Mitral Valve	DONE	1 M

Table 2.1 A sample table page of the database cases which were re-labeled and renamed.

2.4. Tested Scanning Protocols

In the planned project study, the minimum characteristics that the image data to be included in the evaluation should be carried in order to be suitable for the desired work were determined. It was clarified which protocols should be used for the output of the imaging devices (CT and MR), which can provide multi-section image data to be used in the study. The image data obtained from routine scans in different hospitals were examined, and as a result of the comparisons, the conditions that could provide the necessary and sufficient conditions for mathematical modeling were determined. The protocols established for CT and MR are as follows:

2.4.1. MR Scan Protocol:

Pediatric thoracic angiography MRI scans were performed following the following protocol requirements. Screening with congenital vascular anomalies (vascular ring, pulmonary sling, pulmonary vein anomalies, systemic-pulmonary collateral vascular structures or bronchopulmonary sequestration, and all congenital anomalies and follow-up with ve ‘Pediatric Thorax MRI Standards’ were evaluated for obtaining the proper scan requirements for segmentation of the pediatric heart and vessels.

MRI Scan Requirements:

- Clear contrast and no misalignments is a must.
- Incremental slices or equal slice distance is required.
- The more the high slice number, the more the re-construction quality.

- 1.5 Tesla MRI acquisition is recommended (not to lose ECG triggering effect).
- Holding the breath (if it is not possible, sedation practice is needed).
- Heart Rate variability affects the integrity of the examination.
- Diastolic protocol with contrast material is required.
- T1 based localizer frame images should contain the whole heart.
- Bright Blood images are required.

Position: The patient should be placed in the supine position.
Choosing coil: Choosing the coil should match the size of the kid. In general, the smallest coil that can be used should be preferred in order to obtain an optimal signal-to-noise ratio and spatial resolution.
Inspection area: It covers all the examination area required for indication and has high resolution.
Sequences and section thickness: Imaging of T1-weighted, proton density, and/or T2-weighted sequences and isometric examination (axial, sagittal, or coronal). Section thickness may vary depending on the region being examined and the size of the patient. When evaluating vascular structures, 2D or 3D time-of-flight (TOF) gradient-echo sequences, phase contrast, and contrast-enhanced 3D angiography sequences should be obtained. In these sequences, a 1 mm thick volume screening should be performed.
Contrast agent: Extracellular gadolinium chelates are used intravenously at a dose of 0.1-0.2 mmol/kg for standard examination. An automatic injector is not required.
The scan, which could provide field data for engineering and clinicians at the same time, was planned to be completed within a minimum of 8 and 12 minutes within the specified sequence list.

Cardiac MRI Scan

Cardiac MRI can be performed with superficial body coils or detached cardiac coils. The device must have the necessary hardware and software to synchronize the acquisition of images with the cardiac cycle, as well as necessary cardiac sequences. Image processing software is required for post-process operations such as quantitative functional evaluation and flow quantification.

A cardiac MRI scan for babies requires a high spatial resolution (in-plane resolution $1mm^2$) (Figure 2.5). Axial steady SSFP images (T2 is not necessary). Black-blood spin-echo, 2DSSFP, and 3DSSFP techniques, as well as contrast-enhanced MR angiography, are the most famous sequences for anatomical imaging in congenital heart diseases.

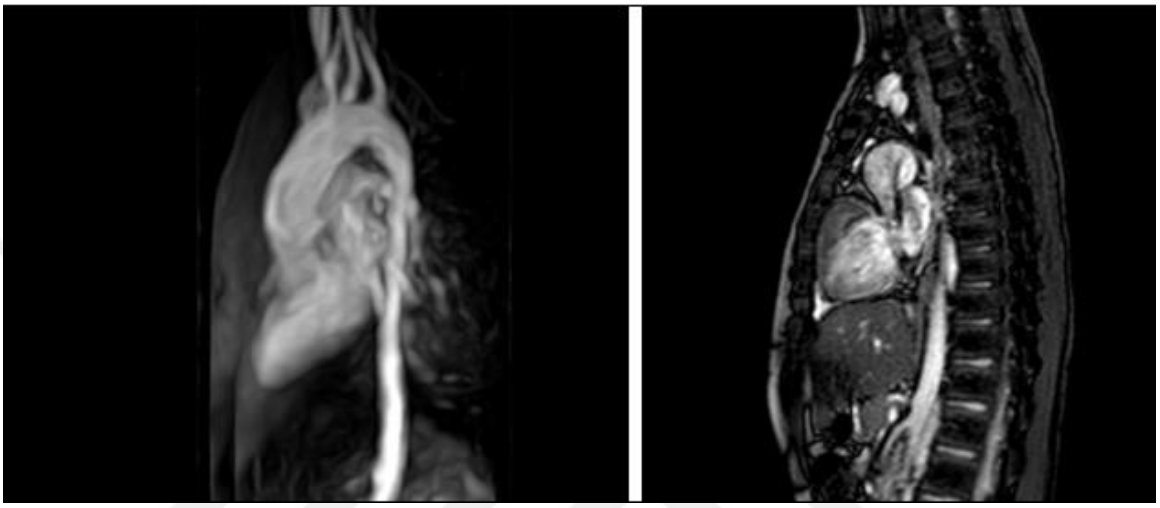

Figure 2.5 3D RENAL MIP sequence section samples were taken with a Philips Ingenia 1.5 Tesla MR device.

Cardiac MRI examinations can be performed with 1.5 Tesla or 3 Tesla devices. 3 Tesla systems are more susceptible to a balanced steady-state free precession (bSSFP) sequence artifact. There is a possibility of artifacts that require optimizations. In contrast, 3 Tesla systems are more advantageous in first-pass contrast perfusion imaging, tagging sequences, and 4B flow techniques due to increased signal to noise ratio.

Cardiac MRI Scan Protocol:

Single-shot fast spin-echo or b-SSFP in the axial plane, morphological imaging consists of imaging of white blood functional cine in the primary axes of the heart. In functional cine imaging, 2, 3, and 4 chamber cine images are taken in at least one cross-sectional plane, while the short axis images are taken in a plurality of cross-sectional planes in the form of consecutive cross-sections covering the entire ventricle. Sample protocol steps are listed below:

1. **Guide images:** Axial, coronal, sagittal.

2. Axial morphological imaging: Single-shot fast spin-echo or b-SSFP sequence into the entire thorax obtained.

3. Long axis guide images to reach the short-axis image plane: Although single-shot can be taken, cine imaging is preferred.

a. Vertical long axis: From the left ventricular apex and mitral valve center on axial images cross-section plane.

b. Horizontal long axis: Vertical long axis image from the left ventricular apex and mitral valve cross-section.

4. Short axis cine images: Long axis guide images are taken in the form of consecutive sections that are planned perpendicular to the interventricular septum and lateral wall from the mitral valve plane to the apex. Optionally, sequential short-axis images can be planned after real four-room long axis images are obtained.

5. Long axle cine images:

a. 4-chamber long-axis image: The plane passing between the anterior free wall of the right ventricle and the inferior wall of the right ventricle and the anterior and posterior papillary muscles of the left ventricle. The vertical long-axis image should be confirmed to pass through the left ventricular apex and mitral valve center.

b. Long axis cine image in 2 rooms (left ventricle): Anterior and left ventricle on short-axis images. It is obtained by moving the plane passing through the posterior junction points to the middle of the left ventricle.

In the 4-chamber long-axis image, it should be confirmed that it passes through the apex of the left ventricle and the center of the mitral valve. If the long vertical axis is obtained as a guide image, the two chambers correspond to the same plane as the long axis and may not be retrieved.

c. Three-room (Left ventricular outflow tract) long axis sine image: Basal short-axis images are planned to center the left ventricular outflow tract and aortic valve, and also pass through the left ventricular apex and mitral valve center.

6. Cine imaging for the right ventricle: Diagnosis and postoperative follow-up of some congenital heart diseases and right axillary images in the baseline cardiac MRI.

Although it is possible to evaluate the right ventricle, right axial cine images that cover the right ventricle entirely may be preferred for right ventricular volume calculation. T1 based localizer frame images should contain the whole heart, SVC, IVC, and hepatic veins. Sequences less than 30 sections do not provide sufficient detailed information, and the 2D BOLUSTRAC sequence does not provide meaningful information even in multiple sections. Different coils can be used in pediatric patients depending on the size of the infant. Children under six years of age may need to be examined under sedation or anesthesia. Similar sequences with adults are used in pediatric patients, but the technical parameters of the sequences should be revised according to the size of the child. Too small to hold breath. In these cases, the image is obtained by making arrangements in cine and stationary sequences.

2.4.2. CT Scan Protocol

64-slice multi-detector-row computed tomographic (MDCT) angiography cases were investigated for the study (100-120kV, 550-700mAs).

CT Scan Requirements:

- Clear contrast and no misalignments is a must.
- The more the high slice number, the more the re-construction quality.
- Standard ECG-triggered diastolic protocol is suitable for structural information of the heart. No ECG triggering required for vessel information.
- The heartbeat should be below 65.

Position: The patient should be placed in the supine position.

Inspection area: It covers all the examination area required for indication and has high resolution.

Section Thickness: Slices are incremental or (at least) equal to slice distance (for determining the degree of sectional overlap to improve image quality, P=1) at around 0.625 mm.

Figure 2.6 shows an image data that is not created with equal length planes. Although the resolution of such data is excellent, reconstruction will not be possible at once, and the cardiac structures desired to be modeled will not be fully formed.

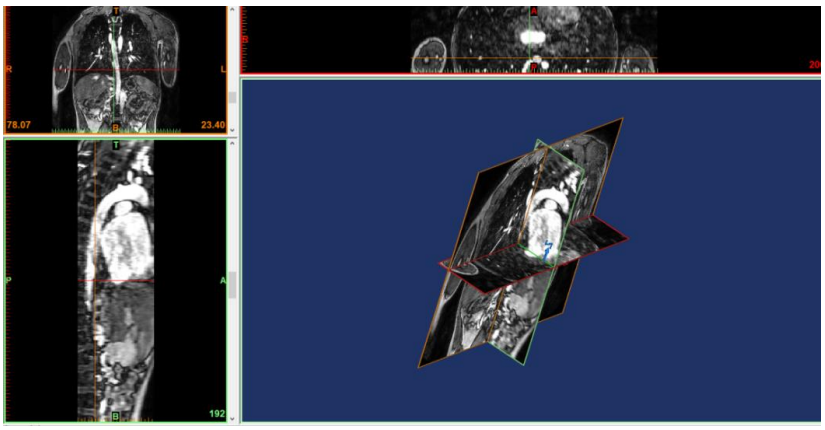

Figure 2.6 MR dataset with proper resolution but no isometric planes.

If there are sections taken with different sequences in the same scan, the sections taken without isometric volume aim will not provide the necessary and sufficient condition even though they will be completed with them.

Therefore, in case of need of MR data to be used in reconstruction, the technician should be informed that the shooting technician should create isometric voxel and the protocol should be followed to apply the correct 3D sequence (Figure 2.7).

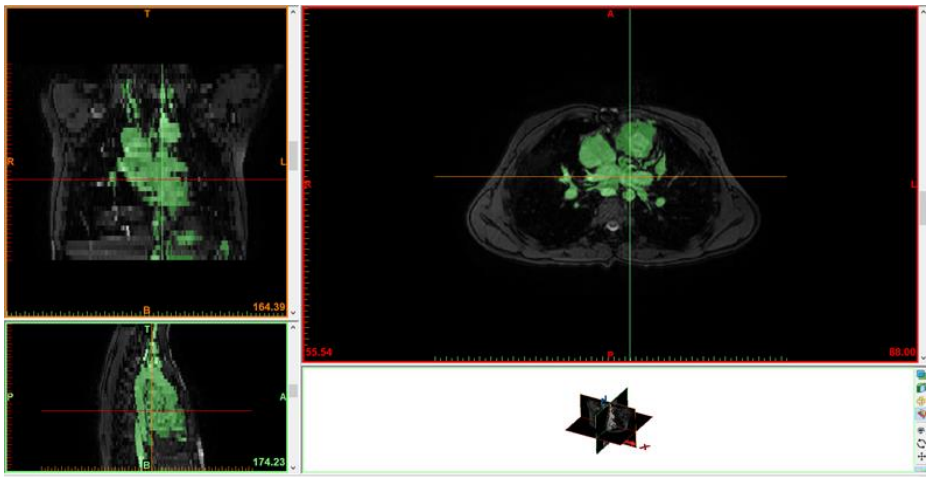

Figure 2.7 MR dataset does not have a proper resolution but suitable for segmentation. It produces isometric voxels, which are enough to have raw volume information about the heart but not for small atrial defects.

CHAPTER 3

3. MATHEMATICAL METHODS

The construction of subject-specific geometric models from medical imaging data has enabled an entirely new application of cardiovascular mechanics, namely the prediction of changes in blood flow resulting from possible therapeutic interventions for complex congenital cases. Patient-specific modeling of blood flow mechanics requires methods to (a) re-construct realistic anatomical models from multi-sliced DICOM data; (b) extract pre-operative image data with the tools of image processing; (c) modify the pre-operative model to incorporate a surgical plan with CAD tools; (d) assign boundary conditions incorporating upstream cardiovascular models and downstream microcirculation models; (e) discretize volumetric models using automatic mesh generators; (f) solve the differential equations governing blood flow and vessel wall dynamics; and (g) visualize and quantify resulting physiologic information (Figure.3.1).

In this thesis, three common CHD topics are examined using the same mathematical methods. Priority is given to the description of the mathematical methods used, and the segments related to CHD are explained in detail in the Surgical Planning Chapter. Thus, it is aimed to protect the subject's integrity.

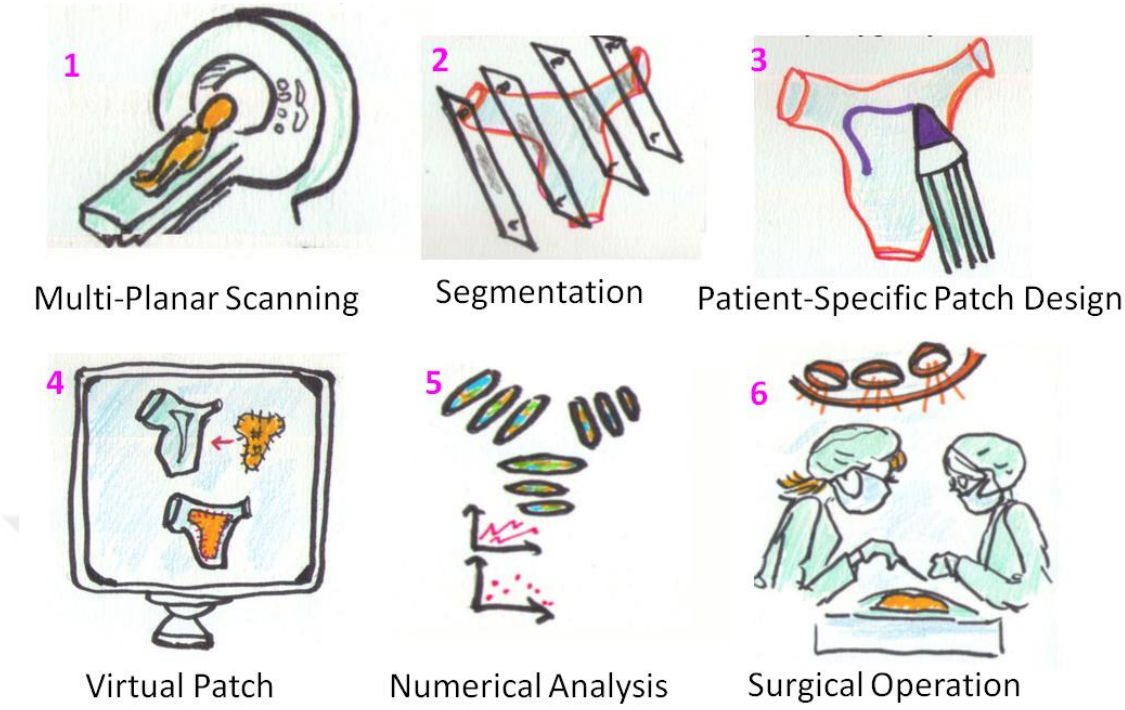

Figure 3.1 The workflow of surgical planning with patient-specific blood flow analysis.

3.1. Vascular and Intracardiac Modeling

Repair of complex cardiac pathologies requires advanced diagnostic imaging techniques [139]. It is essential to reveal anatomy and spatial relationships. In order to decide what kind of treatment is needed, a thorough evaluation of the council decisions should be made, and when a surgical repair is decided, the available information may not be sufficient in planning the surgery.

Currently, diagnostic evaluation and preoperative planning of CHD is based on two-dimensional (2D) and multi-section imaging of volumetric data such as ECHO, MRI, and CTA (computed tomographic angiography). The first preferred and widely used approach is ECHO for the clinical diagnosis process. [140][141][94]. Despite the tremendous information that can be obtained from ECHO, these two pathologies are discussed in the complex CHD spectrum. ECHO is useful when planning surgery, but it may be insufficient because it provides images in a single plane. Moreover, the pulmonary valve, aortic valve, and VSD are complicated to reveal in a single image. Therefore, it may be impossible to make decisions in complex DORV (Double outlet right ventricle) patients with ECHO only [20][79].

The main obstacle with imaging devices that perform ultrasound imaging is that the probe is placed in the correct position to ensure that the anatomy to be viewed is at an appropriate angle and that the resolution is not very good due to data pollution that may occur during the conversion of the quartz vibration to the signal and the signal. Therefore, it will be performed by experienced clinicians who will capture the best and most accurate images for each section [20][142][143]. In the current era, this feature should readily be determined with cross-sectional imaging. Although cross-sectional ECHO interrogation is now the mainstay of the diagnostic work-up with 3D displays now facilitating decision making, it is the detailed analysis made possible by multi-sliced scanning that now reveals with precision all the required anatomical information.

Although these modalities like 3D TTE are currently less widely available, particularly for clinical application in small patients, and concerns remain regarding the use of ionizing radiation to produce computed tomography images, the images provided show with exquisite accuracy, for example, the fundamental differences between the area through which the ventricular chambers communicate as opposed to the area requiring surgical closure so as to produce biventricular circulations [144][145]. In order for the multi-section ECHO images to contain meaningful structural information, the experienced physician must take careful shooting. It is necessary to reconstruct the desired area to be imaged and taking care to ensure that a sufficient number of frames are taken [20]:

1. To identify the details of the heart anatomy using 2D ECHO, each of which should be taken when the adequate resolution is achieved at the correct angle.
2. To avoid any artifacts, the viewing window should be optimized, and the moments of resolution that best capture the structure of the image focus should be captured.
3. In order to be reconstructed, the clusters to be formed must be obtained with consistent and sufficient resolution with each other.
4. The 3D image data can also be sorted after a single sampling time point (middle systole or final diastole) is taken, and the frames are saved in DICOM format.

CTA, MRI, and 3D TTE have been used in the diagnosis of pediatric heart diseases, and they undoubtedly eliminate anatomical deficiencies [20][146]. A 3D model of the

heart-based upon data derived from CTA and MRI may contribute to a complete appreciation of the intra-cardiac anatomy in detail compared to 3D TTE. Studies have shown that the virtual models generated using this image data are compatible with the actual patient data, and the virtual models obtained by this method can be used for mathematical modeling and to produce 3D physical prototypes [147], [148]. In order for 3D virtual models to be obtained from medical imaging data to be realistic, they must have sufficient spatial resolution. In image processing terminology, spatial resolution is the smallest soluble distance between two different objects or two different properties of the same object [149].

When this feature is not sufficient, different tissues with similar properties may appear as the same tissue. The intensity values in two different tissues in a tomography data, the hydrogen atom ratio in MR data, and the acoustic impedance in sonography should be different. Limits between two different regions may be lost when performing without enough sampling data. Therefore, it is essential that the image data created in the virtual model can display the structures in a distinguishable degree.

In this thesis, the most appropriate radiological data were selected from the database, which was suitable for the main study subjects. Multi-planar images were used as basic geometries for mathematical modeling for intracardiac models and coarctation models. The images were selected by evaluating reports from pediatric cardiology, radiology, and pediatric cardiovascular surgery units. The pre-planning of the images and the decision-making process was completed before the operation for the Fontan section.

The regions to be modeled after being tagged in the database were examined with RadiAnt Viewer [150], and measurements were taken to compare with the measurements on the physical prototype models [151].

3.1.1. Segmentation Tools

Some image processing tools are required for processing (cutting, interpolating, delimiting, segmenting, etc.) on DICOM images. These can be done with commercially prepared software tools (3D Doctor, Mimics Innovation Suite, simpler,

Osirix, etc.), open-source programs (3D Slicer, Invesalius, etc.) or mathematical morphology operator codes can be produced by producing algorithms [152][153][154][155][156][138].

Medical imaging viewer RadiAnt, where measurements were performed on the region of interests shows the whole heart, and large vessel (Figure.3.2).

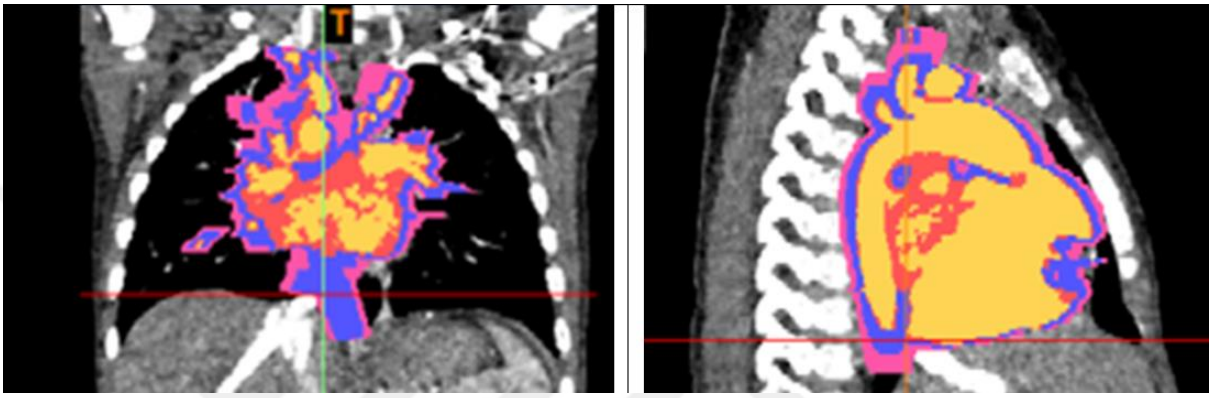

Figure 3.2 Differentiation of different colored pixels by segmentation in segmentation processes.

3.1.2. Reconstruction Workflow

The images in the study database were segmented with 3D modeling tools with the assist of image processing methods. The anatomical geometries to be evaluated in the planned study were digitally converted to 3D form software tools. This stage is different from the image obtained in the post-reconstruction process of imaging devices. The reconstructed models are created in STL (stereolithography CAD / Standard Triangle Language) format, which provides a suitable base for the studies of 3D rotation, incision, measurement, 3D printing, and biomaterial configurations.

It should be acknowledged that, as a result of the patient-specific data, many process steps have been introduced during these procedures, and the results should be evaluated together with other information (Medical images, clinical data, etc.). It should be considered the 3D models not only, but as a whole, together with the other data, it will be appropriate to emphasize the risk shares arising from the human factor in these studies with multiple process steps and many auxiliary engineering tools. The performed segmentation and image processing tools can be different from each other (algorithm, user-defined script codes, masking sensitivity, morphology operator diversity, etc.).

The accuracy of artifact cleaning and smoothness, as well as how many times it is renewed, can cause different results in volume and surface information. It is essential to mention the process steps of the method used in these floating studies and to have the physicians and technical teams together to ensure multi-disciplinary approval for each step. For this reason, it would be much more beneficial to emphasize the workflow regarding the methods of the studies in order to emphasize the unquestionable assistance of these implementations.

The workflow steps were used for each dataset imported into the Mimics Innovation Suite 19 segmentation platform [153]. The medical images that meet the conditions (specified in 2.4) were first adjusted after the contrast that best suited the region to be modeled, then the pixels in this region were marked and masked according to the optimal threshold value. Since the image was taken with a contrast medium, the most easily selectable section was the blood pool, and these sections were created first. The remote sections that were included in the mask were left out of the frame by creating a crop mask tab because they were unwanted but of the same pixel color. With the 'Region growing tool,' any area within the desired region was marked from the unwanted areas remaining in the frame, and the surrounding tissues that were not touched but were included in the mask due to pixel color were separated (Figure 3.3).

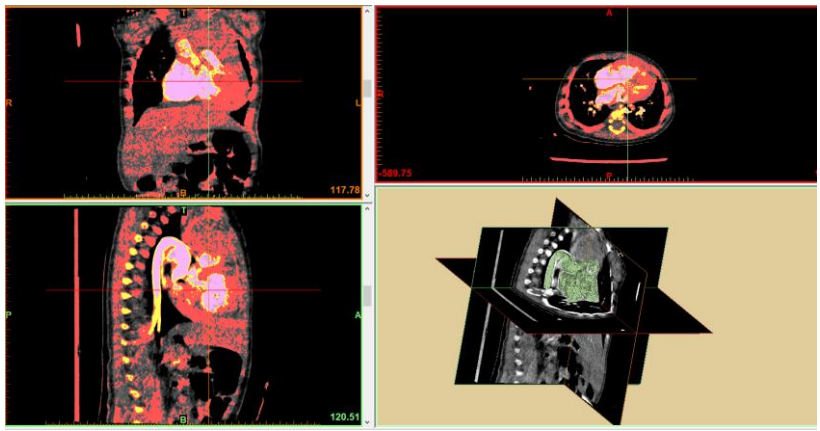

Figure 3.3 Multiple mask definitions on different tissues with Mimics Innovation Suite segmentation software.

For the undesired tissues that were included in the mask because they touched each other, the boundaries of the mask were removed by a pixel inward with the assist of the morphology operations tool. The new masks were expanded by one pixel and

reached their realistic boundaries, and the unwanted tissues were eliminated. According to the situation, possible errors were determined by examining the sections manually. The artifacts that may have been caused by the patient's breathing during resolution or exposure (such problems can be seen in MR or thick-slice CT data) were cleared by multislice editing or boolean algorithms [9][157].

Since the heart is a moving organ, it may not be possible to detect a clear image during radiological scanning. In such cases, the desired regions may be automatically painted to different pixel colors, although they have the same tissue. In these cases, masking operations are performed in separate parts and finalized by combining, subtracting, or intersections with the advance of Boolean Algorithms within the segmentation platform or by importing these parts into separate CAD tools (Figure 3.4).

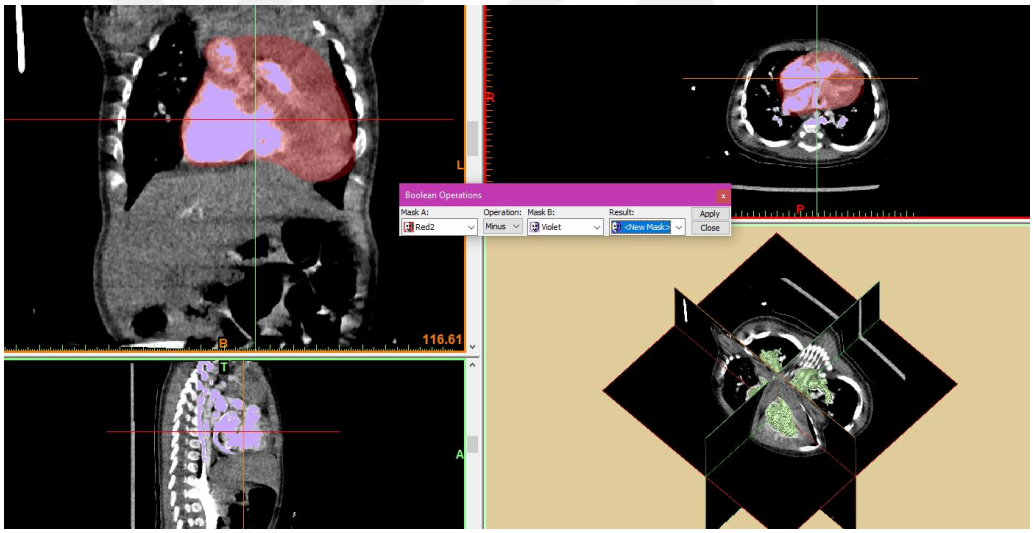

Figure 3.4 The intracardiac model of the heart model created by the Boolean Operations tool. The full heart model was created by 'Multi-slice editing' tool. The intracardiac morphology (red color) was obtained by the subtraction of blood pool mask (violet color) from a full heart mask (green).

Since it is not possible to mask the whole pool with the blood pool at the same time, they can be created separately by creating contrast-free tissues such as myocardium, and they can be obtained manually by means of 'multi-slice editing' tool in sections even if they can be created due to pixel color difference.

Logical steps were taken for each dataset in masking operations with the SimpleWare Scan IP segmentation tool. In the sections of the imported dataset, the desired regions

were marked with ‘Point to point line mode’ and filled with ‘Mask flood fill.’ The mask was obtained after interpolating. The slice propagation tool was completed with interpolation, and changes were made only on the desired sections. In this software program, segmentation and CAD tools are located in the same interface, operations can be converted to 3D objects, CAD models can be edited again and back to continue to masking, and increased processing speed can be increased (Figure 3.5).

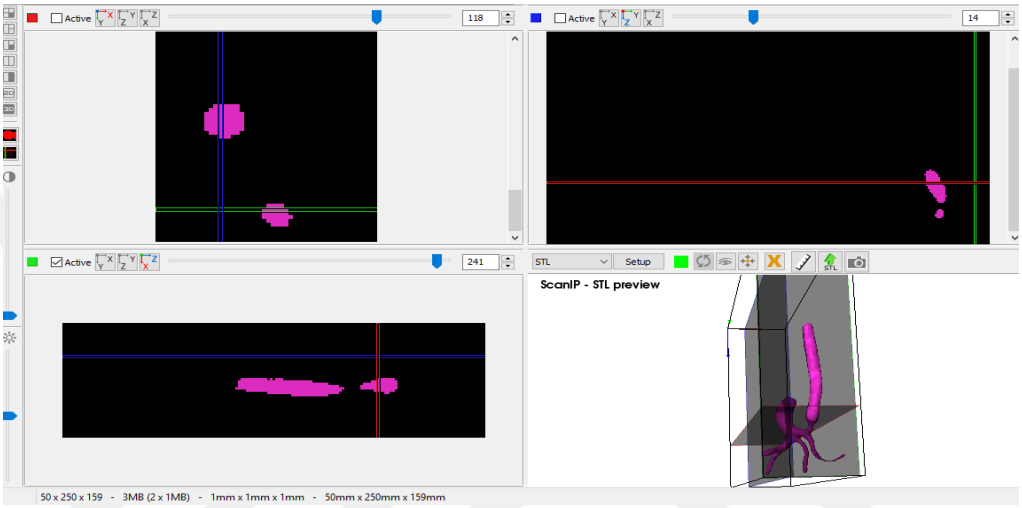

Figure 3.5 A pediatric aorta model segmentation on XY, YZ, ZX planes, and 3D artery model with Scan IP.

When masking with a 3D Doctor segmentation tool, the workflow is created by manually limiting the region, cutting the range of interest before masking. After general masking, the automatic limits were drawn by the program. These limits were then modified to obtain the desired region manually.

It was preferred only when data-masking if the data has a lower resolution, which could not be achieved by other segmentation tools as it required a time-consuming process (Figure 3.6).

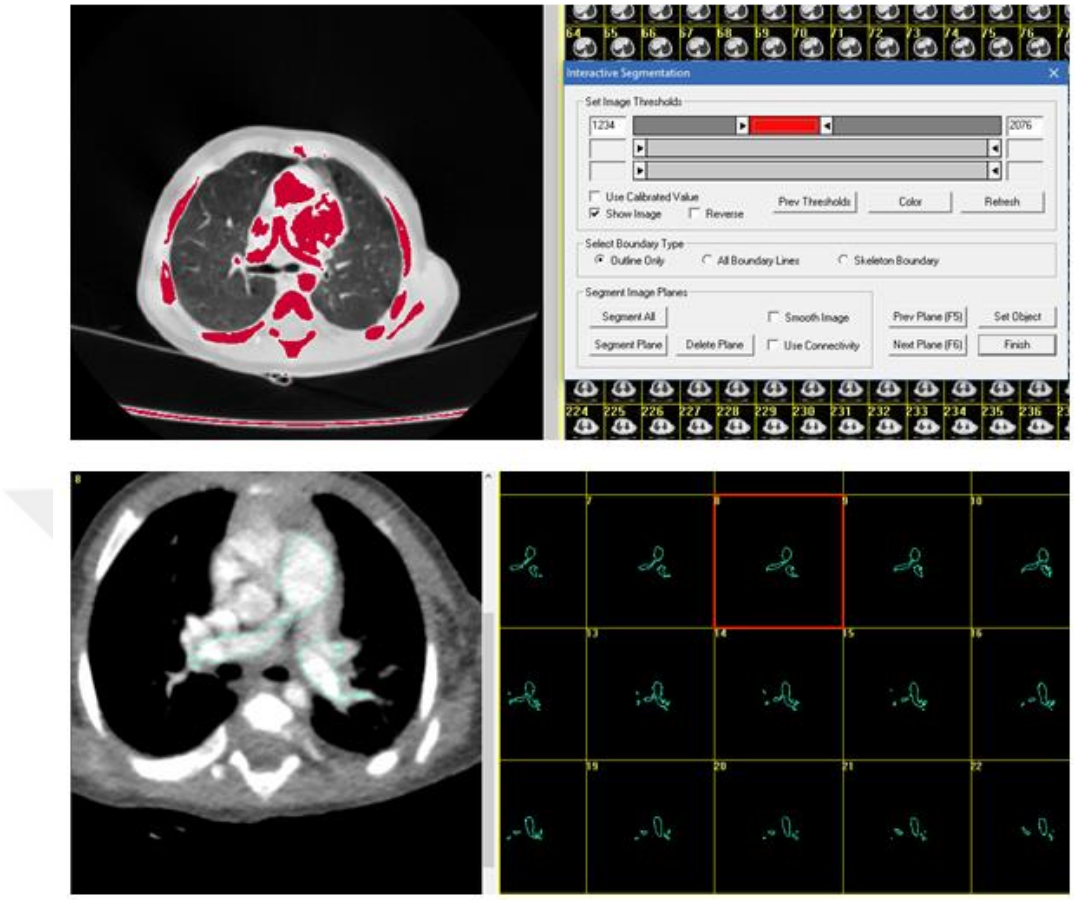

Figure 3.6 3D Doctor CTA dataset thresholding (top) and boundary line editing on 2D slices.

3D Slicer software was used in the CT datasets if the region of interest was more than one and if they had different pixels. In this open-source software, in order to create several masks at a time and to create several different structures at the same time, any point of these regions is marked, and the growth seed option is obtained by saving different time masks for each of them.

With this procedure, the pulmonary artery, aorta, ventricles, hepatic veins, etc. could be masked in different colors at the same time and converted into a 3D object. Unwanted but because of pixel color partnership, the sections were automatically cleaned with ‘Islands tool’ options (Figure 3.7).

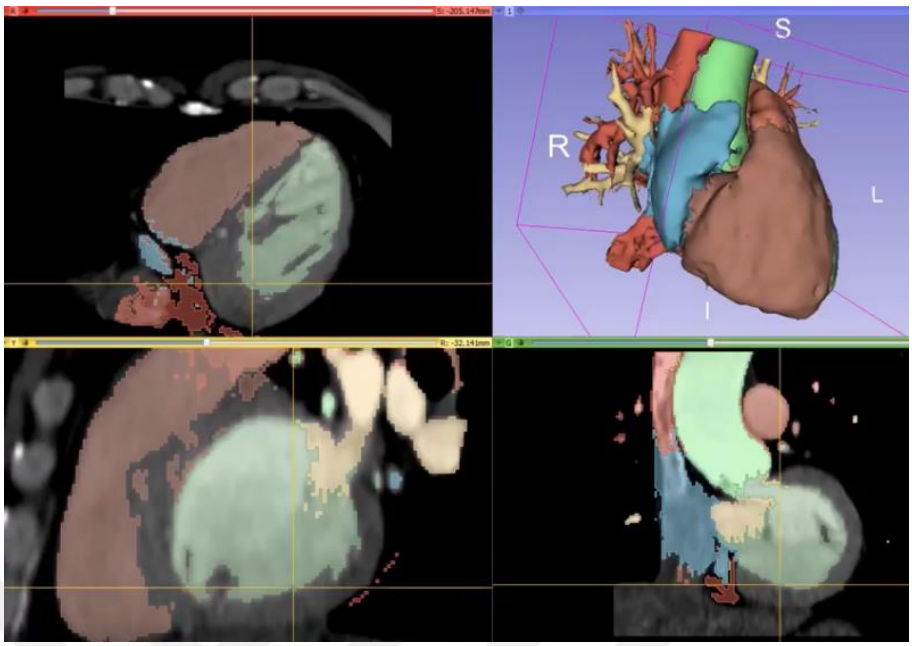

Figure 3.7 Defining different tissues with seed elements on 3D Slicer.

3.1.3. CAD tools

CAD operations are performed on STL models obtained through segmentation programs, improvement, cutting, joining, vessel thickness, preparing for finite element analysis studies, making structural processes such as smoothing, repairing, defining surfaces, designing input and output surfaces, etc. was used (Figure 3.8). In this way, the final models were made ready for 3D printing.

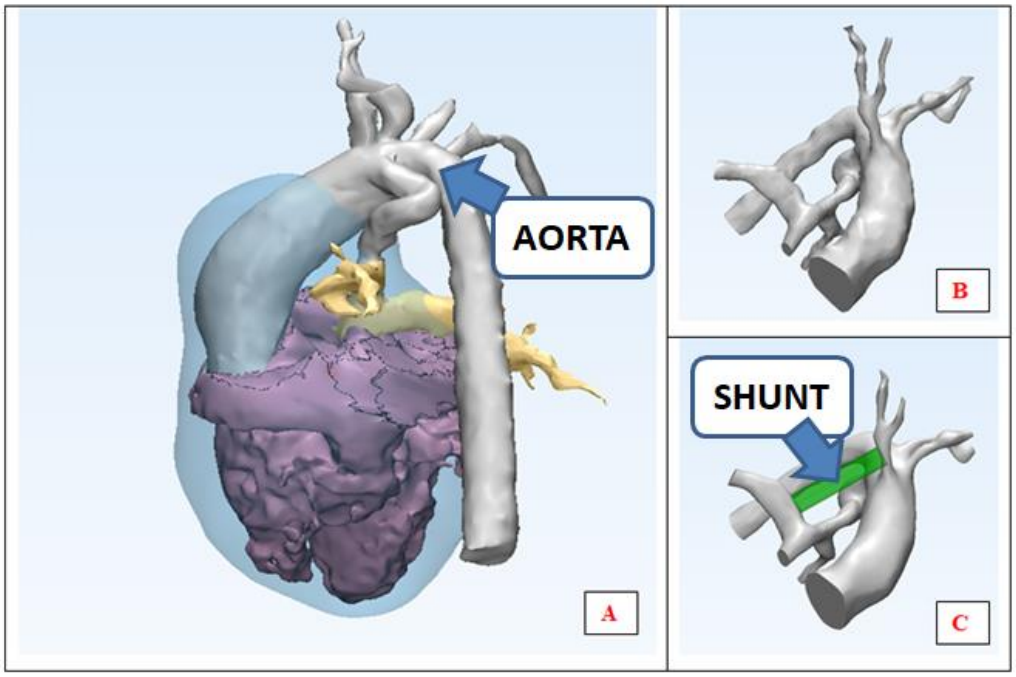

Figure 3.8 3D aorta and patent ductus arteriosus (PDA) (grey), pulmonary artery (yellow), ventricles (pink) (A) modeled by using CAD tools. Part (B) and shunt configuration between the right pulmonary checker and the innominate artery (C) to be used for surgical planning. The model is named as MED_060 in the database.

CAD tools were also used for creating idealized artery models for initial analysis works for the pulmonary artery model. The model was created in ANSYS 18 Design Modeler (Figure 3.9) [158].

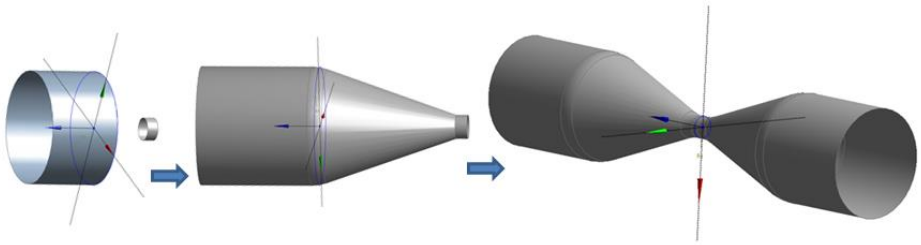

Figure 3.9 The design of the virtual idealized stenosed pulmonary artery model on ANSYS Design Modeler.

This tool was also used for creating extensions and surfaces for inlet and outlet regions of arteries before the computational numerical analysis and designing virtual incisions and patches with the help of points, lines, curves, and planes (Figure 3.10).

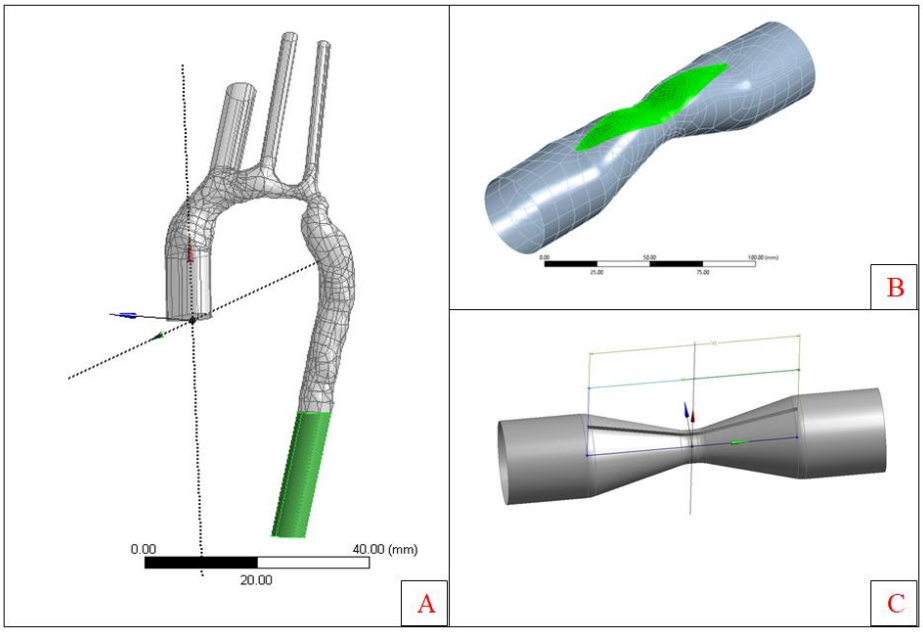

Figure 3.10 The extension of an outlet of the pediatric aorta for pre-processing of the flow analysis (A). The virtual patch design (B). The design of virtual incision with rectangular draw element on ANSYS for the pre-processing of static structural analysis.

In order to perform polygonal deformation for virtual surgery sections and to mimic the operating stage realistically, each step was approved by the clinician and advanced engineering programs were used in more detail than standard CAD programs (Geomagic Wrap, Ansys Design Modeler, Materialise 3-Matic, FreeCad, SolidWorks, RhinoCeros) (Figure 3.11) [159][158][160][161][162][163].

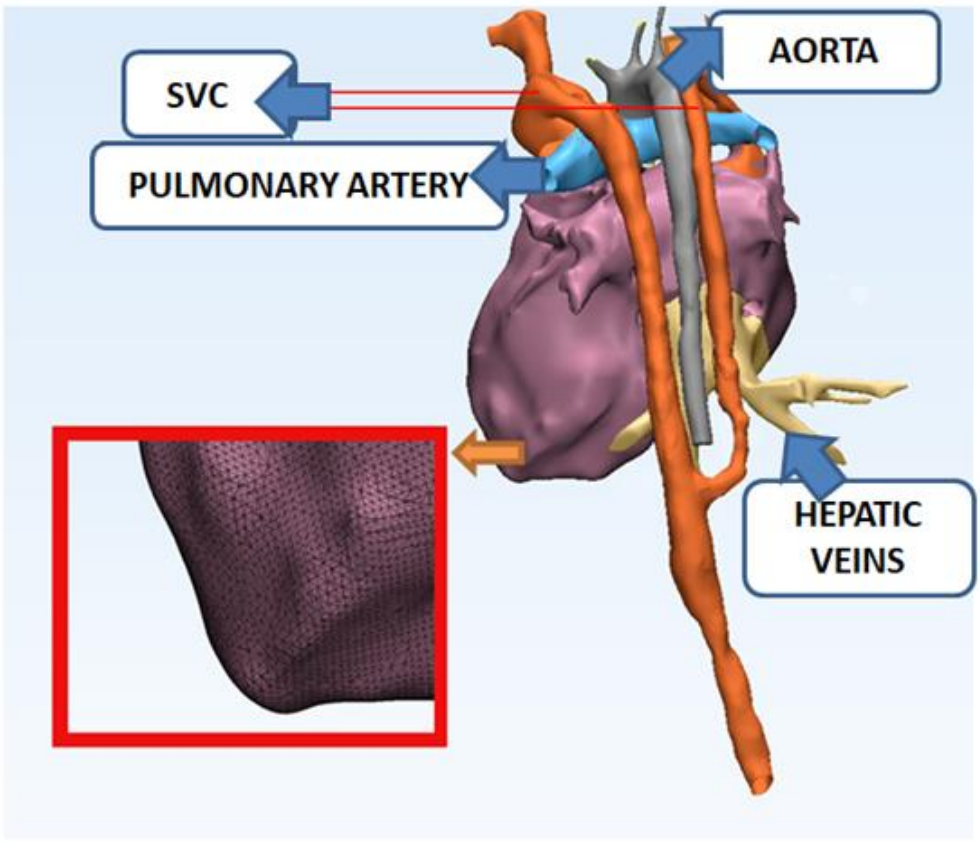

Figure 3.11 A 14-year-old operated patient (Named as SI_M_001 in the database) with a sophisticated pair of SVC shows a 3D model of cardiac MR data for the final planning of the Fontan procedure and a surface defined by unit triangles in the windowed area. As a result of the virtual configurations and hemodynamic analyzes of the patient, the operation was successfully performed with an intracardiac 15 mm shunt between the hepatic veins and the main pulmonary artery.

In order to obtain an intracardiac model, it can be performed in many medical segmentation software tools such as Mimics, 3D Doctor, Simpleware, 3D Slicer, and other CAD tools for editing and offset and merge. In a scenario where Materialize Mimics is selected among these multiple options, the internal structure can be obtained in the form of a cavity for the intra-cardiac model by selecting the different methods (Table 3.1).

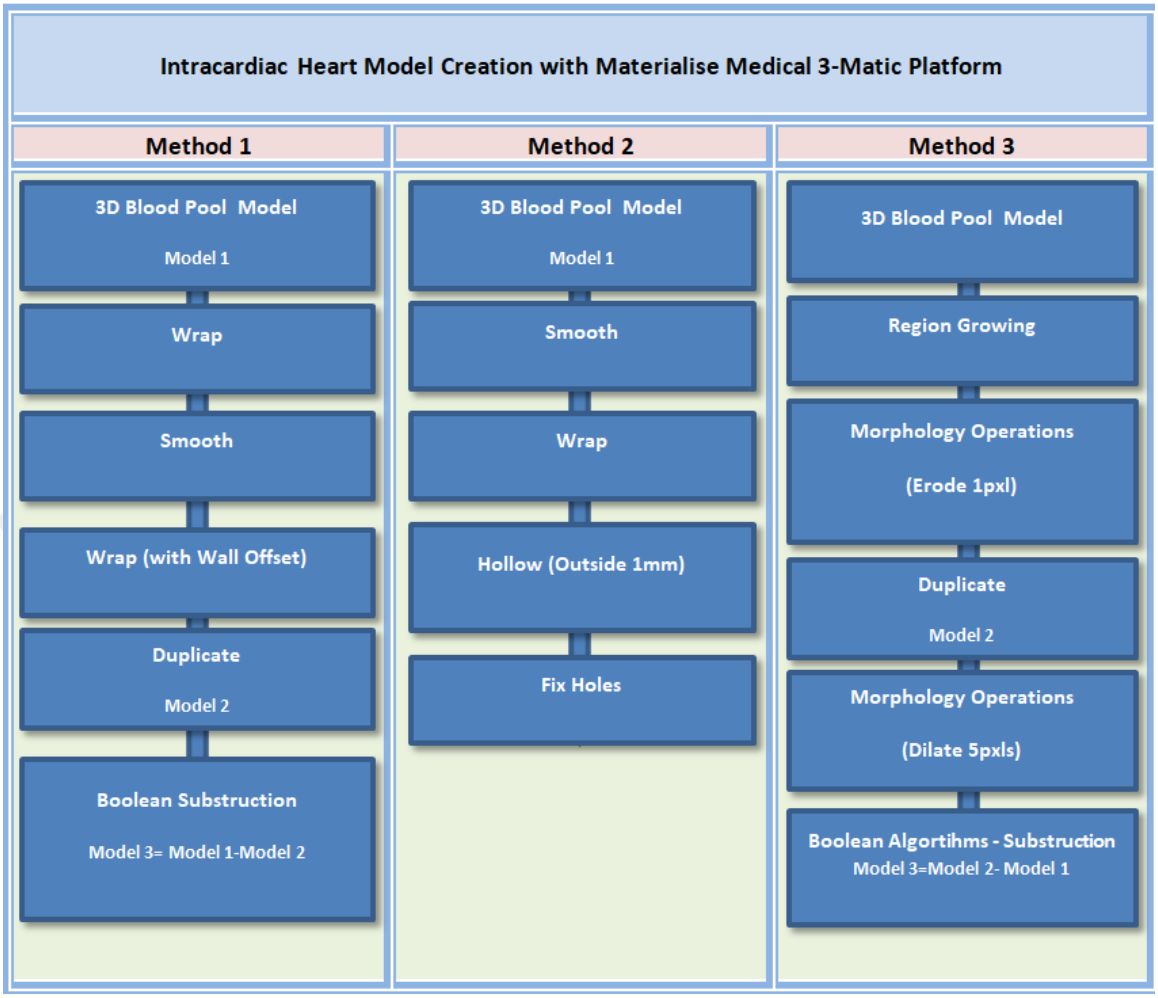

Table 3.1 Intracardiac heart model creation with three different workflow methods on the Materialise Medical 3-Matic Platform.

Although the main structure will not change, there may be minor differences when the results are compared. These differences will gain importance in a narrow CFD or coronary artery or multiple tiny septal defect cases.

3.2. 3D Printing

3D printing technology has shown that in the medical field there have been increasing the use of personalized prostheses, implants, fixtures, and surgical instruments, as well as the increasing use of patient-specific 3D, printed models for surgical preparation in recent years [49][164][165]. 3D printing is an innovative production process that uses computer-aided processing of 3D imaging data to create physical outputs of virtual objects. 3D virtual models created in a computer environment can be converted to physical models utilizing additive methods when they are defined in

appropriate file formats. Models that can be obtained physically instead of 2D screen images; it can be used as a tool for communication of patients with complex cardiac anomalies, surgery plans, training of medical students and operation personnel [166]. 3D models can be used for patient-specific cardiovascular models, as well as for patient-specific biomaterials [10] [47]. The object, which is divided into slices, ends up placing these slices on top of each other, respectively. Support legs are created automatically for models that can be difficult to stand in balance, and when production is completed, they can be distinguished from the product by physical or chemical methods (Figure.3.12) [167][157][168].

Complex CHD provides a unique opportunity to implement 3D printing technology to eliminate gaps in anatomical detailing, communication, and surgical planning. Correctly, complex intra-tracheal pathologies in 3D modeling can be used to clarify whether the tunnel between the LV and aorta is possible. In patients with double outlet right ventricle, these 3D printed models do not only help surgeons increase the understanding of a complicated spatial relationship of VSD to one or both significant arteries and thus help with surgical planning, but they may also improve surgical decision making, and It can also be used to mimic various surgical approaches.

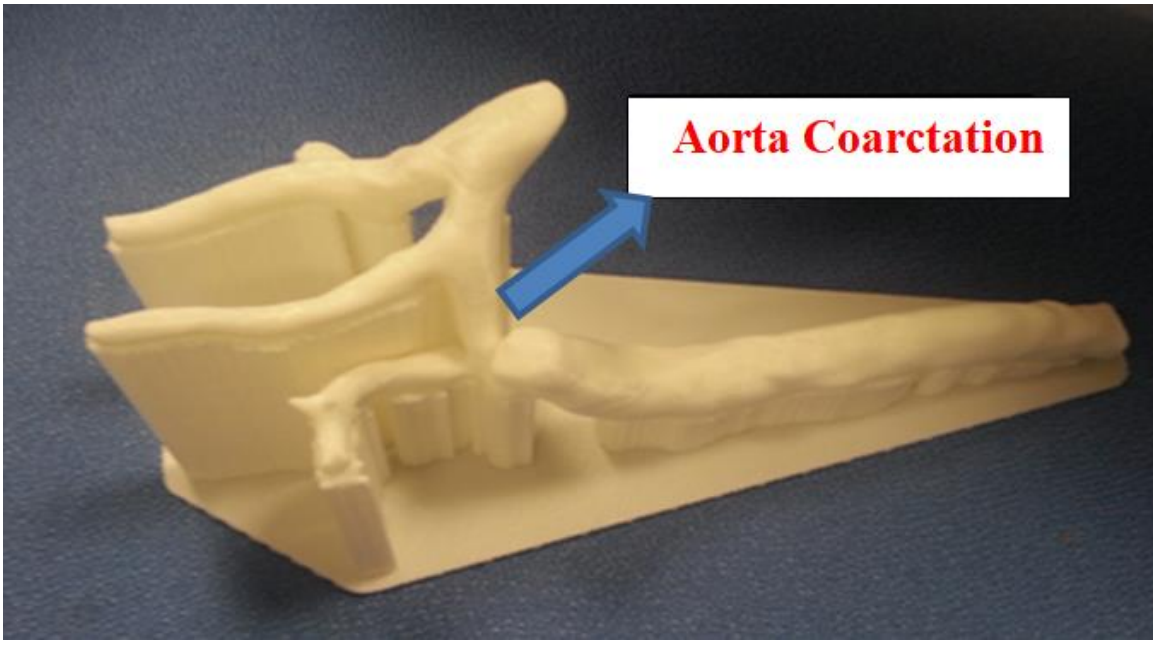

Figure 3.12 3D printing product completed with support legs and insoles of the artery associated with aortic coarctation. The insoles and support legs can then be easily separated from the original anatomy (Named as MED_013 in the database).

3.2.1. Printing Methods

Patient-specific 3D printed cardiac models for surgical planning has shown increasing use in the medical field in recent years. Multiple studies have demonstrated the feasibility and accuracy of 3D cardiac models for the reconstruction of complex cardiac anatomy [169][170]. 3D virtual heart models easily reveal anatomy and eliminate the contradictions associated with terminology.

When converting anatomical models into physical form, it is crucial to choose the right 3D printer [171][78][20].

Digitally obtained 3D reconstructions can be viewed from different angles on the screen -thanks to the highly successful software tools-, can bring transparent form, can be imported to the screen with /and without the surrounding tissues, can be rotated at 360 degrees angle and can be digitally cut from different cross-sections [172][18]. For this reason, it is possible to access the morphological information sought in such 3D modeling studies only on the screen [20]. It is preferable to switch to physical model production in decision-making if the desired information cannot be obtained by changing the rotation, cutting, and scaling or opacity on the screen. When efficiency planning cannot be obtained with a digital model, printing applications should be processed [59][9][61]. In these studies, the most common problem in the cases that require printing is to select a suitable printing method for the purpose of modeling. In such studies, it will be much more meaningful in terms of sharing, dissemination, and comparison of information, to make the methods clear and to gain awareness of the subject [173]. For example, in the studies of cardiac structures and VSD repair, the separation of the support materials in order to depict the inner spaces is more problematic, and the Stereolithography (SLA) printing is not enough for heavy and dense prints [174][149][49] [20][164]. There are many factors, such as the way of production, the properties of the material used, the sensitivity range of the injectors of the device, and the volume of the production platform. The anatomical models produced for use in clinical training can be produced from a flexible and soft material to resemble the actual tissue and make incision/suture, and a permanent and robust material can be used as a guide in surgical planning. There are many different printer types and material options for creating a model consisting of several colors,

producing several products at a time, producing light-permeable materials, and molding. In order to be able to make cuts after printing in the samples to be used for educational purposes, printing devices working with softer and flexible consumables should be preferred [166]. In cases where susceptible sources need to be depicted, needle tip detail or sintering solutions give successful results, while models to be kept in the operating room should be produced from materials that can withstand the temperature values of sterilizing or pass through post-processing as ultra-violet curing [20][133].

The most common 3D printing methods are performed by various techniques, such as spraying, sintering, and bonding. These methods are summarized below.

3.2.1.1. Fused Deposition Modeling (FDM)

It is based on the melting of thermoplastic material on the model building platform by adding it to the slicing map in layers.

Production is performed by laying the material in the desired contour on the platform with partial melting (Figure.3.13).

Preferred materials are acrylonitrile butadiene styrene (ABS), polylactic acid (PLA), and nylon, which are filaments [175].

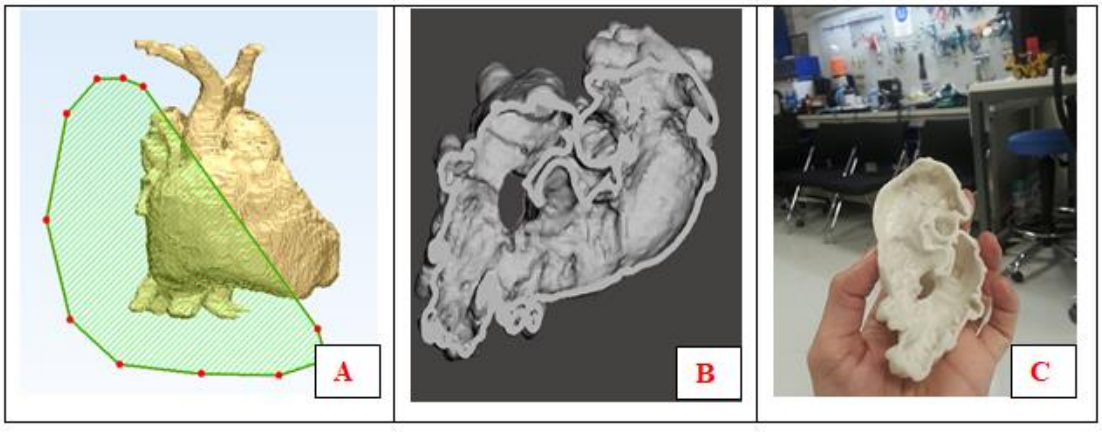

Figure 3.13 Cross-sectioning of a 3-year intracardiac model (A) from a 1-year-old sample of VSD diagnosed by intracardiac anatomy (B), 3D sectioned model (C) printed by FDM printer. The model is named as IMA_0018 in the database).

3.2.1.2 Bioprinters

Biological or compatible materials to be used in their creation are based on the transfer and layering of a sensitive injector to the platform [49][176]. It is mostly used for combining tissues, growth factors, and biomaterials or for the production of fragments close to natural tissues/organs and research in this field [41].

According to the object to be produced, the material may be a cell, polymer, gelatin, extrusion matrix, alginate. It is possible to produce various materials during production. These devices may have diversified instrumentation according to their intended use. Skeleton may have multiple injectors for many different purposes, such as a hydrogel, and, if necessary, removable support materials with solvents [97][49].

3.2.1.3 Laser Sintering - Selective Laser Sintering (SLS)

It is based on the principle of combining high strength laser beam with powdered composite material to provide the desired form. Materials may vary, as are polyamide-containing mixtures that are often preferred [49]. The liquid monomer material is solidified by laser. This process is repeated for each section. In the process of laser stereolithography, the liquid plastic resin material is also known as a photopolymer.

3.2.1.4 Electron Beam

This method works by combining the powdered material like that in SLS production. For this, it uses an electron beam. Electrons at high speed are directed to metal powder, and thermal energy is obtained. That helps the metal powder become fluidized. The layers are heated and sintered. Cobalt and Titanium alloys are among the materials. The final product needs to be cooled by vacuuming.

3.2.1.5 Stereolithography (SLA)

The fluid resin used to form the layers is cured in each tab with ultraviolet light. Photopolymers are preferred as materials [171]. In particular, the fluidic interface is based on the principle of solidifying each layer of photopolymers with ultraviolet light such as SLA, but during the production, the platform is raised in a weighted manner.

The ultraviolet light reaches the object through a transparent window under the resin material.

3.2.1.6 Binding Material (Inkjet)

A fluid binder is used to form the object and to hold the layers together. An example of this is the use of water-based binders as binders in the tank of powdery material containing gypsum and starch. In the Polyjet method, a binder is used for the adhesion of the layers, but the photopolymer-based solutions are sprayed between each layer and hardened by ultraviolet light. Polypropylene, polystyrene, polycarbonate materials are used.

The platform creates a new volume at each step for the layers to be created. Materials with different mechanical properties can be introduced to the platform, and multiple prints can be produced at the same time.

Colorjet production (CJP) method can be printed with color information and color prints of 3D models. The number of injectors in the FDM printers and the coloration restricted by the material color has the option of full CMY coloring in this method. CMY (cyan, magenta, yellow-cyan, magenta, yellow) is an extractor color model used in color printing and also used to describe the printing process itself.

3.2.1.7 Lamination

In this method, materials such as plastic, metal, ceramic, which are cut into the desired form in layers, are applied on top of each other. With the help of surface engineering methods, adhesion and cutting of the layers coated with adhesive surface materials are done with the help of laser. Polyvinyl carbon plastic, metal laminates, and paper are among the materials used.

3.2.2. 3D Printing for CHD

Anatomic and virtual operation models based on multislice image data can be embodied by choice of instrumentation and material that are appropriate for the methods (Figure.3.14) or biomaterials [166].

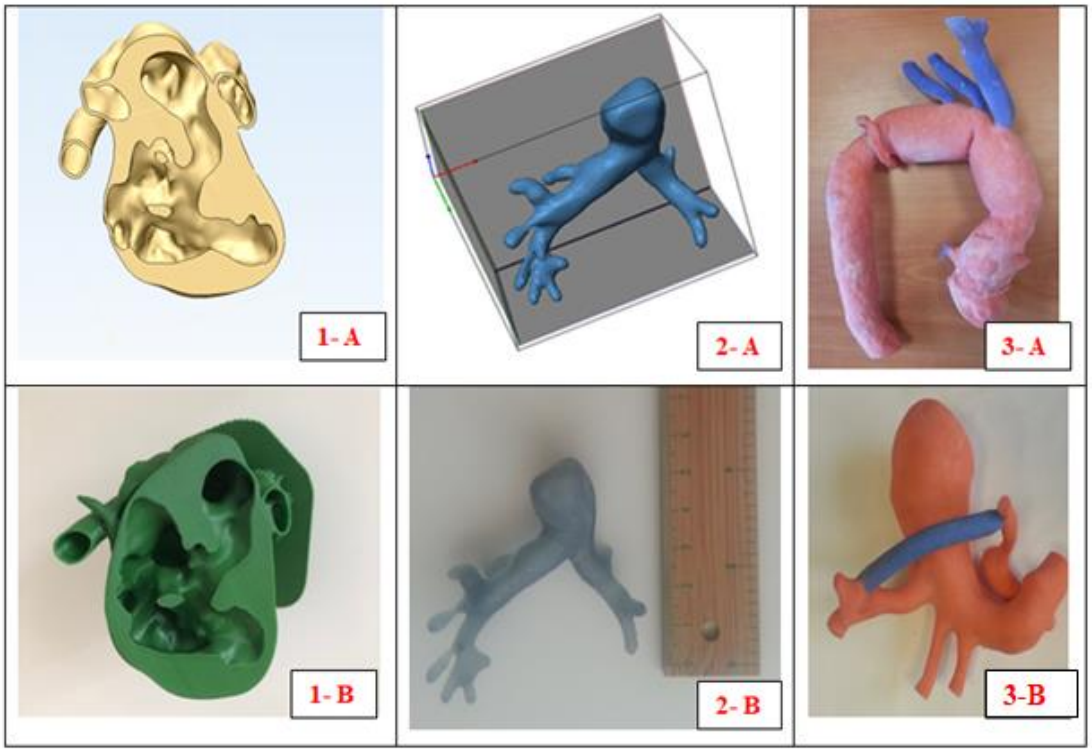

Figure 3.14 The purpose of this study was to investigate the relationship between VSD and aorta in a patient-specific intracardiac 3D model created by CAD devices and to perform surgery planning (1-A). The same model was printed with PLA material with an FDM production Zaxe X1 printer (1-B). Surgery planning was performed after the evaluation of virtual and physical models. A one-year-old patient-specific pulmonary artery model (2-A) was created with the Simpleware Scan IP software program, and the elastic printing was produced by the Formlabs2 printer (2-B). In this way, it is possible to make physical incisions after printing. The artery models printed with the Projet 260 C printer, which can perform multicolor printing simultaneously with the composite powder material, are a neonatal aortic model after surgery (3-A) and ductus arteriosus (3-B).

In Figure 3.15, 3D modeling was performed based on the image data of the preoperative and postoperative period of a one-year-old patient with a diagnosis of aortic coarctation, and PLA pressure was obtained with Zaxe X1 Printer which is producing FDM [177].

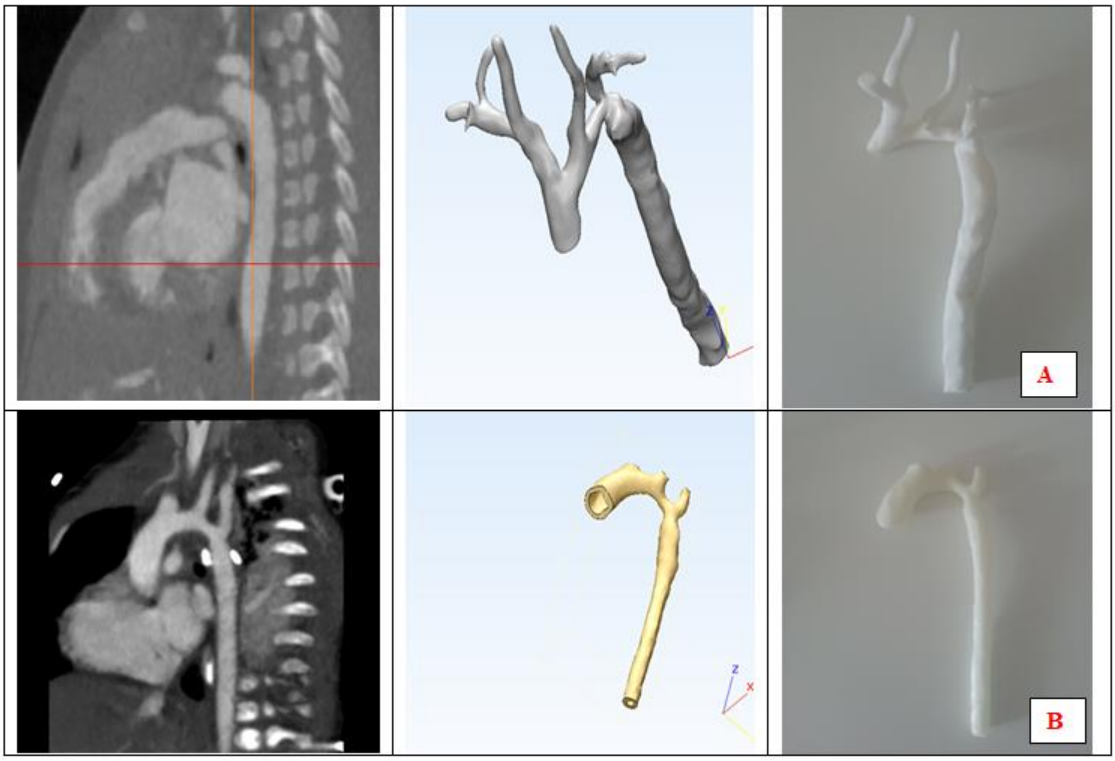

Figure 3.15 Images of the prints obtained from the PLA material obtained by preoperative radiological, 3D model, and FDM printer belonged to the patient with aortic coarctation modeled as 3D modeled by image processing tools (A). After the treatment of the same vessel with the anastomosis, the image data obtained by scanning, the post-operative 3D model, and the composite powder material were printed (B).

3D models of 3D cardiovascular anatomy can be used in many stages of scientific research in the creation of patient-specific biomaterial prototypes, in experimental setups, in malformations in basic, internal, or surgical sciences, in obtaining training materials for pathologies or in the visualization of expected and innovative operational phases. For example, the production steps of a pulmonic patch intended to be placed for the patient with tetralogy are shown in Fig.3.16 [30][47].

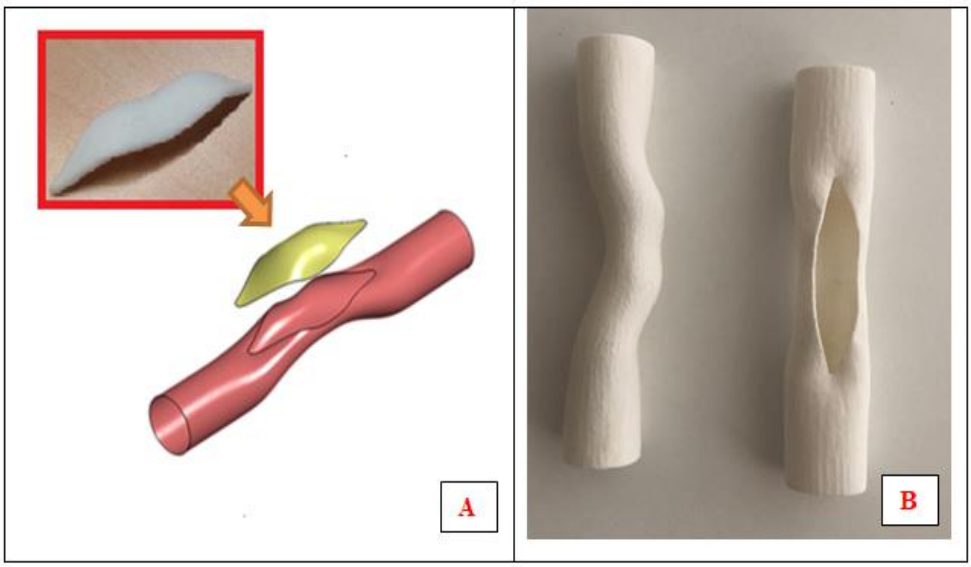

Figure 3.16 Printing of the patch material created on the patient-specific 3D model by the Projet 26O C printer (A). Printing of patched and non-patched 3D models (B) [178].

3D printing technologies have the potential to alter the usual clinical routine in severe CHD samples. Repair of complex congenital heart defects; it should include skilled and experienced clinicians as well as detailed structural information to provide the necessary information (Figure 3.17).

Figure 3.17 A pediatric pulmonary artery lumen prototype printed on an FDM printer. The wall thickness is obtained from the CT dataset with image processing tools due to the pixel color difference.

Three-dimensional structural morphology can be achieved by creating physical prototypes without opening the patient's chest (Figure 3.18). Making the right decision and reducing the processing time is very important for these critical cases.

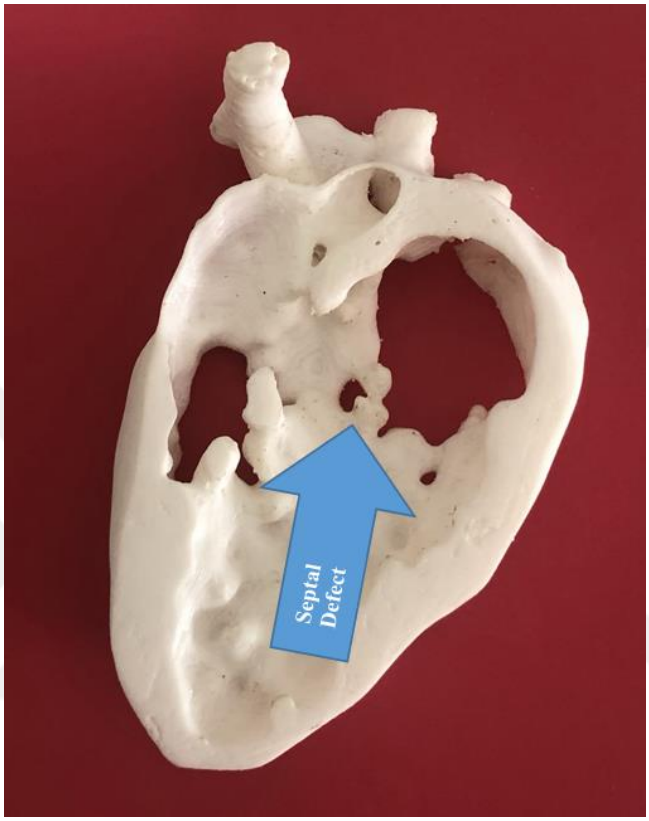

Figure 3.18 A 3D printed prototype of a perimembranous muscular outlet septal defect case obtained from thoracal MRI angiography dataset. Since the defect is tiny, it was produced with elastic material to examine whether it is suitable for closure by intravenous intervention and to make an application on the prototype.

3.3. Finite Element Analysis (FEA)

The term FEA was first used in 1960 to find approximate solutions to problems in areas such as stress, fluid flow, heat transfer analysis. FEA is a numerical method for solving problems of engineering and mathematical physics. Stress and load analyze for simple structures in analytical solutions are based on idealized situations.

In calculating complex physical problems, analytical solutions are based on simplification (where the mass is concentrated in the center of gravity, the beam is considered as simple as a line segment, and the designs are drawn as idealized). It is preferred in cases where the safety factor does not require details.

FEA solutions are preferred in cases where geometry is more complex and accuracy.

It is used to understand the physical behavior of a complex body (loss of power, heat transfer property, fluid velocity, shear stress, pressure, etc.) and for estimating the performance and behavior of design, calculating safety margin; and accurately identifying the weakness of the design; and to determine the optimal design with confidence (Figure 3.19).

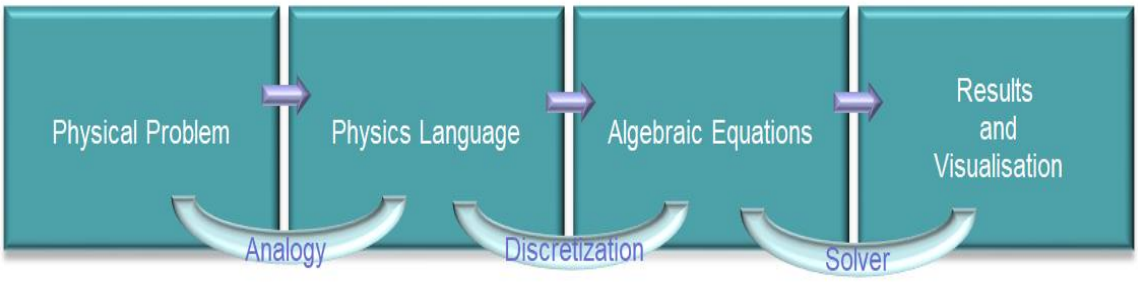

Figure 3.19 FEA steps for the solutions to complex physical problems.

FEA can handle very complex geometry, elaborate restraints, and complex loading. The word 'finite' is used to describe the degrees of finite or finite degrees of freedom used to model its behavior in each partitioned cell. The cells are connected, but only interconnected joints known as nodes. The elements are small-sized regions, are not separate entities such as bricks, and there are no other surfaces or cracks in different geometries between them. In this way, there will be no part of the system in the analysis.

Governing (differential) equations and boundary conditions give a set of simultaneous algebraic equations by numerical analysis (Eq 3.1). K represents property (viscosity, stiffness, etc.), F represents action (body force, charge, etc.), and u represents behavior (displacement, velocity, etc.), which is the final solution of the analysis (Eq 3.2).

$$\{ L(\varphi) + f = 0 \} + \{ B(\varphi) + g = 0 \} \text{ ——FEA —> } \{ [K] \{u\} = \{F\} \quad (3.1)$$

$$\{u\} = \{F\} [K]^{-1} \quad (3.2)$$

3.3.1. Meshing

The process of representing a component as a collection of finite elements, known as discretization, is the first step of finite element analysis. Grid or mesh generation is the initial step in solving a process where the computational domain is divided into a

finite number of smaller sub-domains called elements, cells, or voxels over which governing equations. The complete set or collection of elements is known as meshing (Figure 3.20).

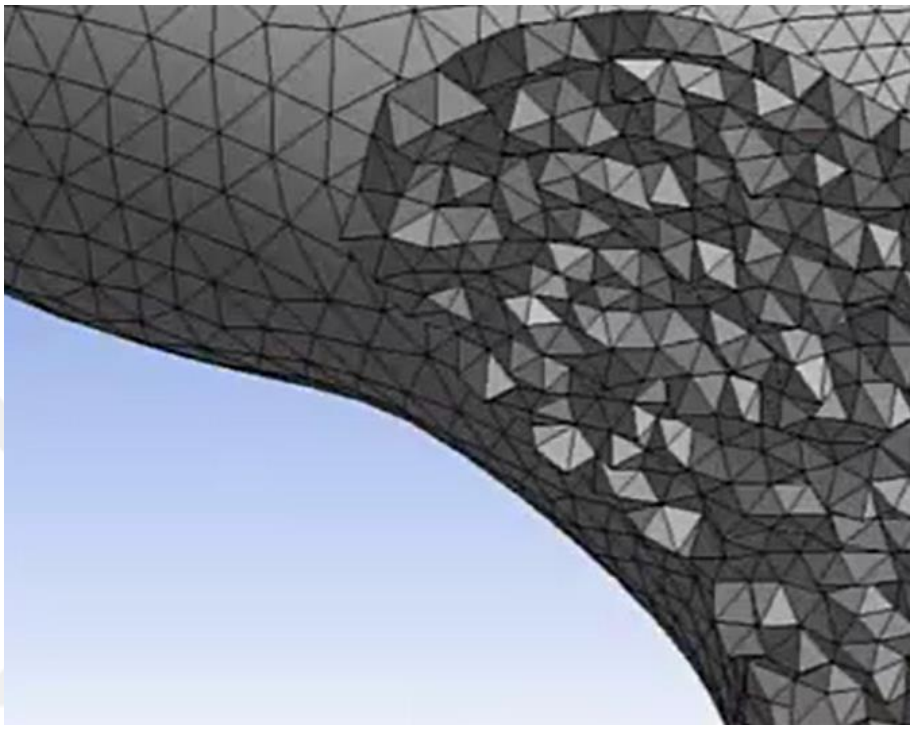

Figure 3.20 The tetrahedron mesh elements after face sizing with 642 faces, 8.e-004 m element size, and 3.e-004 m defeature size.

The finite element network that separates geometry into small particles on which the set of equations is solved is also a factor that can affect the accuracy of the FEA model. Therefore, it is necessary to separate the right elements into the right dimensions. The equations to be solved represent the main equation with a series of polynomial functions defined on approximately every element. The smaller these elements, the closer the calculated equation to the real solution. Grid sizes have a significant impact on the rate of convergence, solution accuracy, and the required processing time. Structured meshes can be used in a relatively regular and straightforward geometry, while the unstructured mesh is used in complex geometries.

The artery models to be used for FEA were imported into ANSYS 18 Meshing software by adding cylinders to the inlet and outlet sections by adding extension cylinders through CAD software (Geomagic Wrap and ANSYS 18 Design Modeler) [179][180].

This mesh refining process is an essential step in validating the validity of any finite element model and gaining confidence in the software, models, and results (Figure 3.21).

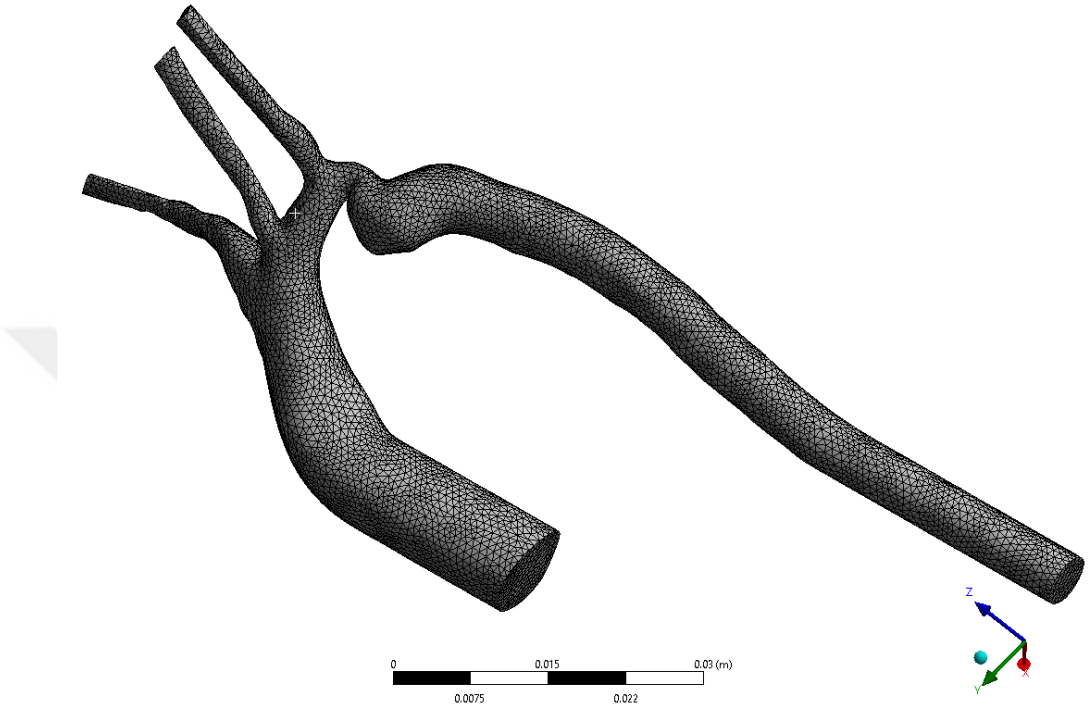

Figure 3.21 A Pre-op pediatric aorta coarctation model meshed on ANSYS 18.

Performing convergence requires choosing a proper mesh refinement metric. This metric can be either local (at one location) or global (the integral of the fields over the entire geometry) [181]. The models for numerical blood flow analysis meshed on ANSYS 18 Fluid Flow Meshing section. The average minimum element size was 6.e-004 m, and the maximum element size was 9.e-004 m for single artery models. The approximate node number was 28746, and element numbers were 138659 for per artery volume (Table.3.2).

Details of "Mesh"	
Element Order	Linear
Sizing	
Size Function	Curvature
Relevance Center	Fine
Transition	Slow
Span Angle Center	Fine
Curvature Nor...	Default (12.0 °)
Min Size	6.e-004 m
Max Face Size	9.e-004 m
Max Tet Size	1.8e-003 m
Growth Rate	Default (1.10)
Automatic Mesh ...	On
Defeature Size	Default (3.e-004 m)
Minimum Edge L...	4.6195e-005 m
Quality	
Check Mesh Qua...	Yes, Errors
Target Skewn...	Default (0.900000)
Smoothing	High
Mesh Metric	Skewness
Min	1.1594e-003
Max	0.8352
Average	0.22706
Standard Devi...	0.11967
Inflation	
Use Automatic In...	None
Inflation Option	Smooth Transition
Transition Ratio	0.272
Maximum Lay...	5
Growth Rate	1.2
Inflation Algorit...	Pre
View Advanced ...	No
Assembly Meshing	
Method	None
Advanced	
Number of CPUs ...	Program Controlled
Straight Sided El...	
Number of Retries	0
Rigid Body Beha...	Dimensionally Reduced
Mesh Morphing	Disabled
Triangle Surface ...	Program Controlled
Topology Checki...	No
Pinch Tolerance	Default (5.4e-004 m)
Generate Pinch o...	No
Statistics	
Nodes	28746
Elements	138659

Table 3.2 Mesh details of artery models on ANSYS 18 Fluid Flow (Fluent) Meshing tool.

The definition of the inlet and outflow, wall, and blood regions of the artery volume are done after global meshing and mesh refinement in the pre-procession for fluid dynamics analysis.

3.3.2. Computational Fluid Dynamics (CFD)

The branch of science which explains the movement of blood in the circulatory system and the factors affecting it through physical laws is 'hemodynamic.' In order to be able to monitor hemodynamic situations, evaluate and test these parameters of blood flow in the body, it is also important to provide information by calculating and measuring mathematical conditions as well as applicable and evaluable systems without harming the patient. Although the amount of information obtained by clinical routines under difficult conditions is very limited, the numerical hemodynamic calculations of fluid dynamics can provide precise information.

CFD tools have been extensively applied to study hemodynamics. The CFD method is used to simulate flow through physical equations. It has been preferred in blood dynamics research since it is possible to perform quantifiable and quantifiable experiments.

The axioms of CFD, a sub-branch of mechanics, include conservation of mass, conservation of momentum, and conservation of energy laws [182]. It serves to solve numerically the problems which are difficult to solve analytically using mathematical approaches [85]**.** The sensitivity of the solution; the problem is correctly defined by mathematical analogy, the number of finite elements divided by nodes, and their formulation depends on [183]**.**

Numerical data are obtained as a result of modeling the problem, determination of boundary conditions, and calculation with experimentally validated solvers in the preliminary stage [184][185][29]**.** This data is visualized through post-processing applications. Many physical parameters , such as velocity patterns, shear stress, power loss, and pressure distributions, can be simulated for the purpose of the study [186][187]**.**

Numerical hemodynamic studies simulate blood flow by the laws of physics with the help of mathematical models and provide 3D information about flow patterns. The

anatomical geometry is created by using models designed with CAD tools or 3D scanning data. The modeling process considered the initial conditions of the patient's reported clinical flow parameters, and mathematical calculations include mapping of mechanical influences in critical areas (speed, pressure, shear stress, etc.) [84][39].
In the cardiovascular system, this method is used to reveal the behavior of blood in the circulatory system, reveal their quantitative status at different coordinates, and reveal flow patterns. It can be used to improve our understanding of the pathophysiology and progression of diseases and also plays an essential role in comparing virtual surgery scenarios, evaluating the effect of biomaterials on flow, introducing ventricular and valve diseases, and their innovative solutions.

Fluid flow is studied in one of the three ways. Theoretical fluid dynamics is crucial in understanding concepts and predicting performance. It can obtain much information using simplifying assumptions. However, it does not always provide sufficient information. The experimental fluid dynamics method is costly and a difficult way to achieve exact conditions for complex cases. Due to human errors or limitations of the repetitions, it is not possible always to develop real situations. The numeric fluid dynamic method provides a qualitative prediction of fluid flow with any conditions. With the use of algorithms, it has the potential to provide a tremendous amount of data at a fraction of the cost of experiments [184][185][188]. A fluid is any substance that flows because its particles do not bind to each other in the same way as in solids. The fluid includes both liquids and gases.

In fluid behavior study, it is essential to understand the properties of the fluid correctly.
The various properties of fluids include temperature, pressure, density, viscosity, etc. This section describes the properties of fluid that were considered in the flow phenomena.

Fluid flow equations are governed from partial differential equations (PDE), which represents the conservation laws for mass, momentum, and energy. CFD is the method of replacing such PDE systems by a set of algebraic equations and then can be solved with the help of computers. CFD provides a numerical approximation to the

equations that govern the fluid flow. CFD approach is used for the blood flow analysis of coarctation and Fontan sections of the thesis.

The pre-processing stage of the study consists of input to the flow problem. It involves the definition of the computational domain, grid generation, dividing the domain into a finite number of small sub-domains for meshing, the definition of fluid properties, and specification of appropriate boundary conditions for the case.

The general steps of these numerical algorithms consist of the integration of the governing equations, discretization of the integral equations into a system of algebraic equations, and the solution of the algebraic equations by an iterative method on CFD solver.

In the post-processing stage, the calculated results are visualized and interpreted utilizing streamlines, realtime flow frames, vectors, contours, and plots [34][179][189].

The density of the blood is defined as $\rho = 1060 \text{kg/m}^3$. The blood is assumed as an incompressible and Newtonian fluid. A Newtonian fluid is a fluid whose stress versus strain rate curve is linear. The constant of proportionality is called viscosity (η) is the ratio of the shearing stress (Eq 3.3) to the velocity gradient ($\Delta v_x/\Delta_z$ or dv_x/d_z) in a fluid (Eq 3.4).

The formula to calculate average shear stress is force per unit area is τ, where F is the force applied, and A is the cross-sectional area of material with area parallel to the applied force vector.

$$\tau = \frac{F}{A} \tag{3.3}$$

$$\mu = \frac{\tau}{dv_x/d_z} \tag{3.4}$$

Blood is approximately four times more viscous than water. It does not exhibit constant viscosity and is non-Newtonian, especially in the microcirculatory system [190][191]. That happens due to the presence of the red blood cells, which are small semisolid particles which increase the viscosity of the blood and affect the behavior of the fluid [192][193][194]. Generally, in large and medium-sized arteries, blood behaves as a Newtonian fluid, and it is used as a common assumption in blood flow

analysis. Hence, the blood was assumed a Newtonian fluid with constant viscosity is defined as $\mu = 0.0038\ \text{Pa} \cdot \text{s}$.

3.3.2.1 Continuity

3D mass conservation or continuity notation for a fluid is defined by Eq. (3.5):

$$\left(\frac{\partial \rho}{\partial t}\right) + \rho\ \nabla.u = 0 \tag{3.5}$$

For an incompressible fluid, the density [ρ] is constant (Eq. (3.6)):

$$\rho \nabla.u = 0 \tag{3.6}$$

Except that, cylindrical polar coordinate system is useful for the calculations of arteries. In this coordinate system the dimensions are r, θ and z. Advance of Eq. (3.7) and Eq (3.8), the incompressible continuity equation is obtained in Eq. (3.9):

$$\nabla = i_r\ \frac{d}{dr} + i_\theta \frac{d}{d\theta} + i_r \frac{d}{dz} \tag{3.7}$$

$$\vec{V} = i_r v_r + i_\theta\ v_\theta + i_r v_z \tag{3.8}$$

$$\nabla.\vec{V} = \frac{1}{r}\frac{dr v_r}{dr} + \frac{1}{r}\frac{dv_\theta}{d\theta} + \frac{1}{r}\frac{dv_z}{dz} = 0 \tag{3.9}$$

3.3.2.2 Navier and Stokes Equations

Momentum formulation in r direction is:

$$\rho\left[\frac{dv_r}{dt} + v_r\frac{dv_r}{dr} + \frac{v_\theta}{r}\frac{dv_r}{d\theta} - \frac{v_\theta^2}{r} + v_z\frac{dv_r}{dz}\right] = -\frac{\partial p}{\partial r} + \rho g_r + \mu\left(\frac{1}{r}\frac{d}{dr}\left(r\frac{dv_r}{dr}\right) - \frac{v_r}{r^2} + \frac{1}{r^2}\frac{d^2 v_r}{d\theta^2} - \frac{2}{r^2}\frac{dv_\theta}{d\theta} + \frac{d^2 v_r}{dz^2}\right) \tag{3.10}$$

Momentum formulation in θ direction is:

$$\rho\left[\frac{dv_\theta}{dr^2} + v_r\frac{dv_\theta}{dr} + \frac{v_\theta}{r}\frac{dv_\theta}{d\theta} - \frac{v_r v_\theta}{r} + v_z\frac{dv_\theta}{dz}\right] = -\frac{1}{r}\frac{\partial p}{\partial \theta} + \rho g_r + \mu\left(\frac{1}{r}\frac{d}{dr}\left(r\frac{dv_\theta}{dr}\right) - \frac{v_\theta}{r^2} + \frac{1}{r^2}\frac{d^2 v_\theta}{d\theta^2} + \frac{2}{r^2}\frac{dv_r}{d\theta} + \frac{d^2 v_\theta}{dz^2}\right)$$

(3.11)

Momentum formulation in the z-direction is:

$$\rho\left[\frac{dv_z}{dt} + v_r\frac{dv_z}{dr} + \frac{v_\theta}{r}\frac{dv_z}{d\theta} + v_z\frac{dv_z}{dz}\right] = -\frac{\partial p}{\partial z} + \rho g_r + \mu\left(\frac{1}{r}\frac{d}{dr}\left(r\frac{dv_z}{dr}\right) + \frac{1}{r^2}\frac{d^2 v_z}{d\theta^2} + \frac{d^2 v_z}{dz^2}\right) \tag{3.12}$$

The additional terms on both sides of the r and θ components of Navier&Stokes Equation components in Eq. (3.10) and Eq(3.11), Eq(3.12) come up whereby the unique nature of cylindrical coordinates [195], [196]. Namely, when the movement is

in the θ direction, the unit vector also changes direction; thus, r and θ components are coupled.

6 independent components of the viscous stress tensor are depicted in cylindrical coordinates in Eq. (3.13):

$$\tau_{ij}=\begin{bmatrix}\tau_{rr} & \tau_{r\theta} & \tau_{rz}\\ \tau_{\theta r} & \tau_{\theta\theta} & \tau_{\theta z}\\ \tau_{zr} & \tau_{z\theta} & \tau_{zz}\end{bmatrix}=\begin{bmatrix}2\mu\frac{dv_r}{dr} & \mu\left[r\frac{d}{dr}\left(\frac{v_\theta}{r}\right)+\frac{1}{r}\frac{dv_r}{d\theta}\right] & \mu\left(\frac{dv_r}{dz}+\frac{dv_z}{dr}\right)\\ \mu\left[r\frac{d}{dr}\left(\frac{v_\theta}{r}\right)+\frac{1}{r}\frac{dv_r}{d\theta}\right] & 2\mu\left(\frac{1}{r}\frac{dv_\theta}{d\theta}+\frac{v_r}{r}\right) & \mu\left(\frac{dv_\theta}{dz}+\frac{1}{r}\frac{dv_z}{d\theta}\right)\\ \mu\left(\frac{dv_r}{dz}+\frac{dv_z}{dr}\right) & \mu\left(\frac{dv_\theta}{dz}+\frac{1}{r}\frac{dv_z}{d\theta}\right) & 2\mu\frac{dv_z}{dz}\end{bmatrix} \quad (3.13)$$

Substituting relationships and simplifying, the momentum equations reduce to the form of Eq (3.10), Eq (3.11) and Eq (3.12); Eq (3.13), the general form of Navier&Stokes Equations is defined in Eq. (3.14):

$$\rho\frac{d\vec{V}}{dt}+\rho\vec{V}.\nabla\vec{V}=-\nabla p+\rho\vec{g}+\mu\nabla^2\vec{V} \quad (3.14)$$

Where $\rho\frac{d\vec{V}}{dt}$ is the local acceleration, $\rho\vec{V}.\nabla\vec{V}$ is the convective acceleration, $-\nabla p$ is the pressure force per unit volume $\rho\vec{g}$ is the body force per unit volume, and $\mu\nabla^2\vec{V}$ is the viscous force per unit volume.

3.3.2.3 Boundary Conditions

Boundary conditions are required components of a numerical model of fluid flow. In numerical simulations, it is essential to define the boundary conditions for the selected region of the problem, as one might not be interested in simulating the region.

Inappropriate boundary conditions might result in non-physical solutions. Common boundary conditions are classified either in terms of numerical parameters that have to be set in terms of physical conditions. The physical boundary conditions principally used in fluid flow analysis are fluid properties, walls, inlets, and outlets, symmetry boundaries, pressure and outflow boundary conditions, periodic/pulsatile conditions, waveforms, etc. [68][127][39].

Inlet is the entrance region where the fluid enters the cylindrical domain; therefore, its velocity, mass flow rate, or the pressure gradient should be known. The pressure gradient drives the fluid in confined fluid flows [188].

3.3.2.4 Solver Setup

The validated CFD solver ANSYS Fluid Flow (FLUENT) is used for numerical flow analysis [197][128][198]. Blood was assumed an incompressible-Newtonian fluid.

For aortic coarctation, patients' user-defined function is used to specify the velocity profile for the pediatric aorta prepared for four cycles, was used in setup settings where the transient laminar model solution was preferred. Blood density was 1060 $kg/m^{3,}$ and blood viscosity was 0.0038 kg/ms. The solution method was a SIMPLE algorithm, Green-Gauss Node Based gradient, pressure for spatial discretization, and second-order upwind for momentum. The transient formulation was made with Bounded Second-Order Implicit [197][68][195]. The number of time steps was 54000, and time step size was 0.001 for the calculation. The user-defined function imported to the analysis for the coarctation section is in APPENDIX A.

For Fontan surgical planning, typically, there four inlet vessels. So four scalars were specified due to multiple inputs, and the constant coefficients were taken as 1e-9 for each of them.

The user-defined function file was prepared for the Outlet Gauge Pressure with the resistance parameters obtained from the clinical data of the patients [199][200][72]. The SIMPLE algorithm is used in the viscous laminar transient model for Fontan patients. The mass flow rate monitor was set for the following process of all simulation runs.

The user-defined function imported for resistance boundary conditions of the Fontan section is in APPENDIX B.

3.3.3. Structural Analysis

Stress calculations examine the state of a whole or part in the structural loading environment, depending on various models and materials. In the surgical design to be reviewed, safety factors, pressures, forces, and displacements are compared. In

research containing the analysis of tension and pressure distributions of biomaterial (shunt, graft, patch, cannula, etc.) configurations on the anatomical model of the patient and the tissue behavior under mechanical loads, simulations can be performed with finite element analysis considering the mechanical properties of materials and tissue [30][41].

3.3.3.1 Von Mises Yield Criterion Equations

The relations between external forces (which characterize what is called the stress and the deformation of the body), which characterizes strain, are called Stress-Strain relations [201]. These relations represent properties of the material that compose the body and are also known as constitutive equations. When a body (or a part of it) is under given stress that satisfies a particular relation referred to as a yield criterion, plastic components of strain are produced (deformation). One such yield criterion is the von Mises yield criterion (the maximum distortion energy) [201][202][203]. It is part of plasticity theory that applies best to ductile materials. Before yield, the material response can be assumed to be of a nonlinear elastic, viscoelastic, or linear elastic behavior [204]. The definition of the von Mises yield criterion states that the von Mises stress (equivalent tensile stress) of a material under load should not be equal nor higher than the yield limit of the material under uniaxial stress [205].

The elastic limit defines the region where energy is not lost during the process of stressing and straining. This limit is defined as 'yield stress.' Above that limit, the deformations stop being elastic and start being plastic, and the deformation includes an irreversible part. The stress value of the elastic limit is used here as S_y.

The von Mises stress is a criterion for yielding, used for ductile materials. It states that yielding will occur in a body if the components of stress acting on it are higher than the criterion [203]. The constant k is defined through experiment, and τ is the stress tensor in Eq 3.15:

$$\frac{1}{6}[(\tau_{11}-\tau_{22})^2+(\tau_{22}-\tau_{33})^2+(\tau_{33}-\tau_{11})^2+6(\tau^2{}_{12}+\tau^2{}_{23}+\tau^2{}_{13})^2]=k^2 \quad (3.15)$$

Standard experiments for defining k are made from uniaxial stress, where the above expression reduces to:

$\frac{\tau^2 Y}{3} = k^2$ (3.16)

If τ_y reaches the simple tension elastic limit, S_y, then the above expression becomes:

$\frac{S^2 Y}{3} = k^2$ (3.17)

Which can be substituted into the first expression in Eq 3.18:

$\frac{1}{6}[(\tau_{11} - \tau_{22})^2 + (\tau_{22} - \tau_{33})^2 + (\tau_{33} - \tau_{11})^2 + 6(\tau^2{}_{12} + \tau^2{}_{23} + \tau^2{}_{13})^2] = \frac{S^2 Y}{3}$ (3.18)

The von Mises stress, τ_v, is defined as:

$\tau^2 y = 3k^2$ (3.19)

Therefore, the von Mises yield criterion is also commonly rewritten in Eq 3.20:

$\tau^2 v \geq S_y$ (3.20)

That is, if the von Mises stress is higher than the simple tension yield limit stress, then the material is expected to yield.

The von Mises stress is a theoretical value that allows the comparison between the general 3D stress with the uniaxial stress yield limit. The von Mises yield criterion is also known as the octahedral yield criterion [206].

This is because the shearing stress acting on the octahedral planes (eight planes that form an octahedron, whose normals form equal angles with the coordinate system) can be written as:

$\frac{1}{3}\sqrt{(\tau_1 - \tau_2)^2 + (\tau_2 - \tau_3)^2 + (\tau_3 - \tau_1)^2} = \tau_{Octahedron}$ (3.21)

Which, for the case of uniaxial or simple tension, simplifies to Eq 3.22:

$\frac{\sqrt{2}}{3}\tau_y = \tau_{Octahedron}$ (3.22)

If τ_y reaches the simple tension elastic limit, S_y, then the above expression becomes:

$\frac{\sqrt{2}}{3} S_y = \tau_{Octahedron}$ (3.23)

By applying this result in the octahedral stress expression:

$\sqrt{\frac{(\tau_1 - \tau_2)^2 + (\tau_2 - \tau_3)^2 + (\tau_3 - \tau_1)^2}{2}} = S_y$ (3.24)

Similarly to the result obtained for the von Mises Stress, this formulation designates a benchmark considering the octahedral stress. Consequently, if the octahedral stress is higher than the simple stress yield threshold, then the yield is expected to take place.

In this case, the von Mises stress is defined in Eq 3.25:

$$\sqrt{\frac{(\tau_z-\tau_t)^2+(\tau_t-\tau_r)^2+(\tau_r-\tau_z)^2}{2}} = \tau_v \quad (3.25)$$

Where z, r, and t are the axial, radial, and tangential stresses. The criterion is the same as before if the von Mises stress obtained from the above expression is equal or greater than the simple tension yield stress of the material, then yielding is expected to occur [205].

3.3.3.2 Solver Setup

In this thesis, the results of the studies with FEA are explained in the 'Results Chapter,' but for modeling studies, static structural analysis in the idealized coarctated artery is used to obtain the geometry with the opening of the surgical incision under load and for ideal patch modeling studies for final analysis.

'ANSYS Static Structural' tool is used for mechanical analysis of pulmonary coarctation cases. Program controlled solver type, and solver pivot checking is selected. Stress and strain output controllers were set.

The material properties set into the 'Outline of Schematic Engineering Data' in ANSYS Workbench. The pediatric artery material properties set on ANSYS are in Table 3.3:

Outline of Schematic B2: Engineering Data

	A	B
1	Contents of Engineering Data	
2	Material	
3	artery	
4	PATCH_Pericardium	
5	PATCH_PTFE	
6	Structural Steel	
*	Click here to add a new material	

Properties of Outline Row 3: artery

	A	B	
1	Property	Value	
2	Material Field Variables	Table	
3	Isotropic Elasticity		
4	Derive from	Young's Modulus and Poisson's Ratio	
5	Young's Modulus	1E+06	Pa
6	Poisson's Ratio	0.49	
7	Bulk Modulus	1.6667E+07	Pa
8	Shear Modulus	3.3557E+05	Pa

Table 3.3 The material properties for the human artery, which is set into ANSYS Structural Analysis Engineering Data for the pulmonary patch section.

The sequence of the surgery, simulated through the structural analysis, start with the reduction of intramural pressure to the 0 level, due to the cardiopulmonary by-pass and aortic cross-clamp [207].

The residual stresses are introduced through the 'pressure equivalent residual stress' technique, where a finite intramural pressure corresponding to the desired residual stress distribution is applied to the configuration, which is typically 5 mmHg [208]. This 3D curve of the incision is converted to a zero-gap slit at finite element method model where the cross-sectional area of the cut in both sides is opened slightly due to the release of residual stresses in ANSYS [30]. The surface pressure (from the inside outward) was set as - 0.0001 MPa. Line Pressure was set in four steps for the virtual incision for each line region, which are created on ANSYS design modeler. The load (line pressure) was defined 5 N/mm for a section and -5 N/mm for b section. The load was defined 1 N/mm for c and d sections and -1 N/mm for a and f sections by following the same path (Figure 3.22).

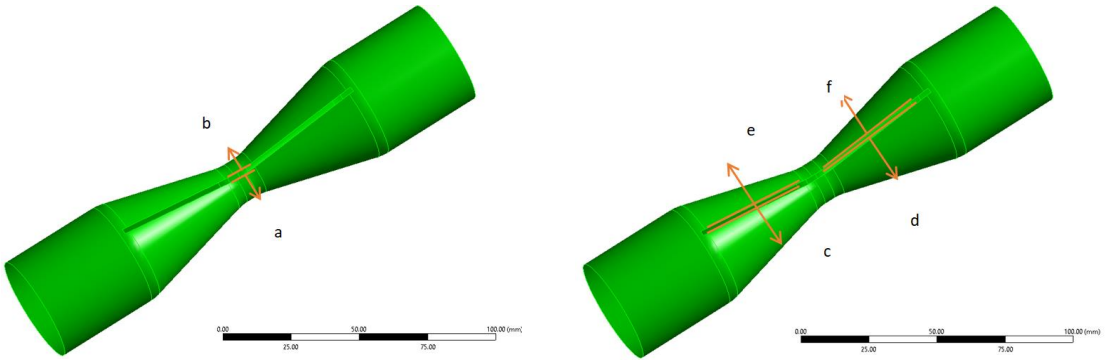

Figure 3.22 The load locations and directions on idealized stenosed pulmonary artery [5 N/mm for and b (at left) 1 N/mm for c,d,e,f (at right)].

Equivalent Stress and Total Deformation were set at deformation conditions on ANSYS. And the new geometry deformation under stress is obtained after the structural analysis (Figure 3.23).

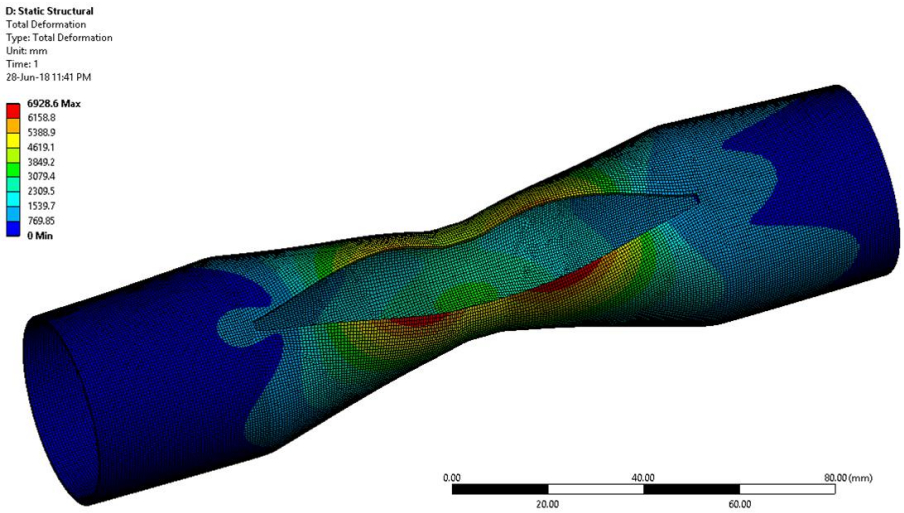

Figure 3.23 Total deformation distribution on the incision line after internal surface pressure on the artery wall.

The width of the opened gap depends on the magnitude and direction of the force applied by the surgeon and the residual stress level. This gap, which is prepared just before the patch implantation, can be precisely controlled in the surgical procedure, as this opening is an essential intra-operative geometrical parameter. The new artery model is exported to the CAD tool for obtaining the ideal patch for this geometry (Figure 3.24). The gap was marked with point elements to create a curve in the Geomagic Wrap CAD tool [159].

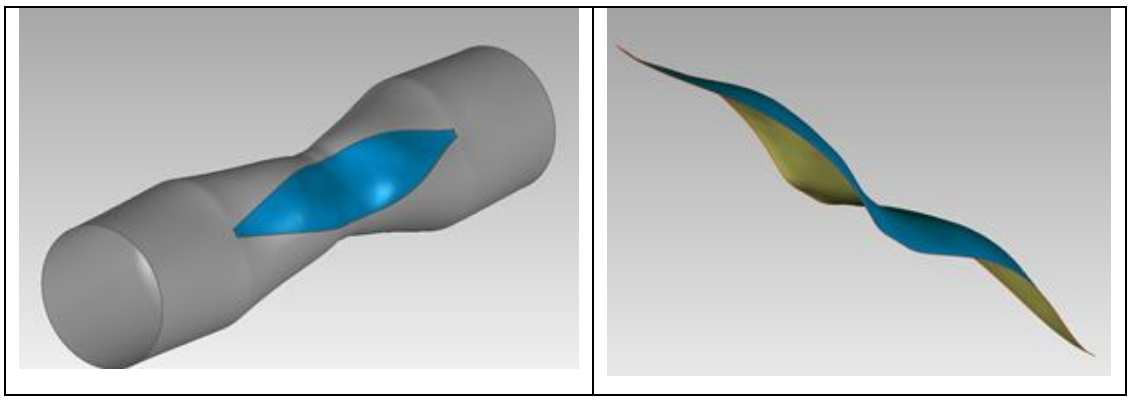

Figure 3.24 The virtual 3D patch design on the gap curve of the artery model.

This curve was converted to a surface that has the same thickness as the artery. Both the artery model with gap and the patch were imported to ANSYS Design Modeler to fit the parts on correct lines. Contact regions were set on ANSYS Structural when the overlap elements were signed for both artery and patch models (Figure 3.25). The Surface Pressure (from the inside outward) is set as -0,003 Mpa [30]. The patch material properties were set due to Table.3.4.

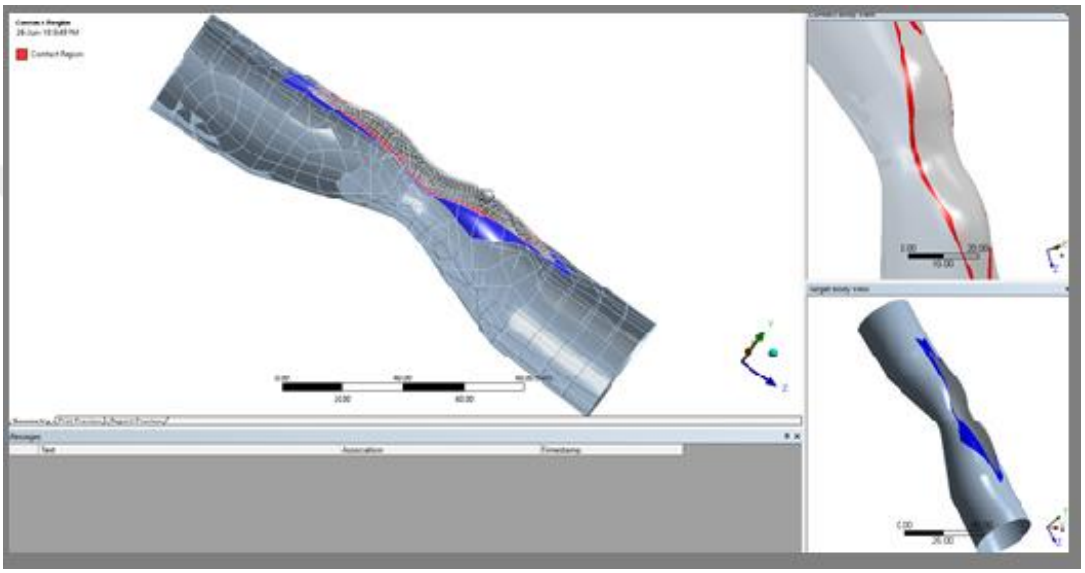

Figure 3.25 Grid generation is set by a mesh tree of the left column. A triangular mesh is created with a 1 mm size, and the mesh quality is checked for zero skewness.

	Poisson's Ratio	Young's Modulus (MPa)	Thickness (mm)
Human Pericardium	**- 0.4**	**3.4**	**0.5**
Polytetrafloretilen (PTFE)	**- 0.31**	**1.4**	**0.7**

Table 3.4 The material properties for most preferred vascular patches.

The main pulmonary artery inlet and the inlet of the branch without patch were defined as fixed supports, and the inlet of the branch with the patch was defined for displacement for patient-specific models. Left inlet for displacement and one right

inlet were for fixed support on the idealized artery. The new patched artery geometry deformation under pressure was obtained after structural analysis (Figure 3.27).

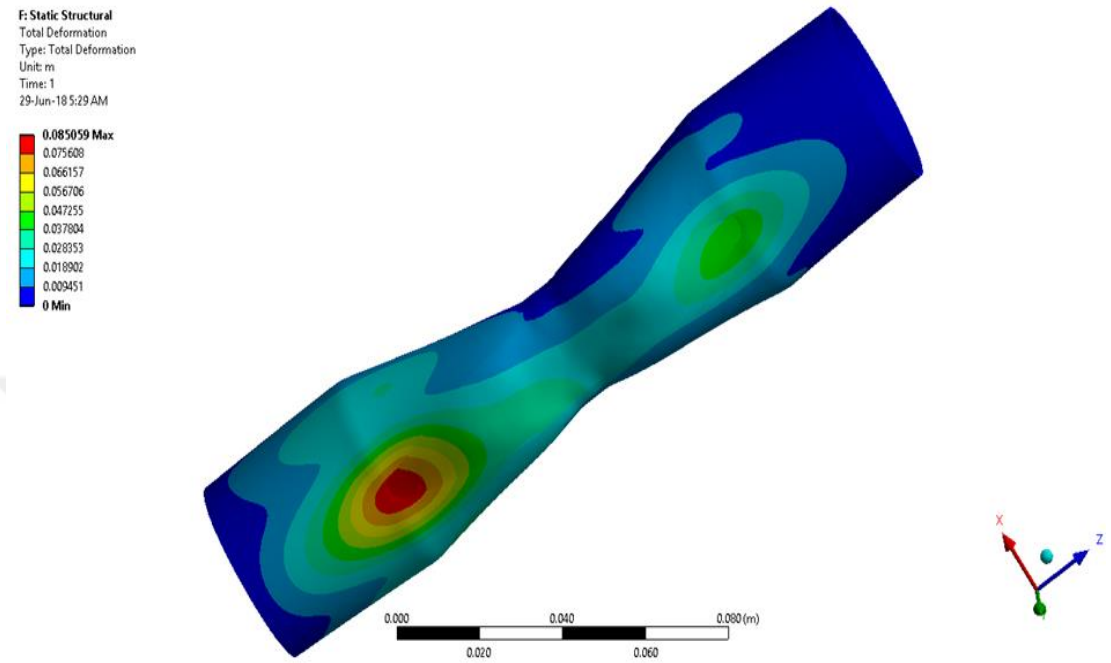

Figure 3.26 Total deformation on patched (with PTFE) virtual artery in the post-process section of structural FEA analysis.

CHAPTER 4

4. SURGICAL PLANNING

In this chapter, treatment planning on CHD and methodology mentioned in the previous chapters are explained in detail under the 'Repair Planning' headings of Intracardiac Malformations, Coarctation, and Fontan Correction.

4.1. Repair Planning for Intracardiac Malformations

The patients with DORV, TGA, and VSD, aged 1 month to 2 years, were enrolled in this section of the study. All patients had previously undergone an extensive clinical evaluation and cardiovascular imaging, and then discussed and reviewed the departmental surgical consultations. 3D virtual models were created if the image-based information is insufficient for surgical planning in the workflow of the study (Figure 4.1).

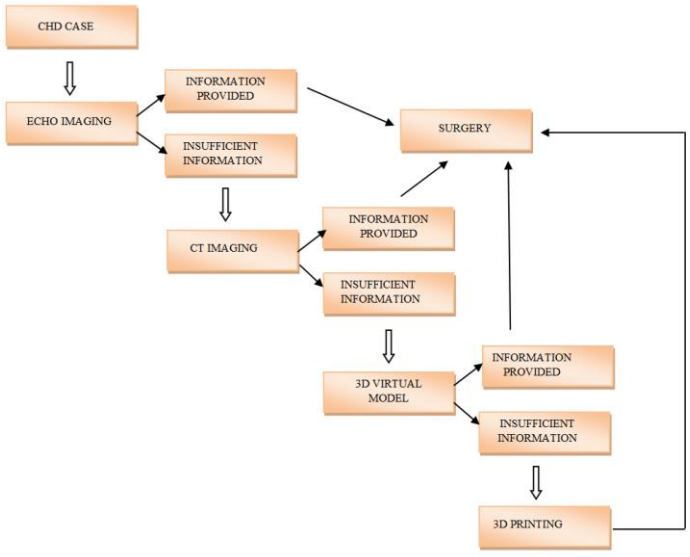

Figure 4.1 The decision tree for surgical planning

The most critical surgical indication for DORV and TGA cases is whether tunneling between the left ventricle (LV) and the aorta is possible via VSD [20][5][95]. Remote VSD may interfere with valve straddling, conal septum narrowing the left ventricular outflow tract, or ventricular hypoplasia, biventricular repair.

In these cases, Glenn anastomosis is also a possibility if aortic root translocation, arterial switch modifications, and double ventricular repair are not suitable [53][59][103]. Patients with possible biventricular repair can be guided to a single ventricular type repair because anatomic identification is incomplete.

The visualization of structural details requires further treatment to create a detailed segmented intracardiac model. 3D heart modeling and printing can provide valuable information for surgical planning. In complex DORV pathologies, 3D intracardiac modeling can be used to clarify whether the LV-aorta tunnel is possible. In order to investigate the suitability of this, intracardiac models were examined, and additional information that might be helpful in surgical planning was searched in this section.

The images obtained with the para-septal sagittal incisions applied to the models were decided to be the most appropriate in terms of planning. Paraseptal incisions were routinely performed on the model. If deemed necessary by the cardiac team, other virtual incisions were applied to the model.

All heart models were created as the default application for each dataset taken into the database. Intracardiac modeling was performed for 120 of these models containing VSD.

Most of the patients were diagnosed with DORV and TGA. In the present section of the study, the axial 3D image on the CT dataset, the 3D virtual model created, the virtual-paraseptal incision performed to view the structural pathology, and the 3D models created with the SLA printer if it is required. 4 cases of this section of the study are selected from the intracardiac repair sub-database for the presentment.

Selected examples of this section are as follows:

- **1st CASE**

A patient (named IMA_0019 in the database) who was thirty weeks old and diagnosed with restrictive ASD, VSD, DORV. The past intervention was pulmonary banding aortic arch repair. The surgical options were bidirectional Cavo-pulmonary

anastomosis or LV to aorta baffle and RV to PA conduit. The virtual and physical prototype models are generated for the decision-making process.

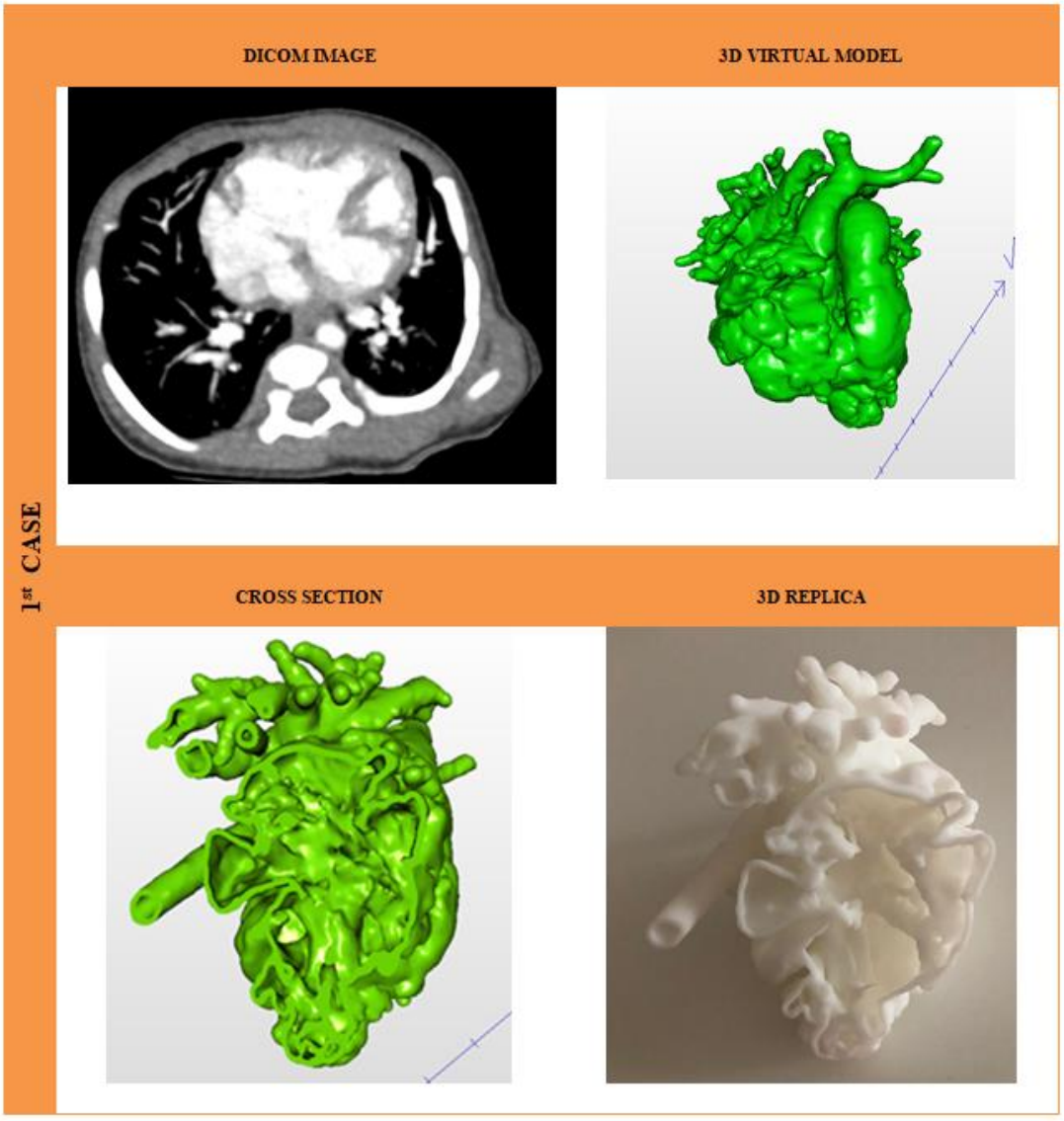

Figure 4.2 Image data (top-left), 3D model (top-right), virtual cut (bottom-left) and 3D physical model (bottom-right) of Case-1.

- **2nd CASE**

Three weeks old, a male who was diagnosed with a small, sub-aortic VSD is the first case that was not able to be diagnosed on the existed imaging data (Figure 4.3).

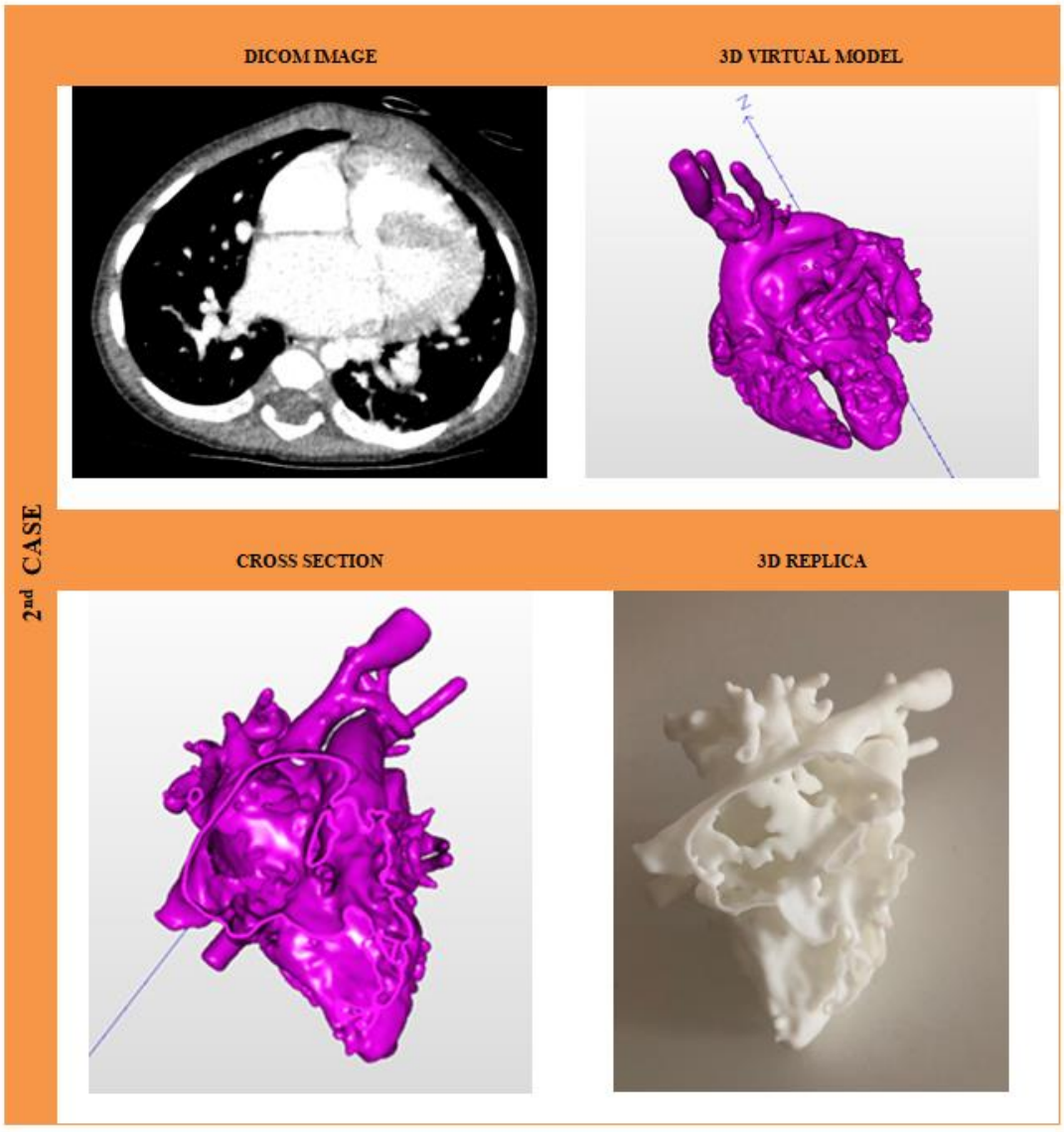

Figure 4.3 Image data (top-left), blood pool(top-right) , intracardiac cross-section(bottom-left) and physical(bottom-right) models of Case-2.

The second case is a 13 months old male patient diagnosed with d-TGA, VSD, and severe pulmonary stenosis with moderate annular hypoplasia.

The past intervention was PDA stenting. The surgical options were LV-Aorta tunnel and RV-PA conduit or pulmonary root translocation with VSD enlargement.

- **3rd CASE**

Forty-eight weeks old, 18 kg patient was diagnosed with double inlet left ventricle and atrioventricular discordance (Figure 4.4).

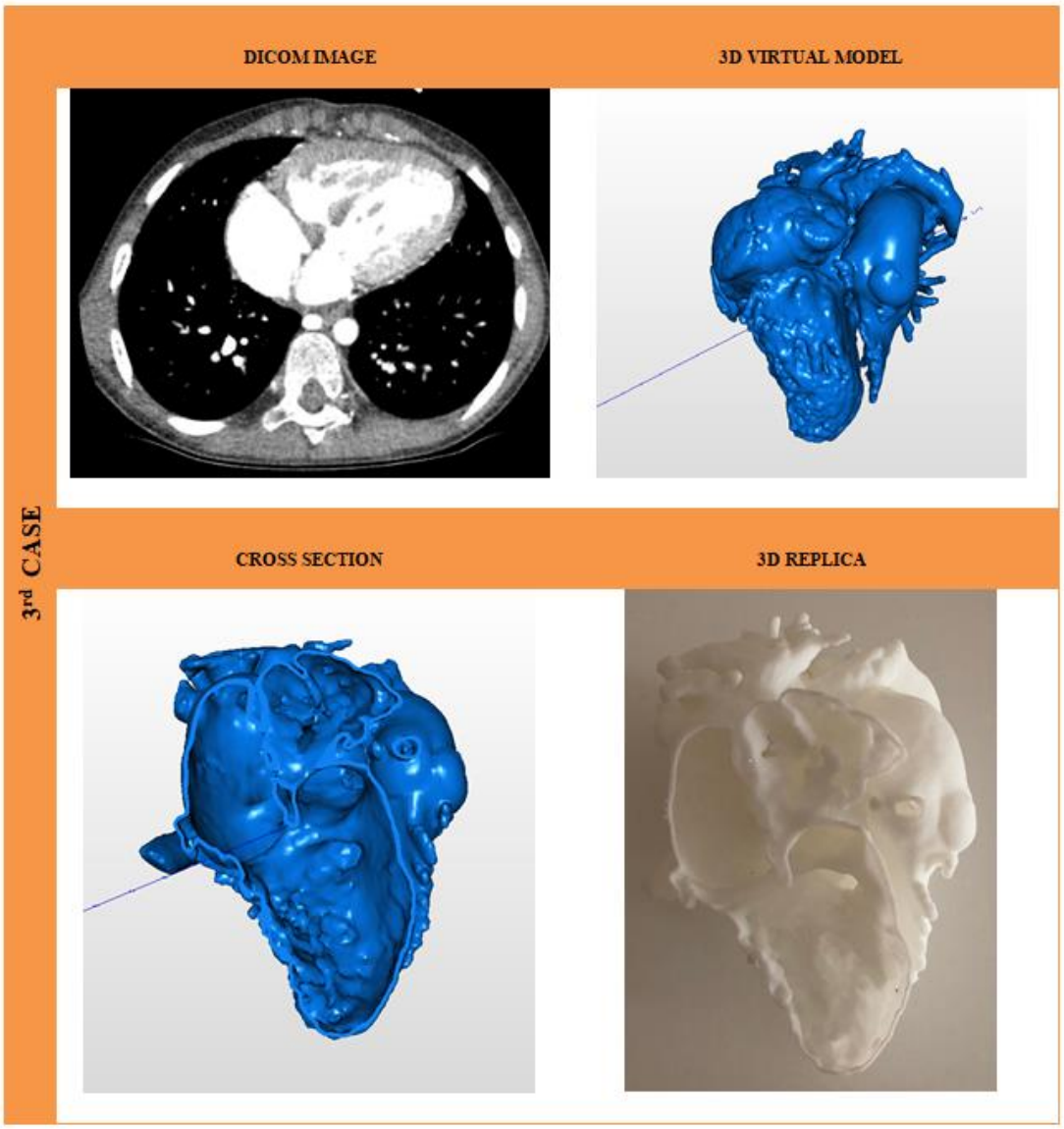

Figure 4.4 Image data (top-left), blood pool(top-right) , intracardiac cross-section(bottom-left) and physical(bottom-right) models of Case-3.

The past interventions were pulmonary bending and bidirectional cavopulmonary anastomosis. The surgical options were VSD enlargement or Damus-Kaye-Stansel procedure [92][79][25].

- **4th CASE**

Thirty months old 12 kg patient was diagnosed with DORV, large inlet VSD and sub-valvular aortic stenosis (Figure 4.6).

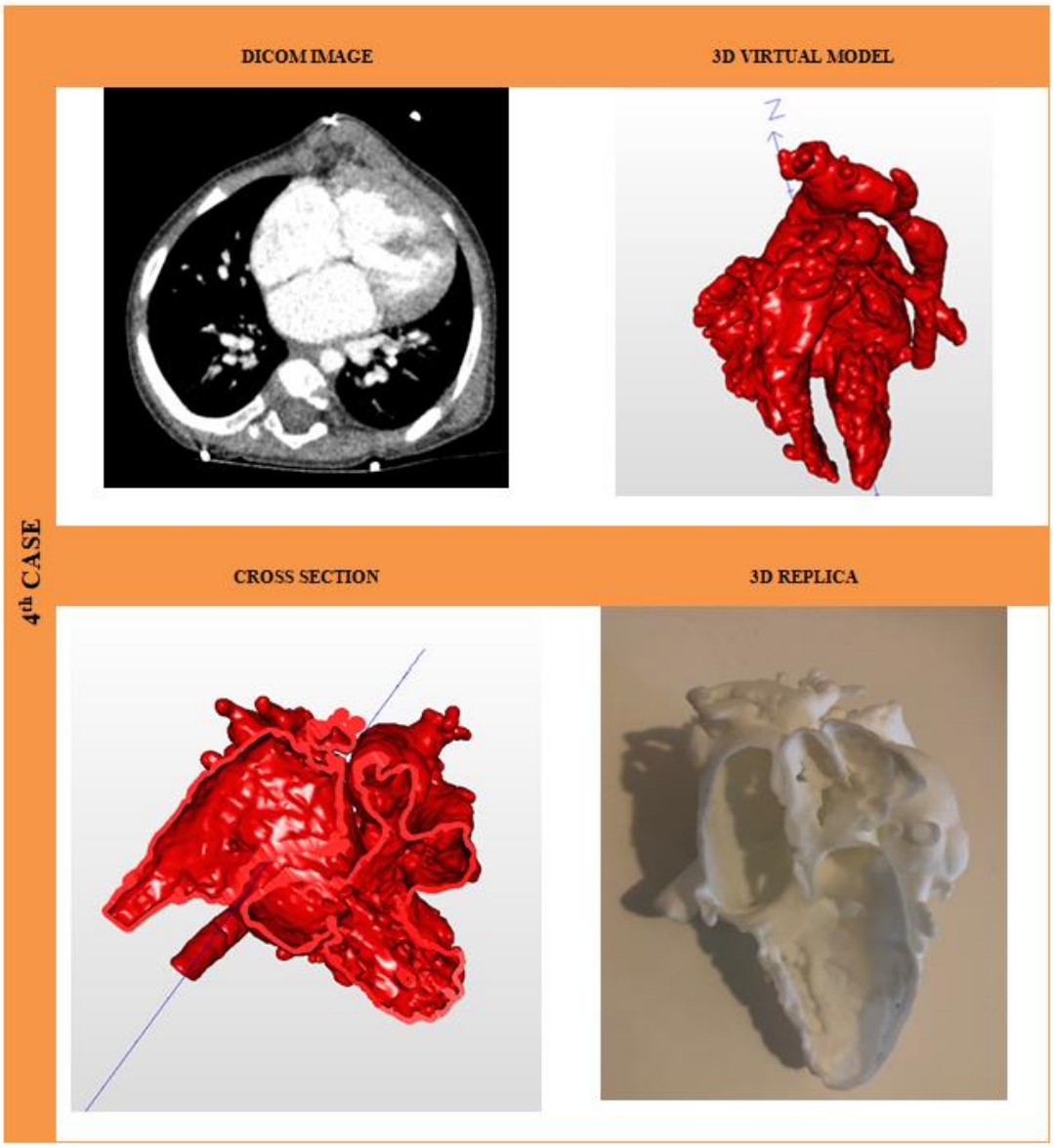

Figure 4.5 Image data (top-left), blood pool(top-right) , intracardiac cross-section(bottom-left) and physical(bottom-right) models of Case-4.

The past intervention was pulmonary banding. The optional surgical repairs were LV to aorta baffle and RV to PA conduit or bidirectional cavopulmonary anastomosis.

4.2. Virtual Surgery

In this chapter, pre-operative planning in CHD cases is mentioned under several headings. Thus, in the examples of different complex disease groups, planning studies to be performed with the tools mentioned in the 'Methods' chapter was performed on the actual patients and the actual clinical data that were contributed to the correct decision-making process in terms of patient's health status and future outcome (Figure 4.6).

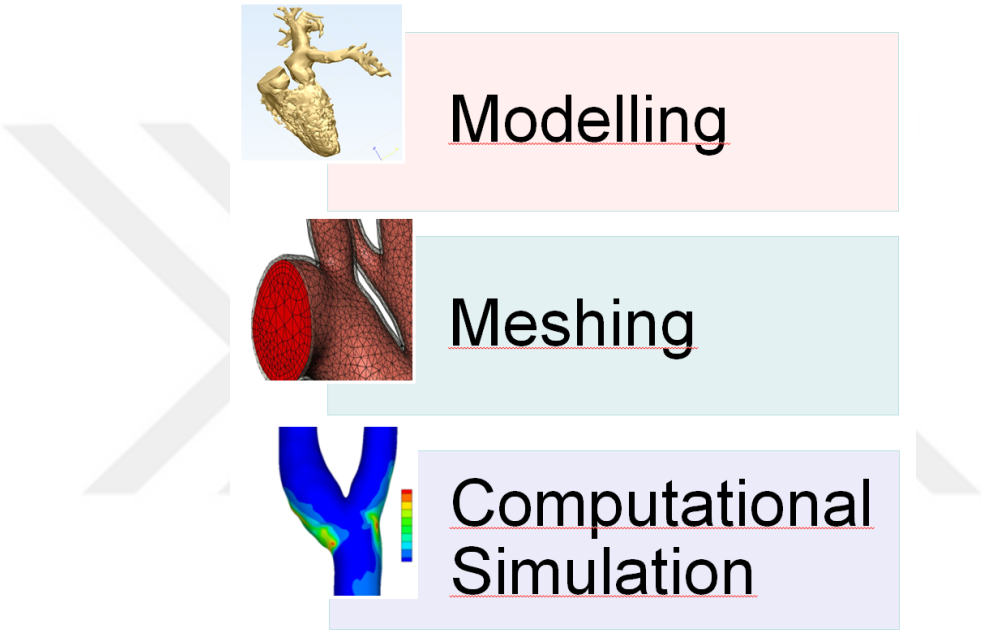

Figure 4.6 The workflow for pre-operative planning with FEA.

The primary motivation is to emphasize the importance of pre-operative studies and to show how particular mathematical methods can contribute to this. The flow condition resulting from the repair of vascular stenosis was examined separately for aortic and pulmonary arteries, and the Fontan study hemodynamic analysis evaluated for various shunt configurations. Centerlines of distributed flow were calculated by the estimation algorithm of the segmentation tool (Figure 4.7).

Flow rates of the inlet and outlet parts, and inlet velocity parameters were calculated due to the flow distributions, clinical estimations, areas of cross-sections of the region of interests for each case [3]. The resistances of these regions are also calculated for the shunt configurations study of Fontan patients. The blood flow volume per time is presented as Q; the pressure change is presented as ΔP (mmHg) and the resistance to flow is presented. R (mmHg $_{x}$ min $_{x}$ mL^{-1}) in Eq 4.1. The resistance parameters were

obtained from pressure gradients per-flow rate quantities at the open ends of the artery model [209][200][66][77].

$$R = \frac{\Delta P}{Q} \qquad \text{(Eq 4.1)}$$

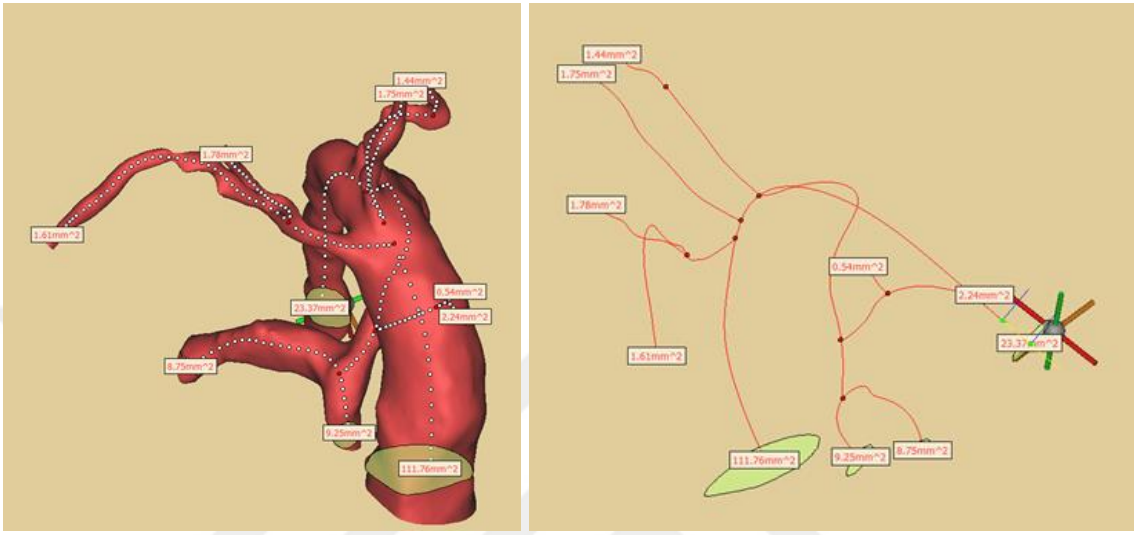

Figure 4.7 Surface areas of open-ends and the centerline of blood flow are calculated on the image processing and segmentation tools.

4.2.1. Coarctation

4.2.1.1 Aortic Coarctation Repair

Congenital aortic arch hypoplasia has various treatment options depending on the location and severity of the case [210][124][139].

When deciding, the surgeon takes into account the short and long-term consequences in light of the conventional methods and his/her experience. In this part of the study, five patients with aortic hypoplasia agreed to participate in the study, and preoperative computerized tomography (CT) images and virtual surgical planning techniques were used to evaluate possible various repair options (Figure 4.8).

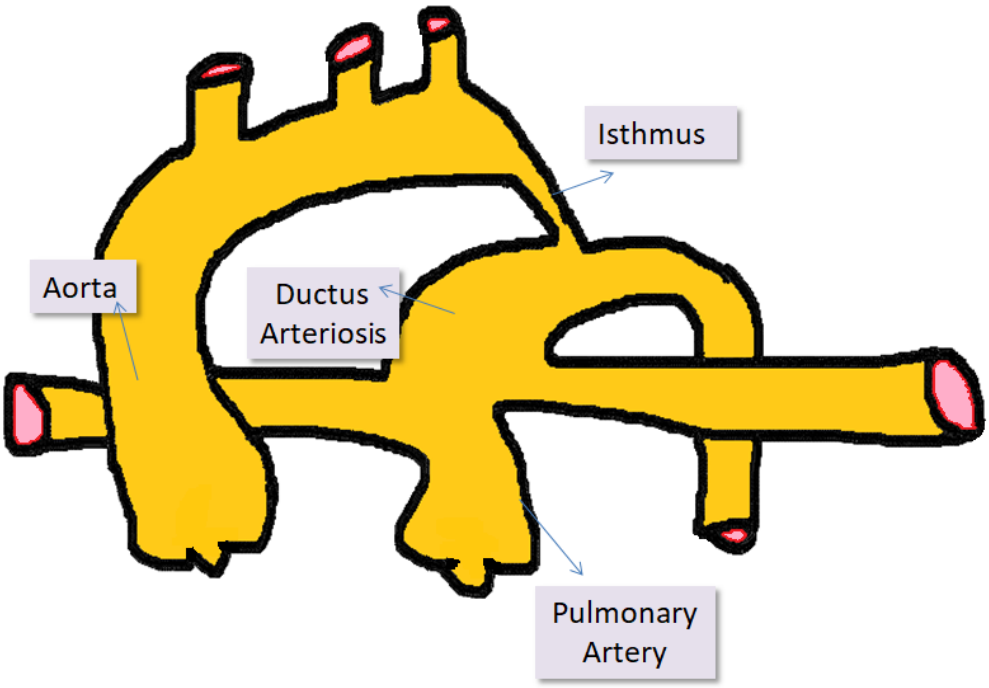

Figure 4.8 The selected models had narrow segments on the aortic arch. The illustrative 2D model of one of the selected patients depicts a coarctation (proximal to PDA) on the pre-ductal segment of the aortic arch.

A comparison of the virtual repair technique in the hypoplastic aortic pathologies with the actual data in the evaluation of hemodynamic performance is evaluated in the aortic coarctation part for each patient. Treatment options included resections, end-to-end anastomosis, patch angioplasty, subclavian flap, and combinations of these tailoring methods (Figure 4.9). The postoperative CT data of the patients were also modeled and compared with the virtual repair results and expectations for each patient.

For each file, drafts were first created with two-dimensional drawings, and then virtual repair was performed with CAD tools (Figure 4.10).

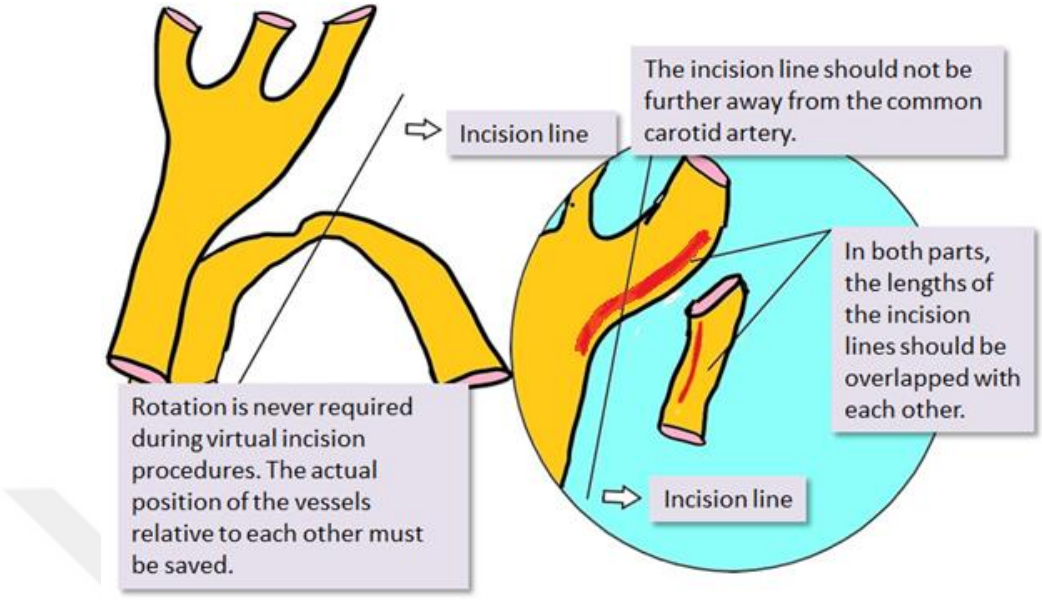

Figure 4.9 The repair precepts draft for an interrupted aortic arch of one of the cases in the study sub-database.

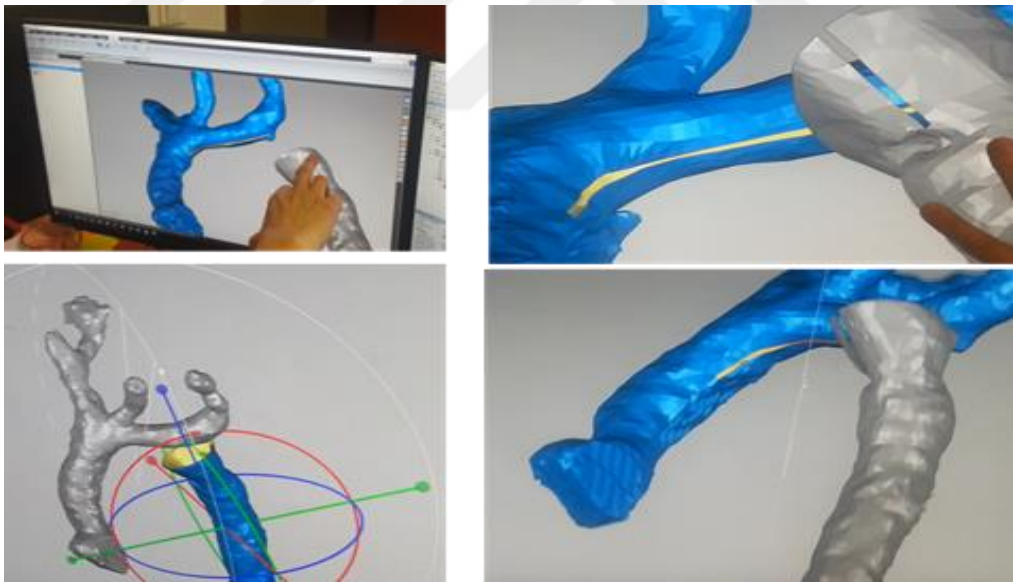

Figure 4.10 Mimicking of the steps made during the real operation in the computer environment with the cooperation of the surgeons and engineers.

Virtual patch reconstructions are performed due to the opened gaps, as mentioned in the 'Methods Chapter.' Boundary conditions derived from clinical data, postoperative blood flow behavior is simulated with a validated computerized fluid dynamics software tool.

Five cases in detail are as follows:

- **1st CASE**

The first of the patients selected by meticulous examination of complex coarctation data recorded in the database was a patient with pre and post-operative multi-sliced data (Figure 4.11). This case was a three-months-old female patient's case diagnosed with a complex coarctation on the isthmus segment with a large PDA, as mentioned in Figure 4.8.

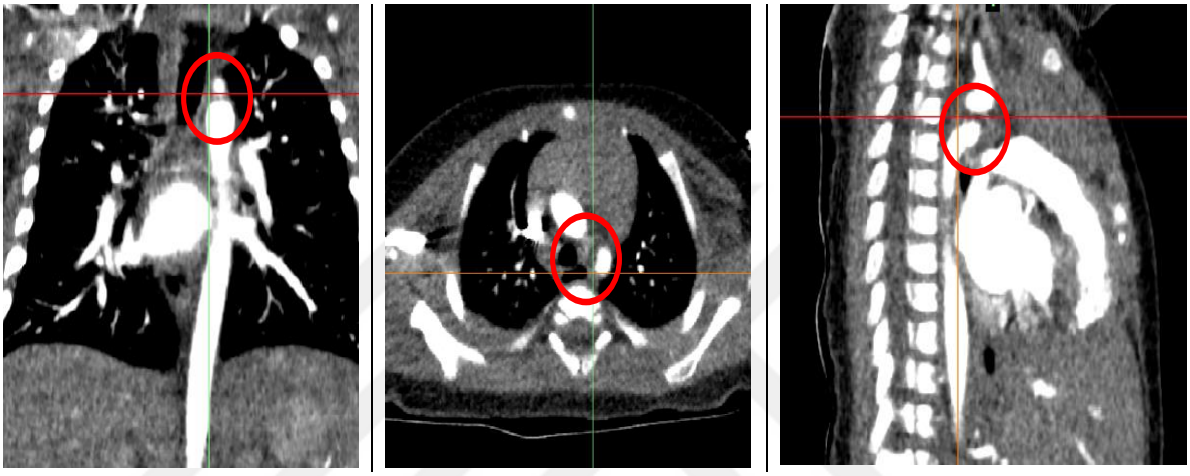

Figure 4.11 The coarctation region of the artery of the first selected patient (three months old) on axial, sagittal, and coronal planes of the pre-operative CT dataset. The case is named IMA_023 in the database.

Three different surgical repair methods were performed for this patient. In addition, preoperative and postoperative models were included in the study in all coarctation cases for comparison of FEA analyzes. In patients with coarctation, conventional aortic valve or ventricular problems were recorded in the database to be taken into consideration when necessary.

Therefore, intracardiac cavity models were also created by modeling the whole heart model, then the large vessels and ventricles separately for each patient. (Figure 4.12).

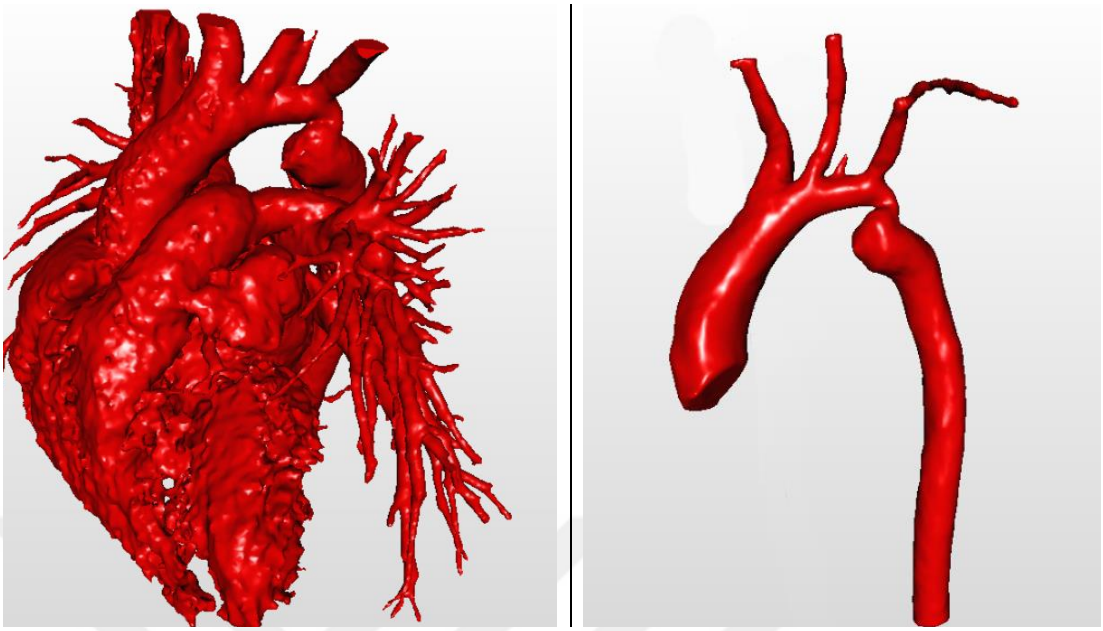

Figure 4.12 The whole heart (left) and the aorta model re-constructed from the pre-operative image dataset of the first selected patient.

- **Native Artery**

The pre-operative aorta model is re-constructed with image processing tools and names as A1-1.

	Models of First Patient for FEA
1	**Pre-Operative (Native) / A1-1**
2	**Resection and Extended Anastomosis (A curved Joint) / A1-2**
3	**Resection Method and End-to-End Anastomosis (A perpendicular Joint) / A1-3**
4	**Patient-Specific Patch Angioplasty/ A1-4**
5	**Post-Operative/ A1-5**

Table 4.1 The subsection models and the code labels of the first aortic coarctation case.

- **1st Virtual Repair of the First Patient: Resection and Extended Anastomosis**

The first of the repair options were planned as an expanded anastomosis to protect the curve of the arch. First, the PDA was allocated to simplify the workspace. After the resection of the deformed tissue segment and the surrounding area, a curvature was created to connect the remaining sections with the most significant

slope. The steps to be performed in the surgery were tried to be mimic as realistic as possible. In the first repair, the first two incisions were made, as shown in Figure 4.13.

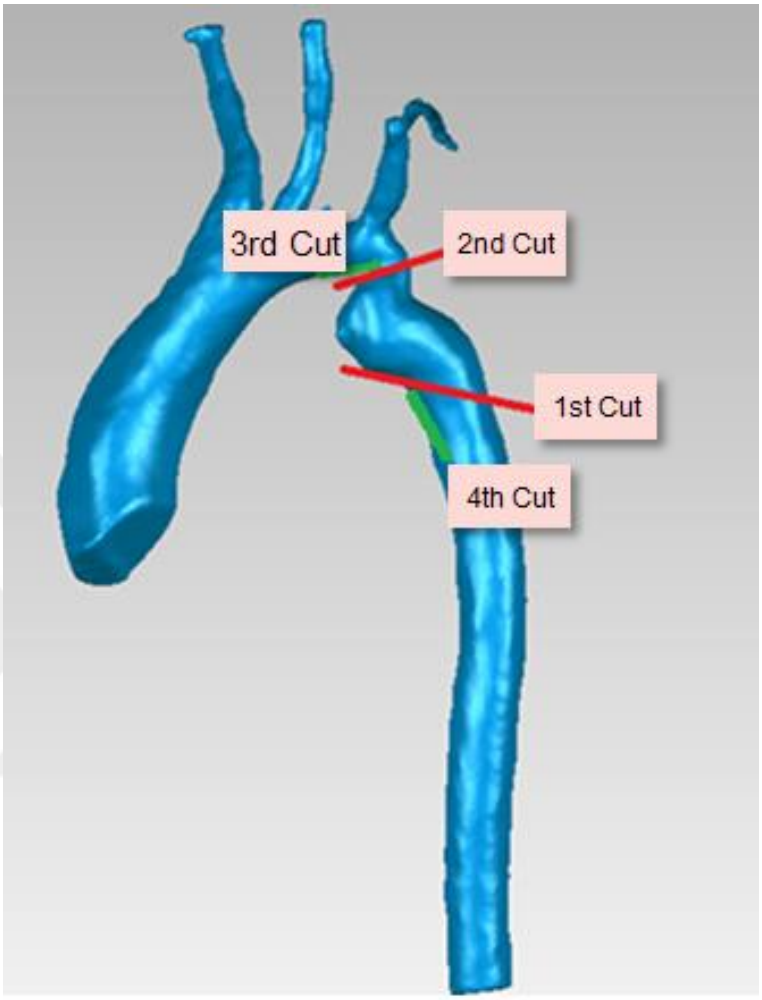

Figure 4.13 The 1st, 2nd, and 3rd cut lines on the native geometry of the first selected patient with aortic arch coarctation. 1st, 2nd are for resection (red lines), and the 3rd and 4th cut are for anastomosis (green lines).

While creating the 3rd incision corresponding to the distal arch, it was taken care of not to extend until the proximal arch level.

After this process, incisions overlapping in the upper and lower parts were opened, and joining points were formed. Priority was given to joining the rear (Figure 4.14).

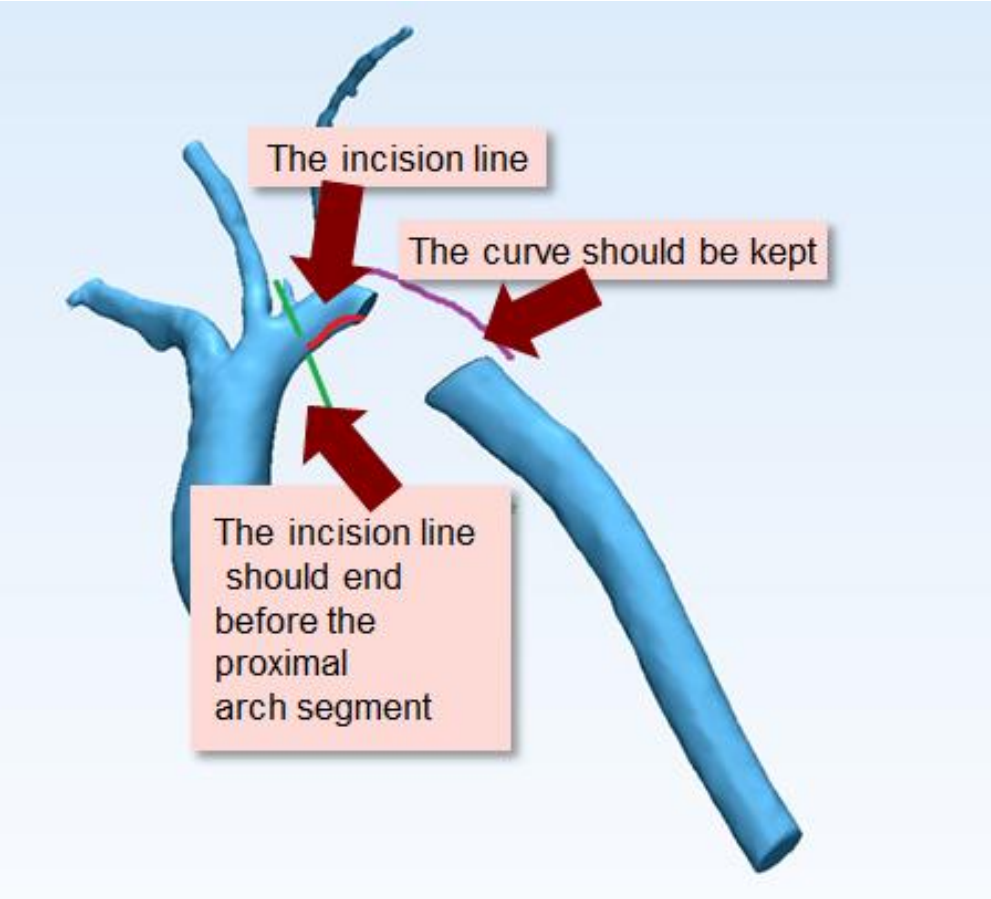

Figure 4.14 The lower adjacent was carried to the region on to 3rd cut region (depicted with a green line) after resection of the abnormal isthmus segment. The lower adjacent was carried to the region on to 3rd cut region (depicted with a green line) after resection of the abnormal isthmus segment.

The lower part was pulled up, and the upper part was pulled down, and the joint was performed. During these operations, the rotation of the parts was never caused, and the surface elements were increased numerically in a limited manner so that the expected stretch during the assembly could be formed as close to the reality as possible.

After the completion of the first virtual operation, the geometries of the models are shown in Figure 4.15. The final model of the first virtual repair is named as A1-2.

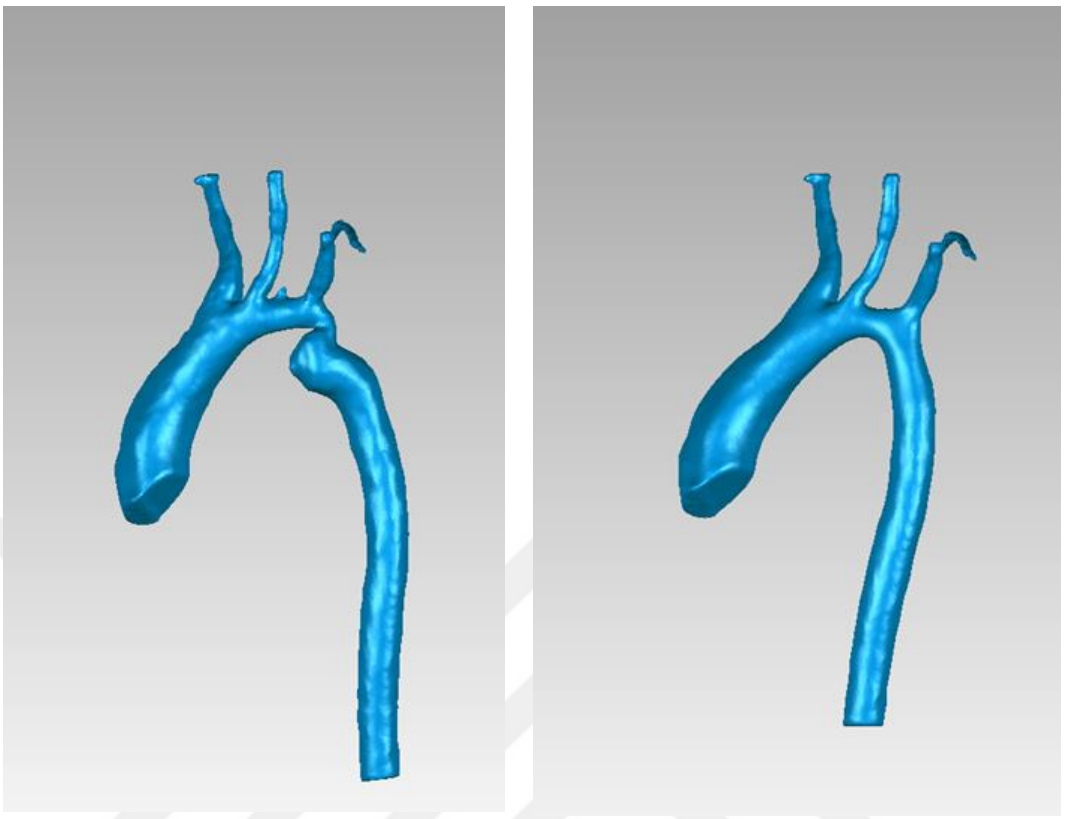

Figure 4.15 The pre-operative model where the virtual repair was performed on (left) and the virtually repaired with 'resection +extended-anastomosis' method of the first case (right).

- **2nd Virtual Repair: End-to-End Anastomosis**

In the second repair method, the virtual correction started with the excision of the coarctation region by incisions at different slopes than the first method. The slope of these incisions was different because the anastomosis process was done directly without an extension. For this reason, the 1st incision created on the upper side was closed when the second was open for anastomosis.

The second incision at the lower side was made straight and was moved directly to the junction, where it would merge upward without rotation to overlap with the 3rd incision (Figure 4.16).

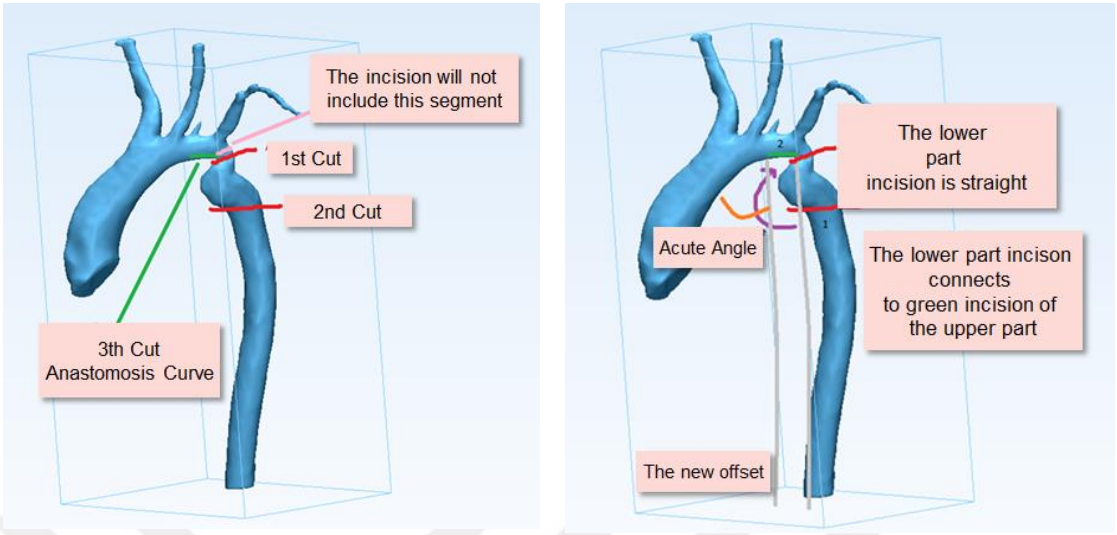

Figure 4.16 The surgical repair of the coarctation was virtually performed with the red cut lines. The lower adjacent (1) was carried to the upper adjacent (2) on to green line (Left) The new offset is depicted with grey descending aorta profile which creates an acute angle (depicted with the orange curve) (Right).

With the direct end-to-end anastomosis technique, correction of adjacent was completed without attempting to create a new curve. The resulting model contained an arch close to the gothic shape, having a smaller angle than the first method. As the distal joint was completed, a bending was left in the segment marked in Figure 4.17. The final model named A1-3.

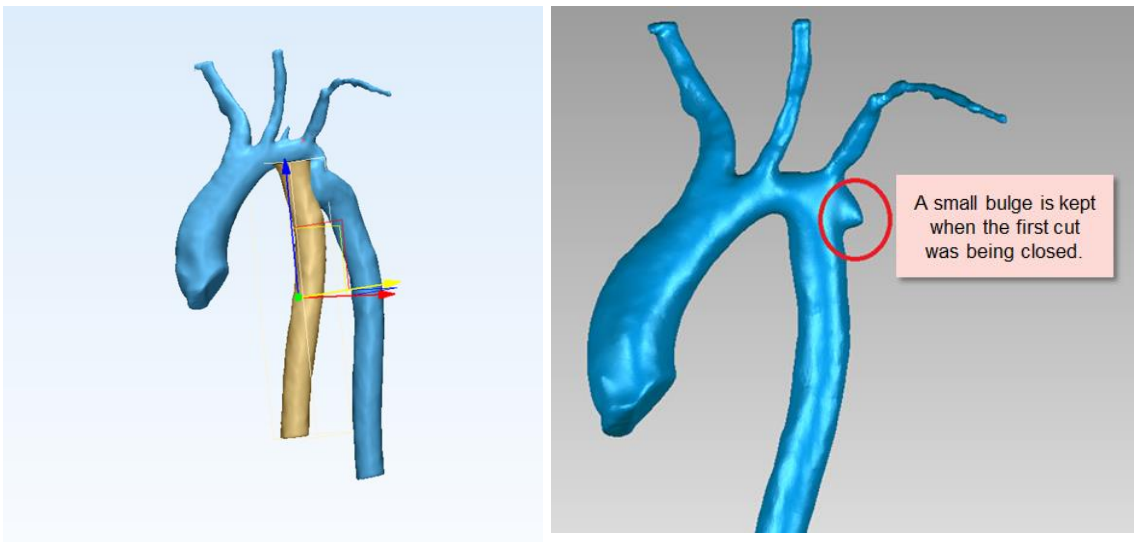

Figure 4.17 The yellow part depicts the new position of the lower part (left). The connection segment (just after left subclavian artery and before the isthmus) of the upper and lower adjacent left as a small bulge (right).

- **3rd Repair: Patch Angioplasty**

The coarctation segment was removed by making the incisions indicated in Figure 4.18. With the incision made just below the upper part, the length of the cut laterally opened in the lower part was kept equal. The upper part kept the remaining part for usage at the posterior tissue connection. The arch curve of the incision did not pass the projection of the left carotid artery segment.

The upper part was pulled evenly from all directions and was distally attached to the lower part so that they were distally connected. In this case, while anastomosis was performed on the backside, the patch gap was left on the anterior side. 1/3 of the back-side connection of the patch was provided using the path, and the rest is provided by the tissue to keep the natural tissue at the curve. The first patch hole after resection and posterior tissue connection is depicted 5^{th} frame of Figure 4.18. The patch after projecting boundaries to the artery model, and creating the smooth and reverse volume of the gap was created on CAD tool.

The patch surface at the anterior position was larger due to the gap position. The 7^{th} frame of Figure 4.18 shows the position of the patch on the transparent artery profile. The final patch surface and the repaired 3D model: The patched model is saved as A1-4.

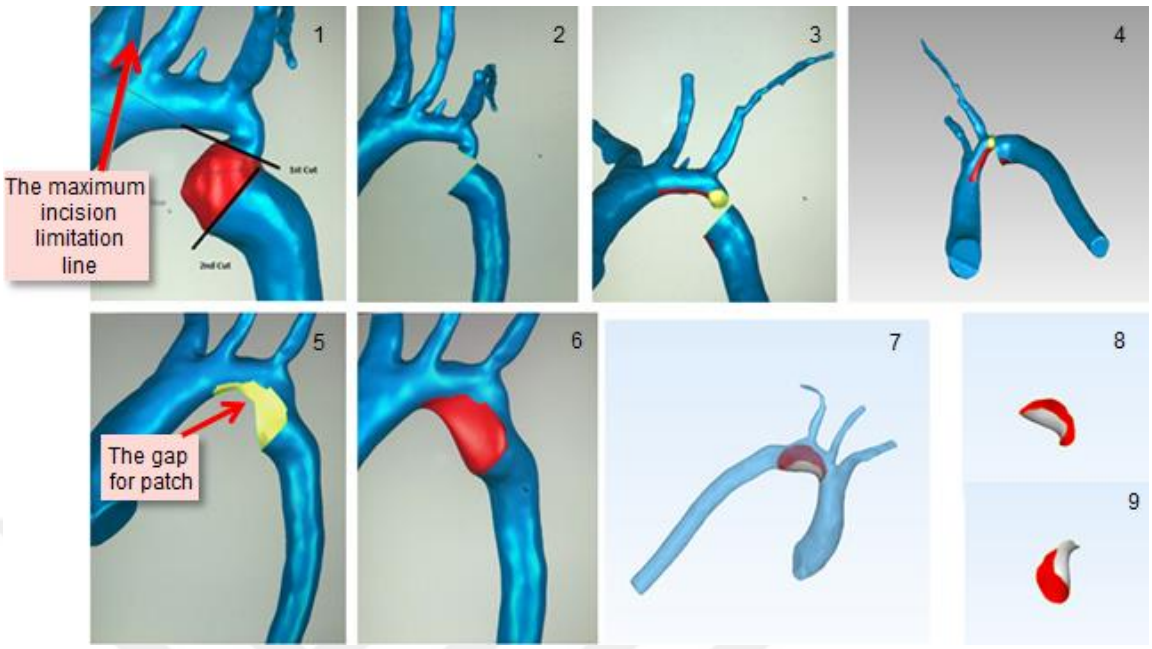

Figure 4.18 The virtual patch angioplasty: The resection segment on the native artery depicted with the red part is at 1. The adjacent parts after resection are depicted at 2. The 3rd and 4th cut curves after resection are shown at 3. The inferior projection of the 3rd cut is shown at 4. The gap for patch after anastomosis of the distal parts of adjacents is shown at 5. The patch created with reverse engineering is depicted at 6. The patch position on the transparent artery is sown at 7. The patch view on different planes is at 8 and 9.

- **Post-Operative Artery**

When selecting patients, patients with image data on actual surgical results were preferred. For this reason, the 3D model was created from the post-operative (patch angioplasty) image data to perform the same procedures for each patient.

All artery geometries were created as surfaces in STL format, converted into STEP format with CAD tools, and made ready for FEA analysis with ANSYS Design Modeler tool. 3D models of the 1st case are depicted in Figure 4.20.

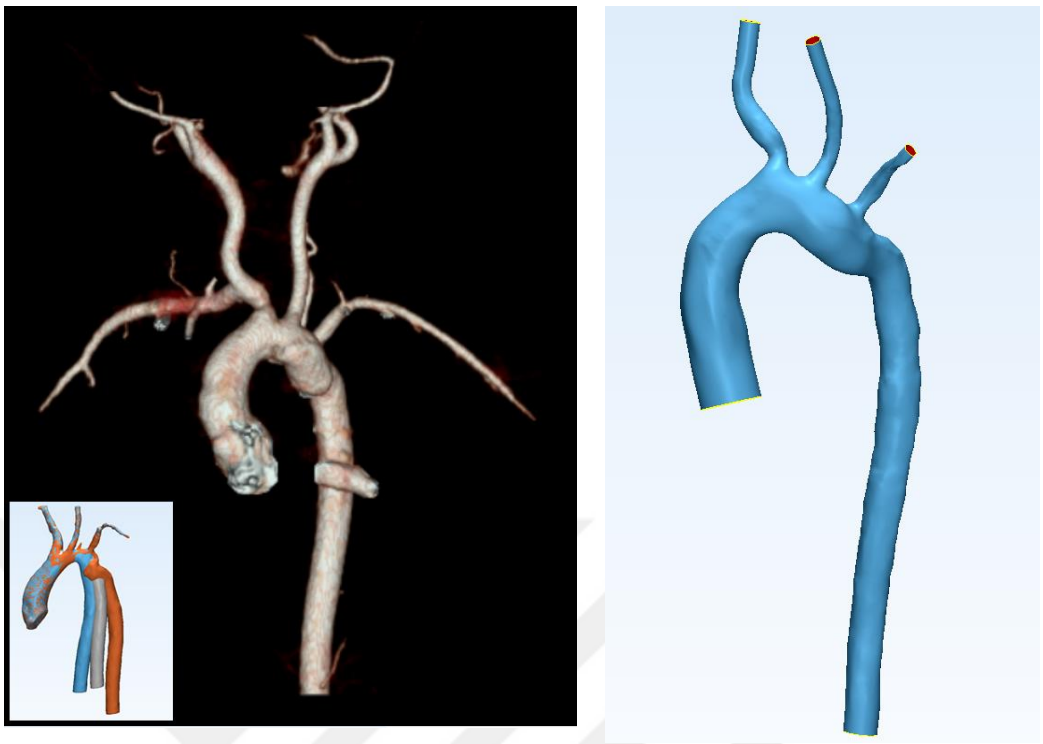

Figure 4.19 The post-operative artery model reconstructed from the CT dataset (left) when the patient was five-months-old (right). The left bottom frame depicts the native artery (orange), first repaired model (grey), and second repaired model (blue) on the same view. Patch angioplasty with another angle and size was applied to the artery at the operation.

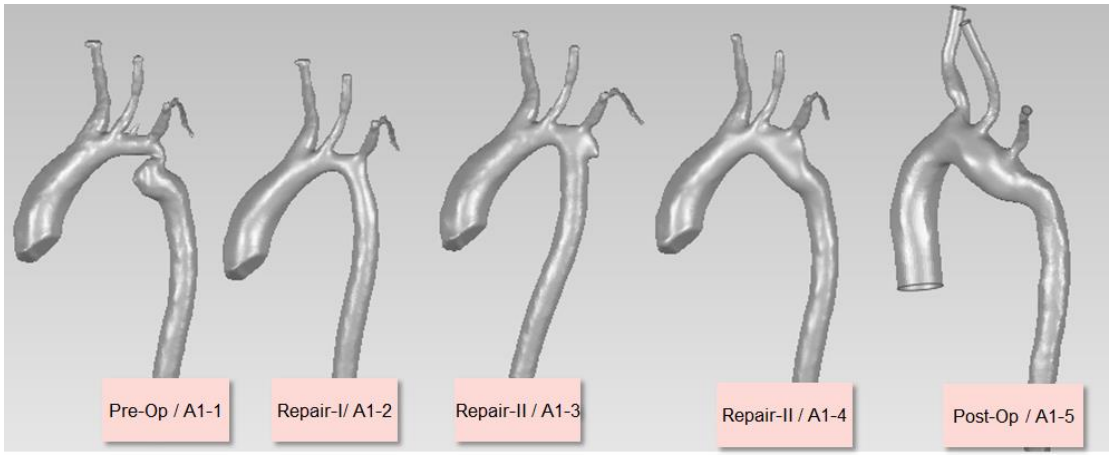

Figure 4.20 Native, repaired, and post-surgery models of 1st case.

- **2nd CASE**

The second selected case was a fourteen days old male patient's case, which was named as MED_035 in the database. In this case, the aortic diameter was 2.2 mm after the subclavian artery, and there was focal coarctation. PDA was present as in the first

patient. The descending aorta diameter was 6.7 mm. A perimembranous 4mm VSD and 5mm ASD were diagnosed. There was enlargement of the right heart cavity and pulmonary artery diameter. The virtual operative methods and naming the final results are done for each model, as shown in Table 4.2.

	Models of First Patient for FEA
1	**Pre-Operative (Native) / A2-1**
2	**Resection and Extended Anastomosis / A2-2**
3	**Patch Angioplasty / A2-3**
4	**Post-Operative/ A2-4**

Table 4.2 The subsection models and the code labels of the second aortic coarctation case.

- **Native Artery**

The pre-operative 3D model was reconstructed from the CT dataset (Figure 4.21).

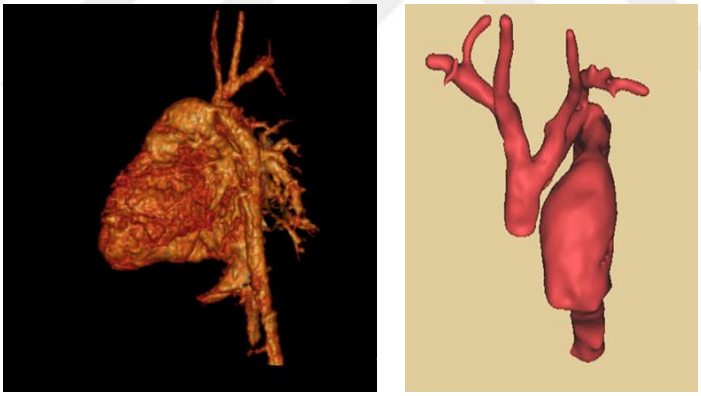

Figure 4.21 The radiologic view of the heart of the 2nd patient(left), and the reconstructed artery model (right).

- **1st Virtual Repair of the Second Patient: Resection and Anastomosis**

The virtual repair method was the same as the surgical method. Even if the applied method is the same, conditions such as incision length, angle, human factor affecting each step change the final results.

After the diameters of the radiological data and the model formed were validated, the resection was performed with the first two incisional structures (Figure 4.22). PDA connection was removed for obtaining the region of interest to work on.

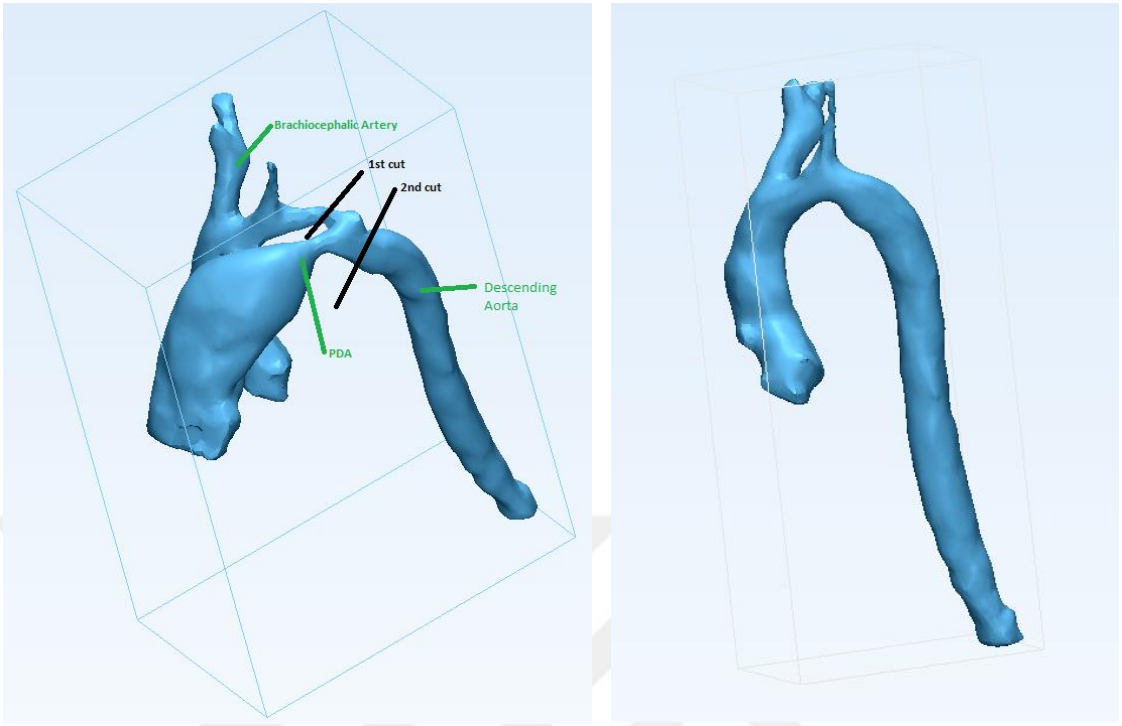

Figure 4.22 The incision sections of the first repair method are depicted with black lines on the native artery of the second patient (left), The final geometry of the first virtual repair of the second patient(right).

The lower part was moved without upward rotation to the point where the side branch emerged. It was tried to mimic the stretching dimensions in a real artery tissue, and necessary surface additions were provided. Each step was carefully carried out with the instructions of the surgeon to prevent pseudebulging.

- **2nd Virtual Repair: Resection and Extended Anastomosis**

As the second virtual correction model, as in A2-2, resection and extended anastomosis method were applied. As shown in Figure 4.23, the first three incisions marked respectively were made.

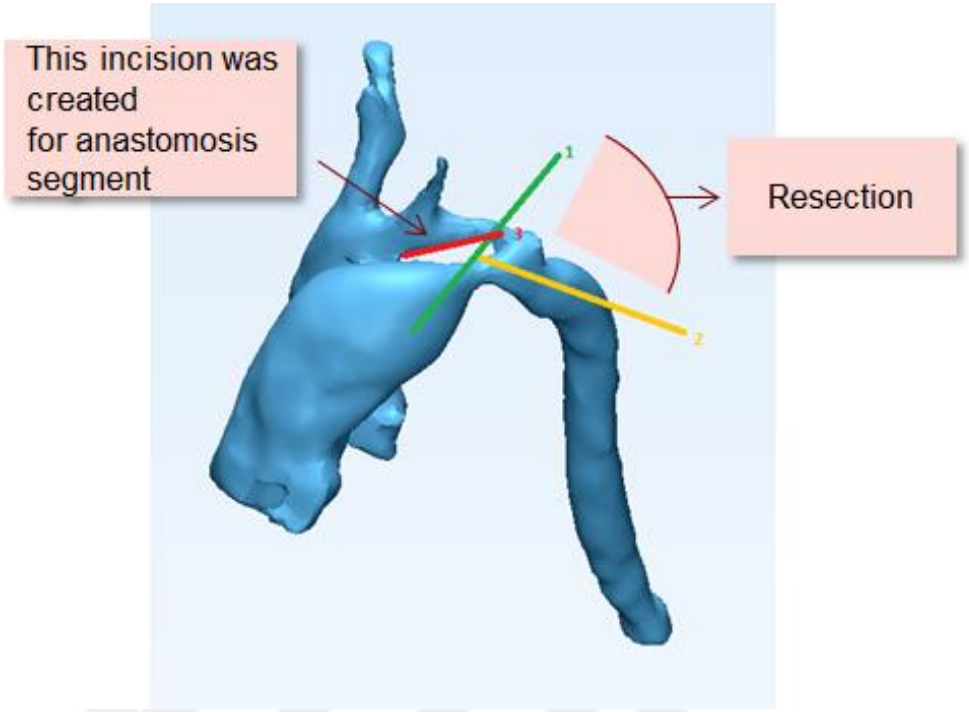

Figure 4.23 The incisions made for correction are shown on the native artery, marked with the colors green, yellow, and red c, respectively.

The discrete parts formed were brought closer to each other, and the end apertures were arranged to allow anastomosis. With the separation of the opening gap formed after the third incision in Figure 4.24, the connection was completed with the CAD tool.

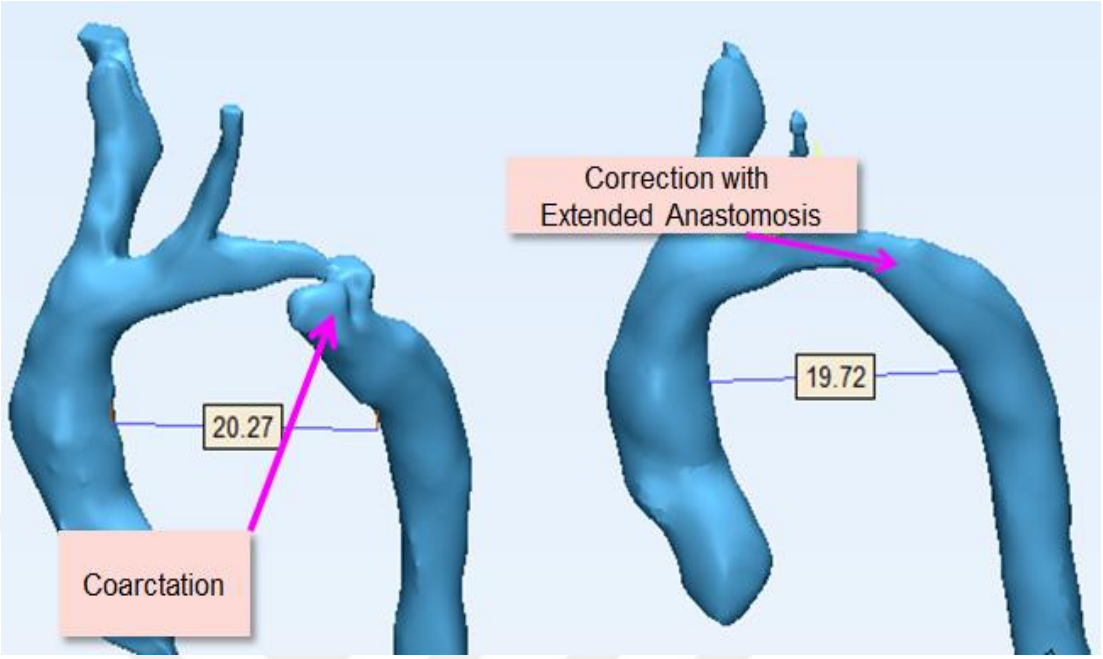

Figure 4.24 The native model with coarctation(left) and the corrected model with resection & extended anastomosis (right).

- **3rd Repair: Patch Angioplasty**

Patch repair was the third preferred forming. In this method, resection was performed with incisions at the angle indicated in Figure 4.25.

The two discrete parts were brought closer to each other without rotation, with the posterior walls overlapping each other.

The opening of the anterior opening according to internal pressure was tried to be as close to real as possible, and a patch was added to the opening to provide acceptable diameter (Figure 4.26).

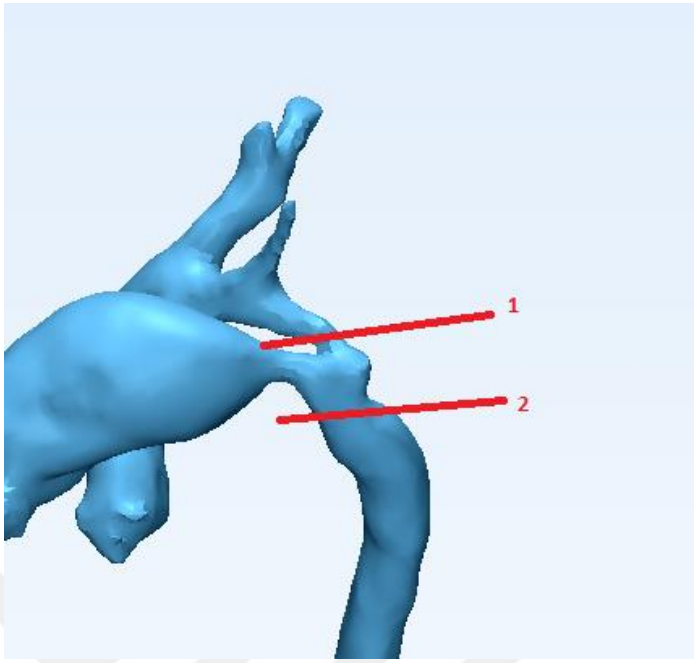

Figure 4.25 Incisions made for virtual patch repair on the second patient's vein, respectively.

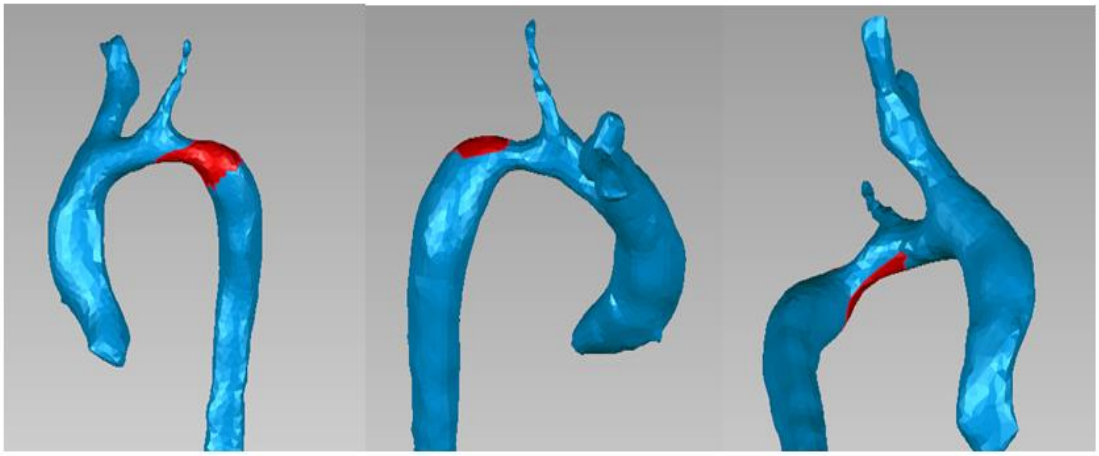

Figure 4.26 The repaired artery with patch angioplasty.

The patch was designed in a unique shape due to the opened gap (Figure 4.27).

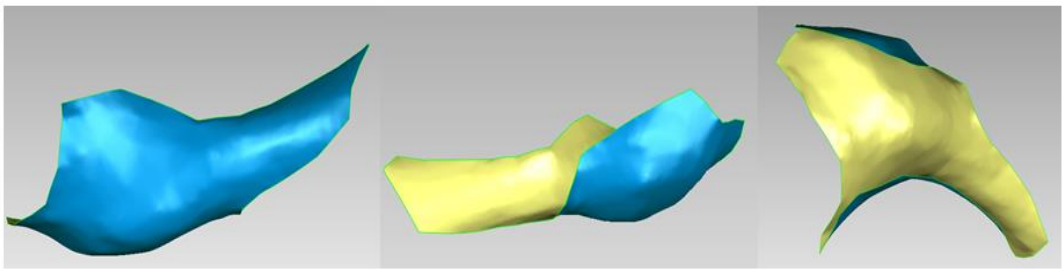

Figure 4.27 The virtual patch geometry of the second case view on different planes.

- **Post-Operative Artery**

  The post-operative model was created from the CT dataset of the patient. The operation was done when the patient was forty-five days old (Figure 4.28). It was performed as resection of PDA, a vertical incision on the arch, an extension on the initial descending aorta. The angioplasty was done with a polyproline mesh patch.

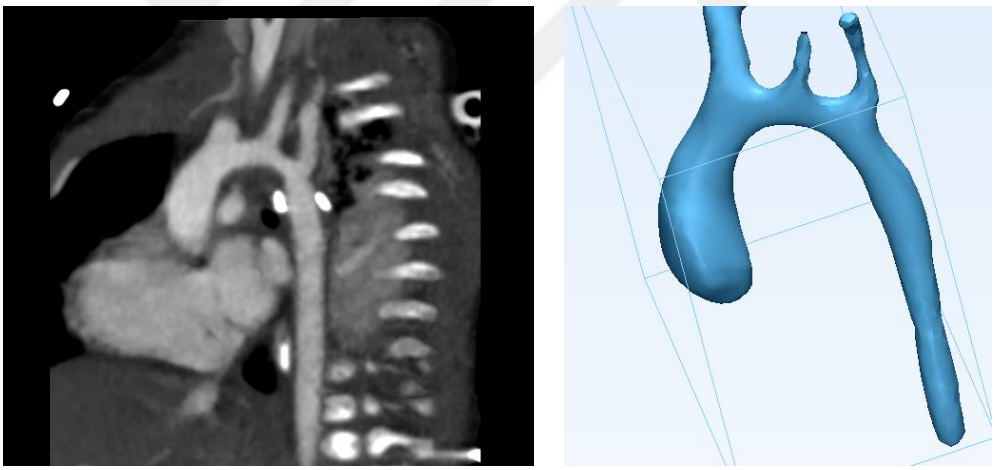

Figure 4.28 The post-operative artery model of the second case.

3D models of the 2nd case is depicted in Figure 4.29:

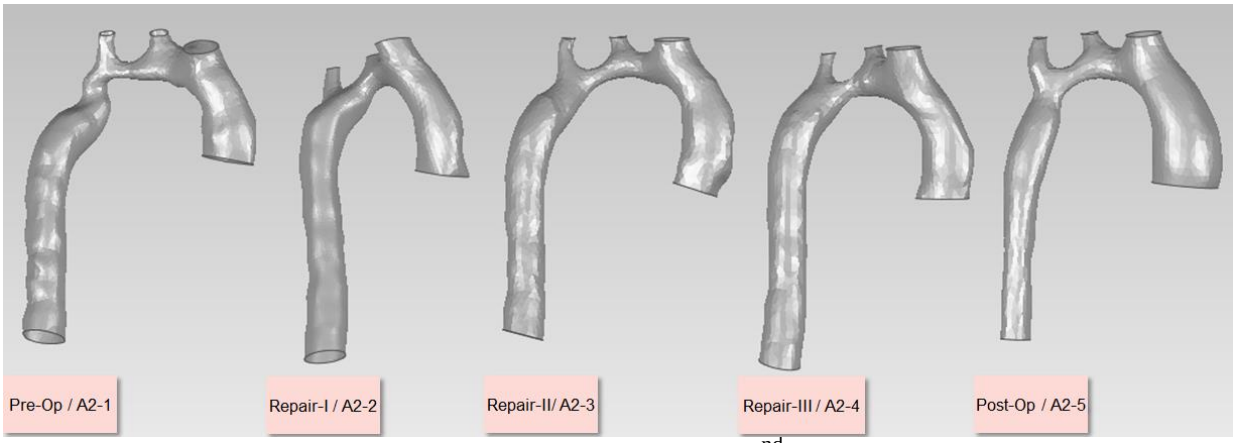

Figure 4.29 Native, repaired, and post-surgery models of 2nd case.

- **3rd CASE**

The 3rd case was a nine days old female patient who was diagnosed with transverse aortic arch, diffuse tubular hypoplasia, and distal coarctation, PDA, and ASD. The case was named as MED_036 in the database).

The patient had a patch angioplasty and pulmonary banding seven months later after birth. CT dataset was obtained when the patient was three years old. The native artery geometry of the patient was similarly had a large PDA. Firstly, 3D models of the native artery with PDA and the region of interest on the artery are reconstructed. The virtual operative methods and naming the final results are done for each model, as shown in Table 4.3.

	Models of First Patient for FEA
1	**Pre-Operative (Native) / A3-1**
2	**Resection and Extended Anastomosis / A3-2**
3	**Resection Method and End-to-End Anastomosis / A3-3**
4	**Post-Operative/ A3-4**

Table 4.3 The subsection models and the code labels of the third aortic coarctation case.

- **Native Artery**

The pre-op virtual model of the patient was re-constructed, as seen in Figure 4.30.

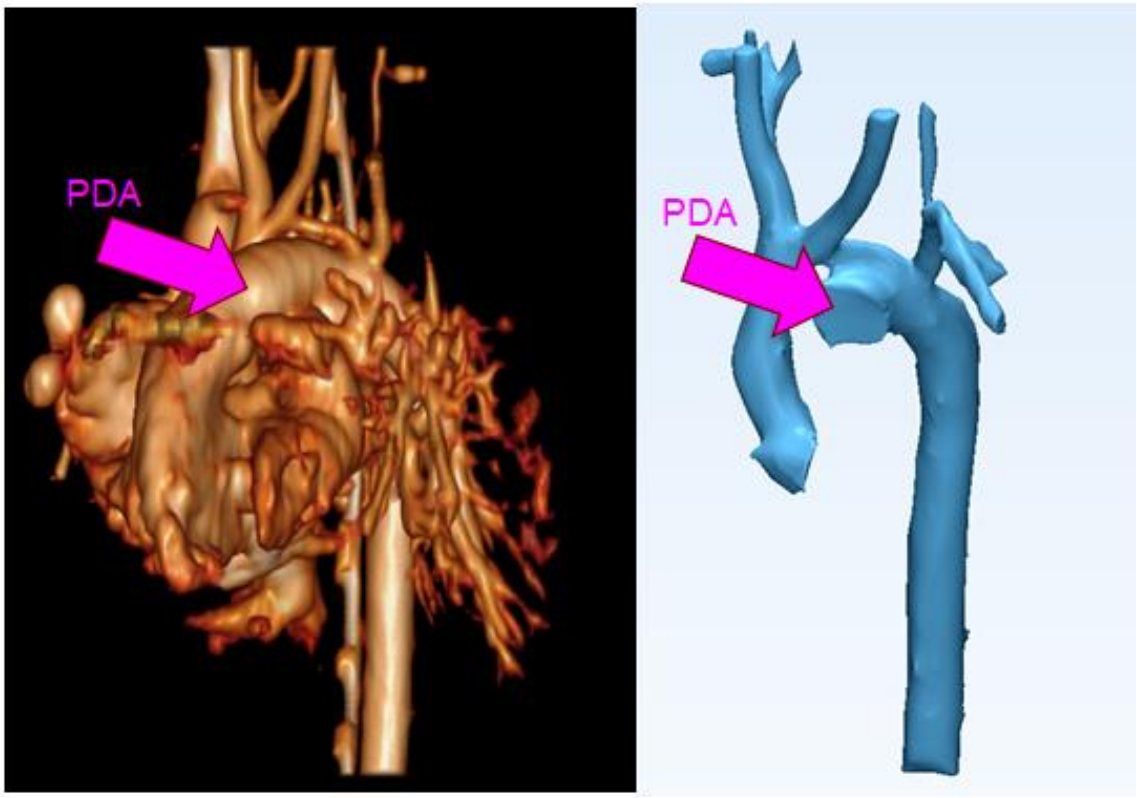

Figure 4.30 CT view (left) and 3D virtual pre-op artery of the 3rd case (right).

- **1st Virtual Repair of the Third Patient: Patch Angioplasty**

In this case, patch angioplasty was chosen for the first virtual repair method. First, the aberrant left subclavian artery, which was occluded, was excised due to the location of the coarctation segment (Figure 4.31). The two remaining parts were joined distally and closed with a patch to fit into the remaining gap after reverse engineering with converting the opening to the surface (Figure 4.32).

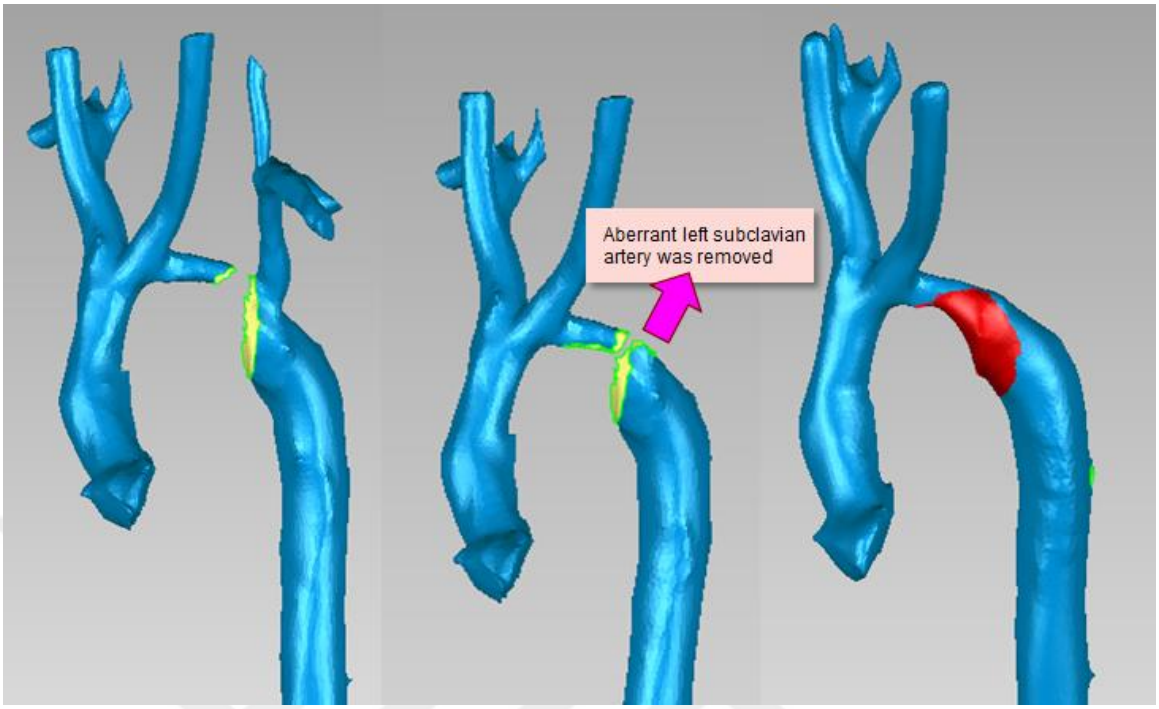

Figure 4.31 The incisions applied to the 3rd native artery (left and middle) and the virtual patch created for gap diameter after distal anastomosis (right).

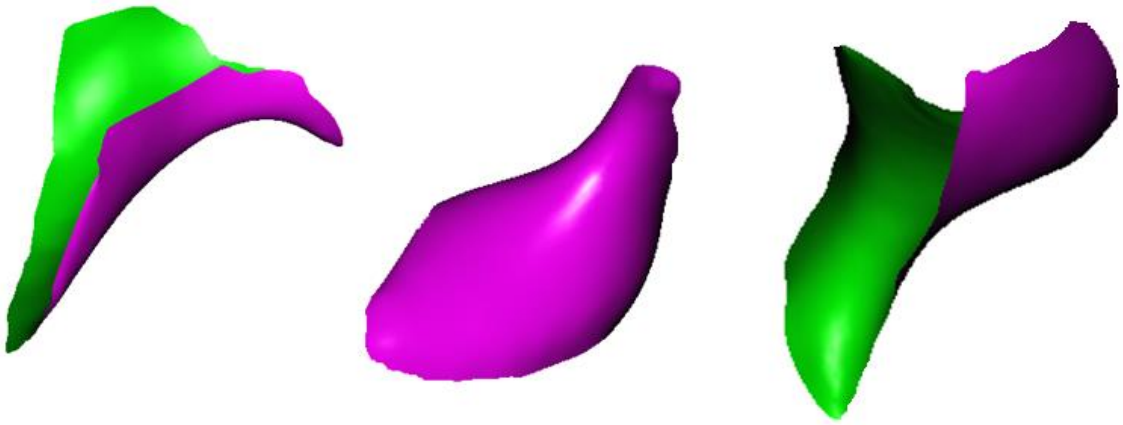

Figure 4.32 Virtual patch for 3rd case on different plane views.

- **2nd Virtual Repair: Resection and Extended Anastomosis**

The second virtual repair method was chosen as resection and anastomosis. After the incisions marked in the figure were made, the coarctation site was separated intravenously (Figure 4.33).

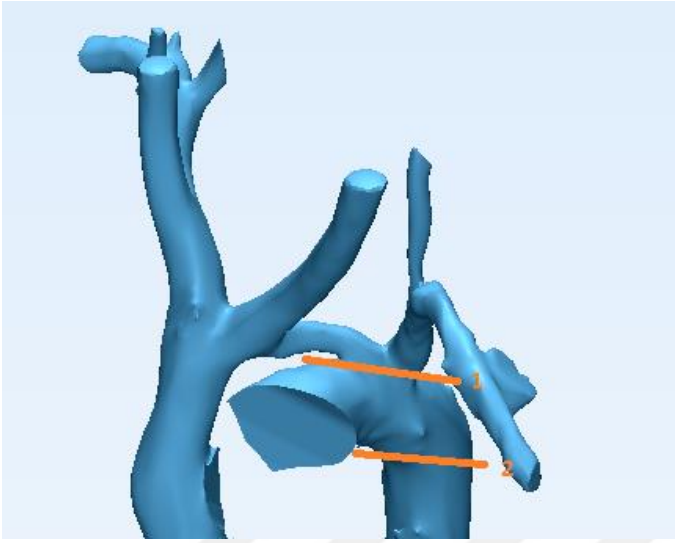

Figure 4.33 The first and second incisions on the native artery for anastomosis.

Unlike the previous repair, the aberrant left subclavian artery was not separated from the arch in this resection. If a simplified visualization is required to look at the initial and final states, the relationship between the native model and the repaired model is as follows in Figure 4.34. Blue represents the geometry generated by the second repair method, and yellow represents the preoperative artery.

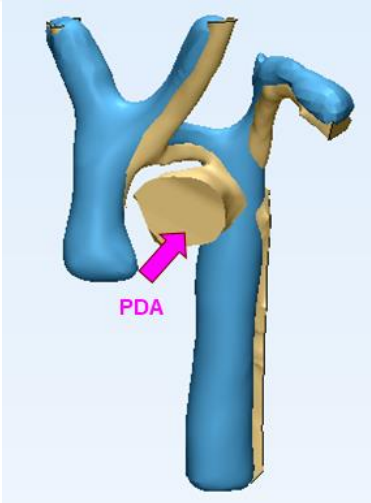

Figure 4.34 The symbolic repaired artery (blue) on the projection of the native artery yellow).

- **Post-Operative Artery**

The operative repair was with a biological patch angioplasty at the age of 3rd. There was a collateral re-canalization of the left subclavian artery, which has total proximal

occlusion to the vertebral artery after three years of the birth. The image dataset was used for segmentation as in other aortic coarctation cases (Figure 4.35).

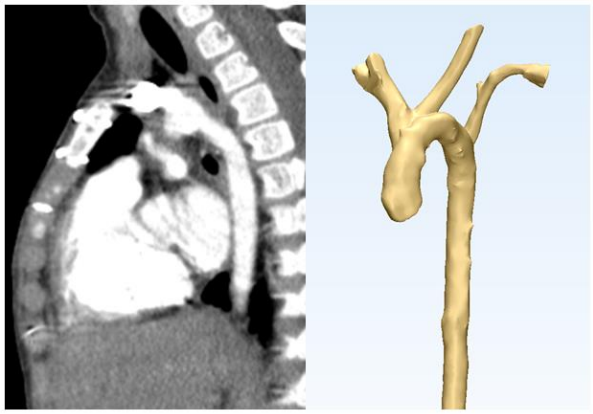

Figure 4.35 The post-operative scan of the 3rd case (left) when the patient was three years old, and the reconstructed virtual model (right).

3D models of the 3rd case are depicted in Figure 4.36:

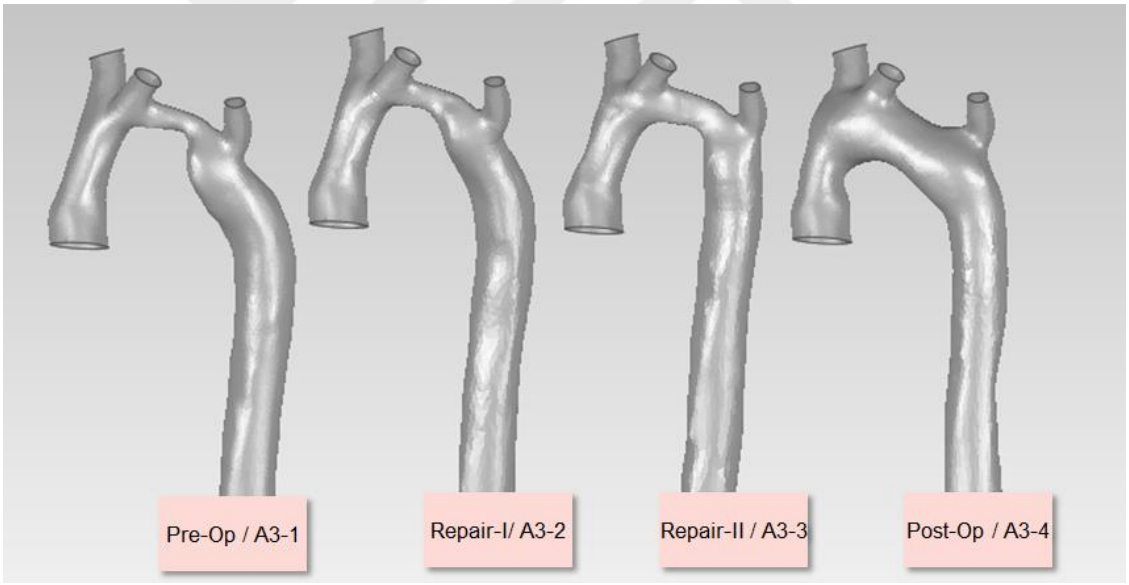

Figure 4.36 Native, repaired, and post-surgery models of 3rd case.

- **4th CASE**

The fourth case was two years old male patient who was diagnosed with DORV, VSD, PDA, sub-aortic stenosis (without a gradient), aortic arch hypoplasia, and coarctation. The surgery with patch angioplasty was performed when the patient was two weeks old. The virtual operative methods and naming the final results are done for each model, as shown in Table 4.4.

	Models of First Patient for FEA
1	**Pre-Operative (Native) / A4-1**
2	**Resection and Extended Anastomosis / A4-2**
3	**Resection Method and End-to-End Anastomosis / A4-3**
4	**Post-Operative/ A4-4**

Table 4.4 The subsection models and the code labels of the fourth aortic coarctation case. The case was named as MED_040 in the database.

- **Native Artery**

The post-operative model was reconstructed from the CT dataset. The lumen diameter of the ascending aorta was 13 mm, but the arch diameter was 6mm. The subclavian artery branch was after the distal hypoplasic arch. The pulmonary artery was at the projection of the left subclavian artery branch, and PDA was behind the aorta (Figure 4.37).

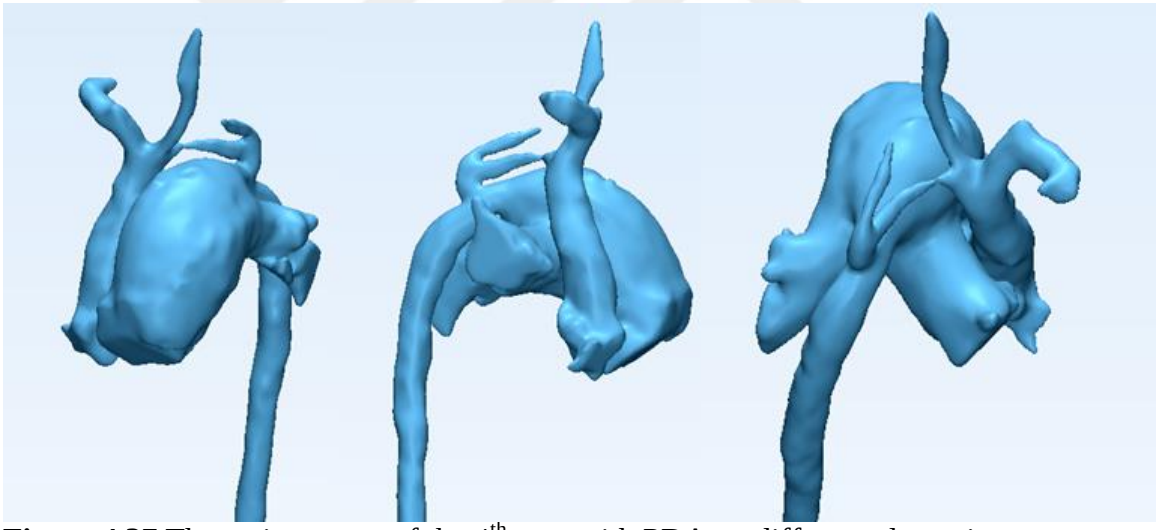

Figure 4.37 The native artery of the 4th case with PDA on different plane views.

In this patient, because the blood flow was not observed in the hypoplasic region, the continuity was not observed because of the blood flow regions characterized by a contrast agent. However, because multi-section CT imaging with proper resolution can be used to detect vascular walls with image processing methods, real anatomy obtained by combining the cavity area between the wall borders with blood pool images.

1st Virtual Repair of the First Patient: Patch Angioplasty

In this case, as the tissue to be treated was scarce, two incisions were made to remove only the coarcted area, and the model was divided into two parts (Figure 4.38).

After the lower part was moved upwards without rotation, distal jointing was performed to obtain the appropriate opening for patching (Figure 4.39). Patch geometry was defined by converting the space into objects with reverse engineering (Figure 4.40).

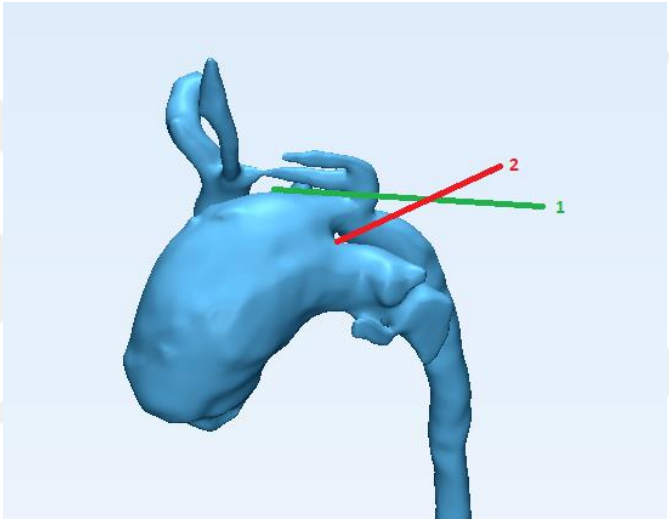

Figure 4.38 The first and second incisions for resection on the native artery of the 4th case.

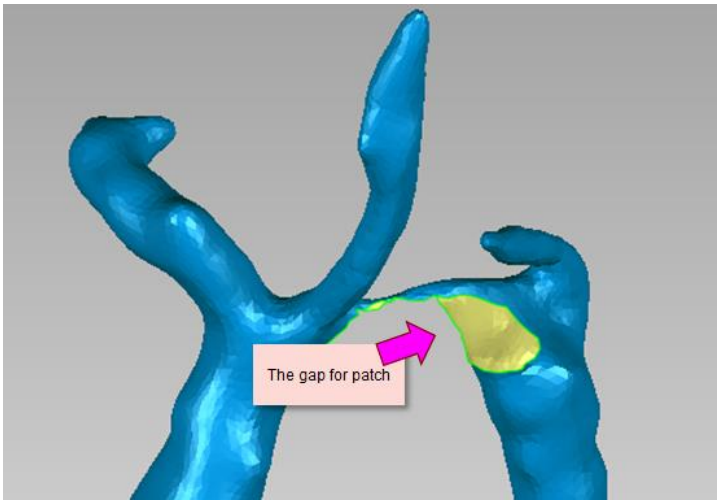

Figure 4.39 The gap before creating the patient-specific virtual patch.

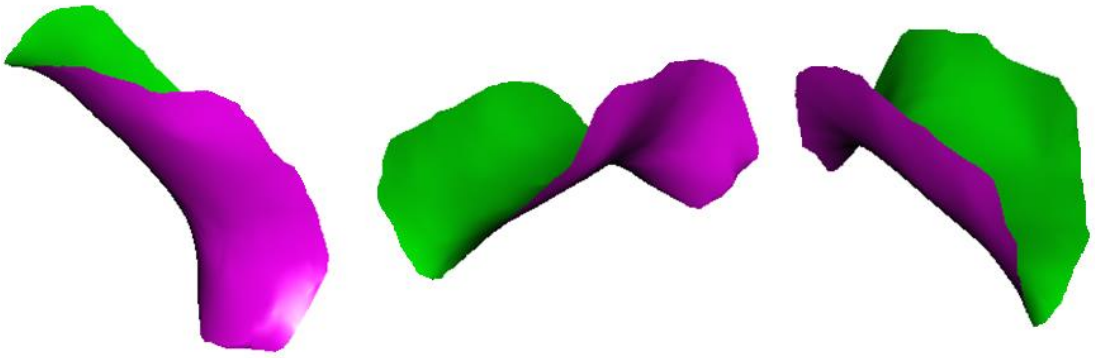

Figure 4.40 The patient-specific virtual patch surfaces on different plane views.

- **2nd Virtual Repair: Anastomosis**

Another correction applied to the native artery was an anastomosis method. The artery was divided into two adjacent (Figure 4.41).

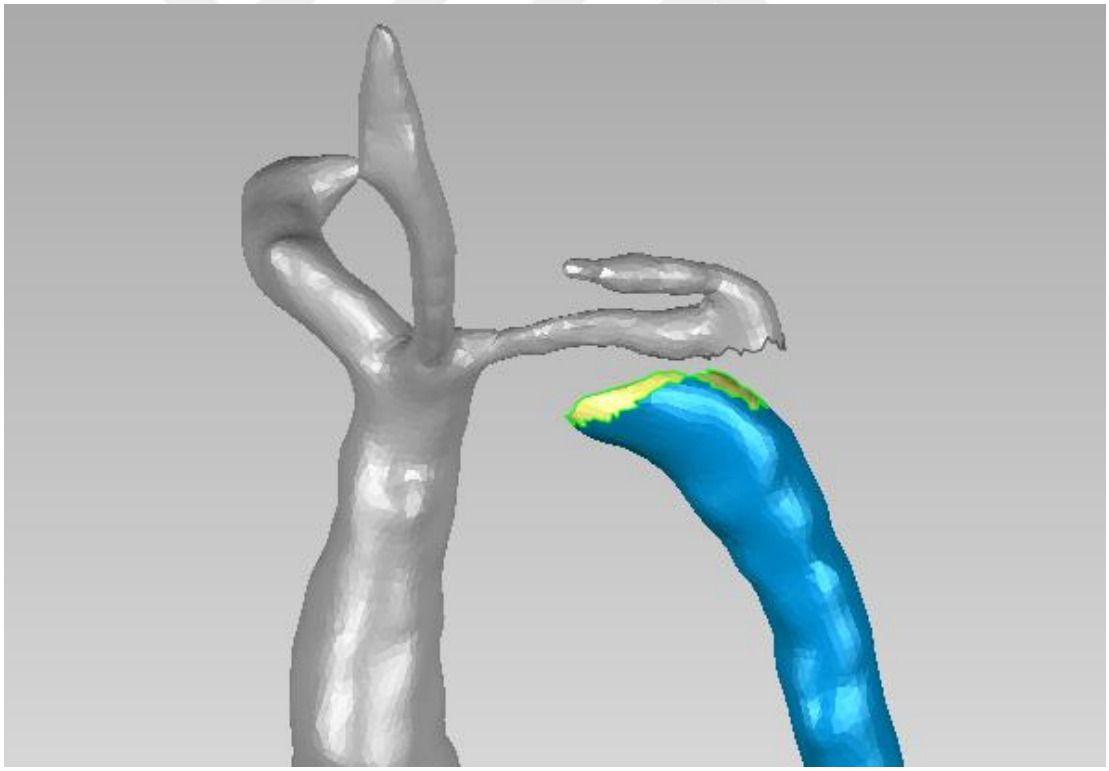

Figure 4.41 The upper (grey) and lower (blue) are adjacent for the 2nd repair on the native artery of the 4th case.

The upper part had an incision for providing the new diameter size after connection. The anastomosis was tried to be completed by keeping the diameter as same as possible in transverse continuity (Figure 4.42). Although an ideal repair could not be

achieved due to the lack of adequate tissue, the most realistic and approximate solution was tried to be produced. Care was taken not to create more than the actual elongation rates.

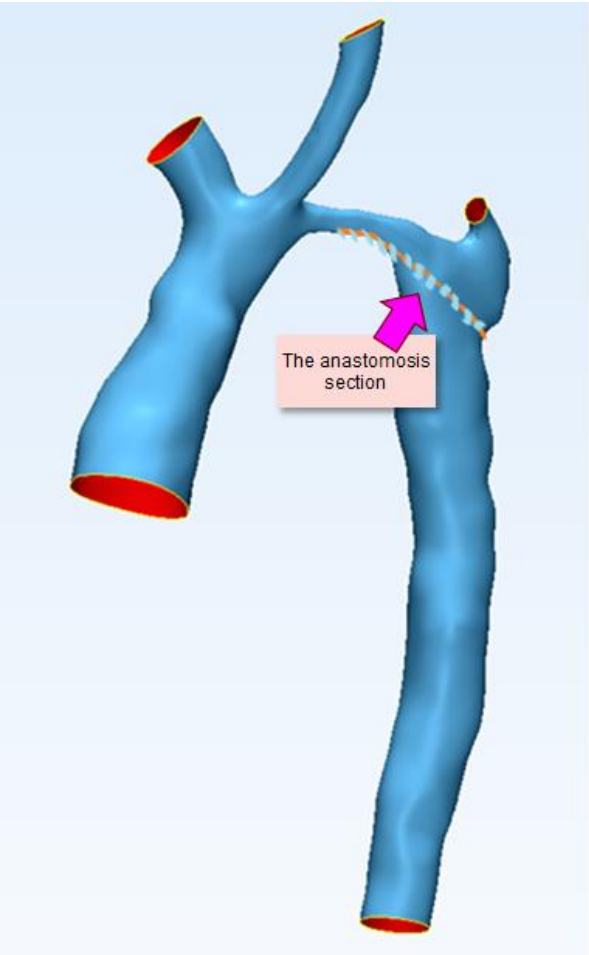

Figure 4.42 The final model after 2nd virtual repair and the anastomosis section on 2D view.

- **Post-Operative Artery**

The image data after real surgery was re-constructed with segmentation tools. The blood pool results were surprisingly seen as there was a sharp narrow segment. The images and the clinical information are shown that the patch sutured on to the artery had probably buckled inside the lumen (Figure 4.43).

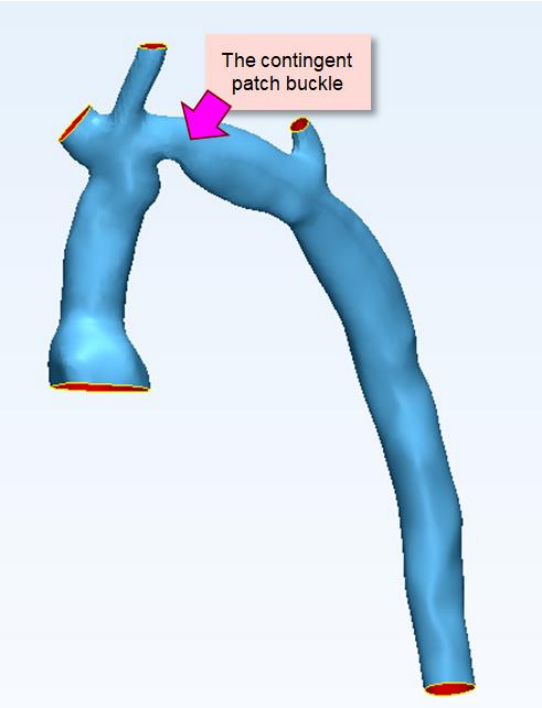

Figure 4.43 The reconstructed virtual model after the surgery of the 4th case.

In such a case, although the vessel diameter may appear to be the same from the outside, the blood flow occurs in a narrow space caused by a folded patch. The models created for 4th patient is depicted in Figure 4.44.

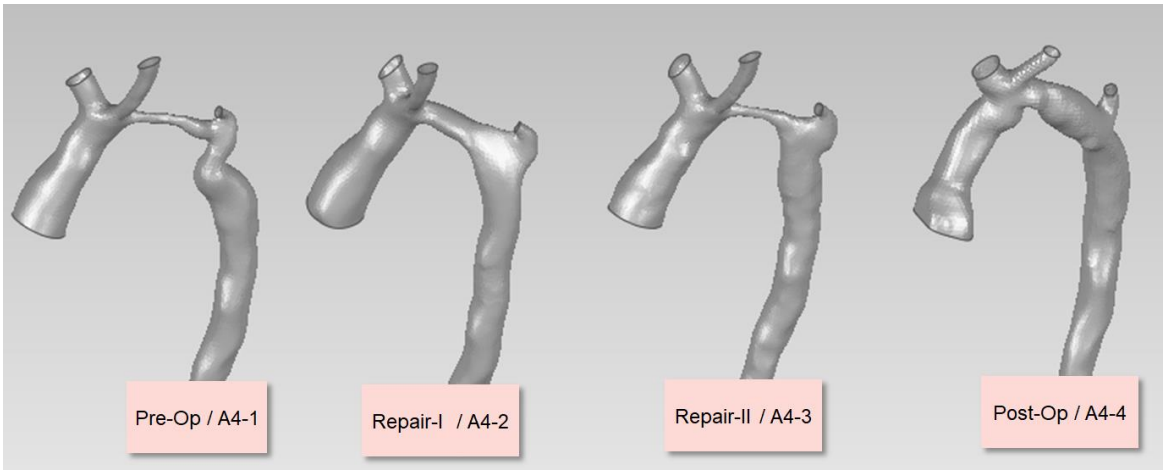

Figure 4.44 Native, repaired, and post-surgery models of 4th case.

- **5th CASE**

5th patient was an eight-month-old case with a hypoplastic distal arch and coarctation. The patient had repair surgery when he was one month old. The repair was a reverse

subclavian flap for keeping antegrade gradient of the left subclavian artery. The pre-operative, post-operative, and the virtual artery profiles are listed in table 4.5:

	Models of First Patient for FEA
1	**Pre-Operative (Native) / A5-1**
2	**Patch Angioplasty / A5-2**
3	**Reverse Subclavian Flap / A5-3**
4	**Post-Operative/ A5-4**

Table 4.5 The subsection models and the code labels of the fifth aortic coarctation case. The case was named as MED_041 in the database.

- **Native Artery**

The virtual pre-surgery artery was obtained with segmentation tools. The blood pool mask validated the ECHO report, which had remarked a very low radiant on the patient (Figure 4.45). After changing the segmentation tool and the intensity of the structural element for detecting the pixels of the blood pool. In many anatomical segmentation studies, the mistake is not to compare patient reports with the results and not to pay attention to obtaining standard information with different tools as a result. As in other patients, the report, radiological data, clinical data, and information that did not provide consistency as a result of segmentation were eliminated and continued with the most appropriate tools (Figure 4.46). The native hypoplastic aorta obtained after validation with different image segmentation tools in Figure 4.46 (Matlab, 3D Slicer, Simpleware Scan IP).

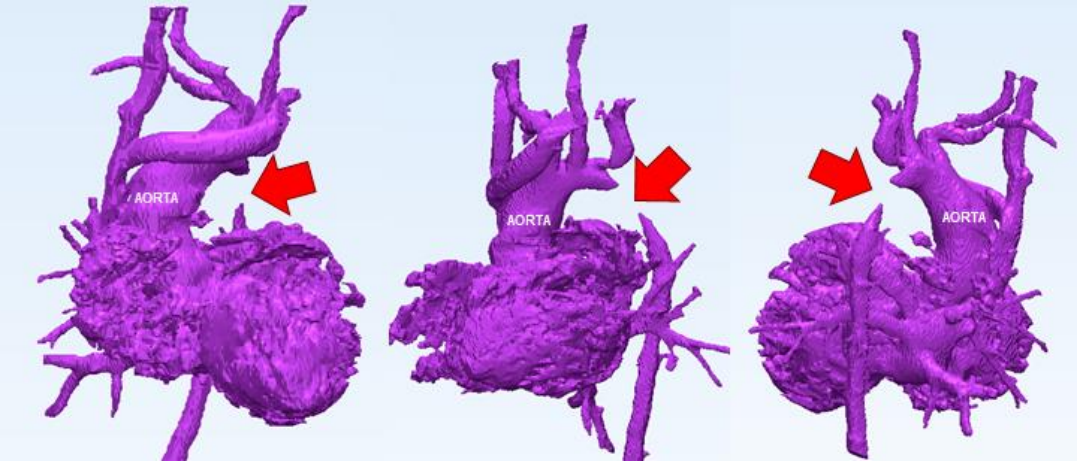

Figure 4.45 The lost flow segment on the re-constructed blood pool model in different plane views.

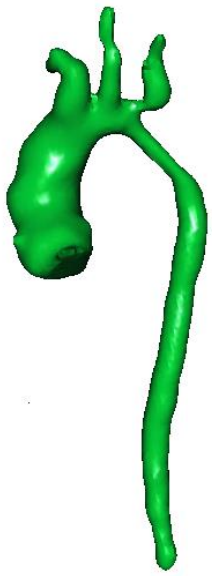

Figure 4.46 The final pre-operative virtual model of the 5th case.

- **1st Virtual Repair of the First Patient: Patch Angioplasty**

The operative correction was chosen as patch angioplasty for the first virtual repair of the case. A long incision was applied to the undersurface of the arch, and the descending aorta segment includes stenosis (Figure 4.47).

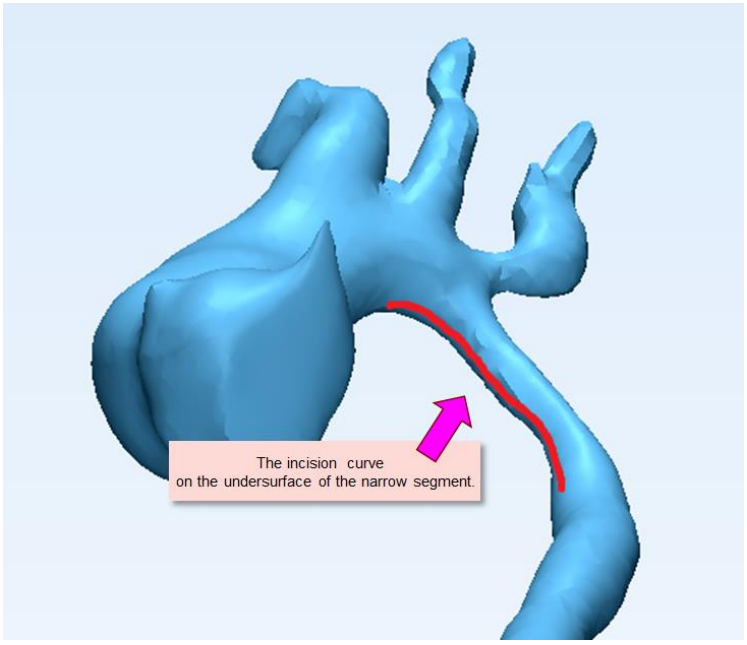

Figure 4.47 The incision before patch angioplasty on the 5th case on the bottom view.

The 3D patient-specific patch was designed to keep the descending aorta and arch diameters balanced, as seen in Figure 4.48. The patch surface area which fits within the gap was 206 $mm^{2.}$ The 3D view of the patch on different planes is depşcted in Figure 4.49.

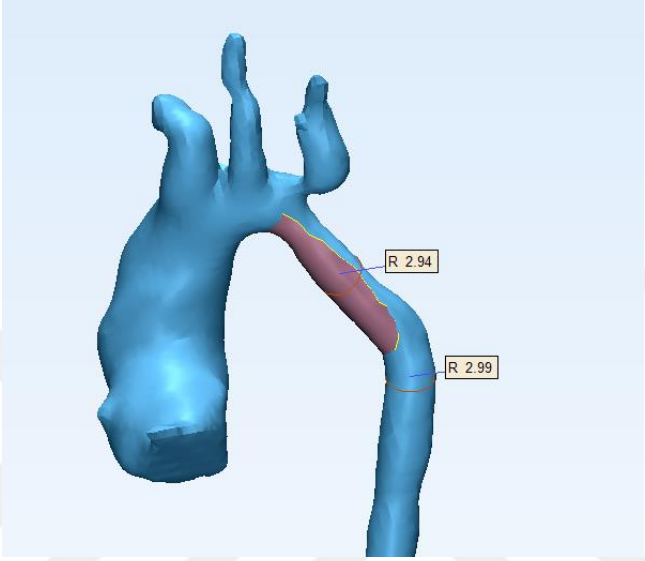

Figure 4.48 The virtual patient-specific patch surface that maintains lumen continuity to an acceptable extent.

Figure 4.49 The virtual patch images of the 5th case.

- **2nd Virtual Repair: Subclavian Flap**

The virtual technique selected for the 2nd section was the reverse subclavian flap method.

This method was preferred to augment the hypoplastic aortic arch with a flap which to provide an autologous upper surface patch. The surgical procedure of reverse flap on to the upper surface of the narrow segment of the descending aorta is depicted in Figure 4.50.

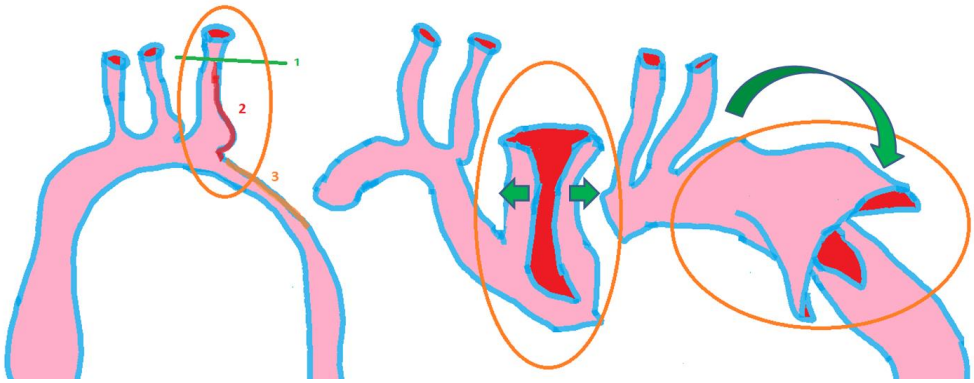

Figure 4.50 In the left image, incisions to be made on the subclavian artery and descending aorta are indicated. The circled (orange) areas indicate the position of the left subclavian artery during the procedure. These include making incisions, opening them sideways through the 3rd incision (middle), and closing the opening on the descending aorta (right).

In this method, the incision on the subclavian artery was made to make the surface open and serve as a flat patch. The descending aorta was closed on the gap formed by the incision on the dorsum of the aorta, and both augmented and repaired without adding any foreign prosthetic material. The incision lines on the reconstructed artery profile and the final repaired geometry are depicted in Figure 4.51.

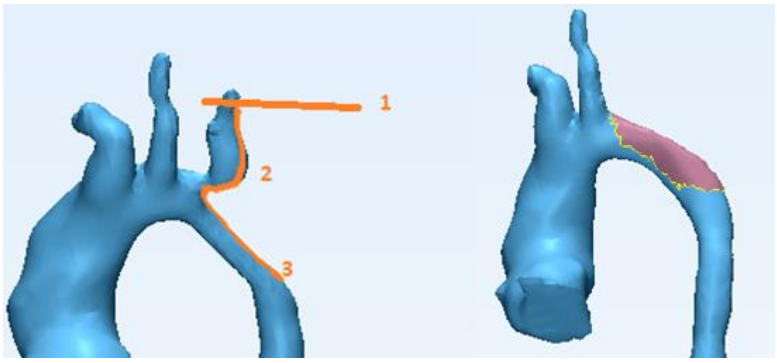

Figure 4.51 The incision curves and lines on the native artery (left) and the final repaired artery with reverse subclavian flap method.

- **Post-Operative Artery**

The surgical intervention was applied when the patient was one month old, and the scan date was one month later after the correction with reverse subclavian flap (Figure 4.52).

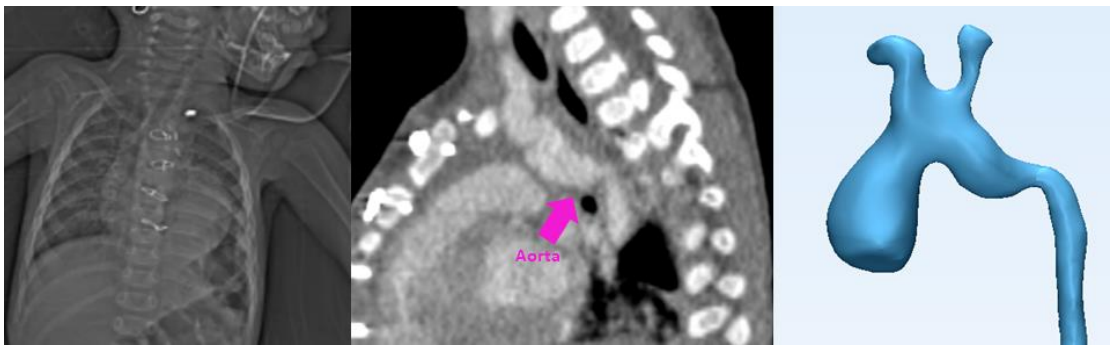

Figure 4.52 The CT scanogram (left), a slice on the sagittal view of the image dataset (middle), and the re-constructed post-surgery model of the 5th patient (right).

Four virtual 3D models created for 5th patient are depicted in Figure 4.53.

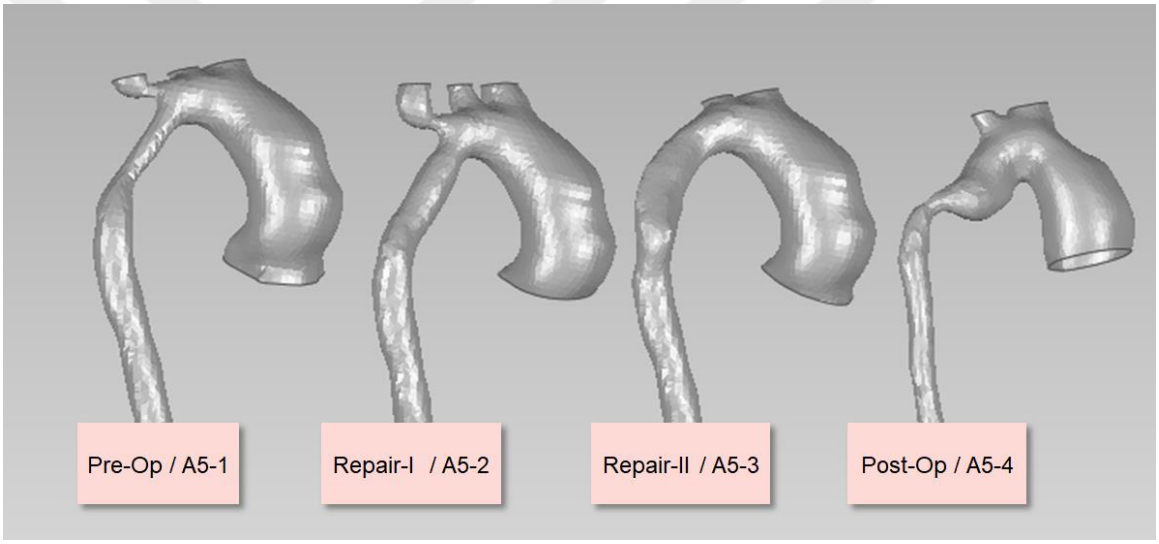

Figure 4.53 Native, repaired, and post-surgery models of 5th case.

4.2.1.2 Pulmonary Coarctation

The use of the finite element method for calculating the changes of the vascular and patch tissues against mechanical load was described in the methods section. With the help of this method, the surgical repair of the stenosis in the pulmonary artery obtained from the patient's image data was examined in this section. The comparison of the vascular deformation on the arteries, which are patched with PTFE and pericardium for the pulmonary coarctation segment.

The method started with virtual incision according to vascular morphology as in aortic hypoplasia samples. Arterial internal pressure and expansion of this precision were

calculated by using the finite element analysis method. A virtual patch has been created, which will fully overlap here (Figure 4.54).

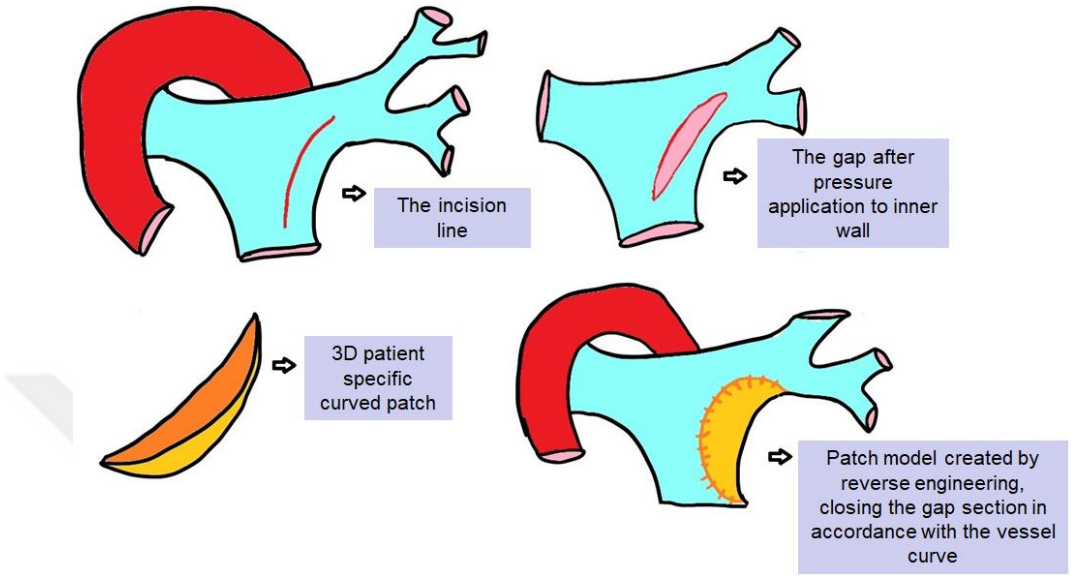

Figure 4.54 The illustrated patch angioplasty on the pulmonary artery.

The selected patient (MED_051) for virtual pulmonary artery repair was one-week old patient with stenosis on the right pulmonary artery. The patient-specific artery was reconstructed from the CT image datasets (Figure 4.55).

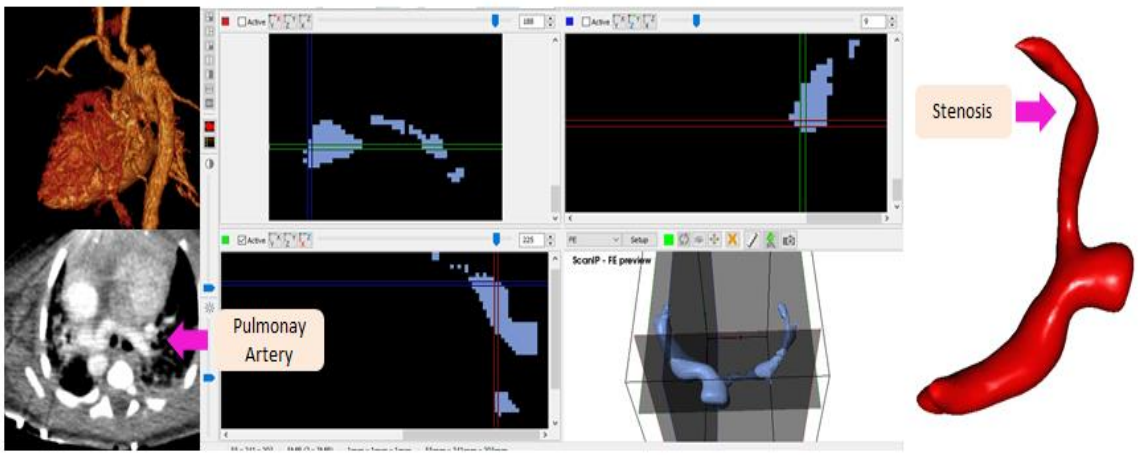

Figure 4.55 The image dataset views at left, the segmentation view on Simpleware Scan IP at the middle, and the 3D artery at right.

The modeling workflow was the same as aortic cases with obtaining pre-op, virtual post-op artery profiles of the selected patient (Table 4.6).

	Models of First Patient for FEA
1	**Pre-Operative (Native) / P1-1**
2	**The Patch with gap angioplasty (with structural FEA) / P1-2**
3	**The Patch with angioplasty (with structural FEA) / P1-3**
4	**The deformed patch -PTFE (with structural FEA) PI-4**
5	**The deformed patch -Pericardium (with structural FEA) PI-5**

Table 4.6 The subsection models and the code labels of the pulmonary stenosis case.

Under the heading 'Structural Analysis,' the procedure for the idealized pulmonary artery (Figure 3.22) was performed in this case with an incision containing the actual patient morphology and the curve fitting the organic structure (Table 4.7).

A. Patch Creation after FEA and CAD
B. FEA Static Structural for the comparison of patches
C. FEA Fluids – Pre-Op Morphology
D. FEA Fluids – Post-Op Morphologies

Table 4.7 The workflow sections for pulmonary stenosis models of the selected case.

The incision was applied with a free curve on the right pulmonary artery. The line pressures were defined 5 N/mm on the centerline flaps and 1 N/mm on the following segments through the edges, as mentioned in the section.

The gap region was obtained after surface pressure (from the inside outward) load -0.0001 Mpa when the displacements were set zero for the main and left pulmonary (Figure 4.56).

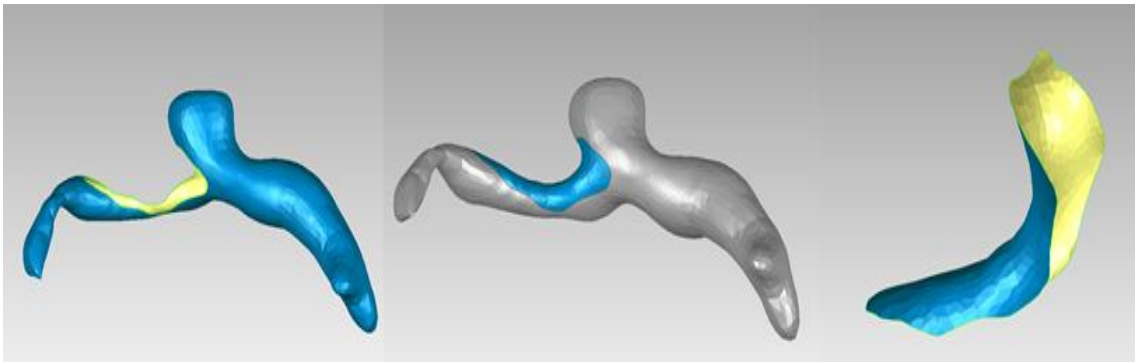

Figure 4.56 The gap that obtained after structural deformation on the artery (left), the virtual patch that designed with reverse engineering methods with the CAD tool (middle), and the patient-specific patch surface (right).

The same procedures were implemented to the patient-specific 3D models with PTFE and pericardium for obtaining the patched arteries. The contact regions with the artery (target body) and patch (contact body) are depicted in Figure 4.57.

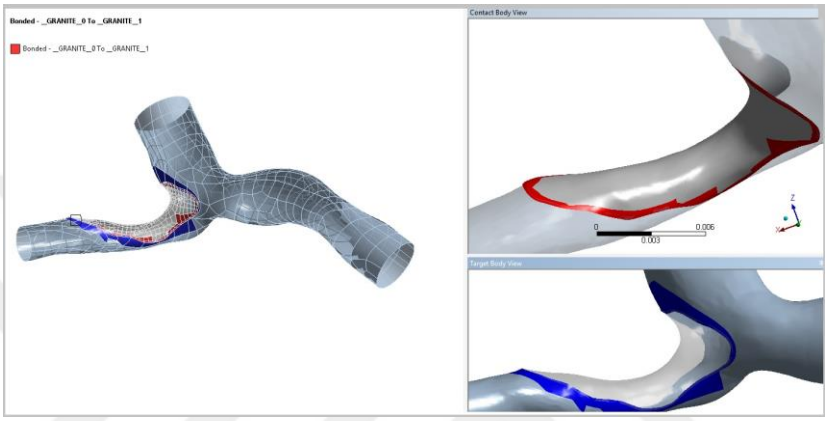

Figure 4.57 The contact region definitions on the artery wall and the patch surface before structural analysis on ANSYS.

The pressure on **the** surface was applied in the arrow direction through to the inner wall of the pulmonary artery (Figure 4.58). The final models are obtained after FEA for patched arteries with PTFE and human pericardium patch (Figure 4.59).

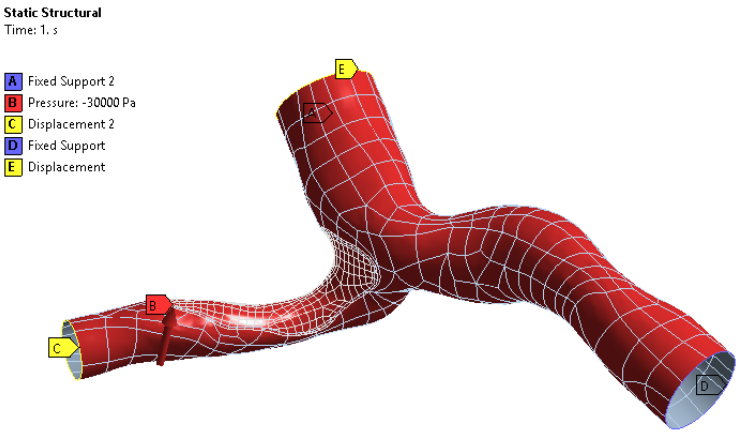

Figure 4.58 The meshed artery model with the patch on ANSYS Static Structural.

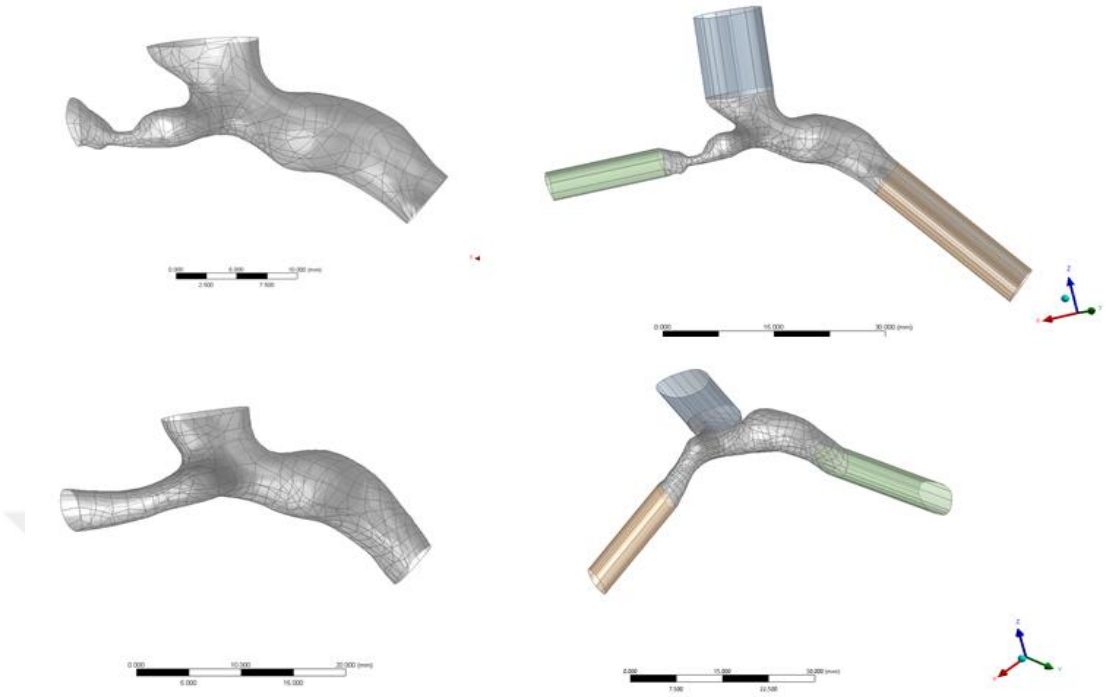

Figure 4.59 The pre-op geometry and its form with extruded inlet and outlet regions (top). The post-op geometry and its form with extruded regions (bottom).

Since the models obtained from the actual preoperative and postoperative image data are defined as surface, the preparation and importation of the CFD solver can be performed without problems, while the same procedures are not possible for the deformed artery obtained with FEA. Since the material properties are defined by the FEA, the thickness of the patch and lumen are defined, so the deformed geometry procured as an outcome of the simulation is obtained with the given thickness. For this reason, the final virtual patch angioplasty model volumes of structural analysis were exported. The surfaces of the models were selected and saved as new objects. Thus, the proper surface data of the arteries after FEA were obtained for CFD analysis. The resulting STL models were also converted into step format with CAD tools (Geomagic Studio) and imported into ANSYS Workbench. The blood streamlines are simulated with CFD for comparison. The CFD runs were analyzed pre-op, virtual PTFE, virtual pericardium post-op models.

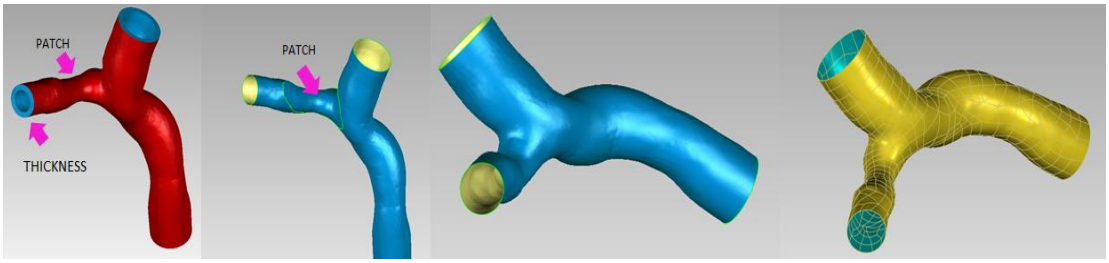

Figure 4.60 The surface selection is defined with red on the artery that had virtual angioplasty with pericardium (left). Then, left to right, respectively, the wall of the artery defined by patch, final wall geometry, and step format of the pulmonary artery.

4.2.2. Fontan Procedure

In patients with interrupted IVC with azygos continuation diagnosis, shunt placement surgery was planned to ensure equal distribution of growth factors from hepatic veins to lungs.

Some patients who had single ventricle repair before, have cavopulmonary anastomosis, which helps all systemic venous return to the pulmonary artery [28][212]. The hepatic growth factor cannot be added to pulmonary circulation in this configuration [63][3]. That is why atriovenous fistulas, protein-losing enteropathy, and low tissue oxygenation was seen in these cases. Intra and extracardiac baffle designs of different lengths, ages, and curves were placed in the vein, and the flow distributions were examined. The patients who were provided systemic venous return and planned to undergo the final stage of surgical correction by Fontan Procedure were selected as 14, 8, and 3 years old.

MRI images were selected differently from the coarctation cases of this chapter. The first patient underwent prospective screening with cardiac MRI. The shooting protocol is in the Cardiovascular Imaging Chapter. For the other two patients, thoracic angiographic MRI was performed, which took less time and could provide the desired information for the radiologists, clinicians, and surgeons. Because of the second patient's age, sedation was preferred to provide breath-holding conditions. The workflow of the study is depicted in Figure 4.61:

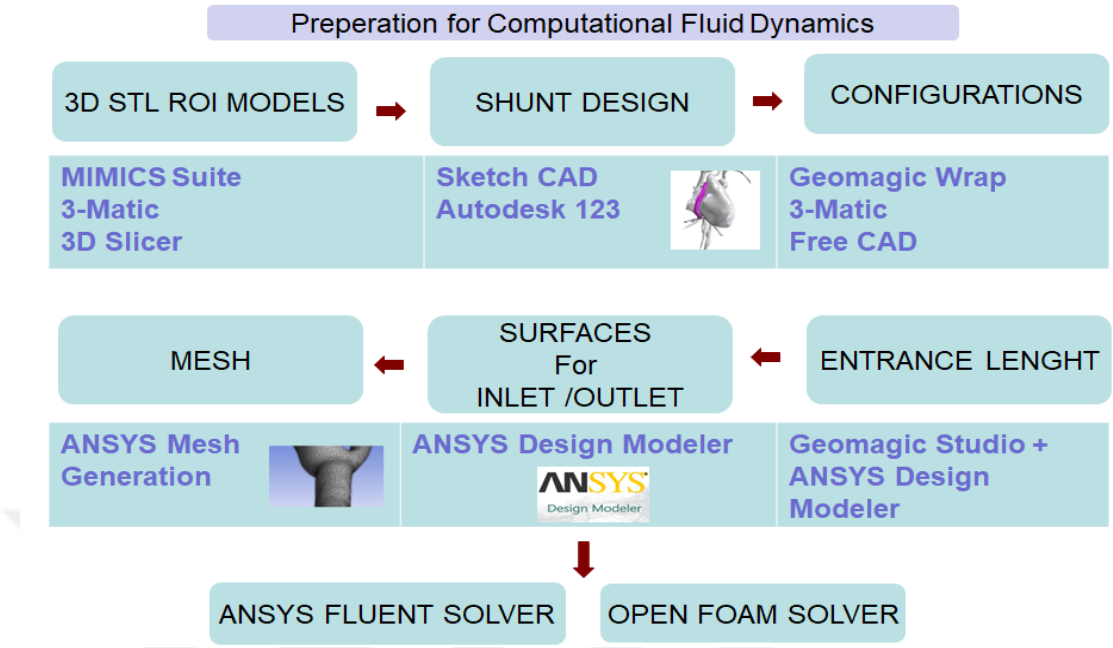

Figure 4.61 The software tools of the workflow of the Fontan section.

- **1st CASE**

The first case was a patient who is 14 years old with the diagnosis with left atrial isomerism, standard inlet right ventricle, complete atrioventricular septal defect, DORV, and pulmonary stenosis. The patient had an operation in the neonatal period.

A cardiac MRI scan without sedation was obtained for the reconstruction process. The obtained models were compared with radiological images, and the study was continued with the approval of the clinicians.

The lumen diameters were meticulously reconstructed in order to keep up the accuracy of the simulation results and to make accurate calculations (Figure 4.62).

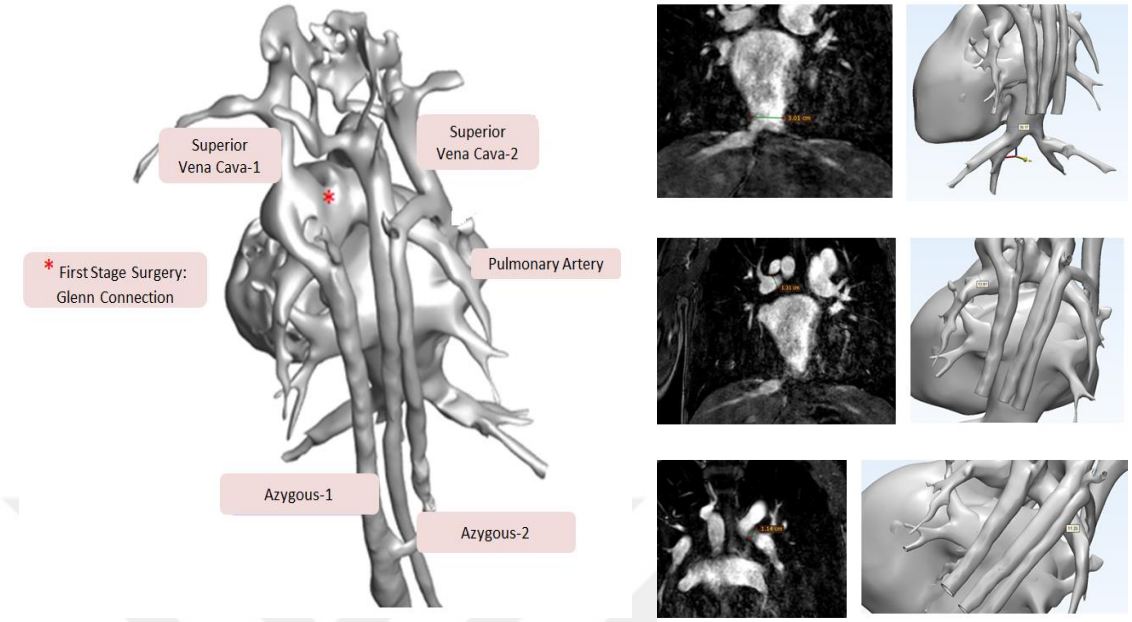

Figure 4.62 Bilateral SVC and azygous veins, and Glenn anastomosis are depicted on the reconstructed heart 3D model (left). The cine-heart views of cardiac MRI scan consistency of the models were checked with measurement analysis (right).

Each artery and veins are reconstructed separately, and the region of interest for blood flow simulation was defined. This region involved the SVC and pulmonary artery joint and azygous vein and hepatic veins.

Even though there is no need for an aortic connection in the vena flow cycle needed in the simulation, the aorta was also added to the configuration models to see about the position of each structure (Figure 4.63).

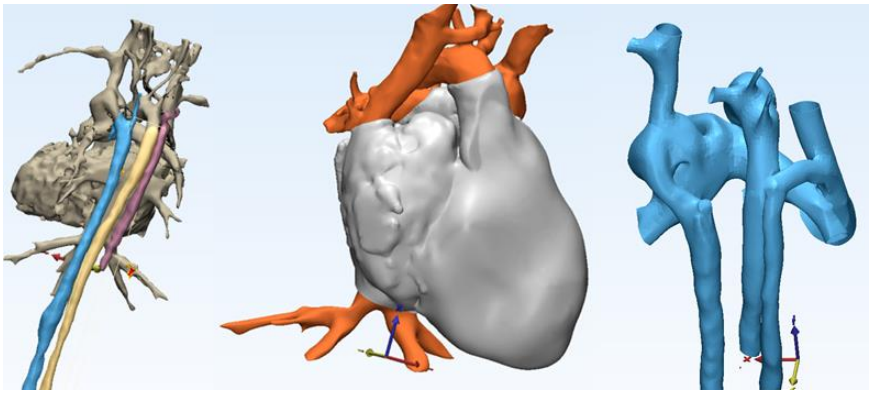

Figure 4.63 The final lumens in different colors (left), the myocardium tissue and blood pool models (middle), and the region of interest with the aorta (right). The case was named SI_M_001 in the database.

The surgical planning of the Fontan procedure was performed with virtual possible shunt configurations (Figure 4.64). Each shunt configuration was prepared in different positions and sizes as a result of the joint work of clinicians and engineers.

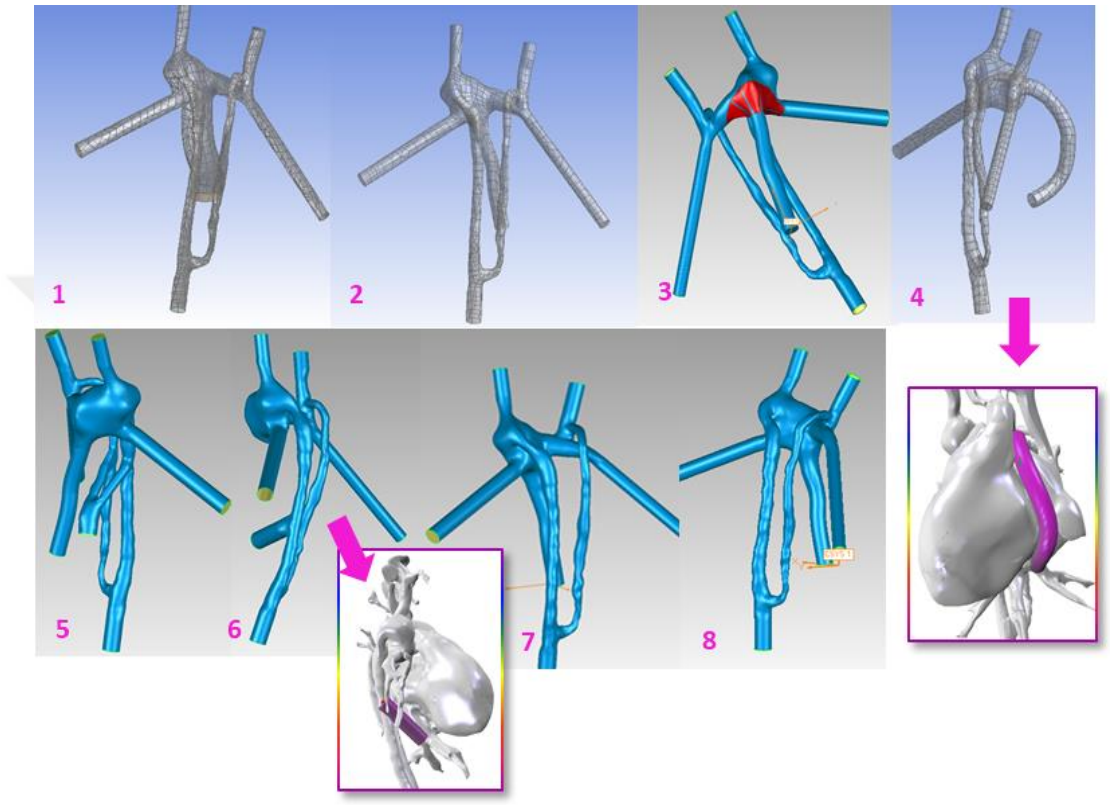

Figure 4.64 Possible samples of systemic venous return configurations designed on CAD tools for the first Fontan study patient.

- **2nd CASE**

9 Years Old, a female patient who operated with Kawashima surgery when nine months old. Diagnosed with pulmonary stenosis, VSD, and L-TGA. 3D anatomy was reconstructed after a pediatric cardiology examination, and a thoracic MRI scan was performed. As in the first patient, the consistency of the virtual model was checked in this patient (Figure 4.65).

Then the base model was created by preserving the relative structures to be used in the study. Baffle connections in different configurations were designed and implanted on this model (Figure 4.67).

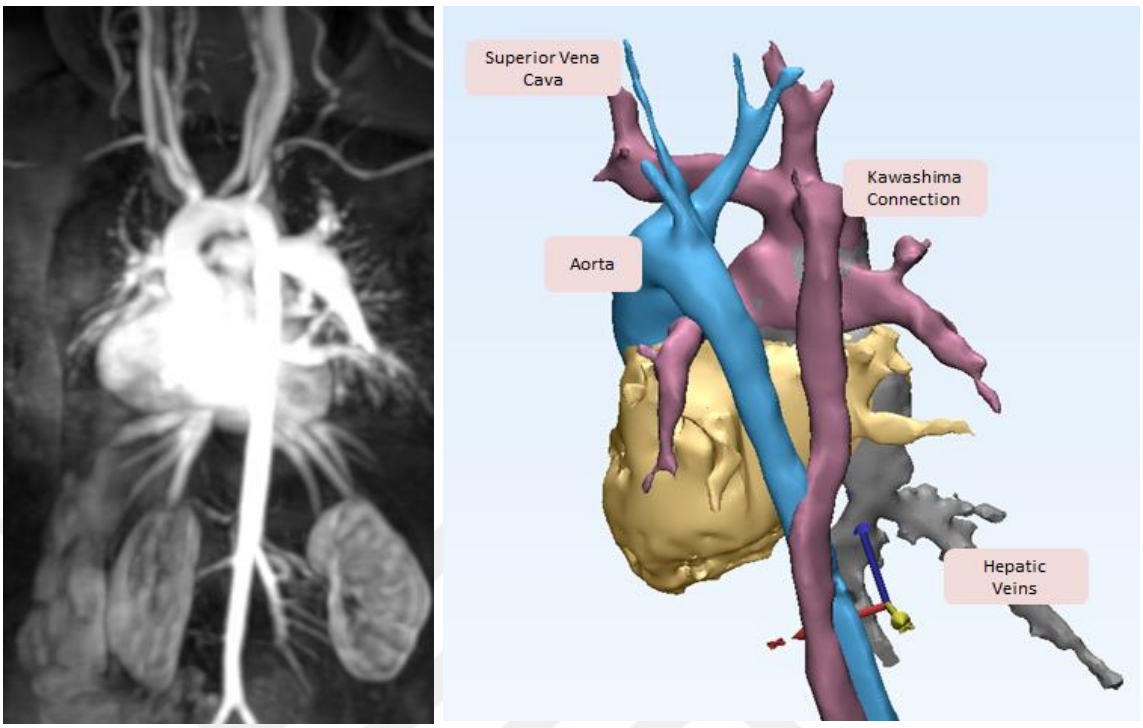

Figure 4.65 The MRI view and the reconstructed virtual heart model of the 2nd patient.

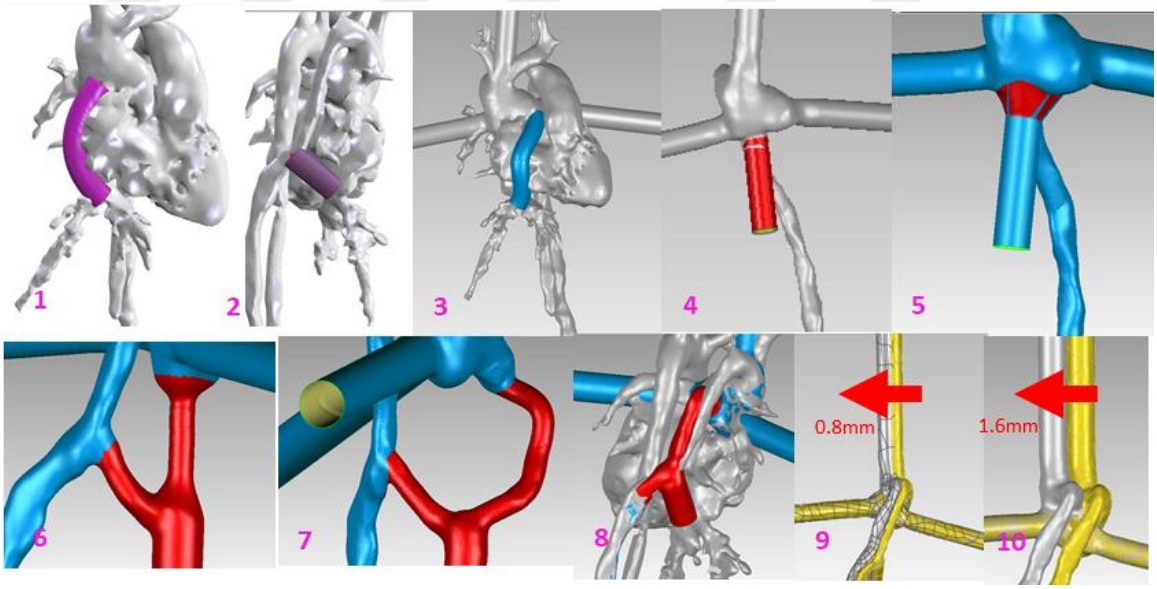

Figure 4.66 The shunt configurations (n=10) for the second case. The case was named SI_M_002 in the database.

- **3rd CASE**

The reconstruction of the 3rd case (Figure 4.67) and the shunt configurations (Figure 4.68) were performed as in other cases. The patient was diagnosed with left atrial

isomerism, not continuous IVC at the right atrium connection, and azygous connection to SVC.

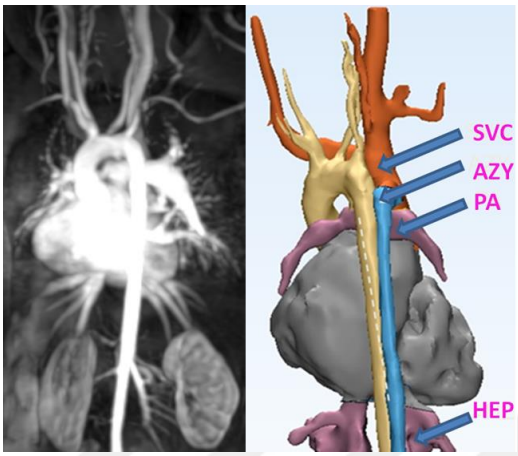

Figure 4.67 MRI dataset scanogram and the 3D model of the patient.

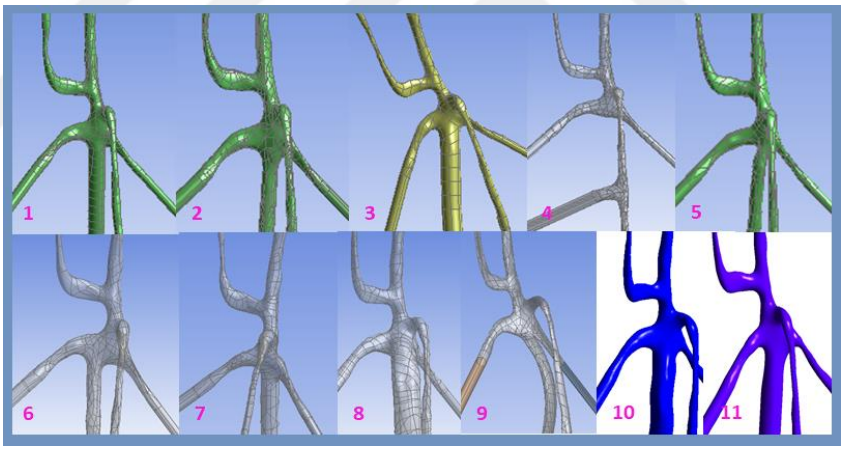

Figure 4.68 The virtual baffle configurations of the 3rd patient. The case was named SI_M_002 in the database.

CHAPTER 5

5. RESULTS

Using the tools and workflows in the Methods Chapter, the outcomes of the studies under the subheadings of surgical planning, intracardiac planning, and coarctation are presented in this section.

The primary purpose is to provide accurate data with additional information and planning techniques that will contribute to the treatment planning with image-based data and virtual surgery methods in the treatment of the aforementioned diseases.

The results of the study with selected samples in intracardiac cases and numerical simulation results in virtual surgery cases are explained under separate headings.

5.1. Repair Planning for Intracardiac Malformations

In this section, when sufficient data could not be provided with the available information, it was aimed to contribute to the process of clinical decision making by examining the intracardiac anatomy in more detail with the processing of multi-slice image data and the creation of cavity models.

All of the four cases aimed at relieving the doubts about the planning of the treatment would be beneficial either by vascular intervention or surgical operation. The results presented in the first part, possible treatment methods in VSD cases to be repaired by the operation and the repair technique decided after this study was applied in eleven selected patients and. In the second part, the results are presented.

5.1.1. Catheter Interventional or Surgical Planning?

Catheterization was preferred in six of ten cases and surgical repair in four cases.

With the help of modeling and 3D prototyping, position, diameter, and close tissues could be examined in more detail. These tools were efficient when catheterization decisions cannot be adequately taken with ECHO or CT techniques.

The cases of VSD for which a surgical intervention and a catheterization intervention were decided:

TGA → [Rastelli Procedure]:

After the 3D blood pool and intracardiac models of a two-year-old patient with TGA, VSD, ASD, subvalvular pulmonary stenosis pathology, physical information that could not be obtained by radiological images was examined, and the treatment planning was performed on the virtual model (Figure 5.1).

The patient's treatment was decided as the Rastelli procedure and was successfully performed.

The wide VSD was enlarged up to the anterior. VSD aortic tunneling was closed with a patch. Patent foramen ovale primary was closed. The distal anastomosis of the conduit was performed at the level of pulmonary bifurcation. Post-planning implementation was completed, and the patient's condition is monitored.

The patient was named AAB_003 in the database.

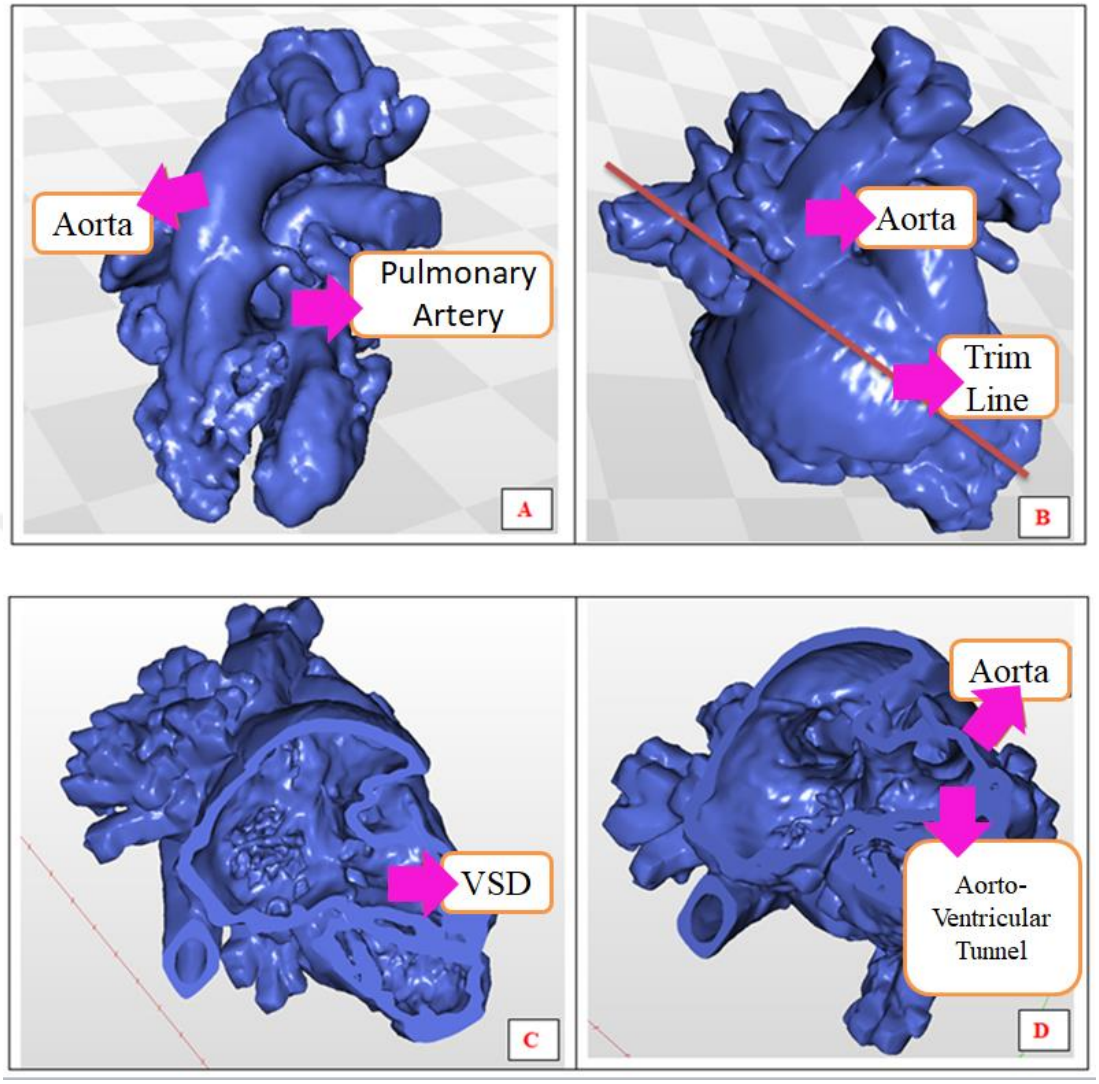

Figure 5.1 The blood pool model visualized on ModuleWorks STL (A) [213]. Virtual incision (B), VSD (C), and VSD (to aortic valve) tunnel visualization model (D) on the created intracardiac model.

Pulmonary Atresia → [Transcatheter Pulmonary Valve Implantation]: In the case of operative Fallot with pulmonary atresia and enlargement of the right heart chambers, blood pool, intracardiac models and 3D model of vessels were created (Figure 5.2). The patient was named AAB_003 in the database.

With additional information on the lumen volume that can be examined by rotation, the treatment plan was planned by catheter and pulmonary stent (35 mm with 23x4 Z Med balloon) and valve (Edwards 23) implantation.) [214].

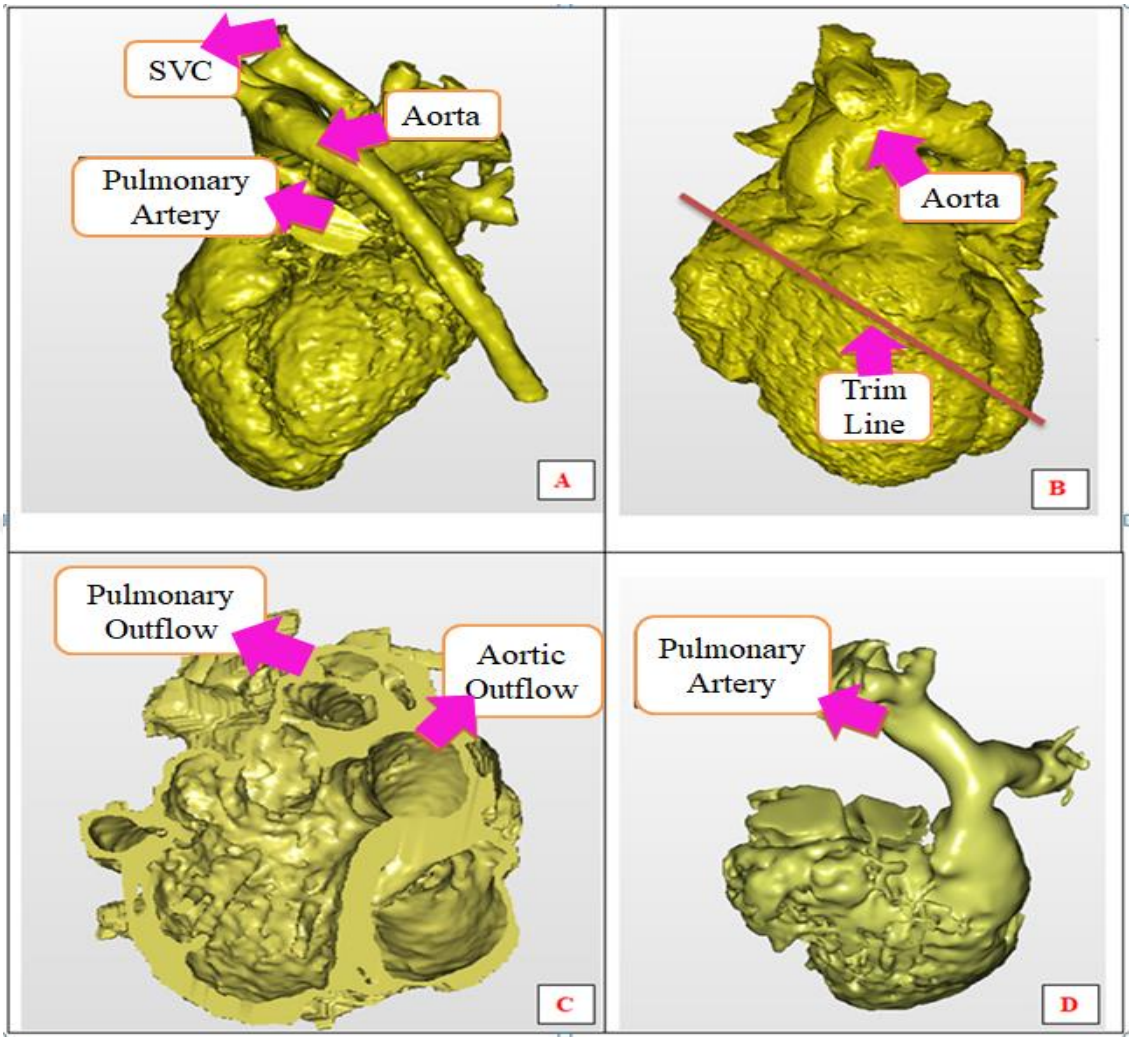

Figure 5.2 3D model with the help of segmentation tools to obtain a cross-section of the sample and the virtual vascular-ventricular relationship showing the virtual model.

5.1.2. Which Surgical Technique?

The advanced imaging information helps to diagnose; surgical decision-making demand needs a better understanding of the intra-cardiac anatomy for optimum treatment alternatives in CHD. Therefore this section includes patient-specific virtual and 3D printed heart models for surgical planning routinely in clinical management. The correlations of the 3D reconstructions with anatomical details are examined before the repair operation. The benefits of 3D intracardiac virtual modeling in the preoperative planning of complex cardiac pathologies are reported.

A total of fifty-five CHD cases were finally performed in this study. There was a strong correlation between the 3D models of these patients and the condition detected

during the operation. The para-septal incision through the 3D virtual model and the VSD appearance and its association with the aorta are very similar to the view in the surgery.

Clinical details and anatomical diagnosis of the selected fifteen cases are summarized in Table 5.1. The patient's age, diagnosis by ECHO imaging, past interventions, location of VSD, and methods that could be used to repair it was indicated for each patient in the table. The repair methods given after 3D modeling are also listed in the right column.

Models were evaluated by pediatric cardiologists, congenital heart surgeons, and imaging engineers. The images obtained with the paraseptal sagittal incisions applied to each case routinely. If deemed necessary by the cardiac team, other incisions were added, or 3D prototypes were printed.

Patient Demographics, Diagnosis, and Surgical Outcome								
	Age / Weight (kg)	ECHO Diagnosis	Segmental anatomy	Past interventions	Additional diagnoses	Surgical Options	VSD position	Surgery Performed
1	7 months/ 5,5 kg	DORV, D-malposed great arteries, severe PS with annular hypoplasia	S,L,D	RVOT stenting	None	BCPS or LV - aorta tunnel and RV - PA conduit	Remote	Biventricular repair, LV -aorta tunnel and RV - PA conduit
2	3 age/12 kg	DORV, anteroposterior great arteries, severe PS with annular hypoplasia	S,L,D	BCPS	RV hypoplasia	BCPS or LV to aorta baffle and RV to PA conduit	Remote	BCPS
3	9 months/10,5	DORV, D-malposed great arteries, severe PS with mild annular hypoplasia	S,L,D	Non	None	BCPS or LV to aorta baffle and RVOT procedure	Subaortic	Biventricular repair by LV to aorta baffle and RVOTO
4	2 years, 9.7	TGA, VSD, anteroposterior great arteries, severe PS with annular hypoplasia	S,L,D	PDA stenting	LPA stenosis	BCPS or LV to aorta baffle and RV to PA conduit	Subaortic	Biventricular repair by LV to aorta baffle and RV to PA conduit
5	9,5 months/9 kg	TGA, VSD, D-malposed great arteries, pulmonary atresia	S,L,D	Central Shunt	None	BCPS or LV to aorta baffle and RV to PA conduit	Remote	BCPS
6	11 months, 5	TGA, D-malposed great arteries, severe PS with mild annular hypoplasia	S,L,D		None	BCPS or LV to aorta baffle and RV to PA conduit	remote	Awaiting surgery
7	18 years/ 45 kg	c-TGA, VSD, situs inversus D malposed great arteries, severe PS with annular hypoplasia	I,L,D	Non	Situs Inversus	BCPS or Double Switch operation	Remote	BCPS
8	30 months/ 12 kg	DORV, VSD, restrictive ASD, normally related great arteries, pulmonary banding	S,L,D	Pulmonary banding and aortic arch repair	Restrictive ASD, LV hypoplasia	BCPS or LV to aorta baffle and RV to PA conduit	Remote	BCPS
9	30 months/12	DORV, large inlet VSD, side-by-side great arteries, subvalvular aortic stenosis	S,L,D	PA banding	S.valvular aortic stenosis	BCPS or LV to aorta baffle and RV to PA conduit	Subaortic	Biventricular repair by LV to aorta baffle and LVOT resection, debanding
10	13 months 7kg	TGA, VSD, D malposed great arteries, severe PS with moderate annular hypoplasia, PDA stenting	S,L,D	PDA stenting	Coronary anomaly (1 RCA-LAD, 2Cx)	LV -aorta tunnel and RV - PA conduit or pulmonary root translocation with VSD enlargement	Subaortic, small	Biventricular repair by LV to aorta baffle (VSD enlargement), and pulmonary root translocation
11	48 months, 18 kg	DILV, VA discordance	I,L,D	Pulmonary banding, BCPS	Restrictive BVF	VSD enlargement or DKS operation	Subaortik	VSD enlargement and Fontan procedure

BCPS, bidirectional cavululmonary anastomosis; RV, right ventricle; PA, pulmonary artery; LV, left ventricle; LVOTO, left ventricular outflow tract obstruction; PS, pulmonary stenosis; LPA, left pulmonary artery; c-TGA, corrected- transposition of great arteries; DILV, double inlet left ventricle; BVF bulboventriculare foramen; DKS, Damus-Kaye-Stansel.

Table 5.1 Details of selected cases of surgical intracardiac modeling section.

5.2. Repair Planning for Coarctations

In this section, which is based on repair in coarctation and hypoplasia cases, attention was paid to patch implantation in all cases. Samples with actual post-operative scans were selected as compared to the different repair options in the selected samples.

In both sections, as a study plan, virtual surgeries were performed on the model created from preoperative images. The pre-op model, virtual repair models, and postoperative models were compared in terms of numerical post-process results. The preferred repair method, the size, angle, priority order of the incisions in these methods were examined, and different anatomies of these materials were examined, and the differences of flow lines in these geometries were evaluated.

According to the properties of the implanted patch material and the artery wall opening, the incisions are performed in the 'Pulmonary Artery' section. The final shape of the flow lumen calculated numerically.

5.2.1. Aorta Coarctation Repair

In this section, which aims to make more objective and patient-specific decisions with virtual surgical planning techniques, computerized and postoperative data were evaluated comparatively. The reconstructed patient-specific aorta models of each patient are depicted in (Figure5.3).

The blood flow simulations with computational fluid dynamics solver performed in the models obtained after the virtual operation described in detail in the 'Surgical Planning' section is reported below.

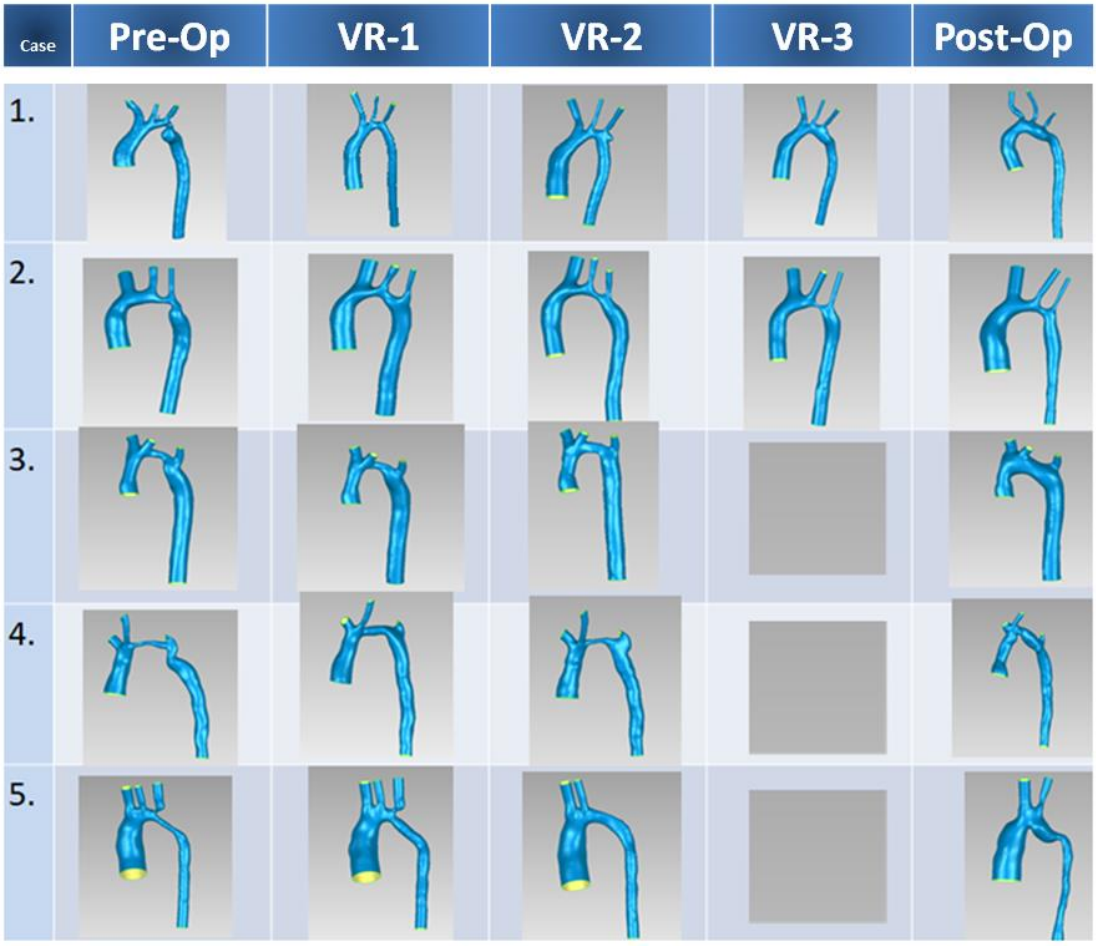

Figure 5.3 The CAD models for all pre-op, post-op, and virtually-repaired aorta cases.VR=Virtual Repair.

CFD post-process visualizations were tabulated separately to evaluate the scenarios in their entirety. In order to make comparisons, the same order was applied for each scenario as velocity, WSS, and pressure distribution.

1st Case:

The distributions of the first patient's pre-op model showed a maximum velocity of 1.9 m/s in the coarctation region.

Although this was not too high, the flow streamlines depicted a flow that proceeds completely twisted. In the WSS distribution, a severe and dramatic WSS change was observed in the narrow arch region of the patient. WSS, which was 5.5 Pa at the beginning of the arch, was found to be 1.6 Pa under the left common carotid artery just before the coarctation segment. Although the pressure distribution was not as remarkable as the velocity streamline and WSS distributions, the highest pressure

value was found to be around 23.7 mmHg in the descending aorta mound after coarctation (Figure 5.4).

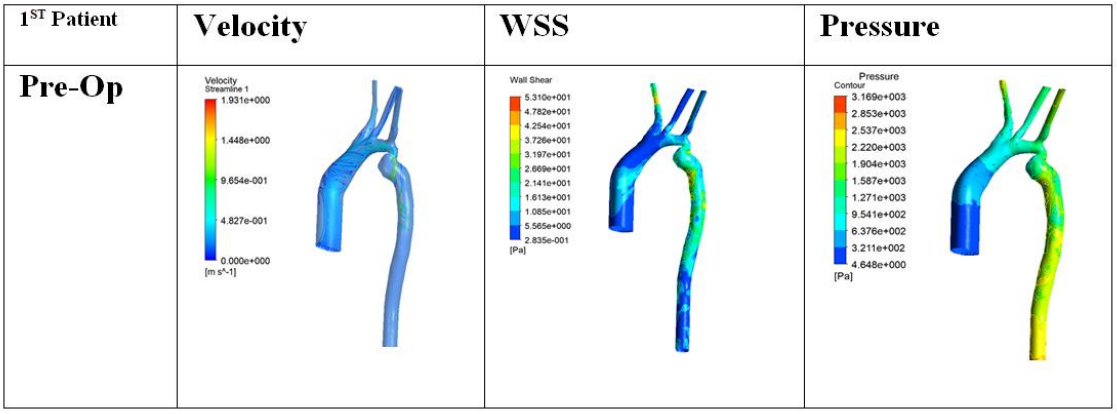

Figure 5.4 Velocity, WSS, and pressure distributions on the pre-op model of the first selected case.

When virtual anastomoses (VR-1 and VR-2) were compared with virtual patch angioplasty, none of the twisted streamline and sudden WSS changes were observed.

In the virtual patch repair, the distal patch border, and the virtual extended anastomosis repair, a WSS decrease was observed at the beginning of the arch. The most significant pressure drop was observed in the VR-2 (Figure 5.5). In the patch repair method (VR-3), velocity flow paths were of the preferred order but were critical for the subclavian artery region with dramatic changes due to luminal diameter variation.

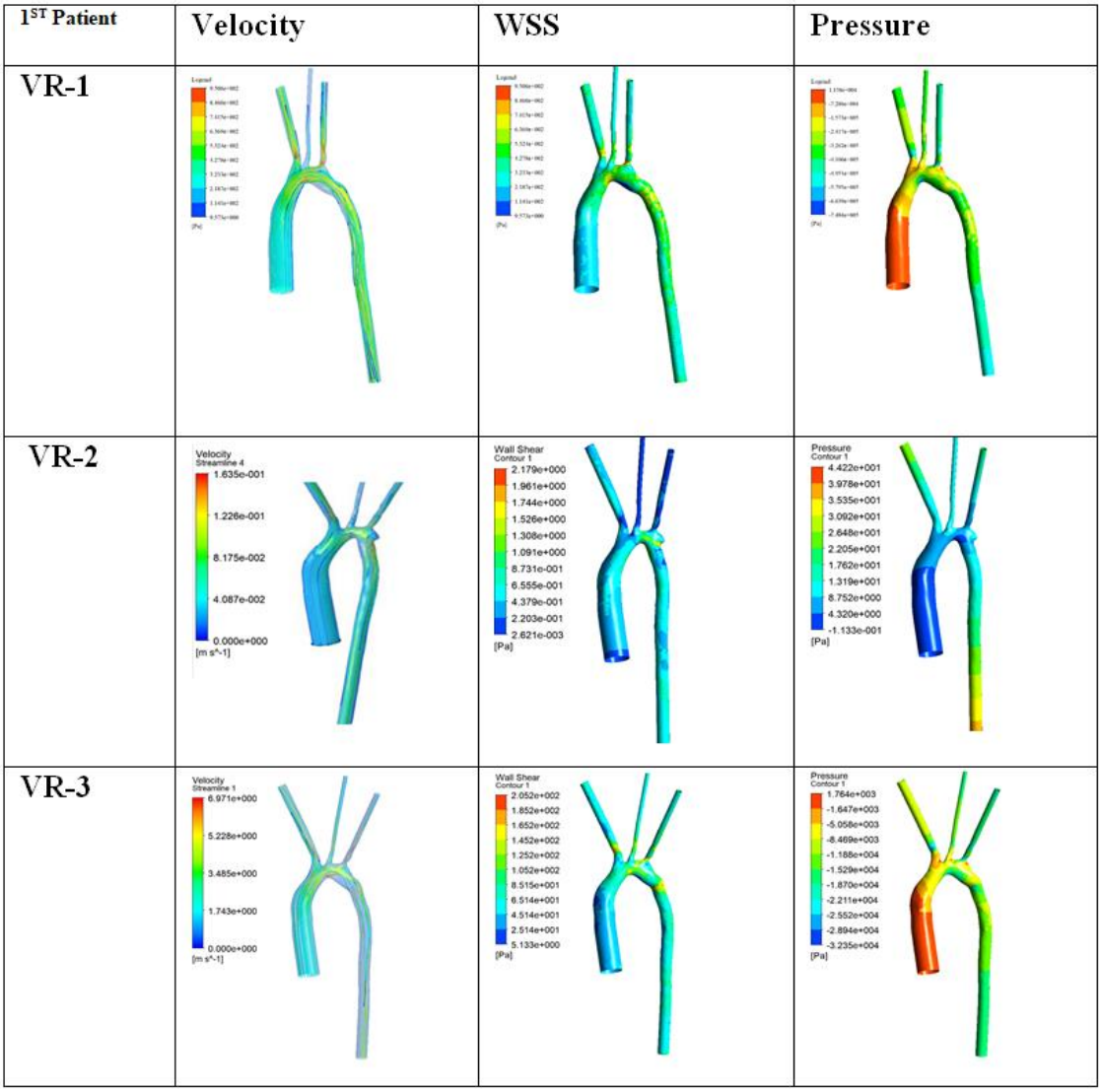

Figure 5.5 Velocity, WSS, and pressure distributions on VR-1 and VR-2 and VR-3 models of the first selected case.

Smooth flow lines were observed in the virtual repair models without any flow differences such as backflow, vortex, and reverse streamlines in the patch region extending in the post-op model. In terms of the shear stresses, the WSS changes in the virtual repair models were less variable than the post-op model.

As a result of the CFD study based on the patient's actual surgery, the velocity streamline was found to be acceptable, although not as smooth as the virtual ones (Figure 5.6).

No sudden ascents and descents were observed in the WSS distribution as in others, but reductions were observed after the left common carotid artery and left subclavian

artery distinctions, although the difference between the pressure values in the ascending aorta and descending aorta was not significant.

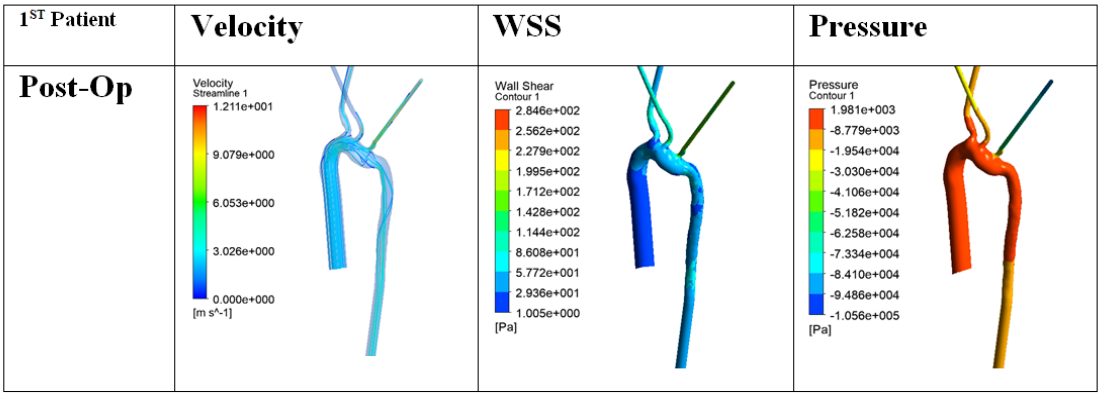

Figure 5.6 Velocity, WSS, and pressure distributions on the real post-op model of the first selected case.

The calculated calcification values were 19 mmHg for the natural vessel, 03 mmHg for the curved anastomosis method, 0.34 mmHg for secondary, and 0.1 mmHg for the patch repair technique. The highest-pressure level of 33.1 mmHg was observed for vertical anastomosis repair technique.

2nd Case:

In the second case, the results of the CFD study with the pre-op model showed that the velocity pathway continued after the separation of the brachiocephalic artery in the pre-coarctation region and after the isthmus in the descending aorta. At the beginning of the coarctation zone, the velocity reached its highest value. This region also showed the situation requiring intervention with critical reductions in WSS and pressure distribution visualizations (Figure5.5).

2nd Patient	Velocity	WSS	Pressure
Pre-Op	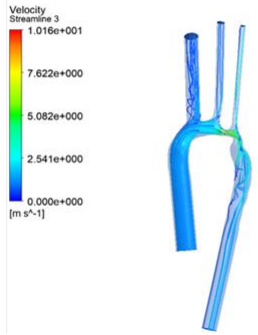	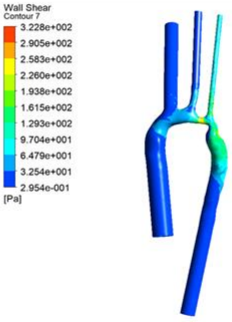	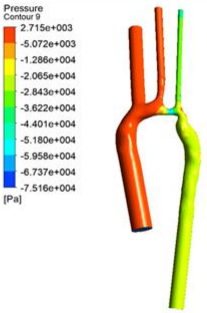

Figure 5.7 Velocity, WSS, and pressure distributions on the pre-op model of the second selected case.

Despite the expansion in VR-1 repair, it was observed that the flow did not descend by completely sweeping this region. The stenosis starting from the projection of the left common carotid artery affects this flow down to the descending aorta. Except for the sudden increase in the stenosis of the subclavian artery in the WSS and pressure distributions, no critical distribution scheme was observed for the repair site (Figure 5.8).

2nd Patient	Velocity	WSS	Pressure
VR-1	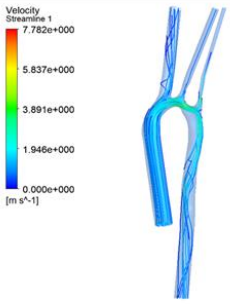	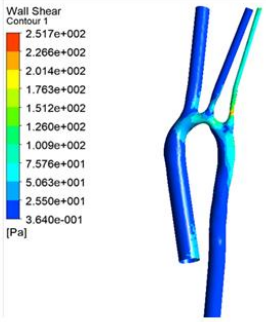	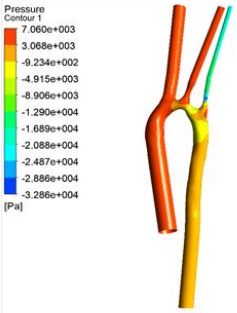

Figure 5.8 Velocity, WSS, and pressure distributions on the VR-1model of the second selected case.

Despite the expansion in VR-2, it was observed that the blood flow velocity did not descend completely by scanning this region, and the distributions were similar to VR-1 in terms of velocity. On the distal arch, a critical region was detected, which was not

apparent in the velocity pathway but observed in the WSS distribution. Pressure distribution was also decreased with the same segment (Figure 5.9).

In VR-3, the same segment was the critical region, and it was clearly seen with this velocity pathway (Figure 5.10). The velocity decreasing and the twisted descending flow caused critical strokes in WSS distribution. The pressure distributions were similar in VR-2 and VR-3 but decreased to low values in patch repair (-7 Pa).

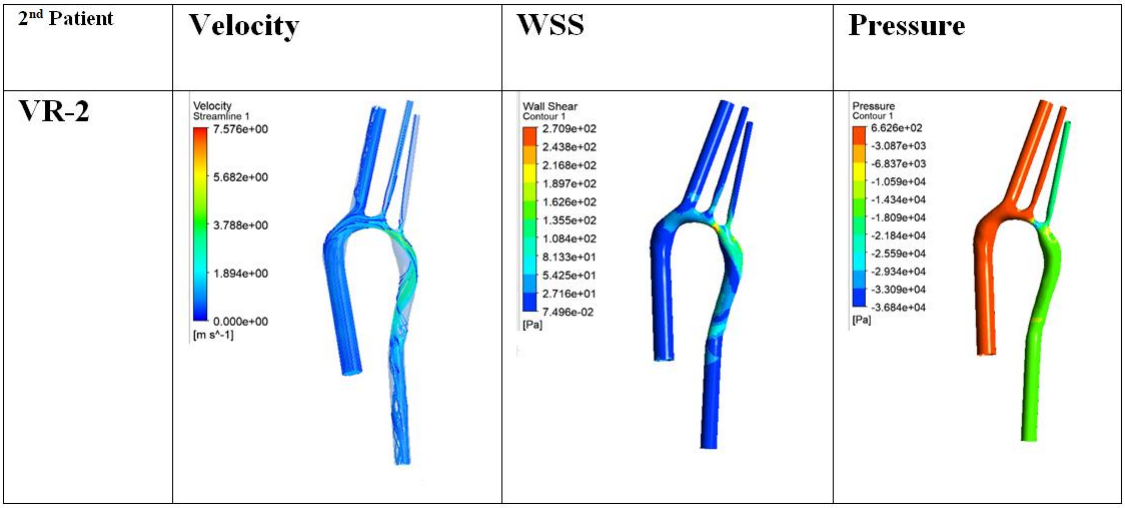

Figure 5.9 Velocity, WSS, and pressure distributions on the VR-2 model of the second selected case.

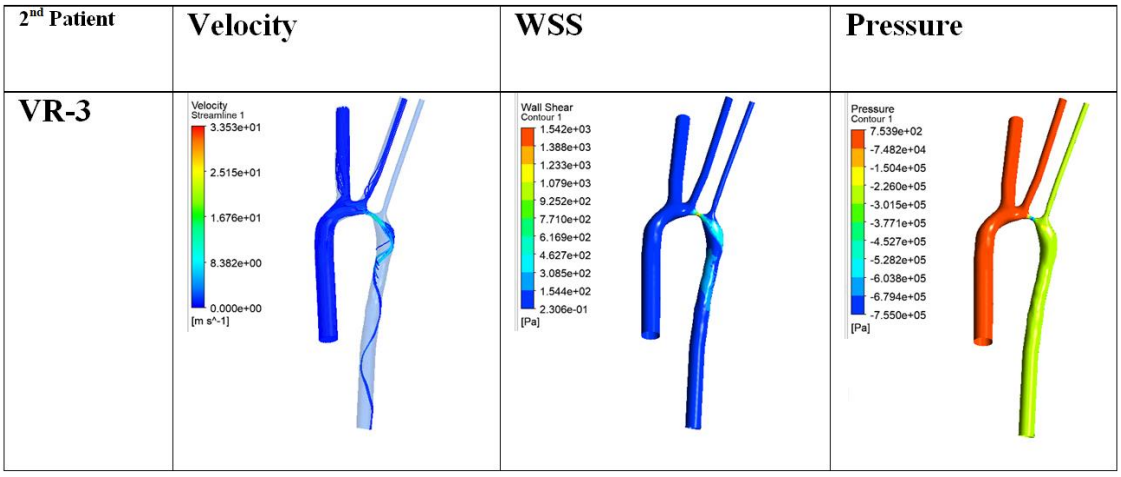

Figure 5.10 Velocity, WSS, and pressure distributions on the VR-3 model of the second selected case.

In the second case, a real post-op geometry CFD study showed sudden changes in the distal arch in velocity streamlines, WSS, and pressure distributions. Velocity values were not as large as in VR-2 (Figure 5.11).

2nd Patient	Velocity	WSS	Pressure
Post-Op	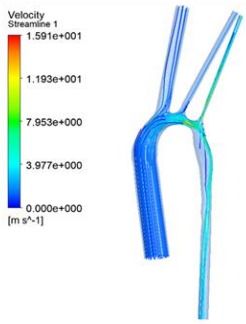	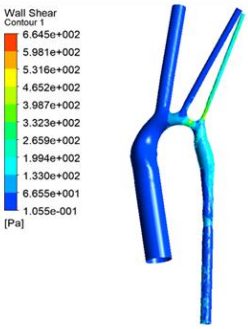	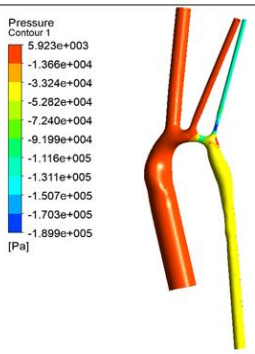

Figure 5.11 Velocity, WSS, and pressure distributions on the post-op model of the second selected case.

3rd Case:

In the third case, the twisted flow was observed with the coarctation segment in the pre-op model. At the same critical point, the WSS distribution also exhibited a sudden change, but in the visualization of the pressure distribution, the dramatic change was observed from the beginning of the proximal arch (Figure 5.12).

In the first (VR-1) and second (VR-2) virtual models, the critical velocity change in the pre-op model was observed with equal velocity values. Pressure distributions were similar (Figure 5.13).

3RD Patient	Velocity	WSS	Pressure
Pre-Op	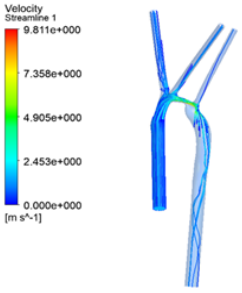	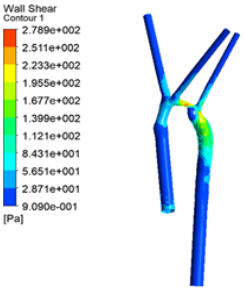	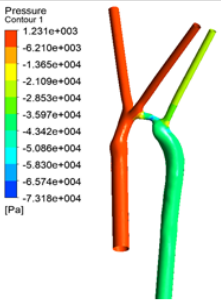

Figure 5.12 Velocity, WSS, and pressure distributions on the pre-op model of the third selected case.

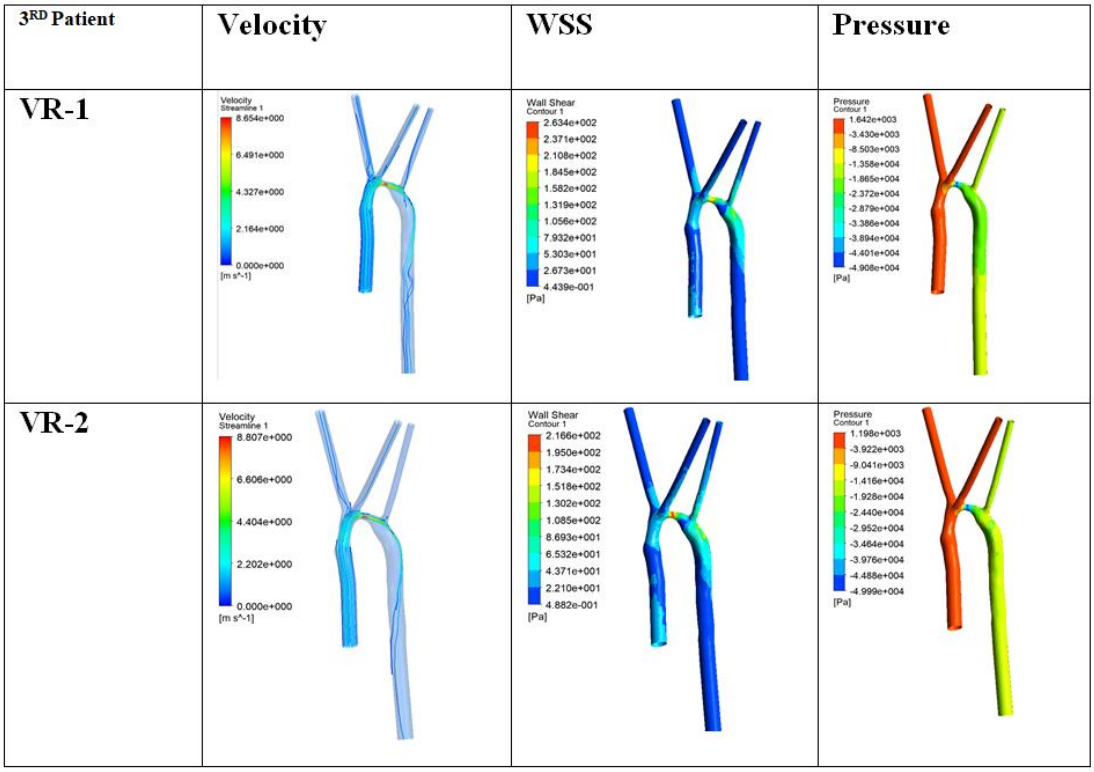

Figure 5.13 Velocity, WSS, and pressure distributions on VR-1 and VR-2 models of the second selected case.

A more acceptable flow path was observed in the visualization of the geometry generated by the actual surgery than in the virtual models. No dramatic changes were observed in WSS and pressure distributions (Figure 5.14).

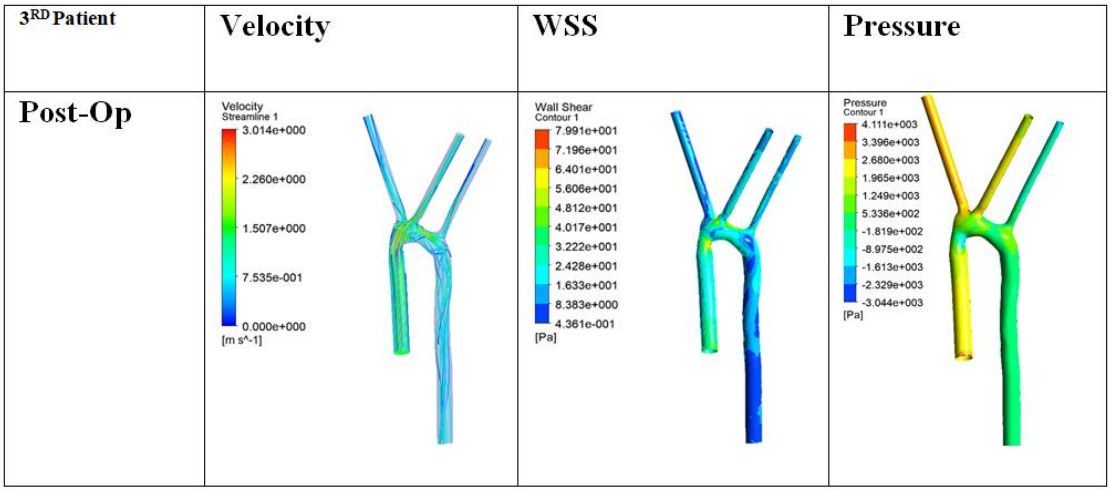

Figure 5.14 Velocity, WSS, and pressure distributions on the post-op model of the third case.

4th Case:

In the fourth model, critical velocity flow streamlines, WSS, and pressure distribution were observed from the proximal arch due to the very narrow aortic arch and the bump in the isthmus region (Figure 5.15).

The maximum velocity reached to 5.22 m /s inside the arch for the pre-op model, while the max velocity in the VR-1 arch was 3.11 m/s. For the VR-1 model, WSS increased in the arch zone, and low WSS was observed throughout (Figure 5.16).

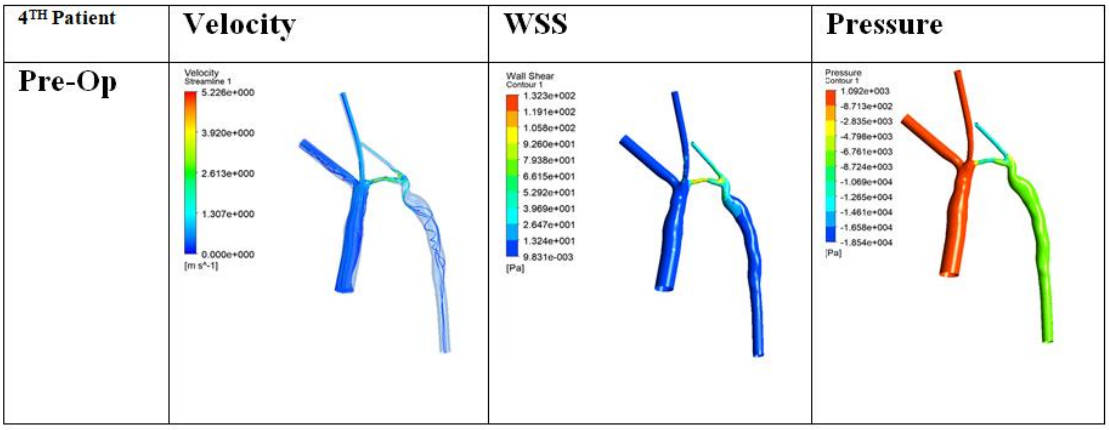

Figure 5.15 Velocity, WSS, and pressure distributions on the pre-op model of the fourth selected case.

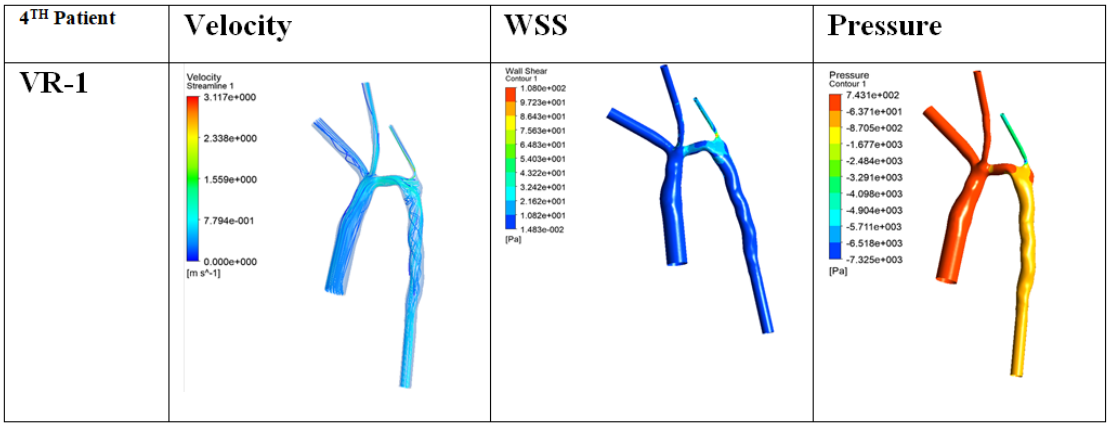

Figure 5.16 Velocity, WSS, and pressure distributions on the VR-1 model of the fourth selected case.

Twisted flow in the descending aorta was also observed in the VR-2 model of the fourth file. The velocity reached 7 m/s in the arch zone. No acceptable distributions similar to those in VR-1 were observed in the same region (Figure 5.17).

4TH Patient	Velocity	WSS	Pressure
VR-2	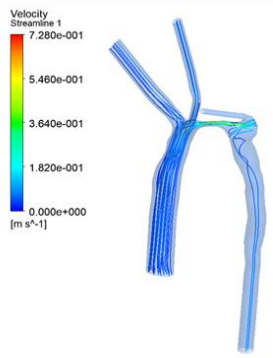	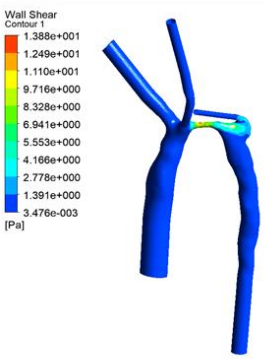	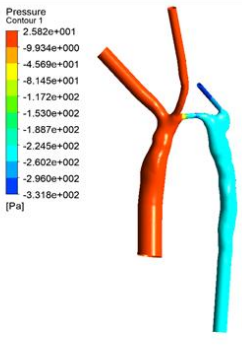

Figure 5.17 Velocity, WSS, and pressure distributions on the VR-2 model of the fourth selected case.

The WSS distribution showed acceptable distributions outside the arch segments but found the highest value in the proximal arch (Figure 5.18).

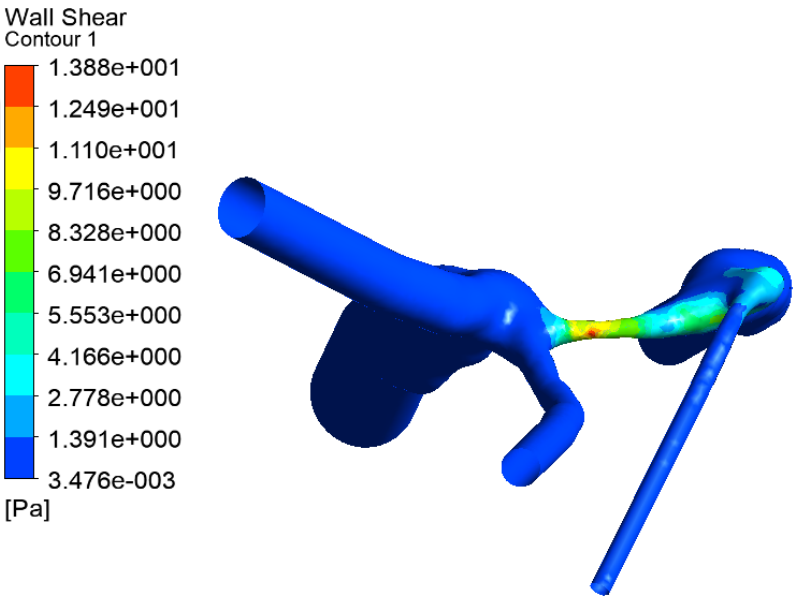

Figure 5.18 WSS distribution on the VR-2's arch of the fourth selected case.

As a result of the actual post-op treatment of the case, the outcomes of the CFD study performed by the geometry showed a significant decrease in WSS in the patch anastomosis area and a significant decrease in pressure at the left subclavian artery exit compared to the whole model. The flow lines were in the acceptable range (Figure 5.19).

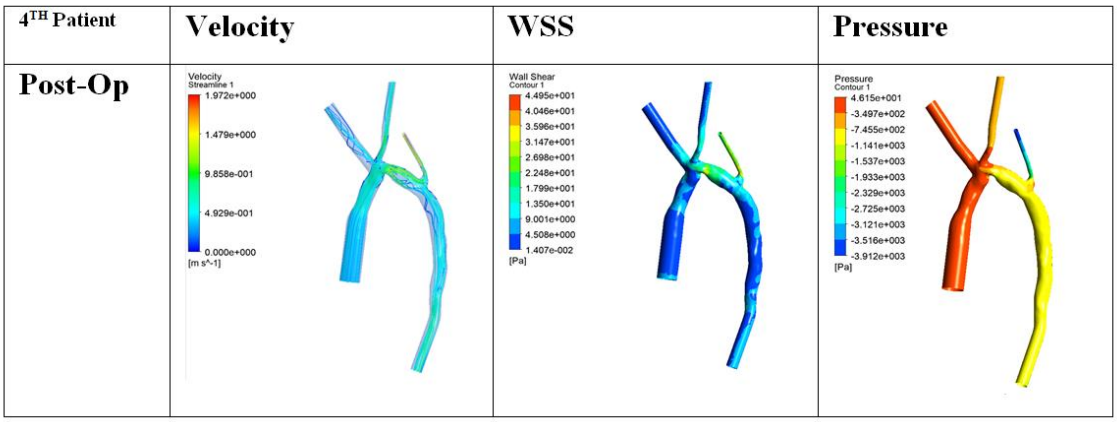

Figure 5.19 Velocity, WSS, and pressure distributions on the post-op model of the fourth selected case.

For all models, no critical flow lines were observed in the arch. In the post-op model, WSS changes that did not reach a critical level were observed.

5th Case:

In the results of the study performed with the pre-op model of the fifth patient, jet-flow at the narrowest point on the aortic arch followed by a helical progressive pathway was observed. WSS and pressure distributions also showed low velocity, starting just before the subclavian artery (Figure 5.20).

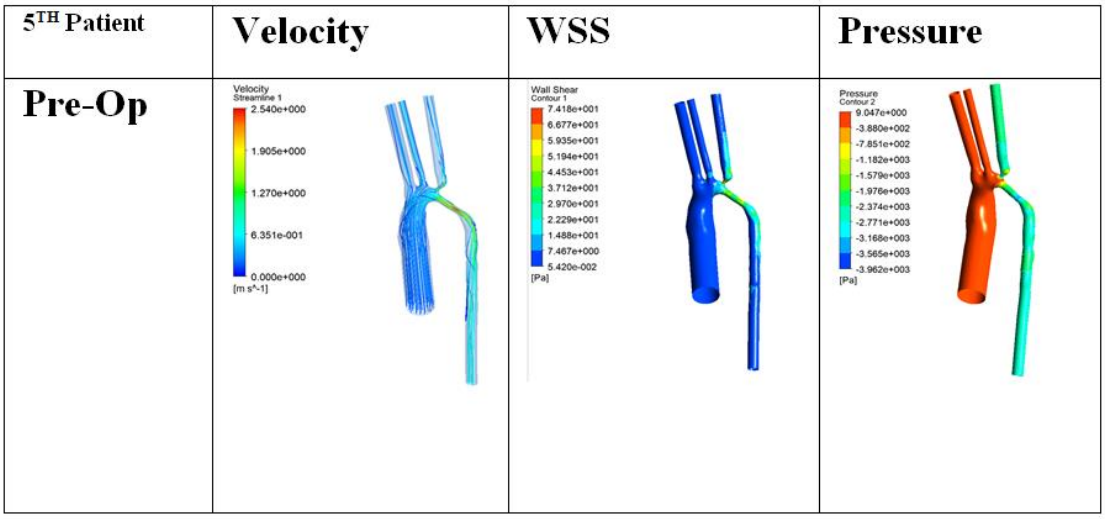

Figure 5.20 Velocity**,** WSS, and pressure distributions on the VR-2 model of the fifth selected case.

In the fifth case, smooth velocity flow lines were observed in VR-1 repair. No sudden velocity changes were observed.

In VR-2 repair, although the velocity measurements were not far from each other as in VR-1, the flow pathway was not as smooth as the first one. In this repair, small contours were observed, which showed sudden changes in WSS distribution. Although there were differences in the arch in the geometries, there were similarities in the pressure distributions in the first and second repairs (Figure 5.21). The pressure drop was 31 mmHg for the first repaired model (VR-1) and 37 mmHg for the second repaired model (VR-2).

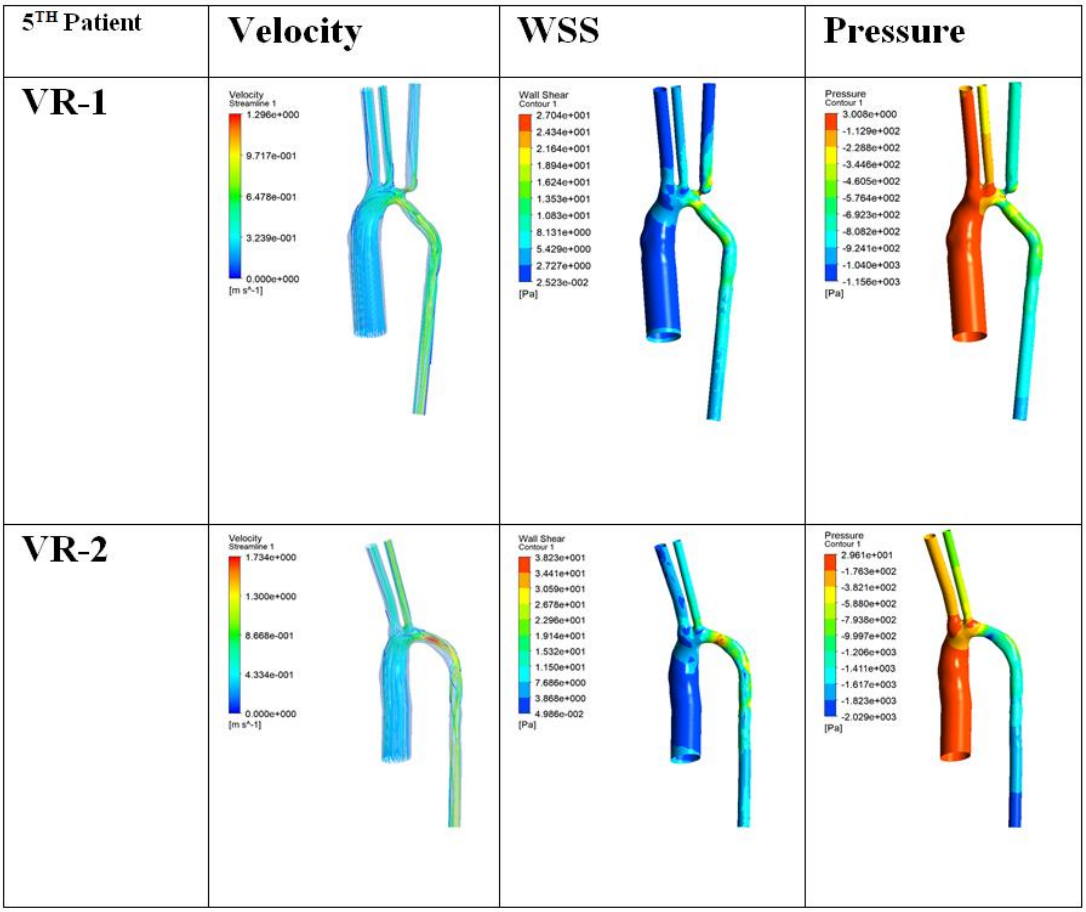

Figure 5.21 Velocity**,** WSS, and pressure distributions on the VR-1 and VR-2 model of the fifth selected case.

The highest velocity values were observed as a result of the CFD study of the model obtained during the actual operation. The fact that the stenosis at the distal border of the junction area was very close to the old diameter of the stenosis was evident by the high-velocity values in the critical region. A sudden increase in WSS was seen in the

same region. The lowest pressure was observed in the left common carotid artery (Figure 5.22).

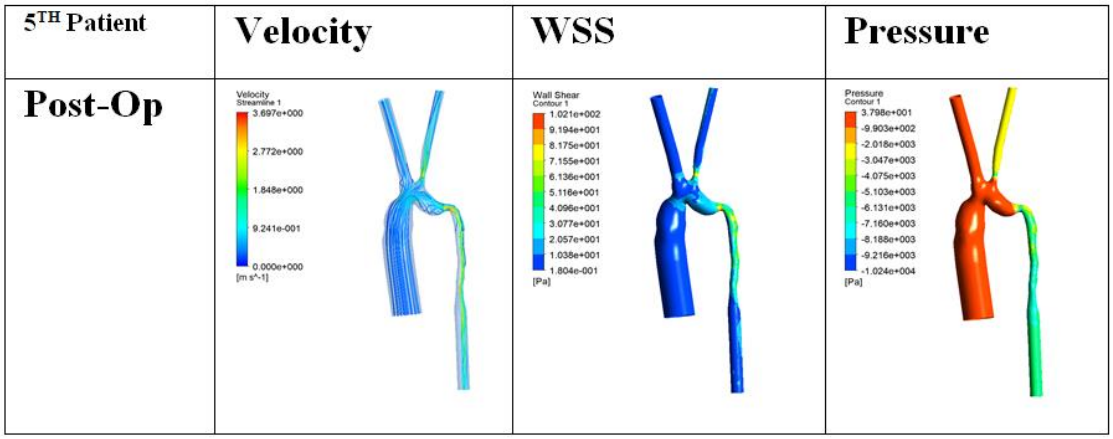

Figure 5.22 Velocity**,** WSS, and pressure distributions on the post-op model of the fifth selected case.

5.2.2. Pulmonary

In Chapter 4, idealized stenosis was created for the pulmonary coarctation section, and the methodology for patch angioplasty was explained. In the 'Virtual Surgery' Chapter, a virtual repair was performed on a real pediatric pulmonary artery with a stenosis, and patch angioplasty was terminated. The only difference of this section from the aortic coarctation section is not that the projected artery is different, but also the material properties of the implanted patch and endothelium are included in the evaluation, and the difference in the same repair is made with different materials.

5.2.2.1. PTFE Patch or Human Pericardium for Patch Angioplasty on This Artery?

The artery geometries obtained for this purpose included preoperative and postoperative volumes for the selected sample. After PTFE and human pericardium patch angioplasty, vascular wall deformations were obtained by structural FEA, and the geometries were exported. The geometries obtained for hemodynamic analysis are shown in Figure 5.23. Total deformation values were different in patch angioplasty specimens with the same geometry but different materials.

While the deformations of the artery and patch materials were approximately 4.25 mm in average during the evaluation of the deformation of the artery and patch materials, the deformation on the wall with pericardium patch implantation and the

surrounding deformation was more varied and unsteady. Deformation at the free end of the right pulmonary artery was around 2 mm for PTFE and 7 mm for pericardium.

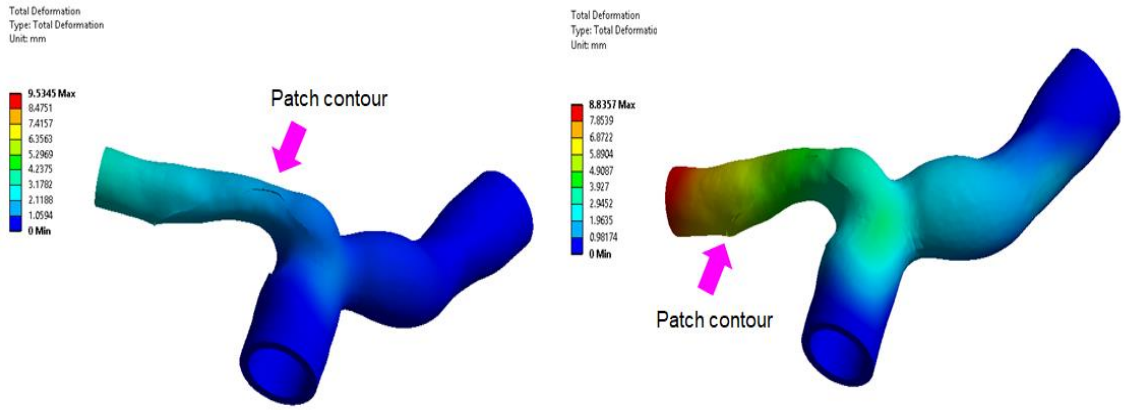

Figure 5.23 Total deformation distributions for PTFE (left) and pericardium (right) patches.

When only the X-axis deformation was examined, no change was observed in the lower part of the lumen where the pericardium patch was implanted, but the deformation in the X direction was similar to the PTFE patch (Figure 5.24).

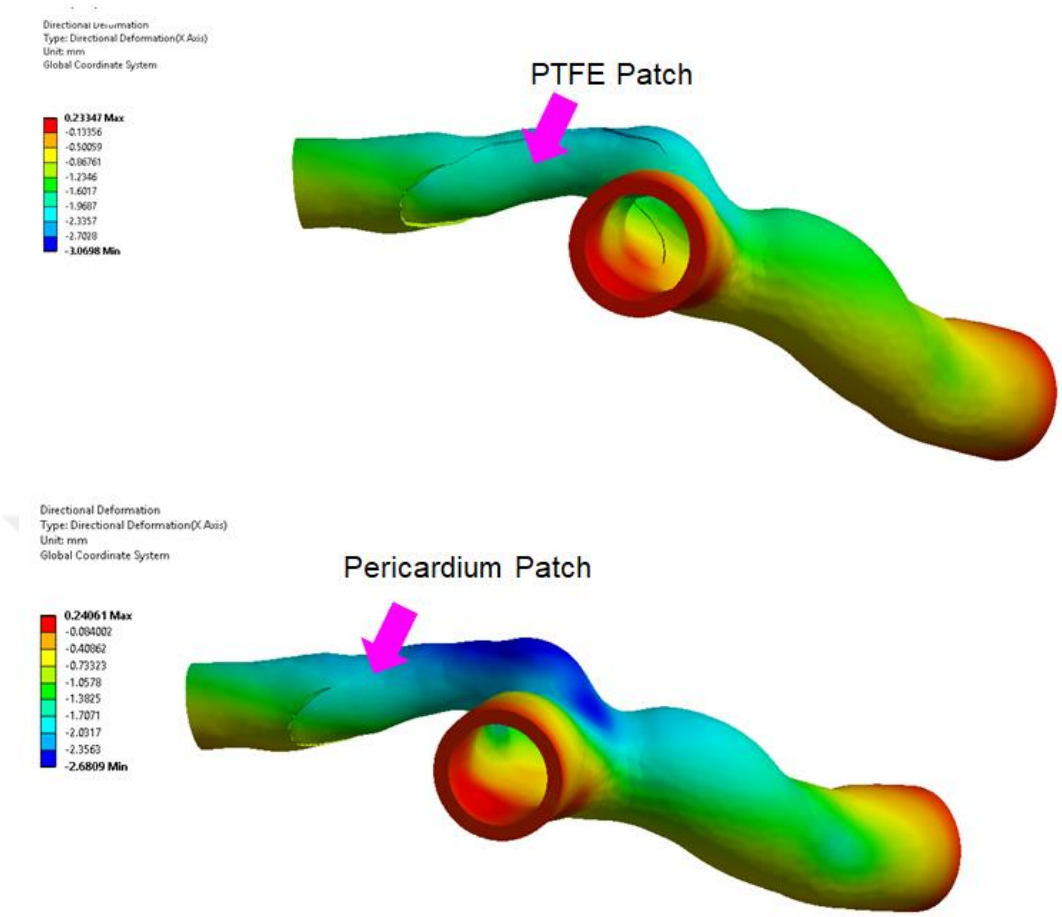

Figure 5.24 Directional deformation on the X-axis for PTFE and Pericardium patches.

When PTFE and pericardium patch angioplasty Von-Mises stress was examined for stress distribution, close contours were seen on the patch. Although the artery model and material, the effecting load and patch suture were equal, differences were observed in the distribution of the vascular tissues. Stress contours diversion was also observed in adjacent vascular tissue at the intersection where the Pericardium patch had the highest value with 0.3 mPa. However, the maximum and minimum values in the distributions were similar (Figure 5.25).

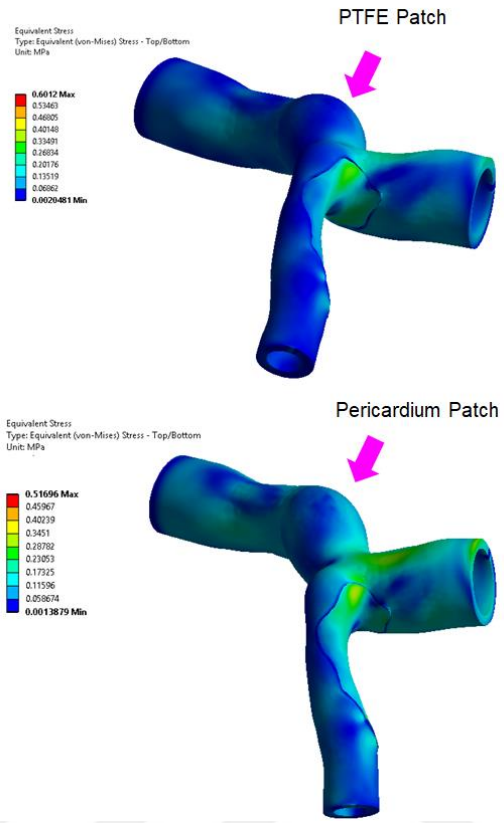

Figure 5.25 Von Mises Stress distributions for PTFE and pericardium patches on the same pulmonary artery model.

Despite the similarity of stress intervals, the occurrence of variable contour was compared with isoline visualization. When the upperside projection was examined, variable contours were observed on the PTFE patch (Figure 5.26).

Equivalent stress distributions were found on the cross-section, and when the patch was examined from the inside, significant stress contours were found on a larger area on the pericardium patch. However, the maximum stress values in the two did not exceed 0.6 MPa (Figure 5.27).

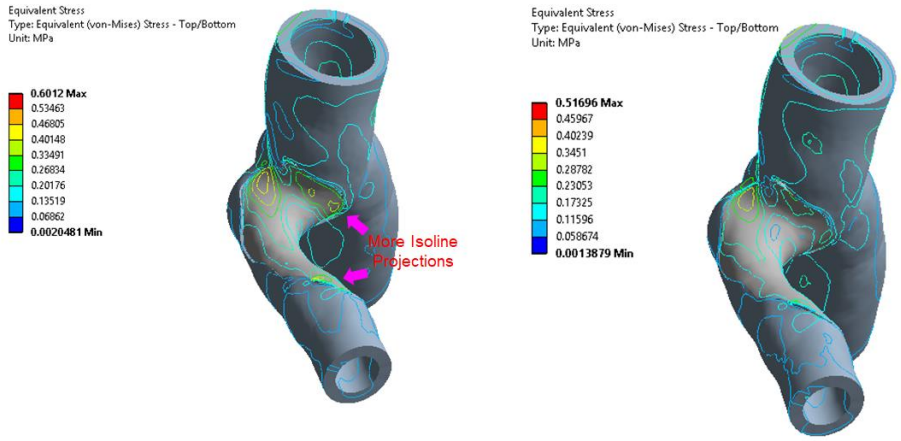

Figure 5.26 Von Mises Stress contour isoline projections for PTFE (left) and pericardium (right) patches on the same pulmonary artery model.

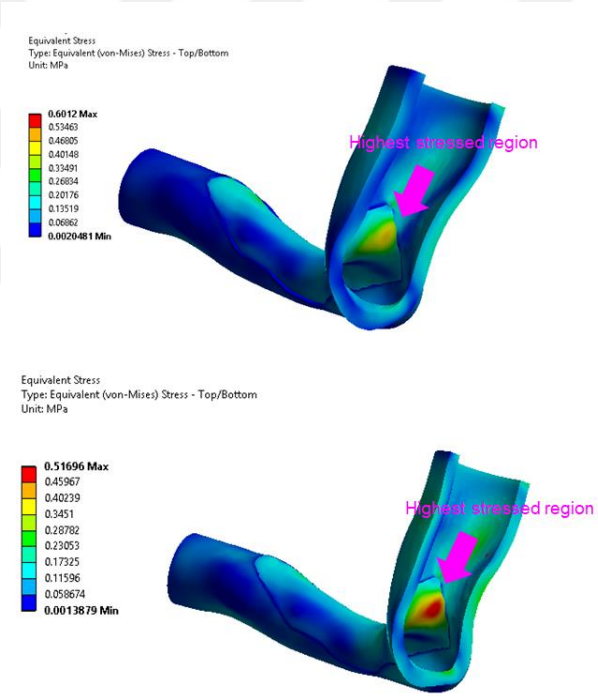

Figure 5.27 Von Mises Stress distributions for PTFE and pericardium patches in the cross-section.

As illustrated in the 'Pulmonary Section' figures above, the FEA performed to determine the deformed wall deformation by the effect of the pressure to be generated from inside to outside by blood flow was exported, and the obtained models were listed in Figure 5.28. The CFD analysis was performed for four different pulmonary artery models. WSS, flow lines, and pressure distributions were compared for the model with congenital stenosis, the model with virtual patch implantation, the

deformed PTFE patch by FEA, and the pericardium patch whose deformation was also defined.

In the structural analysis study, since the material properties of endothelium and patch were evaluated, their deformed models in the final could be exported with thickness information into the workbench. For this reason, the blood flow areas of the pulmonary artery models with exported vessel thickness were defined as new volumes and created with the help of CAD tools. The surfaces of these volumes were prepared for CFD analysis as a CAD object. As in the aorta coarctation study, entrance length and outlet extrusion operations were performed with ANSYS design Modeler, and the mesh was assigned for importing to the CFD solver.

The WSS distributions did not depict the same ranges for all four models. In the pre-op model, the decrease in WSS in the stenosis compartment was significant compared to the whole, while a similar decrease was observed on the PTFE patch.

This similarity was related to the fact that the same segment was pointed out as the critical point of the model (Figure 5.29).

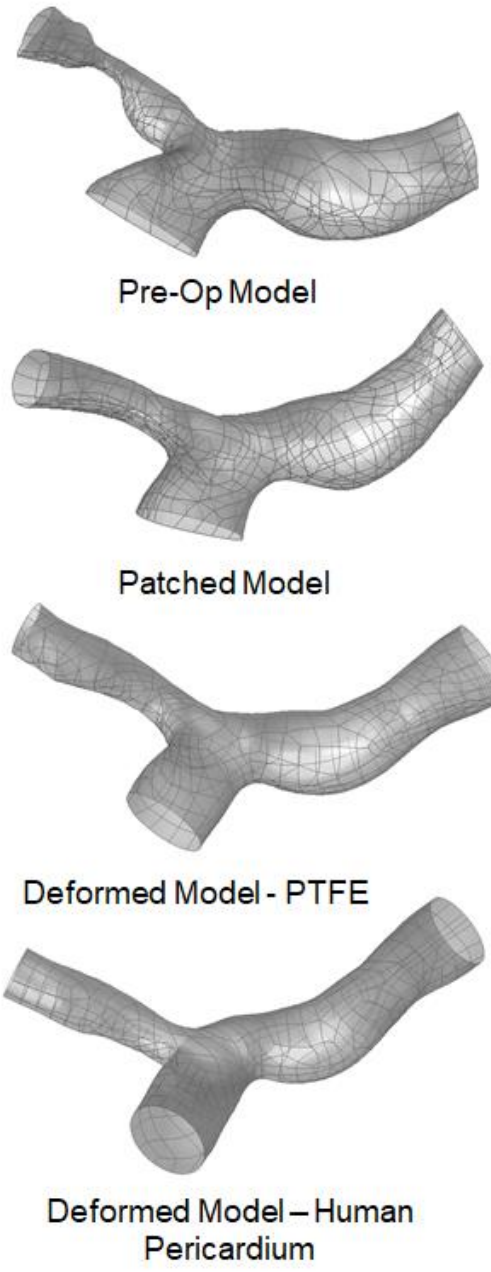

Figure 5.28 The final models (native, patched, deformed PTFE, and deformed pericardium) for CFD analysis.

When pre-op and virtual patch models were compared, low values were observed in the patch and adjacent artery, but it was considered acceptable because it showed gradual descents. This change was visualized with a more pronounced but acceptable change in the suture area on the pericardium patch.

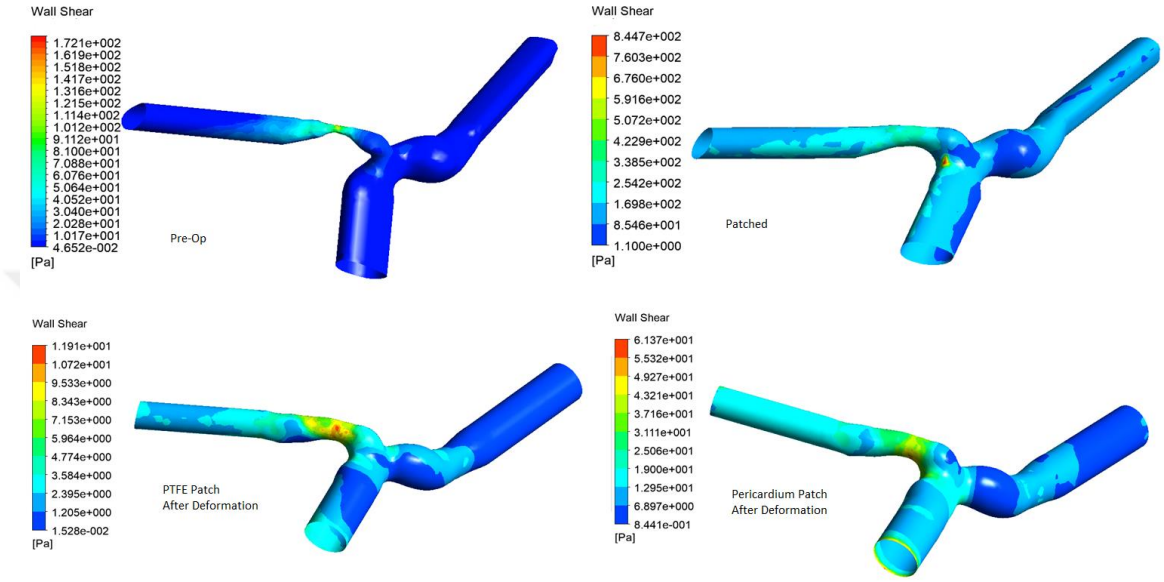

Figure 5.29 The WSS distributions of the native and virtual scenarios of the selected pulmonary artery coarctation.

When evaluated in terms of flow pathways, helical streamlines were observed in pre-op and virtual patch models, while smoother flow lines were observed in PTFE and pericardium patched arteries.

In both of these, a fast flow region was observed in the patch region, but no vortex was formed after this segment, and no large velocity differences were observed. The maximum velocity was 3.2 m/s in the pre-op model and 0.5 and 0.6, respectively, in PTFE and pericardium patched arteries (Figure 5.30).

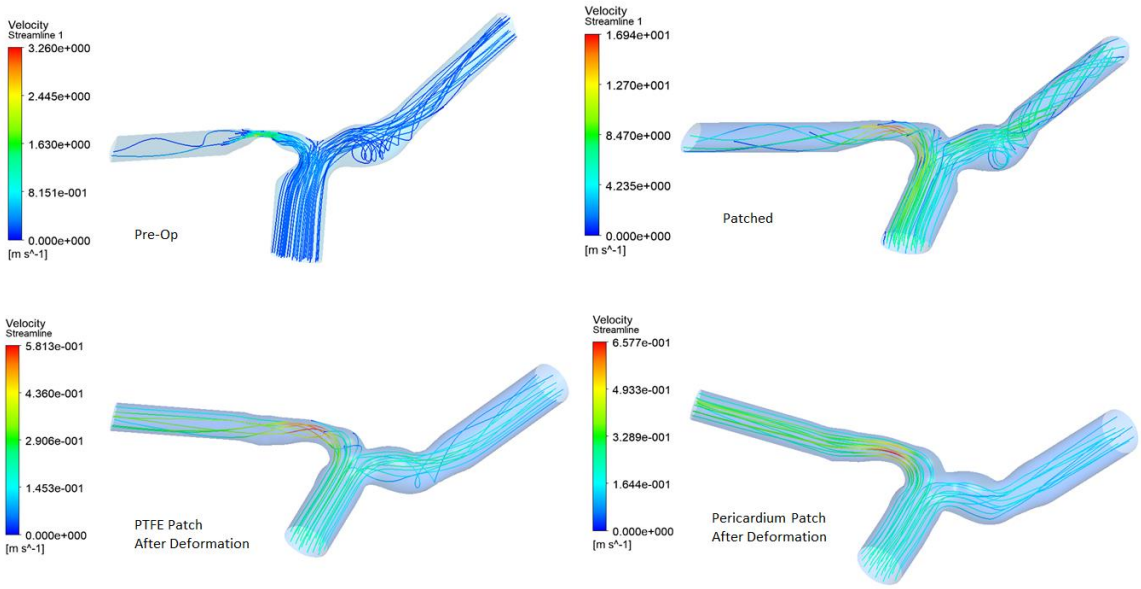

Figure 5.30 The velocity streamlines of the native and virtual scenarios of the selected pulmonary artery coarctation.

When pressure distributions were compared, the sharp difference in the stenosis artery was not seen in all other models. While the most uniform distribution was observed in the virtual patch model, contours showing similarities were observed in the deformed models (Figure 5.31).

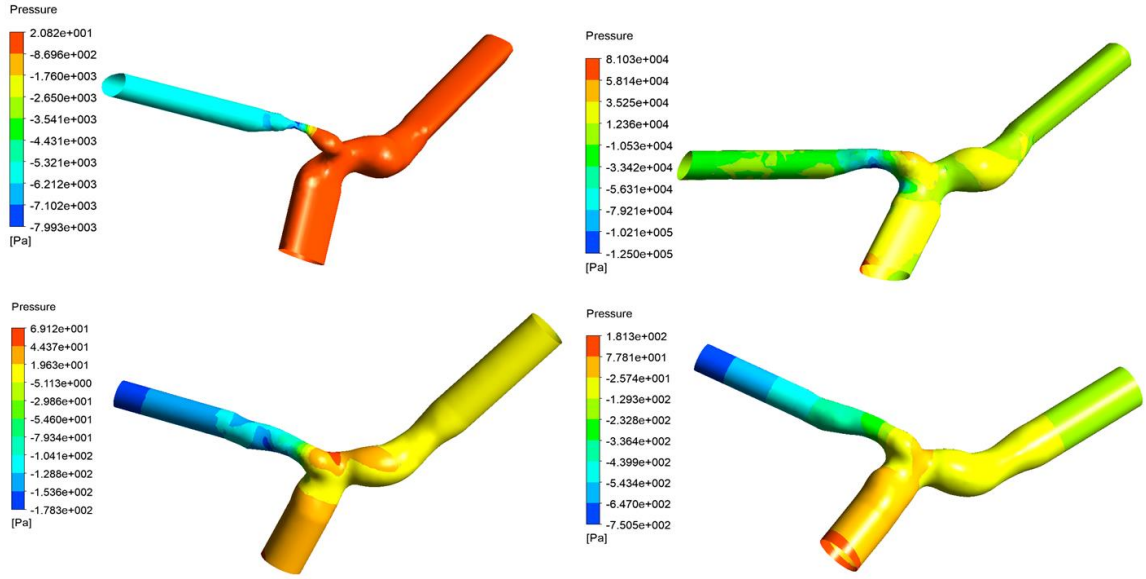

Figure 5.31 The pressure distributions of the native and virtual scenarios of the selected pulmonary artery coarctation.

5.3. Repair Planning for Fontan Patients

Various shunt configuration options are analyzed for each patient through multiple computational fluid dynamics simulations. The hepatic-to-azygous templates provided balanced hepatic flow distribution in both lungs. This configuration resulted in the most optimum performance level considering all hemodynamics parameters together at the selected configuration on the right-bottom at the case result chart figures.

1st Case:

The first case was an operated heart model. The patient was 14 years old. Nine configurations were designed for obtaining equal hepatic flow distribution to both lungs.

Seven intracardiac, two extracardiac, and one hepatic vein to azygous shunts were virtually implanted to the region of interest for Fontan last-stage circulation.

The optimal distribution (%38 to LPA and % 62 to RPA) was obtained with the extracardiac 12 mm shunt. The total flow was %55 to LPA and %45 to RPA at this configuration (Figure 5.9).

Patient A

Baffle type	D (mm)	IVC Offset (mm)	SVC Offset (mm)	Hepatic Flow Distribution (%)		Total Flow Distribution (%)		Power Loss (mW)
				Left	Right	Left	Right	
Intracardiac	6	-	-	5	95	65	35	53.7
Intracardiac	8	-	-	36	64	60	40	48.4
Intracardiac	10	-	-	55	45	69	31	32.8
Intracardiac	6	3.5 / Right	-	16	84	66	34	43.6
Intracardiac	6	3.5 / Left	-	100	0	62	38	44
Intracardiac	10	3.5 / Right	-	35	65	63	37	35.7
Intracardiac	8	-	7.5 / Left	13	87	43	57	70
Extracardiac	6	-	-	28	72	60	40	49.8
Extracardiac	12	-	-	38	62	55	45	48.9
Hepatic to Azygos	6	-	-	52	48	69	31	213.2

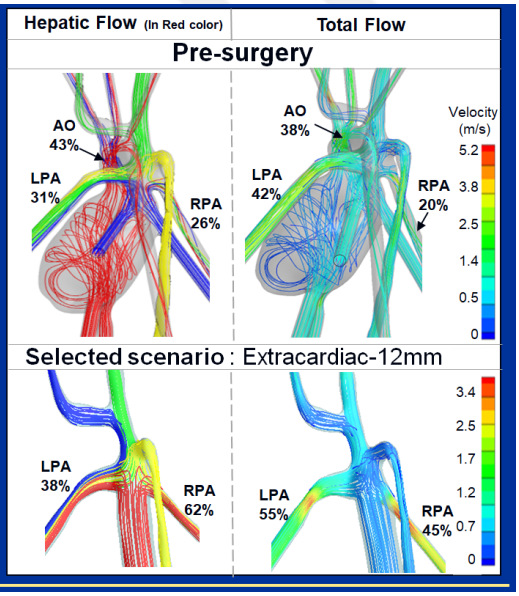

Figure 5.32 The first case of the Fontan configuration study.

2nd Case:

The second case was an operated heart model. The patient was nine years old (Figure 5.10).

Patient B

Baffle type	D (mm)	IVC Offset (mm)	SVC Offset (mm)	Hepatic Flow Distribution (%)		Total Flow Distribution (%)		Power Loss (mW)
				Left	Right	Left	Right	
Intracardiac	15	-	-	92	8	52	48	4.1
Intracardiac-flared	15	-	-	100	0	53	47	4.8
Extracardiac	15	10 / Right	-	15	85	51	49	4.8
Extracardiac	15	10 / Left	-	100	0	53	47	4.4
Hepatic to Azygos	15	-	-	20	80	53	47	13.1
Hepatic to Azygos	15		8 / Left	43	57	52	48	13.5
Hepatic to Azygos	15	-	16 / Left	35	65	52	48	15.1
Y-graft Hepatic to Azygos Hepatic to mid-PA	15 7.5 7.5	-	-	50	50	53	47	9.4
Y-graft Hepatic to LPA Hepatic to mid-PA	15 7.5 7.5	-	-	65	35	53	47	9.2

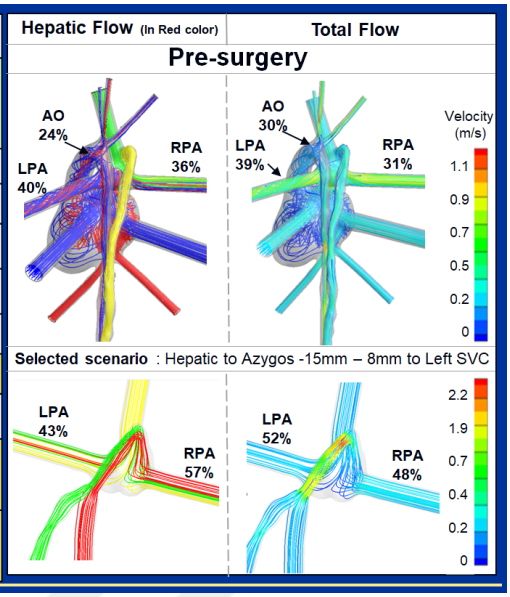

Figure 5.33 The second case of the Fontan configuration study.

The patient had Kawashima operation at the first stage of the repair procedure. Ten virtual baffle connection was designed to the base model. Two intracardiac, two Hepatic veins to Azygous, two 'Y' graft, and two extracardiac baffles were designed. The optimal Hepatic flow distribution was obtained with an intracardiac 15mm shunt (43% to LPA, 57% to RPA).

3rd Case:

The third case was from a patient who was three years old. Eleven virtual baffle models were designed. Five intracardiac, one extracardiac, two Hepatic veins to Azygous, and one 'Y' graft was designed. The optimal hepatic flow distribution was with a 15 mm extracardiac baffle (69% to LPA and 31% to RPA).

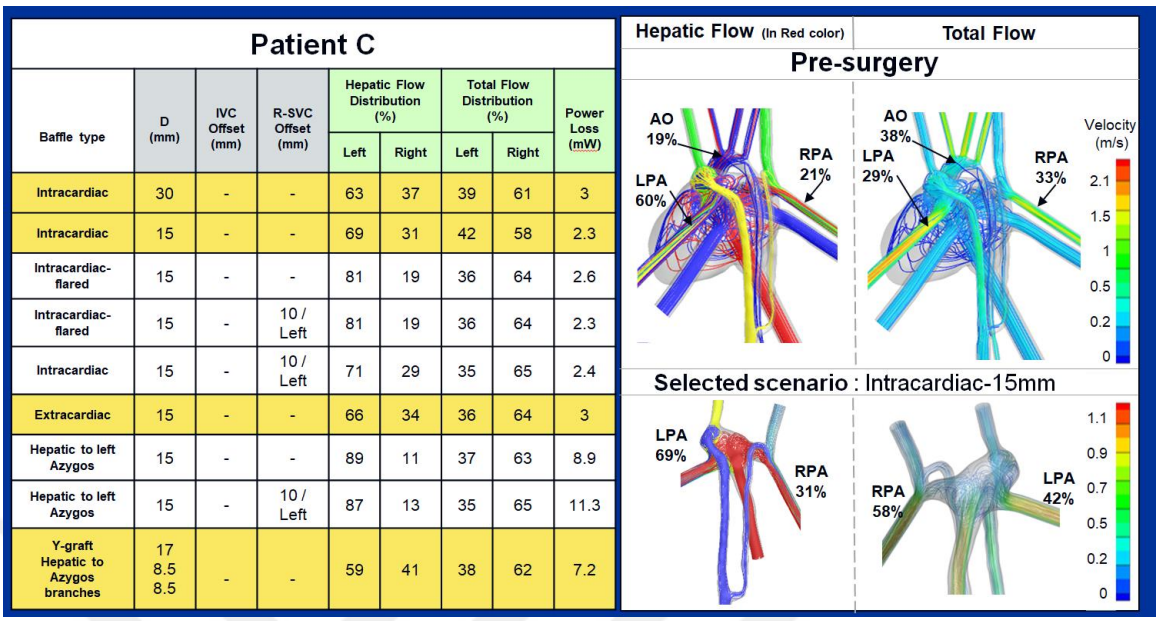

Figure 5.34 The third case of the Fontan configuration study.

CHAPTER 6

6. DISCUSSION

Enhancing patient-specific 3D models and numerical methods for cardiovascular mechanics in treatment planning is presented in this thesis, followed by a recounting of selected virtual repair methods on CHD cases. In closing, numerical structural and flow analysis with validated tools are performed, and the results are described.

If the thesis is examined through the main titles within the progress;

I. Intracardiac

Since the ‘Intracardiac’ planning section is based on an extensive database and can provide real-time clinical decision support, it is possible to provide meaningful information following the purpose. Thus, 3D visualization and CAD tools can be examined in various sizes and sections; both the clinician was provided with comprehensive and satisfactory information, and it could be very beneficial for the hospital team and the patient side. If necessary, detailed and meaningful information could be obtained about the region and its surroundings before the surgery or catheter intervention with the physical prototypes created. The outcomes of this section can be used for educational purposes in cardiology and cardiovascular surgery.

Above all, it was able to provide effective and helpful information in the process of planning for the determination of optimal intervention for the patient and was actively involved in the clinical routine.

II. Coarctation

In the 'Coarctation' cases, the surgical planning section, all of the selected cases with preoperative and postoperative image datasets and different anatomies were selected.

In this study, the steps of virtual operations were performed with the help of multiple image processing and CAD tools, and virtual artery profiles were created. A minimum of four separate models was created for each patient in the aortic coarctation section. As a result of the flow simulations, it was seen how the artery geometry affects the flow, and even with the different techniques, the differences in the same stenosis can occur. Thus, the importance of meticulously deciding the patient-specific method was seen. Blood flow and WSS distributions were found to provide essential data to predict future outcomes. In preoperative CFD studies, the patch repair method had the closest flow to the natural arch model. When the idealized virtual surgery model and post-op real data were evaluated together, it was found that the predicted data could show differences for pressure changes, although they were consistent in terms of flow. In the first case, acceptable velocity flow pathways were observed in the post-process results of 'resection and extended anastomosis' method and the results of virtual angioplasty. In the results of patch angioplasty geometry performed in the actual operation of the patient, excellent results were observed even though the flow lines were not as smooth as the virtual model. Dramatic WSS changes that may pose a risk of modelization on the endothelium in the pre-op model were not observed in virtual and real repair results.

For the second patient, the problematic flow behavior from the mid-arch was fixed, but the expected flow distribution was not observed in patch angioplasty. In VR2, the volume generated by anastomosis could not be utilized due to streamlining behavior. The preferable repair was VR1 formed by resection and extended anastomosis method. Although the results of the actual surgery were preferable in terms of speed, it was found to be unsuccessful in terms of WSS and pressure distribution compared to VR2.

In the third case, the results obtained in the virtual repairs were compared with the actual postoperative geometry analysis, and it was observed that there was not enough arch diameter, and post-op results showed preferable velocity distribution.

Since undesirable variable contours were observed in the WSS distribution, it was decided that more successful results could be obtained in a repair option in which diameter can be maintained smoothly. Another reason why post-op results were

preferable compared to stenosis in virtual models was that the volume and modelization also changed the results because the screening was performed when the patient was three years old.

In the fourth case, the results of the VR-1 model with resection and extended anastomosis for the fourth patient were preferable. The results of repair with end-to-end anastomosis were undesirable due to the high WSS segment on the arch and jet flow in the region. Post-op results were similar with VR-1, but the velocity reached 1.9 m / s.

In the fifth aortic case, the VR-1 model was found successful in terms of velocity, pressure and WSS distribution. Critical flow behaviors and possible effects of endothelial modelization risk were predicted in VR-2, including reverse subclavian flap repairs and real post-op results.

In general, it was observed by comparison with actual post-op samples that it would be more meaningful to create a patient-specific configuration that would provide optimum distribution of lumen morphology and flow distribution rather than creating a classical and ideal shape for the virtual repair of hypoplastic arches and isthmus coarctations.

During the virtual evaluation and comparison of the possible techniques, it was seen which method would be preferable in terms of future outcomes or a frame that could be formed with innovative approaches based on the performed repairs. Thus, it was found that it can offer the opportunity to reduce the conditions that cause common hypertension problems after coarctation repair.

In the pulmonary artery section of the surgical planning chapter, the soft tissue behavior against the mechanical load was analyzed, and the patency of the incision and the deformation of the wall with internal pressure after different patch aortoplasty were examined. Patches made with two different patches were compared. As with the aortic study, the difference between the geometries was compared with flow simulations.

In this study, instead of comparing only the pre-op and virtual repair methods, the models formed by the change of two different materials under pressure were also included in the evaluation. Thus, a virtual repair and material effect were compared, and the possibility to choose between two virtual materials for the sample was

created. Critical flow and pressure distribution in the stenotic segment were eliminated in all virtual models. When the PTFE and human pericardium patches were compared, the pericardium patch was found to be significant in terms of WSS and velocity distribution.

No significant difference was observed in pressure drop values. The virtual patch repair in the selected pulmonary artery contains an idealized result, showing preferable distributions, while the pericardium patch showed excellent results among the models obtained by structural analysis in which material differences were evaluated.

The effects of the incision, material, and artery shape under blood pressure were observed. It was seen that the incisions that can be applied in the same artery stenosis, their directions, and angles, the material of the patch to be used, would produce a separate result for each patient.

III. Fontan

In the Fontan section of the surgical planning chapter, the workflow was applied to three different patients by modeling the images obtained from MR data and creating new models on which various shunts were placed. This section aimed to distribute the growth factors from the hepatic veins equally to the right and left lungs. A minimum of nine configurations was designed for each patient, and flow simulations and distributions were examined. Instead of the models to be applied in the routine clinical procedure, the desired distribution was achieved in other models that were handled with the help of configurations. Another useful aspect of this method is that if the desired result is not achieved in the simulation model, a design that can provide or approach the correct distribution with the shunt (or shunts) can be created. It is possible to provide meaningful information with the available physiological and image data seen in all the examples, and also to report beneficial and meaningful results for the evaluation of different scenarios and materials.

Besides, the database, which was created with the data of real patients, was able to create a cumulation that could be useful in many retrospective studies as well as in this study.

Patient-specific virtual 3D modeling, virtual surgery applications, and numerical analysis simulations did not eliminate the difference between actual applications, but

the results were close. The difference was thought to be based on virtual models, which were idealized repairs, but the actual surgical applications were due to the surgeon's technical skills, patient tissues, and / or patch material changes over time. It was seen that idealized models were guided to predict the hemodynamic and structural outcomes of different surgical techniques for each patient and reported with concrete examples.

6.1. Conclusion

In the treatment of congenital heart diseases, 3D visualization provides a significant contribution to the pathologies of clinicians, operation team, engineers, patient/patient family, and in collaborations on producing solutions. Since anatomic modeling and virtual repair models do not only contribute significantly to surgical planning processes but also allow them to perform numerical hemodynamic and structural analyzes, they contribute to innovative studies to develop new methods and novel biomaterials.

Through this approach, which is compared with experimental tests with interdisciplinary studies, it will be possible to bring new standards to existing procedures and to work on education.

It was observed that the hemodynamic study was necessary for performing new surgical methods and for innovative biomaterials. Investigations of blood flow dynamics are useful to clarify the characteristics of vascular flow in detail, which were invisible to experimental measurements such as wall shear stress distributions.

It requires structural, physiological, pathophysiological, and mechanical evaluation of the circulatory system and its components for a comprehensive understanding of the expected functioning. As the importance of lately understood more, there is a significant role of arterial geometry as a risk and reason parameter for CHD.

This is because the idealized repair of virtual surgical techniques has been established, but the actual surgical applications, the material used, the technical skill of the surgeon, the change in the tissues of the patient over time are the results of this difference. However, idealized models are guiding in comparing different surgical techniques. It is foreseen that after this preliminary study, more realistic results can be obtained with more data and interdisciplinary cooperation.

In order to ensure the closeness of the results to the reality, additional expansions that require long term follow up and material (various tissue, suture line, and more patch) behavior are needed. After this preliminary study, it is predicted that more realistic results will be possible with more data and interdisciplinary (vascular science, fluid dynamics, material engineering) cooperation.

6.1.1. Limitation

A limited number of datasets were used, and only patients with postoperative images could be followed up. It will be possible to obtain more detailed and statistically significant data with a study in which the number of samples and post-op scanning data taken at regular intervals will be included in the evaluations, and the material and flow interaction are evaluated together.

6.1.2. Future Work

The design of devices such as stents, baffles, heart valves, ventricular assist devices, patches, and cannulas are very substantial in terms of producing innovative and customized solutions. Evaluating the material performances with long term predictions by using the contribution of numerical analysis, which is used to test and compare under various virtual scenarios.

6.1.3 Validation

In the treatment of complex and vital diseases, the decision-making process is essential, and the reliability of the methods used for this purpose should be in a way that can be clinically verified and reproducible in parallel.

If the findings obtained from the studies using numerical analyses are consistent with the clinical data, the numerical methods are validated. Verification of a computational method is defined as the assessment of numerical accuracy to which the method is implemented to a computer. During the planning of CHD treatments, the tools to be used for the treatment planning of actual clinical cases should also be made with tools previously approved in other studies.

In this case, the tools used must be corrected in themselves, and the results obtained through them must be validated.

In this study, preferred image processing, CAD, and numerical analysis tools are validated. Procedures performed using these tools were also performed using the information consistent with the clinical data of the selected cases and adhering to the preferred systematic in approved studies.

APPENDIX A

User Defined Function for Aortic Coarctation Section on CFD Solver

```
/* Velocity_zed_inlet_udf.c
/* Infant Aorta UDF, chop 30
//Pekkan Biofluids Lab
#include "udf.h"
#define PI 3.141592654
//Coefficients for Fourier Series Expansion for each time step//
#define	a1	3.827052
#define	b1	0.090536
#define	b1	0.090536
#define	c1	0.639621
#define	a2	2.594921
#define	b2	6.910614
#define	c2	2.572046
#define	a3	2.353114
#define	b3	40.284822
#define	c3	-1.182012
#define	a4	1.699405
#define	b4	33.368668
#define	c4	-2.232007
#define	a5	1.036934
#define	b5	47.740545
#define	c5	-0.281068
#define	c5	-0.281068
#define	a6	0.134085
```

```
#define		b6	61.313412
#define		c6	-0.709898
//
DEFINE_PROFILE(inlet_z_velocity, thread, position)
{
real z[ND_ND]; real r;
	//float x[3]; /*Position vector*/
//float y;
//float z;
//float yy;
face_t f;
begin_f_loop(f, thread)
{
//double t = (CURRENT_TIME*2-floor(CURRENT_TIME*2))/2; //t is the local time within each period
real t = RP_Get_Real("flow-time");
F_CENTROID(z,f,thread);
//y = x[1];
//z= x[2];
if(t<=0.005)
	F_PROFILE(f, thread, position)= 0;
else
if(t>0.005 && t<=0.44)
  F_PROFILE(f, thread, position)= a1*sin(b1*t+c1) + a2*sin(b2*t+c2) + a3*sin(b3*t+c3) +a4*sin(b4*t+c4) + a5*sin(b5*t+c5) + a6*sin(b6*t+c6);
else
	if(t>0.44 && t<=0.455 )
		F_PROFILE(f, thread, position)=0;
else
	if(t>0.455 && t<=0.89)
```

```
F_PROFILE(f, thread, position)= a1*sin(b1*(t-0.45)+c1) + a2*sin(b2*(t-0.45)+c2) +
a3*sin(b3*(t-0.45)+c3) +a4*sin(b4*(t-0.45)+c4) + a5*sin(b5*(t-0.45)+c5) +
a6*sin(b6*(t-0.45)+c6);
else
        if(t>0.89 && t<=1.34 )
                F_PROFILE(f, thread, position)=0;
else
        if(t>1.34 && t<=1.79)
F_PROFILE(f, thread, position)= a1*sin(b1*t+c1) + a2*sin(b2*t+c2) +
a3*sin(b3*t+c3) +a4*sin(b4*t+c4) + a5*sin(b5*t+c5) + a6*sin(b6*t+c6);
else
        if(t>1.79 && t<=2.25 )
                F_PROFILE(f, thread, position)=0;
else
        if(t>2.25 && t<=2.7)
F_PROFILE(f, thread, position)= a1*sin(b1*t+c1) + a2*sin(b2*t+c2) +
a3*sin(b3*t+c3) +a4*sin(b4*t+c4) + a5*sin(b5*t+c5) + a6*sin(b6*t+c6);
}
end_f_loop(f, thread)
}
// end
```

APPENDIX B

User Defined Function for Fontan Section on CFD Solver

```
/* Resistance_PatientC_udf.c
/* Infant Fontan Resistance UDF,
//Pekkan Biofluids Lab
#include "udf.h"

#define R_LPA 31.501338e6
#define R_RPA 31.501338e6

#define A_RPA         11.811e-06
#define A_LPA         25.627-06

#define rhoBlood 1060
#define Pa    798 //6mmhg

//RPA
DEFINE_PROFILE(RBC_RPA, t, position)
{
 face_t f;
 real Q;
 real Ps;
 real A;
 real R;

/* initialize variables*/
```

```
 Q = 0.0;
 Ps = 0.0;
 A = A_RPA;
 R = R_RPA;

/*calculate the flow rate at the outlet*/
 begin_f_loop(f,t)
  {
   Q += F_FLUX(f,t)/F_R(f,t);
  }
 end_f_loop(f,t)

/* assign this pressure to all outlet faces */
 Ps = Q*R + Pa - 0.5*rhoBlood*Q*Q/(A*A);

 begin_f_loop(f,t)
  {
   F_PROFILE(f,t,position) = Ps;
  }
 end_f_loop(f,t)
}

//LPA
DEFINE_PROFILE(RBC_LPA, t, position)
{
 face_t f;
 real Q;
 real Ps;
 real A;
 real R;

/* initialize variables */
```

```
 Q = 0.0;
 Ps = 0.0;
 A = A_LPA;
 R = R_LPA;

/* calculate the flow rate at the outlet */
 begin_f_loop(f,t)
  {
   Q += F_FLUX(f,t)/F_R(f,t);
  }
 end_f_loop(f,t)

/* assign this pressure to all outlet faces */
 Ps = Q*R + Pa - 0.5*rhoBlood*Q*Q/(A*A);

 begin_f_loop(f,t)
  {
   F_PROFILE(f,t,position) = Ps;
  }
 end_f_loop(f,t)
}
//end
```

BIBLIOGRAPHY

[1] S. Phillips and M. Pirics, “Congenital Heart Disease and Reproductive Risk: An Overview for Obstetricians, Cardiologists, and Primary Care Providers,” *Methodist Debakey Cardiovasc. J.*, vol. 13, no. 4, pp. 238–242, 2017.

[2] S. Jacobs, R. Grunert, F. W. Mohr, and V. Falk, “3D-Imaging of cardiac structures using 3D heart models for planning in heart surgery: a preliminary study,” *Interact. Cardiovasc. Thorac. Surg.*, vol. 7, no. 1, pp. 6–9, 2008.

[3] D. A. De Zélicourt, K. Pekkan, J. Parks, K. Kanter, M. Fogel, and A. P. Yoganathan, “Flow study of an extracardiac connection with persistent left superior vena cava,” *J. Thorac. Cardiovasc. Surg.*, vol. 131, no. 4, pp. 785–791, 2006.

[4] L. Chai, J. Ding, and Y. Liu, “Hemodynamics simulation of patient-specific surgical planning for tetralogy of fallot,” *Proc. - 2010 3rd Int. Conf. Biomed. Eng. Informatics, BMEI 2010*, vol. 1, no. Bmei, pp. 294–297, 2010.

[5] P. B. Dydynski, C. Kiper, D. Kozik, B. B. Keller, E. Austin, and B. Holland, “Three-Dimensional Reconstruction of Intracardiac Anatomy Using CTA and Surgical Planning for Double Outlet Right Ventricle: Early Experience at a Tertiary Care Congenital Heart Center,” *World J. Pediatr. Congenit. Heart Surg.*, vol. 7, no. 4, pp. 467–474, 2016.

[6] S. Garekar *et al.*, “Clinical Application and Multidisciplinary Assessment of Three Dimensional Printing in Double Outlet Right Ventricle With Remote Ventricular Septal Defect,” *World J. Pediatr. Congenit. Heart Surg.*, vol. 7, no. 3, pp. 344–350, 2016.

[7] I. Y. Hands, “3D Models for Decision Making in Congenital Heart Disease Disclosures • Glen Van Arsdell.”

[8] K. S. Sundareswaran *et al.*, “Visualization of flow structures in Fontan patients using 3-dimensional phase contrast magnetic resonance imaging,” *J. Thorac. Cardiovasc. Surg.*, vol. 143, no. 5, pp. 1108–1116, May 2012.

[9] J. Charton, M. Laurentjoye, and Y. Kim, “3D Boolean operations in virtual surgical planning,” *Int. J. Comput. Assist. Radiol. Surg.*, vol. 12, no. 10, pp. 1697–1709, 2017.

[10] A. Hosny *et al.*, “Pre-procedural fit-testing of TAVR valves using parametric modeling and 3D printing,” *J. Cardiovasc. Comput. Tomogr.*, no. June, pp. 0–1, 2018.

[11] L. A. R. Ve *et al.*, “Hemodinamik izlem,” pp. 1–50.

[12] P. G. Albal, P. G. Menon, W. Kowalski, A. Undar, R. Turkoz, and K. Pekkan, “Novel Fenestration Designs for Controlled Venous Flow Shunting in Failing Fontans With

Systemic Venous Hypertension," *Artif. Organs*, vol. 37, no. 1, pp. 66–75, Jan. 2013.

[13] C.-Y. Chen, R. Antón, M. Hung, P. Menon, E. A. Finol, and K. Pekkan, "Effects of Intraluminal Thrombus on Patient-Specific Abdominal Aortic Aneurysm Hemodynamics via Stereoscopic Particle Image Velocity and Computational Fluid Dynamics Modeling," *J. Biomech. Eng.*, vol. 136, no. 3, p. 031001, Feb. 2014.

[14] B. T. Chan, E. Lim, K. H. Chee, and N. A. Abu Osman, "Review on CFD simulation in heart with dilated cardiomyopathy and myocardial infarction," *Comput. Biol. Med.*, vol. 43, no. 4, pp. 377–385, 2013.

[15] S. N. Doost, D. Ghista, B. Su, L. Zhong, and Y. S. Morsi, "Heart blood flow simulation: A perspective review," *Biomed. Eng. Online*, vol. 15, no. 1, pp. 1–28, 2016.

[16] D. P. Zipes, P. Libby, R. O. Bonow, D. L. Mann, G. F. Tomaselli, and E. Braunwald, *Braunwald's heart disease : a textbook of cardiovascular medicine*. .

[17] N. Riaz, S. L. Wolden, D. Y. Gelblum, and J. Eric, "Heart Failure in Pediatric Patients with Congenital Heart Disease," vol. 118, no. 24, pp. 6072–6078, 2016.

[18] I. Lau and Z. Sun, "Three-dimensional printing in congenital heart disease: A systematic review," *J. Med. Radiat. Sci.*, vol. 65, no. 3, pp. 226–236, 2018.

[19] G. Biglino *et al.*, "Piloting the Use of Patient-Specific Cardiac Models as a Novel Tool to Facilitate Communication During Cinical Consultations," *Pediatr. Cardiol.*, vol. 38, no. 4, 2017.

[20] K. M. Farooqi, *Rapid Prototyping in Cardiac Disease*. 2017.

[21] C. A. Taylor and C. A. Figueroa, "Patient-Specific Modeling of Cardiovascular Mechanics," *Annu. Rev. Biomed. Eng.*, vol. 11, no. 1, pp. 109–134, 2009.

[22] B. J. Ballermann, A. Dardik, E. Eng, and A. Liu, "Shear stress and the endothelium," *Kidney Int.*, vol. 54, pp. S100–S108, 1998.

[23] M. Krafczyk, M. Cerrolaza, M. Schulz, and E. Rank, "Analysis of 3D transient blood flow passing through an artificial aortic valve by Lattice-Boltzmann methods," *J. Biomech.*, vol. 31, no. 5, pp. 453–462, 1998.

[24] K. M. Tse, P. Chiu, H. P. Lee, and P. Ho, "Investigation of hemodynamics in the development of dissecting aneurysm within patient-specific dissecting aneurismal aortas using computational fluid dynamics (CFD) simulations," *J. Biomech.*, vol. 44, no. 5, pp. 827–836, 2011.

[25] R. Gerrah, S. J. Haller, and I. George, "Mechanical Concepts Applied in Congenital Heart Disease and Cardiac Surgery," *Ann. Thorac. Surg.*, vol. 103, no. 6, pp. 2005–2014, 2017.

[26] D. Shav, R. Gotlieb, U. Zaretsky, D. Elad, and S. Einav, "Wall shear stress effects on endothelial-endothelial and endothelial-smooth muscle cell interactions in tissue engineered models of the vascular wall.," *PLoS One*, vol. 9, no. 2, p. e88304, 2014.

[27] Q. Sun *et al.*, "Numerical simulation of a bidirectional cavopulmonary anastomosis connection with antegrade pulmonary blood flow," *IFMBE Proc.*, vol. 19 IFMBE, pp.

139–142, 2008.

[28] Q. Sun, D. Wan, J. Liu, H. Hong, Y. Liu, and M. Zhu, “Patient-specific computational fluid dynamic simulation of a bilateral bidirectional Glenn connection,” *Med. Biol. Eng. Comput.*, vol. 46, no. 11, pp. 1153–1159, 2008.

[29] S. Piskin, G. Unal, A. Arnaz, T. Sarioglu, and K. Pekkan, “Tetralogy of Fallot Surgical Repair: Shunt Configurations, Ductus Arteriosus and the Circle of Willis,” *Cardiovasc. Eng. Technol.*, vol. 8, no. 2, pp. 107–119, Jun. 2017.

[30] S. S. Lashkarinia, S. Piskin, T. A. Bozkaya, E. Salihoglu, C. Yerebakan, and K. Pekkan, “Computational Pre-surgical Planning of Arterial Patch Reconstruction: Parametric Limits and In Vitro Validation,” *Ann. Biomed. Eng.*, May 2018.

[31] H. M. Snow, F. Markos, D. O’Regan, and K. Pollock, “Characteristics of arterial wall shear stress which cause endothelium-dependent vasodilatation in the anaesthetized dog.,” *J. Physiol.*, vol. 531, no. Pt 3, pp. 843–8, Mar. 2001.

[32] Z.-Y. Li, V. Taviani, T. Tang, M. P. F. Sutcliffe, and J. H. Gillard, “The Hemodynamic Effects of In-Tandem Carotid Artery Stenosis: Implications for Carotid Endarterectomy,” *J. Stroke Cerebrovasc. Dis.*, vol. 19, no. 2, pp. 138–145, Mar. 2010.

[33] I. Chatziprodromou, A. Tricoli, D. Poulikakos, and Y. Ventikos, “Haemodynamics and wall remodelling of a growing cerebral aneurysm: A computational model,” *J. Biomech.*, vol. 40, no. 2, pp. 412–426, 2007.

[34] A. K. Politis, G. P. Stavropoulos, M. N. Christolis, P. G. Panagopoulos, N. S. Vlachos, and N. C. Markatos, “Numerical modelling of simulated blood flow in idealized composite arterial coronary grafts: Transient flow,” *J. Biomech.*, vol. 41, no. 1, pp. 25–39, 2008.

[35] A. Polanczyk, M. Podyma, L. Stefanczyk, and I. Zbicinski, “Effects of stent-graft geometry and blood hematocrit on hemodynamic in abdominal aortic aneurysm,” *Chem. Process Eng. - Inz. Chem. i Proces.*, vol. 33, no. 1, pp. 53–61, 2012.

[36] Z. Keshavarz-Motamed, J. Garcia, and L. Kadem, “Fluid Dynamics of Coarctation of the Aorta and Effect of Bicuspid Aortic Valve,” *PLoS One*, vol. 8, no. 8, p. e72394, Aug. 2013.

[37] E. Karabelas *et al.*, “Towards a Computational Framework for Modeling the Impact of Aortic Coarctations Upon Left Ventricular Load,” *Front. Physiol.*, vol. 9, p. 538, May 2018.

[38] S. Piskin, H. F. Altin, O. Yildiz, I. Bakir, and K. Pekkan, “Hemodynamics of patient-specific aorta-pulmonary shunt configurations,” *J. Biomech.*, vol. 50, pp. 166–171, 2017.

[39] M. F. Brioschi, “Numerical methods for cardiovascular problems : computational electrocardiology and fluid dynamics in moving domains,” 2010.

[40] J. R. Nanduri, F. A. Pino-Romainville, and I. Celik, “CFD mesh generation for biological flows: Geometry reconstruction using diagnostic images,” *Comput. Fluids*, vol. 38, no. 5, pp. 1026–1032, 2009.

[41] F. Sulejmani, A. Pokutta-Paskaleva, O. Salazar, M. Karimi, and W. Sun, “Mechanical and structural analysis of the pulmonary valve in congenital heart defects: A presentation of two case studies,” *J. Mech. Behav. Biomed. Mater.*, vol. 89, no. August 2018, pp. 9–12, 2019.

[42] M. S. Sacks and A. P. Yoganathan, “Heart valve function: A biomechanical perspective,” *Philos. Trans. R. Soc. B Biol. Sci.*, vol. 362, no. 1484, pp. 1369–1391, 2007.

[43] Y. Shi, “Numerical simulation of global hydro-dynamics in a pulsatile bioreactor for cardiovascular tissue engineering,” *J. Biomech.*, vol. 41, no. 5, pp. 953–959, 2008.

[44] M. C. Monge, R. D. Mainwaring, A. Y. Sheikh, R. Punn, V. M. Reddy, and F. L. Hanley, “Surgical reconstruction of peripheral pulmonary artery stenosis in Williams and Alagille syndromes,” *J. Thorac. Cardiovasc. Surg.*, vol. 145, no. 2, pp. 476–481, 2013.

[45] C. D. Malone, T. H. Urbania, S. E. S. Crook, and M. D. Hope, “Bovine aortic arch: A novel association with thoracic aortic dilation,” *Clin. Radiol.*, vol. 67, no. 1, pp. 28–31, 2012.

[46] D. A. De Zélicourt *et al.*, “Individualized computer-based surgical planning to address pulmonary arteriovenous malformations in patients with a single ventricle with an interrupted inferior vena cava and azygous continuation,” *J. Thorac. Cardiovasc. Surg.*, vol. 141, no. 5, pp. 1170–1177, 2011.

[47] F. Kabirian, B. Ditkowski, A. Zamanian, R. Heying, and M. Mozafari, “An innovative approach towards 3D-printed scaffolds for the next generation of tissue-engineered vascular grafts,” *Mater. Today Proc.*, vol. 5, no. 7, pp. 15586–15594, 2018.

[48] A. Polańczyk, “Simulation of blood flow through endovascular prosthesis in patients with Abdominal Aortic Aneurysm,” *Chps.Fsid.Cvut.Cz*.

[49] K. Tappa and U. Jammalamadaka, “Novel Biomaterials Used in Medical 3D Printing Techniques.,” *J. Funct. Biomater.*, vol. 9, no. 1, Feb. 2018.

[50] G. Zhu, M. B. Ismail, M. Nakao, Q. Yuan, and J. H. Yeo, “Numerical and in-vitro experimental assessment of the performance of a novel designed expanded-polytetrafluoroethylene stentless bi-leaflet valve for aortic valve replacement,” *PLoS One*, vol. 14, no. 1, pp. 1–28, 2019.

[51] P. Olejník *et al.*, “Utilisation of three-dimensional printed heart models for operative planning of complex congenital heart defects,” *Kardiol. Pol.*, vol. 75, no. 5, pp. 495–501, 2017.

[52] J. Brown, M. Ruzmetov, P. Vijay, and M. W. Turrentine, “Surgical repair of congenital supravalvular aortic stenosis in children,” *Eur. J. Cardio-Thoracic Surg.*, vol. 21, no. 1, pp. 50–56, Jan. 2002.

[53] R. H. (Robert H. Anderson, *Paediatric cardiology*. Churchill Livingstone/Elsevier, 2010.

[54] C. W. Baird, P. O. Myers, and P. J. del Nido, “Aortic Valve Reconstruction in the Young Infants and Children,” *Semin. Thorac. Cardiovasc. Surg. Pediatr. Card. Surg.*

Annu., vol. 15, no. 1, pp. 9–19, 2012.

[55] J. M. Raul Cayre, *Congenital Heart Diseases*. NEwYork: Nova Biomedical, 2019.

[56] M. S. Mohamed, M. M. Rabeea, H. Saad, A. Saif, and S. Hammad, "Assessment of Renal Functions in Infants and Children with Congenital Heart Diseases," vol. 74, no. January, pp. 219–225, 2019.

[57] K. M. Farooqi *et al.*, "Application of Virtual Three-Dimensional Models for Simultaneous Visualization of Intracardiac Anatomic Relationships in Double Outlet Right Ventricle," *Pediatr. Cardiol.*, vol. 37, no. 1, pp. 90–98, 2016.

[58] G. Grabner, R. Modritsch, W. Stiegmaier, S. Grasser, and T. Klinger, "Aorta cross-section calculation and 3D visualization from CT or MRT data using VRML," vol. 5744, p. 731, 2005.

[59] K. M. Farooqi *et al.*, "Application of Virtual Three-Dimensional Models for Simultaneous Visualization of Intracardiac Anatomic Relationships in Double Outlet Right Ventricle," *Pediatr. Cardiol.*, vol. 37, no. 1, pp. 90–98, 2016.

[60] L. J. Olivieri *et al.*, "Novel, 3D Display of Heart Models in the Postoperative Care Setting Improves CICU Caregiver Confidence," *World J. Pediatr. Congenit. Heart Surg.*, vol. 9, no. 2, 2018.

[61] W. R. T. Witschey *et al.*, "Three-Dimensional Ultrasound-Derived Physical Mitral Valve Modeling," *Ann. Thorac. Surg.*, vol. 98, no. 2, pp. 691–694, Aug. 2014.

[62] A. A. Giannopoulos *et al.*, "3D printed ventricular septal defect patch : a primer for the 2015 Radiological Society of North America (RSNA) hands-on course in 3D printing," *3D Print. Med.*, vol. 1, no. 3, pp. 1–20, 2015.

[63] K. S. Sundareswaran *et al.*, "Correction of Pulmonary Arteriovenous Malformation Using Image-Based Surgical Planning," *JACC Cardiovasc. Imaging*, vol. 2, no. 8, pp. 1024–1030, 2009.

[64] F. Migliavacca *et al.*, "Computational model of the fluid dynamics in systemic-to-pulmonary shunts.," *J. Biomech.*, vol. 33, no. 5, pp. 549–57, 2000.

[65] F. Migliavacca and G. Dubini, "Computational modeling of vascular anastomoses," *Biomech. Model. Mechanobiol.*, vol. 3, no. 4, pp. 235–250, 2005.

[66] M. A. Fogel, R. H. Khiabani, and A. Yoganathan, "Imaging for preintervention planning pre- and post-fontan procedures," *Circ. Cardiovasc. Imaging*, vol. 6, no. 6, pp. 1092–1101, 2013.

[67] U. Morbiducci *et al.*, "Blood damage safety of prosthetic heart valves. Shear-induced platelet activation and local flow dynamics: A fluid-structure interaction approach," *J. Biomech.*, vol. 42, no. 12, pp. 1952–1960, 2009.

[68] V. O. Kheyfets *et al.*, "Patient-specific computational modeling of blood flow in the pulmonary arterial circulation," *Comput. Methods Programs Biomed.*, vol. 120, no. 2, pp. 88–101, 2015.

[69] S. S. Khalafvand, E. Y. K. Ng, L. Zhong, and T. K. Hung, "Fluid-dynamics modelling

of the human left ventricle with dynamic mesh for normal and myocardial infarction: Preliminary study," *Comput. Biol. Med.*, vol. 42, no. 8, pp. 863–870, 2012.

[70] S. Piskin, A. Ündar, and K. Pekkan, "Computational Modeling of Neonatal Cardiopulmonary Bypass Hemodynamics With Full Circle of Willis Anatomy," *Artif. Organs*, vol. 39, no. 10, pp. E164–E175, Oct. 2015.

[71] H. Hong, O. Dur, H. Zhang, Z. Zhu, K. Pekkan, and J. Liu, "Fontan Conversion Templates: Patient-Specific Hemodynamic Performance of the Lateral Tunnel Versus the Intraatrial Conduit With Fenestration," *Pediatr. Cardiol.*, vol. 34, no. 6, pp. 1447–1454, Aug. 2013.

[72] J. Muhammad *et al.*, "Patient-Specific Atrial Hemodynamics of a Double Lumen Neonatal Cannula in Correct Caval Position.," *Artif. Organs*, vol. 42, no. 4, pp. 401–409, Apr. 2018.

[73] M. Neidlin *et al.*, "Hemodynamic analysis of outflow grafting positions of a ventricular assist device using closed-loop multiscale CFD simulations: Preliminary results," *J. Biomech.*, vol. 49, no. 13, pp. 2718–2725, Sep. 2016.

[74] M. Nobili *et al.*, "Numerical simulation of the dynamics of a bileaflet prosthetic heart valve using a fluid-structure interaction approach," *J. Biomech.*, vol. 41, no. 11, pp. 2539–2550, 2008.

[75] N. H. Mokhtar, A. Abas, N. A. Razak, M. N. A. Hamid, and S. L. Teong, "Effect of different stent configurations using Lattice Boltzmann method and particles image velocimetry on artery bifurcation aneurysm problem," *J. Theor. Biol.*, vol. 433, pp. 73–84, 2017.

[76] L. Morris, F. Stefanov, and T. McGloughlin, "Stent graft performance in the treatment of abdominal aortic aneurysms: The influence of compliance and geometry," *J. Biomech.*, vol. 46, no. 2, pp. 383–395, 2013.

[77] K. Pekkan *et al.*, "In vitro validation of a self-driving aortic-turbine venous-assist device for Fontan patients.," *J. Thorac. Cardiovasc. Surg.*, vol. 156, no. 1, pp. 292-301.e7, Jul. 2018.

[78] K. Hadeed, Y. Dulac, and P. Acar, "Three-dimensional printing of a complex CHD to plan surgical repair," *Cardiol. Young*, vol. 26, no. 7, pp. 1432–1434, 2016.

[79] I. Valverde *et al.*, "Three-dimensional printed models for surgical planning of complex congenital heart defects: an international multicentre study," *Eur. J. Cardio-Thoracic Surg.*, vol. 52, no. 6, pp. 1139–1148, Dec. 2017.

[80] A. M. Noecker *et al.*, "Development of patient-specific three-dimensional pediatric cardiac models," *ASAIO J.*, vol. 52, no. 3, pp. 349–353, 2006.

[81] "Current Vascular Surgery : 2012." [Online]. Available: http://021075y4p.y.http.eds.b.ebscohost.com.proxy.medipol.deep-knowledge.net:9797/eds/ebookviewer/ebook?sid=abbb1183-a0bb-4f6f-9a3a-fe9580507022%40sessionmgr104&vid=0&format=EB. [Accessed: 14-May-2019].

[82] I. Valverde *et al.*, "3D printed cardiovascular models for surgical planning in complex congenital heart diseases," *J. Cardiovasc. Magn. Reson.*, vol. 17, no. Suppl 1, p. P196,

2015.

[83] A. A. Giannopoulos *et al.*, “Cardiothoracic applications of 3-dimensional printing,” *Journal of Thoracic Imaging*, vol. 31, no. 5. 2016.

[84] A. . Fallis, *Applied Biofluid Mechanics*, vol. 53, no. 9. 2013.

[85] L. Formaggia, A. Quarteroni, and A. Veneziani, *Cardiovascular Mathematics: Modeling and simulation of the circulatory system*. 2009.

[86] *Paediatric Cardiology*. Elsevier, 2010.

[87] C. E. Rex *et al.*, “Surgical closure of a ventricular septal defect in early childhood leads to altered pulmonary function in adulthood: A long-term follow-up,” *Int. J. Cardiol.*

[88] M. A. Nørgaard, N. Alphonso, A. D. Cochrane, S. Menahem, C. P. Brizard, and Y. d’Udekem, “Major aorto-pulmonary collateral arteries of patients with pulmonary atresia and ventricular septal defect are dilated bronchial arteries,” *Eur. J. Cardio-thoracic Surg.*, vol. 29, no. 5, pp. 653–658, 2006.

[89] Y. Ling, Y. Wang, Q. Fan, and Y. Qian, “Combined perventricular closure of ventricular septal defect and atrial septal defect via lower ministernotomy,” *J. Cardiothorac. Surg.*

[90] H. Nashat *et al.*, “Atrial septal defects and pulmonary arterial hypertension,” *J. Thorac. Dis.*, vol. 10, no. 4, pp. S2953–S2965, 2018.

[91] G. R. Martin, *Paediatric cardiology census*. 2011.

[92] W. K. Park *et al.*, “Revisitation of Double Inlet Left Ventricle or Tricuspid Atresia with Transposed Great Arteries,” *Ann. Thorac. Surg.*

[93] J. Geiger *et al.*, “Postoperative pulmonary and aortic 3D haemodynamics in patients after repair of transposition of the great arteries,” *Eur. Radiol.*, vol. 24, no. 1, pp. 200–208, 2014.

[94] J. K. Perloff and A. J. Marelli, *Perloff’s clinical recognition of congenital heart disease*. Elsevier/Saunders, 2012.

[95] K. M. Farooqi, C. G. Lengua, A. D. Weinberg, J. C. Nielsen, and J. Sanz, “Blood Pool Segmentation Results in Superior Virtual Cardiac Models than Myocardial Segmentation for 3D Printing,” *Pediatr. Cardiol.*, vol. 37, no. 6, pp. 1028–1036, 2016.

[96] S.-J. Yoo *et al.*, “3D printing in medicine of congenital heart diseases,” *3D Print. Med.*, vol. 2, no. 1, p. 3, 2015.

[97] C. Mandrycky, Z. Wang, K. Kim, and D.-H. Kim, “3D bioprinting for engineering complex tissues,” *Biotechnol. Adv.*, vol. 34, no. 4, pp. 422–434, Jul. 2016.

[98] L. M. Meier, M. Meineri, J. Qua Hiansen, and E. M. Horlick, “Structural and congenital heart disease interventions: The role of three-dimensional printing,” *Netherlands Heart Journal*, vol. 25, no. 2. 2017.

[99] Y.-H. Loke, A. S. Harahsheh, A. Krieger, and L. J. Olivieri, “Usage of 3D models of tetralogy of Fallot for medical education: impact on learning congenital heart disease.,”

BMC Med. Educ., vol. 17, no. 1, p. 54, 2017.

[100] E. K. Grant and L. J. Olivieri, "The Role of 3-D Heart Models in Planning and Executing Interventional Procedures," *Can. J. Cardiol.*, vol. 33, no. 9, pp. 1074–1081, 2017.

[101] D. Schmauss, S. Haeberle, C. Hagl, and R. Sodian, "Three-dimensional printing in cardiac surgery and interventional cardiology: A single-centre experience," *Eur. J. Cardio-thoracic Surg.*, vol. 47, no. 6, pp. 1044–1052, 2014.

[102] M. N. V. Forte *et al.*, "3D printed models in patients with coronary artery fistulae: Anatomical assessment and interventional planning," *EuroIntervention*, vol. 13, no. 9, 2017.

[103] B. P. Kottayil *et al.*, "Two-ventricle repair for complex congenital heart defects palliated towards single-ventricle repair," *Interact. Cardiovasc. Thorac. Surg.*, vol. 18, no. 3, pp. 266–271, 2014.

[104] M. Akhtar, M. Hamid, Anwar-Ul-Haq, F. Minai, and N. Rehman, "Feasibility and safety of on table extubation after corrective surgical repair of tetralogy of Fallot in a developing country: A case series," *Ann. Card. Anaesth.*, vol. 18, no. 2, p. 237, 2015.

[105] A. J. A. Leloup, C. E. Van Hove, S. De Moudt, G. R. Y. De Meyer, G. W. De Keulenaer, and P. Fransen, "Vascular smooth muscle cell contraction and relaxation in the isolated aorta: a critical regulator of large artery compliance," *Physiol. Rep.*, vol. 7, no. 4, pp. 1–13, 2019.

[106] A. Della Corte *et al.*, "Surgical treatment of bicuspid aortic valve disease: Knowledge gaps and research perspectives on behalf of the International Bicuspid Aortic Valve Consortium (BAVCon) Investigators," *J Thorac Cardiovasc Surg*, vol. 147, no. 6, pp. 1749–1757, 2014.

[107] C. K. O. (Author) Darling III, R. Clement (Author), "Master Techniques in Surgery: Vascular Surgery: Arterial Procedures." [Online]. Available: http://021075y4s.y.http.eds.b.ebscohost.com.proxy.medipol.deep-knowledge.net:9797/eds/ebookviewer/ebook?sid=faf8aa3c-3605-42d1-8208-be2aa4014ab9%40pdc-v-sessmgr03&vid=0&format=EK. [Accessed: 14-May-2019].

[108] Z. L. Ma *et al.*, "Coarctation of the Aorta with Aortic Arch Hypoplasia: Midterm Outcomes of Aortic Arch Reconstruction with Autologous Pulmonary Artery Patch," *Chin. Med. J. (Engl).*, vol. 130, no. 23, pp. 2802–2807, 2017.

[109] Q. Shang *et al.*, "Assessment of ventriculo-vascular properties in repaired coarctation using cardiac magnetic resonance-derived aortic, left atrial and left ventricular strain," *Eur. Radiol.*, vol. 27, no. 1, pp. 167–177, 2017.

[110] R. Crepaz, "Abnormalities of aortic arch shape after successful repair of aortic coarctation and systemic arterial hypertension," *J. Pediatr. Pediatr. Med.*, vol. 2, no. 1, pp. 34–36, 2018.

[111] S. Pagoulatou and N. Stergiopulos, "Evolution of aortic pressure during normal ageing: A model-based study," *PLoS One*, vol. 12, no. 7, pp. 1–14, 2017.

[112] P.-E. Séguéla *et al.*, "Toward the integration of global longitudinal strain analysis in

the assessment of neonatal aortic coarctation? A preliminary study," *Arch. Cardiovasc. Dis.*, vol. 111, no. 12, pp. 722–729, Dec. 2018.

[113] J. J. O'Sullivan, G. Derrick, and R. Darnell, "Prevalence of hypertension in children after early repair of coarctation of the aorta: A cohort study using casual and 24 hour blood pressure measurement," *Heart*, vol. 88, no. 2, pp. 163–166, 2002.

[114] D. Kenny *et al.*, "Surgical approach for aortic coarctation influences arterial compliance and blood pressure control," *Ann. Thorac. Surg.*, vol. 90, no. 2, pp. 600–604, 2010.

[115] G. Lewis, S. Thorne, P. Clift, and B. Holloway, "Cross-sectional imaging of the Fontan circuit in adult congenital heart disease," *Clin. Radiol.*, vol. 70, no. 6, pp. 667–675, 2015.

[116] J. P. Jacobs *et al.*, "The Society of Thoracic Surgeons Congenital Heart Surgery Database: 2019 Update on Outcomes and Quality," *Ann. Thorac. Surg.*

[117] M. A. Fogel, A. Hubbard, and P. M. Weinberg, "A simplified approach for assessment of intracardiac baffles and extracardiac conduits in congenital heart surgery with two- and three-dimensional magnetic resonance imaging," *Am. Heart J.*, vol. 142, no. 6, pp. 1028–1036, 2001.

[118] R. Ascuitto, N. Ross-Ascuitto, J. Wiesman, and S. DeLeon, "Bidirectional glenn shunt as an adjunct to surgical repair of congenital heart disease associated with pulmonary outflow obstruction: Relevance of the fluid pressure drop-flow relationship," *Pediatr. Cardiol.*, vol. 29, no. 5, pp. 910–917, 2008.

[119] C. M. Gonçalves, J. Noschang, A. C. B. da Silva, R. J. K. de Mello, S. J. Schuh, and A. C. Maciel, "Heterotaxy syndrome: a case report," *Radiol. Bras.*, vol. 47, no. 1, pp. 54–56, 2014.

[120] R. Frober, "Heterotaxy Syndrome: An Embryologic Study," *Ann. Clin. Lab. Res.*, vol. 4, no. 1, pp. 1–9, 2016.

[121] M. Yoshida *et al.*, "Total cavopulmonary connection in patients with apicocaval juxtaposition: optimal conduit route using preoperative angiogram and flow simulation†," *Eur. J. Cardio-Thoracic Surg.*, vol. 44, no. 1, pp. e46–e52, Jul. 2013.

[122] M. M. Samyn and J. F. Ladisa, "World ' s largest Science , Technology & Medicine Open Access book publisher Cardiovascular Magnetic Resonance Resonance Imaging-Based Imaging-Based Computational Computational Fluid Fluid Dynamics Modeling in Pediatric Cardiovascular and Dynamics Modelin."

[123] J. M. Kuijpers *et al.*, "Aortic dissection and prophylactic surgery in congenital heart disease," *Int. J. Cardiol.*

[124] E. Kocyildirim, S. Ozkan, D. Karadag, S. K. Kose, E. Ekici, and C. Ikizler, "Discrete supravalvular aortic stenosis in children: Is it necessary to reconstruct the whole aortic root?.," *Anadolu Kardiyol. Derg.*, vol. 9, no. 4, pp. 311–317, 2009.

[125] M. Hameed, "Closed-Loop CFD Analysis of the Fontan Cardiovascular Circulation," 2016.

[126] S. C. White, J. Sedler, T. W. Jones, and M. Seckeler, “Utility of three-dimensional models in resident education on simple and complex intracardiac congenital heart defects,” *Congenit. Heart Dis.*, Sep. 2018.

[127] P. F. Davies, “Hemodynamic shear stress and the endothelium in cardiovascular pathophysiology.,” *Nat. Clin. Pract. Cardiovasc. Med.*, vol. 6, no. 1, pp. 16–26, Jan. 2009.

[128] L. Boussel *et al.*, “Aneurysm growth occurs at region of low wall shear stress: Patient-specific correlation of hemodynamics and growth in a longitudinal study,” *Stroke*, vol. 39, no. 11, pp. 2997–3002, 2008.

[129] J. A. Pedersen, F. Boschetti, and M. A. Swartz, “Effects of extracellular fiber architecture on cell membrane shear stress in a 3D fibrous matrix,” *J. Biomech.*, vol. 40, no. 7, pp. 1484–1492, 2007.

[130] S. A. Kock *et al.*, “Mechanical stresses in carotid plaques using MRI-based fluid-structure interaction models,” *J. Biomech.*, vol. 41, no. 8, pp. 1651–1658, 2008.

[131] P. B. Bijari, B. A. Wasserman, and D. A. Steinman, “Carotid bifurcation geometry is an independent predictor of early wall thickening at the carotid bulb,” *Stroke*, vol. 45, no. 2, 2014.

[132] E. L. Bove *et al.*, “Use of mathematic modeling to compare and predict hemodynamic effects of the modified Blalock-Taussig and right ventricle-pulmonary artery shunts for hypoplastic left heart syndrome,” *J. Thorac. Cardiovasc. Surg.*, vol. 136, no. 2, 2008.

[133] D. de Zelicourt, K. Pekkan, H. Kitajima, D. Frakes, and A. P. Yoganathan, “Single-step stereolithography of complex anatomical models for optical flow measurements,” *J. Biomech. Eng. Asme*, vol. 127, no. 1, pp. 204–207, 2005.

[134] L. Gundelwein, J. Miró, F. G. Barlatay, C. Lapierre, K. Rohr, and L. Duong, “Personalized stent design for congenital heart defects using pulsatile blood flow simulations,” *J. Biomech.*

[135] F. Boschetti, M. T. Raimondi, F. Migliavacca, and G. Dubini, “Prediction of the micro-fluid dynamic environment imposed to three-dimensional engineered cell systems in bioreactors,” *J. Biomech.*, vol. 39, no. 3, pp. 418–425, 2006.

[136] M. Juhendaja and O. Märtens, “Kopsude 3D Visualiseerimine Ja Segmenteerimine Itk/Vtk/Qt Raamistikus,” 2017.

[137] P. Vcelak, M. Kryl, M. Kratochvil, and J. Kleckova, “Identification and classification of DICOM files with burned-in text content,” *Int. J. Med. Inform.*, vol. 126, no. January 2018, pp. 128–137, 2019.

[138] “3D Slicer.” [Online]. Available: https://www.slicer.org/. [Accessed: 26-Nov-2018].

[139] J. Vodiskar, M. Kütting, U. Steinseifer, J. F. Vazquez-Jimenez, and S. J. Sonntag, “Using 3D Physical Modeling to Plan Surgical Corrections of Complex Congenital Heart Defects,” *Thorac. Cardiovasc. Surg.*, vol. 65, no. 1, pp. 031–035, 2017.

[140] L. Sasson *et al.*, “Right ventricular outflow tract strategies for repair of tetralogy of Fallot: Effect of monocusp valve reconstruction,” *Eur. J. Cardio-thoracic Surg.*, vol.

43, no. 4, pp. 743–751, 2013.

[141] J. Li *et al.*, “Newborn screening for congenital heart disease using echocardiography and follow-up at high altitude in China,” *Int. J. Cardiol.*

[142] A. Mashari *et al.*, “Making three-dimensional echocardiography more tangible: a workflow for three-dimensional printing with echocardiographic data.,” *Echo Res. Pract.*, vol. 3, no. 4, pp. R57–R64, Dec. 2016.

[143] J. Gosnell, T. Pietila, B. P. Samuel, H. K. N. Kurup, M. P. Haw, and J. J. Vettukattil, “Integration of Computed Tomography and Three-Dimensional Echocardiography for Hybrid Three-Dimensional Printing in Congenital Heart Disease,” *J. Digit. Imaging*, vol. 29, no. 6, 2016.

[144] T. Bharucha, A. M. Hlavacek, D. E. Spicer, P. Theocharis, and R. H. Anderson, “How should we diagnose and differentiate hearts with double-outlet right ventricle?,” *Cardiol. Young*, vol. 27, no. 1, pp. 1–15, 2017.

[145] M. Cantinotti, I. Valverde, and S. Kutty, “Three-dimensional printed models in congenital heart disease,” *International Journal of Cardiovascular Imaging*, vol. 33, no. 1. 2017.

[146] A. Mashari *et al.*, “Making three-dimensional echocardiography more tangible: a workflow for three-dimensional printing with echocardiographic data,” *Echo Res. Pract.*, vol. 3, no. 4, pp. R57–R64, 2016.

[147] K. M. Farooqi, C. Gonzalez-Lengua, R. Shenoy, J. Sanz, and K. Nguyen, “Use of a Three Dimensional Printed Cardiac Model to Assess Suitability for Biventricular Repair,” *World J. Pediatr. Congenit. Hear. Surg.*, vol. 7, no. 3, pp. 414–416, May 2016.

[148] N. Hibino, “Three Dimensional Printing: Applications in Surgery for Congenital Heart Disease,” *World J. Pediatr. Congenit. Heart Surg.*, vol. 7, no. 3, pp. 351–352, 2016.

[149] L. Chepelev *et al.*, “Radiological Society of North America (RSNA) 3D printing Special Interest Group (SIG): guidelines for medical 3D printing and appropriateness for clinical scenarios,” *3D Print. Med.*, vol. 4, no. 1, p. 11, 2018.

[150] M. F. Refojo, *Application of Materials in Medice and Dentistry: Ophthalmologic Applications*. 1996.

[151] M. Odeh *et al.*, “Methods for verification of 3D printed anatomic model accuracy using cardiac models as an example,” pp. 1–12, 2019.

[152] “3D-DOCTOR, medical modeling, 3D medical imaging.” [Online]. Available: http://www.ablesw.com/3d-doctor/. [Accessed: 26-Nov-2018].

[153] “Mimics Innovation Suite | Materialise Medical 3D Printing.” [Online]. Available: https://www.materialise.com/en/medical/mimics-innovation-suite. [Accessed: 26-Nov-2018].

[154] “InVesalius home | CTI Renato Archer.” [Online]. Available: https://www.cti.gov.br/pt-br/invesalius. [Accessed: 26-Nov-2018].

[155] “3D Image Processing.” [Online]. Available: https://www.synopsys.com/simpleware.html. [Accessed: 26-Nov-2018].

[156] “OsiriX DICOM Viewer | The world famous medical imaging viewer.” [Online]. Available: https://www.osirix-viewer.com/. [Accessed: 26-Nov-2018].

[157] E. Barnett and C. Gosselin, “Weak support material techniques for alternative additive manufacturing materials,” *Addit. Manuf.*, vol. 8, pp. 95–104, 2015.

[158] “Introduction to ANSYS DesignModeler | ANSYS.” [Online]. Available: https://www.ansys.com/services/training-center/platform/introduction-to-ansys-designmodeler. [Accessed: 02-Aug-2019].

[159] “Geomagic Studio 12 offers fastest way to convert 3D scans of physical objects into parametric models for direct exchange with PTC® Pro/ENGINEER® | 3D Systems.” [Online]. Available: https://www.3dsystems.com/press-releases/geomagic/studio-12-offers-fastest-way-to-convert-3d-scans-of-phy. [Accessed: 10-Dec-2018].

[160] “Materialise Anatomical Modeling and Patient-Specific Design Software | Materialise 3-matic.” [Online]. Available: https://www.materialise.com/en/medical/software/3-matic. [Accessed: 29-Nov-2018].

[161] “FreeCAD: Your own 3D parametric modeler.” [Online]. Available: https://www.freecadweb.org/. [Accessed: 02-Aug-2019].

[162] “3D CAD Design Software | SOLIDWORKS.” [Online]. Available: https://www.solidworks.com/. [Accessed: 02-Aug-2019].

[163] “Rhino 6 for Windows and Mac.” [Online]. Available: https://www.rhino3d.com/. [Accessed: 02-Aug-2019].

[164] J. Garcia, Z. Yang, R. Mongrain, R. L. Leask, and K. Lachapelle, “3D printing materials and their use in medical education: a review of current technology and trends for the future,” *BMJ Simul. Technol. Enhanc. Learn.*, p. bmjstel-2017-000234, 2017.

[165] T. Bartel, A. Rivard, A. Jimenez, C. A. Mestres, and S. Müller, “Medical three-dimensional printing opens up new opportunities in cardiology and cardiac surgery,” *European Heart Journal*, vol. 39, no. 15. 2018.

[166] K. H. A. Lim, Z. Y. Loo, S. J. Goldie, J. W. Adams, and P. G. McMenamin, “Use of 3D printed models in medical education: A randomized control trial comparing 3D prints versus cadaveric materials for learning external cardiac anatomy,” *Anat. Sci. Educ.*, vol. 9, no. 3, pp. 213–221, 2016.

[167] S. Rosales, S. Ferrándiz, M. J. Reig, and J. Seguí, “Study of soluble supports generation in 3d printed part,” *Procedia Manuf.*, vol. 13, pp. 833–839, 2017.

[168] M. A. Habib and B. Khoda, “Support grain architecture design for additive manufacturing,” *J. Manuf. Process.*, vol. 29, pp. 332–342, 2017.

[169] P. Bhatla *et al.*, “Utility and Scope of Rapid Prototyping in Patients with Complex Muscular Ventricular Septal Defects or Double-Outlet Right Ventricle: Does it Alter Management Decisions?,” *Pediatr. Cardiol.*, vol. 38, no. 1, 2017.

[170] L. Zhao, S. Zhou, T. Fan, B. Li, W. Liang, and H. Dong, “Three-dimensional printing enhances preparation for repair of double outlet right ventricular surgery,” *J. Card. Surg.*, 2018.

[171] S. C. Ligon, R. Liska, J. Stampfl, M. Gurr, and R. Mülhaupt, “Polymers for 3D Printing and Customized Additive Manufacturing.,” *Chem. Rev.*, vol. 117, no. 15, pp. 10212–10290, Aug. 2017.

[172] T. Shirakawa, Y. Koyama, H. Mizoguchi, and M. Yoshitatsu, “Morphological analysis and preoperative simulation of a double-chambered right ventricle using 3-dimensional printing technology,” *Interact. Cardiovasc. Thorac. Surg.*, vol. 22, no. 5, pp. 688–690, 2016.

[173] S. C. Ligon, R. Liska, J. Stampfl, M. Gurr, and R. Mülhaupt, “Polymers for 3D Printing and Customized Additive Manufacturing,” *Chem. Rev.*, vol. 117, no. 15, pp. 10212–10290, Aug. 2017.

[174] A. Christensen and F. J. Rybicki, “Maintaining safety and efficacy for 3D printing in medicine,” *3D Print. Med.*, vol. 3, no. 1, p. 1, 2017.

[175] S. Belhabib and S. Guessasma, “Compression performance of hollow structures: From topology optimisation to design 3D printing,” *Int. J. Mech. Sci.*, vol. 133, pp. 728–739, Nov. 2017.

[176] I. T. Ozbolat, K. K. Moncal, and H. Gudapati, “Evaluation of bioprinter technologies,” *Addit. Manuf.*, vol. 13, pp. 179–200, 2017.

[177] “Zaxe 3D Printing Technologies.” [Online]. Available: http://zaxe.com/en/. [Accessed: 11-Dec-2018].

[178] “ProJet CJP 260Plus | 3D Systems.” [Online]. Available: https://www.3dsystems.com/3d-printers/projet-cjp-260plus. [Accessed: 11-Dec-2018].

[179] D. Ryan and C. Engineering, “ANSYS ICEM CFD and ANSYS CFX Introductory Training Course,” *Training*, pp. 1–20, 2011.

[180] “Engineering Simulation & 3D Design Software | ANSYS.” [Online]. Available: https://www.ansys.com/. [Accessed: 03-Aug-2019].

[181] “Finite Element Mesh Refinement Definition and Techniques.” [Online]. Available: https://www.comsol.com/multiphysics/mesh-refinement. [Accessed: 03-Aug-2019].

[182] “Computational Fluid Dynamics : A Practical Approach.” [Online]. Available: http://021074mes.y.http.eds.a.ebscohost.com.proxy.medipol.deep-knowledge.net:9797/eds/ebookviewer/ebook?sid=a44fe135-0b23-4bfb-8dcb-c855882e226a%40sessionmgr4008&vid=0&format=EB. [Accessed: 10-Dec-2018].

[183] G. Pennati, “Computational fluid dynamics models and congenital heart diseases,” *Front. Pediatr.*, vol. 1, no. February, pp. 1–7, 2013.

[184] T. Al, *Engineering Fluid Mechanics T . Al - Shemmeri*. .

[185] L. D. Landau and E. M. Lifshitz, “Fluid Mechanics,” *Image Rochester NY*, vol. 6, no. 1, p. 539, 1987.

[186] P. D. Morris *et al.*, "Computational fluid dynamics modelling in cardiovascular medicine," *Heart*, vol. 102, no. 1, pp. 18–28, Jan. 2016.

[187] C. Gjelsvik, "Modeling and Simulation of the Human Body," no. January, 2016.

[188] T. R. Zienkiewicz, O. C., Nithiarasu, Perumal, *The Finite Element Method for Fluid Dynamics*, 7th ed. Butterworth Heinemann, 2014.

[189] R. L. Zienkiewicz, O. C., Nithiarasu, Perumal, Taylor, *The Finite Element Method for Fluid Dynamics*, 7yh ed. Butterworth Heinemann, 2014.

[190] H. J. Doolarrd, "Single and Multiphase Simulations of Non-Newtonian Blood Flow," *Tu Delft*, 2013.

[191] U. Morbiducci *et al.*, "On the importance of blood rheology for bulk flow in hemodynamic models of the carotid bifurcation," *J. Biomech.*, vol. 44, no. 13, pp. 2427–2438, 2011.

[192] Y. Zhou, C. Lee, and J. Wang, "The Computational Fluid Dynamics Analyses on Hemodynamic Characteristics in Stenosed Arterial Models.," *J. Healthc. Eng.*, vol. 2018, p. 4312415, 2018.

[193] A. Razavi, E. Shirani, and M. R. Sadeghi, "Numerical simulation of blood pulsatile flow in a stenosed carotid artery using different rheological models," *J. Biomech.*, vol. 44, no. 11, pp. 2021–2030, 2011.

[194] A. M. Sallam and N. H. Hwang, "Human red blood cell hemolysis in a turbulent shear flow: contribution of Reynolds shear stresses.," *Biorheology*, vol. 21, no. 6, pp. 783–97, 1984.

[195] A. Fluent, "Ansys Fluent Theory Guide," *ANSYS Inc., USA*, vol. 15317, no. November, pp. 724–746, 2013.

[196] "Fluent Theory Guide." [Online]. Available: https://www.sharcnet.ca/Software/Ansys/16.2.3/en-us/help/flu_th/flu_th.html. [Accessed: 05-Aug-2019].

[197] J. Muhammad *et al.*, "Patient-Specific Atrial Hemodynamics of a Double Lumen Neonatal Cannula in Correct Caval Position," *Artif. Organs*, vol. 42, no. 4, pp. 401–409, Apr. 2018.

[198] J. Jung, R. W. Lyczkowski, C. B. Panchal, and A. Hassanein, "Multiphase hemodynamic simulation of pulsatile flow in a coronary artery," *J. Biomech.*, vol. 39, no. 11, pp. 2064–2073, 2006.

[199] H. I. Andersson, R. Halden, and T. Glomsaker, "Effects of surface irregularities on flow resistance in differently shaped arterial stenoses," *J. Biomech.*, vol. 33, no. 10, pp. 1257–1262, 2000.

[200] K. K. Whitehead, K. Pekkan, H. D. Kitajima, S. M. Paridon, A. P. Yoganathan, and M. A. Fogel, "Nonlinear Power Loss During Exercise in Single-Ventricle Patients After the Fontan: Insights From Computational Fluid Dynamics," *Circulation*, vol. 116, no. 11_suppl, pp. I-165-I–171, Sep. 2007.

[201] “What is von Mises Stress? — SimScale Documentation.” [Online]. Available: https://www.simscale.com/docs/content/simwiki/fea/what-is-von-mises-stress.html. [Accessed: 07-Aug-2019].

[202] A. Niku-Lari, *Structural analysis systems : software, hardware, capability, compatibility, applications. Volume 1*. Pergamon, 1986.

[203] S. K. F. Ansel C. Ugural, *Advanced Mechanics of Materials*, 5th ed. Westford: Prentice Hall, 1394.

[204] S. M. A. Kazimi, *Solid mechanics*. Tata McGraw-Hill, 1984.

[205] “ansys56manual.pdf.” .

[206] J. K. N. Richard G. Budynas, *Shigley’s Mechanical Engineering Design*, 10th ed. Mc Graw Hill.

[207] S. Kutty *et al.*, “Ascending aortic and main pulmonary artery areas derived from cardiovascular magnetic resonance as reference values for normal subjects and repaired tetralogy of fallot,” *Circ. Cardiovasc. Imaging*, vol. 5, no. 5, pp. 644–651, 2012.

[208] S. Donmazov, S. Piskin, and K. Pekkan, “Noninvasive In Vivo Determination of Residual Strains and Stresses,” *J. Biomech. Eng.*, vol. 137, no. 6, p. 061011, Jun. 2015.

[209] K. S. Matthys *et al.*, “Pulse wave propagation in a model human arterial network: Assessment of 1-D numerical simulations against in vitro measurements,” *J. Biomech.*, vol. 40, no. 15, pp. 3476–3486, 2007.

[210] D. B. McElhinney, A. K. Hoydu, J. W. Gaynor, T. L. Spray, E. Goldmuntz, and P. M. Weinberg, “Patterns of right aortic arch and mirror-image branching of the brachiocephalic vessels without associated anomalies,” *Pediatr. Cardiol.*, vol. 22, no. 4, pp. 285–291, 2001.

[211] K. R. Kanter, R. N. Vincent, and D. A. Fyfe, “Reverse subclavian flap repair of hypoplastic transverse aorta in infancy,” *Ann. Thorac. Surg.*, vol. 71, no. 5, pp. 1530–1536, 2001.

[212] Q. Sun *et al.*, “Influence of antegrade pulmonary blood flow on the hemodynamic performance of bidirectional cavopulmonary anastomosis: A numerical study,” *Med. Eng. Phys.*, vol. 31, no. 2, pp. 227–233, 2009.

[213] “ModuleWorks offer free STL viewer for Android and Windows | ModuleWorks.” [Online]. Available: https://www.moduleworks.com/moduleworks-offer-free-stl-viewer-for-android-and-windows/. [Accessed: 28-Nov-2018].

[214] “Z-MED™ & Z-MED II™ | B. Braun Interventional Systems.” [Online]. Available: http://www.bisusa.org/products/pta-ptv-balloons/z-med. [Accessed: 10-Dec-2018].

COMPUTATIONAL FLUID DYNAMICS ANALYSIS IN PRE-SURGERY PLANNING FOR CONGENITAL HEART DEFECT REPAIRS

ORIGINALITY REPORT

15%	9%	9%	7%
SIMILARITY INDEX	INTERNET SOURCES	PUBLICATIONS	STUDENT PAPERS

PRIMARY SOURCES

1	www.doria.fi Internet Source	1%
2	www.simscale.com Internet Source	1%
3	S. Samaneh Lashkarinia, Senol Piskin, Tijen A. Bozkaya, Ece Salihoglu, Can Yerebakan, Kerem Pekkan. "Computational Pre-surgical Planning of Arterial Patch Reconstruction: Parametric Limits and In Vitro Validation", Annals of Biomedical Engineering, 2018 Publication	1%
4	www.cfd-online.com Internet Source	<1%
5	Submitted to Dokuz Eylul Universitesi Student Paper	<1%
6	Submitted to University of Utah Student Paper	<1%